Complex Hydride Compounds with Enhanced Hydrogen Storage Capacity

Final Report

Daniel A. Mosher, Susanne M. Opalka, Xia Tang, Bruce L. Laube, Ronald J. Brown, Thomas H. Vanderspurt, Sarah Arsenault
United Technologies Research Center

Robert Wu, Jamie Strickler
Albemarle Corporation

Donald L. Anton, Ragaiy Zidan, Polly Berseth
Savannah River National Laboratory

February 14, 2008

Prepared for
Department of Energy
Office of Energy Efficiency and Renewable Energy
Hydrogen Program, Hydrogen Storage
Under Contract DE-FC36-04GO14012
Sunita Satyapal, DOE Hydrogen Program Team Leader
Carole Read, DOE Headquarters Technology Manager
Jesse Adams, DOE Field Project Officer

United Technologies Research Center

DOE Hydrogen Program

Table of Contents

Table of Contents

List of Tables

List of Figures

List of Figures

List of Figures

List of Figures

List of Figures

Acknowledgements

The authors would like to thank JoAnn Milliken, Sunita Satyapal, Carole Read, Jesse Adams and George Thomas of the Department of Energy (DOE) for their support and input over the course of this project. Additional thanks go to the following organizations and individuals for their contributions, advice and guidance:

Institutt for Energiteknikk
Bjorn C. Hauback, Hans W. Brinks, O. L. Martin

Norwestern University / QuesTek Innovations
Prof. Greg Olsen, W. Huang

Sandia National Laboratories
Ewa Rönnebro

United Technologies Corporation Power division
Francis R. Preli, Ram Ramaswamy
Michael F. Short, Dave M. Flanaghan

United Technologies Research Center
Craig R. Walker, Jodi A. Vecchiarelli, Susan D. Brandes
Laurence M. Pryor

1 Executive Summary

From 2002 to 2007, the United Technologies Research Center (UTRC), in collaboration with major partners Albemarle Corporation (Albemarle) and the Savannah River National Laboratory (SRNL), conducted research to discover new hydride materials for the storage of hydrogen having on-board reversibility and a target gravimetric capacity of ≥ 7.5 weight percent (wt %). When integrated into a system with a reasonable efficiency of 60% (mass of hydride / total mass), this target material would produce a system gravimetric capacity of ≥ 4.5 wt %, consistent with the DOE 2007 target.

The approach established for the project combined first principles modeling (FPM - UTRC) with multiple synthesis methods: Solid State Processing (SSP - UTRC), Solution Based Processing (SBP - Albemarle) and Molten State Processing (MSP - SRNL). In the search for novel compounds, each of these methods has advantages and disadvantages; by combining them, the potential for success was increased. During the project, UTRC refined its FPM framework which includes ground state (0 Kelvin) structural determinations, elevated temperature thermodynamic predictions and thermodynamic / phase diagram calculations. This modeling was used both to precede synthesis in a virtual search for new compounds and after initial synthesis to examine reaction details and options for modifications including co-reactant additions. The SSP synthesis method involved high energy ball milling which was simple, efficient for small batches and has proven effective for other storage material compositions. The SBP method produced very homogeneous chemical reactions, some of which cannot be performed via solid state routes, and would be the preferred approach for large scale production. The MSP technique is similar to the SSP method, but involves higher temperature and hydrogen pressure conditions to achieve greater species mobility.

During the initial phases of the project, the focus was on higher order alanate complexes in the phase space between alkaline metal hydrides (AmH), Alkaline earth metal hydrides (AeH_2), alane (AlH_3), transition metal (Tm) hydrides (TmHz, where z=1-3) and molecular hydrogen (H_2). The effort started first with variations of known alanates and subsequently extended the search to unknown compounds. In this stage, the FPM techniques were developed and validated on known alanate materials such as $NaAlH_4$ and Na_2LiAlH_6. The coupled predictive methodologies were used to survey over 200 proposed phases in six quaternary spaces, formed from various combinations of Na, Li Mg and/or Ti with Al and H.

A wide range of alanate compounds was examined using SSP having additions of Ti, Cr, Co, Ni and Fe. A number of compositions and reaction paths were identified having H weight fractions up to 5.6 wt %, but none meeting the 7.5 wt%H reversible goal. Similarly, MSP of alanates produced a number of interesting compounds and general conclusions regarding reaction behavior of mixtures during processing, but no alanate based candidates meeting the 7.5 wt% goal. A novel alanate, $LiMg(AlH_4)_3$, was synthesized using SBP that demonstrated a 7.0 wt% capacity with a desorption temperature of 150°C. The deuteride form was synthesized and characterized by the Institute for Energy (IFE) in Norway to determine its crystalline structure for related FPM studies. However, the reaction exhibited exothermicity and therefore was not reversible under acceptable hydrogen gas pressures for on-board recharging.

After the extensive studies of alanates, the material class of emphasis was shifted to borohydrides. Through SBP, several ligand-stabilized $Mg(BH_4)_2$ complexes were synthesized. The $Mg(BH_4)_2*2NH_3$ complex was found to change behavior with slightly different synthesis conditions

and/or aging. One of the two mechanisms was an amine-borane (NH_3BH_3) like dissociation reaction which released up to 16 wt %H and more conservatively 9 wt%H when not including H_2 released from the NH_3. From FPM, the stability of the $Mg(BH_4)_2$*$2NH_3$ compound was found to increase with the inclusion of NH_3 groups in the inner-Mg coordination sphere, which in turn correlated with lowering the dimensionality of the $Mg(BH_4)_2$ network. Development of various Ak-Tm-B-H compounds using SSP produced up to 12 wt% of H_2 desorbed at temperatures of 400°C. However, the most active material can only be partially recharged to 2 wt% H_2 at 220-300˚C and 195 bar H_2 pressure due to stable product formation. A summary of the material performance along with a conversion to system performance based on the parameters of footnote [1] is given in Table 1. The gravimetric & volumetric targets are feasible, but reversibility is a persistent challenge.

Table 1: Summary of synthesized material / system performance.

Hydrogen Storage System Targets [1,2]				
Target	**Units**	**2007 System Targets**	**'05 to '06 Best Alanate $LiMg(AlH_4)_3$ / System**	**'06 to '07 Best Borohydride $Mg(BH_4)_2$*$2NH_3$ / System**
Gravimetric Capacity	kWh/kg (kg H2/kg)	1.5 (0.045)	2.1 / 1.3 (0.070 / 0.042)	3.0 / 1.8 (0.091 / 0.055)
Volumetric Capacity [3]	kWh/L (kg H2/L)	1.2 (0.036)	0.5 / 0.38 [4] (0.015 / 0.011)	1.5 / 1.1 (0.044 / 0.033)
Desorption Rate [5] & Temperature	g/s/kW °C	0.02 (<100)	0.019 165	0.037 100-300

[1] For a system design with the material being 60% of the system mass & 75% of the system volume.
[2] The materials listed are not reversible.
[3] Powders subjected to a standard vibratory densification process.
[4] $LiMg(AlH_4)_3$ was in the as-received condition; ball milling could improve powder densification.
[5] Calculated results based on 5 kg of storage for a 75 kW fuel cell.

Our high level observations and recommendations are as follows:

- First Principles Modeling was productively integrated with syntheses and characterization to screen, investigate and evaluate new materials. Discovery of new materials from modeling alone is very difficult; FPM yields the greatest value when iteratively coupled with experiments.
- There were clear benefits to having multiple organizations apply their distinct synthesis methods concurrently in the same material exploration.
- Multiple organizations conducting characterization can be straightforward to execute, but care should be taken in understanding aging effects when working with potentially unstable materials.
- Based on the current studies, we concur with the trends in the community that the potential of alanates is insufficient to motivate a strong emphasis in future novel materials research.
- While no completely viable storage materials were synthesized in this effort, we feel that potential remains in developing high capacity borohydrides with tailored reactions which could result in adequate reversibility / regenerability.

In addition, 11 publications and over 13 presentations were produced as well as numerous other collaborations, reviews and meetings involving the domestic and international hydrogen storage communities during the performance of this contract.

2 Overview

This final report describes the motivations, activities and results of the hydrogen storage independent project *Complex Hydride Compounds with Enhanced Hydrogen Storage Capacity* performed by the United Technologies Research Center (UTRC) under the Department of Energy (DOE) Hydrogen Program, contract # DE-FC36-04GO14012. This effort officially began in April of 2002 and performed technical research through August of 2007 with subsequent concluding activities and reporting. In addition to UTRC, two organizations had central roles in the execution of this contract: Albemarle Corporation (Albemarle) and Savannah River National Laboratory (SRNL). DOE financial support to UTRC and Albemarle was $1,695 k, with these organizations contributing $785k (31.7%) of cost share resources. SRNL received $450k of DOE funds, resulting in a total contract of $2,930k.

2.1 Project Motivations and Scope

It is well recognized that storage of hydrogen in a compact and lightweight form is critical to the commercial introduction of hydrogen as an energy carrier, particularly for automotive fuel cells, with the benefits of reduced dependence on foreign oil and increased potential for utilizing renewable energy sources. According to the National Academies' February 2004 report on the DOE Hydrogen Program:

> *"A transition to hydrogen as a major fuel in the next 50 years could fundamentally transform the U.S. energy system, creating opportunities to increase energy security through the use of a variety of domestic energy resources for hydrogen production while reducing environmental impacts, including atmospheric CO_2 emissions and criteria pollutants."*

The major classes of established hydrogen storage methods are compressed gas, cryogenic liquid, metal hydrides, chemical hydrides and adsorbents, all of which have advantages and disadvantages, but none is clearly superior for automotive transportation. High pressure compressed gas systems have been certified for automotive use, but do not meet all of the desired targets. Cryogenic liquefied hydrogen has a substantial energy penalty of over 30% for production and is susceptible to boil-off issues. A disadvantage of conventional reversible metal hydrides is their low hydrogen capacities of less than 2 wt% for alloys with discharge temperatures for which the waste heat of a PEM fuel cell (~90 °C) can be used to release the hydrogen.

Complex hydride materials have the potential to store higher capacities of hydrogen than conventional metal hydrides for indefinite periods of time and require only moderate hydrogen gas pressures for recharging. Associated with this are the lower energy losses compared with high pressure gas compression and liquefying processes as well as potential safety benefits. Challenges include developing novel, high hydrogen capacity storage materials which can be discharged at temperatures of PEM fuel cell waste heat (100 °C or below) and charged at pressures with acceptable vessel mass (nominally 100 bar).

The goal of this program is the discovery of new complex hydride compounds capable of reversibly storing hydrogen to a capacity of $\geq$ 7.5 wt% with regeneration for over 500 cycles. When integrated into a system with a gravimetric efficiency of 60%, this will produce a $\geq$ 4.5 wt% system. This goal for the material was driven by the emerging and revised DOE technical targets given in Table 2.

Overview

Initially, the focus of the project was composition systems in the quaternary phase space between sodium hydride (NaH), alane (AlH_3), transition metal or rare earth (M) hydrides (MHz, where z= 1-3) and molecular hydrogen (H_2). In the latter portion of the project, the scope was extended to include other complex hydrides including borohydrides.

Table 2: DOE technical targets for on-board hydrogen storage systems.

Storage Parameter	Units	2007 Target
System Gravimetric Capacity	kg H_2 / kg system	0.045
System Volumetric Capacity	kg H_2 / L system	0.036
System Fill Time	min	10
Minimum Full Flow Rate	(g/s) / kW	0.02
Storage System Cost	$ / kg H_2	200
Cycle Life	Cycles	500
Safety	N/A	Meets C&S

The search for novel, high capacity complex hydride compounds was supported by the development and application of first principles modeling. These simulations were coupled with thermodynamic predictions and characterization experiments to develop the framework which was used both to lead synthesis efforts and to understand existing novel phases. Simultaneously, multiple synthetic methodologies were employed to enhance options for discovery of new hydrides. These methods included Solid State Processing (SSP) at UTRC, Solution Based Processing (SBP) at Albemarle and Molten State Processing (MSP) at SRNL. A high level breakdown of the project is given in Figure 1.

Task / Phase	First Principles Modeling	Solid-State Processing	Solution-Based Processing	Molten-State Processing	Thermo-dynamic Modeling
2004 Known Alanates	Implement finite T predictions.	Search out quaternary systems encompassing known alkali alanates. Validate atomic-thermodynamic modeling.			Establish thermo. databases.
2005 Novel Alanates	Predict candidate properties.	Search out high capacity alanates with alkaline earth or transition metal elements. Characterize properties. Test performance.			Implement reaction design.
2006 Novel Boro-hydrides	Refine phase structure & thermo. predictions.	Synthesize high capacity borohydrides containing alkaline earths, transition metals and/or stabilized with ligands.			Design high capacity reactions.
2007 Final Phase	Probe rx. mechanisms.	Down-select best system and synthesis method. Optimize reversibility and kinetics.			Design reversibility.

Figure 1: Overview of project effort material systems, modeling and synthesis.

Initially, the focus of the composition systems was complex, mixed metal alanates. While novel compounds with good hydrogen capacity were developed, reversibility and discharge temperature did not meet the desired targets. To broaden the scope, high capacity borohydrides were explored in the latter portion of the project. A more detailed breakdown of the composition systems and examination methods is given in Table 3.

Table 3: Summary of composition systems and methods of modeling / synthesis. Tm= transition metal; FPM = First Principles Modeling; SSP = Solid State Processing; SBP = Solution Based Processing and MSP = Molten State Processing.

System	Compositions	Method
Alanates	Na-Li-Al-H	FPM, SSP, MSP
	Na-Tm-Al-H	FPM, SSP, SBP, MSP
	Li-Tm-Al-H	FPM, SSP, SBP, MSP
	Na-Mg-Al-H	FPM, SSP, SBP, MSP
	Li-Mg-Al-H	FPM, SSP, SBP
	Li-Na-Mg-(Ti,V,Cr,Mn,Ni,Co,Fe)-H	SSP, MSP
Borohydrides	Tm-B-H w/ ligands	SBP
	Mg-B-H w/ & w/o ligands or coreactants	FPM, SSP, SBP, MSP
	Ak-Tm-B-H w/ & w/o ligands	FPM, SSP, SBP

This document was prepared in Microsoft Word, and if an electronic copy is available, the Document Map feature can be used to facilitate navigation from section to section. A similar structure has been produced in the PDF file conversion process. The Bookmarks tab of the Navigation Pane provides an outline of the report and a convenient method to jump from section to section. Hyperlinks are also included for in-text section numbers, figures, tables, equations and references.

2.2 Statement of Project Objectives

An abbreviated and reformatted version of the original Statement of Project Objectives is given below. Based on experience gained throughout the project, the detailed approach and objectives were modified while maintaining the same high level structure.

First Principles Modeling

- Evaluate theoretical phase stability
- Simulate new quaternary compositions to recommend for synthesis targets
- Predict reversible hydrogen content of the best hydride candidates
- Identify new catalyzed compositions with decreased dehydrogenation activation barriers
- Guide development of new complex hydride compound phases
- Materials:
  - Known Alanate Characteristics
  - Alanate Phase Predictions
  - Catalyzed Complex Hydrides

Synthesis

- Synthesize materials at UTRC and Albemarle via at least one of two distinct processing routes, which both have potential for commercialization. These are solid state processing (SSP) and solute based processing (SBP).
- SRNL will perform synthesis primarily using Molten State Processing (MSP)
- Materials:
  - Known Alanate Structures
  - Known Alanate Catalysts I

- Known Alanate Catalysts II
- Modeled Structures
- Catalyzed Structures

Analysis

- Primary analysis technique of x-ray diffraction
- Apply on each sample synthesized to identify the presence of new crystal structures or significantly distorted structures of existing phases.
- Once a phase has been identified as a candidate, apply more sophisticated analysis including neutron diffraction and high-resolution X-ray analyses to determine more precisely the structure of material synthesized.

Performance

- Capacity
  - For the Na-Ti-Al-H quaternary phase diagram, provide predictions and theoretical calculations for hydrogen capacity and potential for reversibility.
  - Complete empirical compositional section phase diagrams and pressure-composition-temperature diagrams for evaluation of phase stability and reversible hydrogen content of Na-Ti-Al-H systems.
  - Down-select of materials from Na-Ti-Al-H system that have potential for both capacity and reversibility.
- Reversibility
  - Down-select of material processing routes that have the greatest potential for large-scale commercialization.
  - Make predictions based on first principles modeling for high hydrogen capacity and potential reversibility based on Li-Mg-V, Cr, Mn, Fe, Co, Mo, Ce or other rare earth elements complex hydrides
  - Down-select complex aluminum hydrides containing Li-Mg-V, Cr, Mn, Fe, Co, Mo, Ce or other rare earth elements.

SRNL Objectives

- Materials will be synthesized via Molten State Processing (MSP), utilizing their specialized equipment and technical expertise.
- Materials identical to those listed under “Synthesis” above

If mature storage material candidates are identified, perform the following development activities:

Materials Stability

- Evaluate reactivity with storage system structural materials and study safety issues.

Scale Up

- Move synthesis from the laboratory to the High Pressure Facility at the Albemarle Baton Rouge Process Development Center to evaluate kg scale material production.

Business Analysis

- Develop cost and performance metrics of the complex hydride compound media and the storage subsystems.

Overview

As stated above and described in more detail below, the examinations during the first 1 to 2 years focused on alanate compositions and subsequently broadened the material types pursued to borohydrides during the remainder of the effort. While novel materials with improved performance were developed, they did not meet the maturity level required to justify pursuit of the Stability, Scale Up and Business Analysis tasks.

3 First Principles and Thermodynamic Modeling

3.1 Introduction/Background/Rational

3.1.1 Quaternary Systems Encompassing Known Alanate Phases

The motivation for this study was to overcome the existing reversible H capacity limitations of known hydride systems by seeking out elevated H-bearing compounds akin to the elusive reported compounds yet to be defined crystallographically, such as the titanium alanate compound, $Ti(AlH_4)_4$, with 8 or more wt% retrievable H capacity [Ref. 1]. First principles modeling was deployed to virtually explore selected multi-dimensional composition phase spaces for potential new hydride structures with high capacities of greater than 7.5 wt% retrievable H and to assess the relative stability of these structures with respect to known phases that may compete for existence. Our founding system was the Na-Ti-Al-H quaternary composition phase space bounded by the elements: Na, Al, Ti, H, that encompasses the well-known sodium alanate system and the associated phases that may form upon Ti-doping and/or dehydrogenation of the sodium alanate phases. Possible other competing phases, related lower order phases, including hypothetical end-member phases for varying substitution were also simulated.

The Na-Ti-Al-H phase space quaternary system with the known peripheral binary and ternary phases is shown schematically in Figure 2. Here, the unknown interior of the phase space was surveyed extensively for possible new stoichiometries or structures that may be stable for existence. Our motivation went beyond the reports of high capacity compounds [Ref. 1] and the well-known catalytic effects of Ti in sodium alanates [Refs. 2, 3 and 4], to simulate new complex hydride structures enabled by the accessible and hybridizable Ti 3d electronic states. Here, a series of coupled methodologies were implemented for postulating and evaluating Na-Ti-Al-H complex hydride phase structures with varying Ti coordination numbers and formal changes. Since Ti can essentially catalyze disproportionation or comproportionation reactions by thermodynamically destabilizing alkali alanate complexes [Refs. 5 and 6] and/or by forming very favorable titanium-aluminide compounds [Ref. 7], Ti incorporation also provided the means for tailoring complex hydride thermodynamic properties.

At the outset, the best available hydride system with reversible retrieval of the highest known H capacity under moderate temperature and pressure conditions was the Na-Al-H system with the two sodium alanate phases, $NaAlH_4$ and Na_3AlH_6. In the first year, we progressively built upon our knowledge of the sodium alanate system to seek out and discover higher H capacity alanate and/or complex hydride phases. New protocols were established for model development, simulation, and analyses of phase candidates. These prediction protocols were first validated by benchmarking sodium alanate and Na-Al-H system predictions against experimental data for the Na-Al-H system. We also utilized our understanding of the sodium alanate crystal structures as a guide to systematically propose, simulate and evaluate new quaternary compounds based upon the analog structures of known ternary alkali and/or alkaline earth compounds, ternary alkali/alkaline earth and transition metal compounds, and ternary transition metal compounds.

The utility of the new prediction protocols was demonstrated by executing virtual surveys on systems encompassing some well-known sodium and lithium alanate phases: Na-Ti-Al-H, Li-Ti-Al-H, and

Na-Li-Al-H. The latter two quaternary systems were based on the higher potential capacity, but less reversible Li-Al-H system with the lithium alanate phases, $LiAlH_4$ and Li_3AlH_6. The rationale for the Li-Ti-Al-H system was that replacement of Na in the most favorable Na-Ti-Al-H quaternary phases with Li could provide significant increases in reversible hydrogen capacity both due to the lower Li atomic weight and to the possible formation of H-free Li-Al binary phases upon disproportionation. Mixed alkali compositions also offered the prospect of tailoring both complex hydride reversibly and kinetics. This exploration of mixed alkali systems was motivated by the known existence of a number of mixed alkali complex compounds and structural analogs.

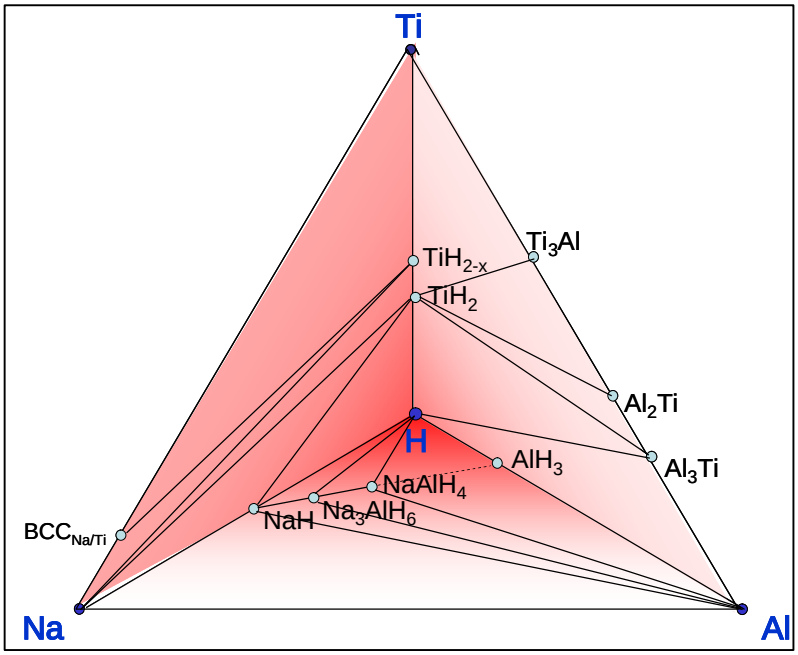

Figure 2: Aerial view of Na-Ti-Al-H quaternary pyramid.

The new simulation protocols were then utilized to explore other lesser-known compositional spaces in the remainder of the program, including the two quaternary systems: Na-Mg-Al-H and Li-Mg-Al-H, formed by adding the Mg alkaline earth to the Na-Al-H and Li-Al-H systems respectively. The Li-Mg-Al-H quaternary space with known peripheral binary and ternary phases is shown schematically in Figure 3. This modeling stage broke new ground on two fronts, demonstrating the ability to: (1) survey lesser known compositional phase spaces with very limited experimental observations (or "leads") of complex hydride compound formation and (2) execute virtual surveys expediently in tandem with experimentation. These two mixed alkali/alkaline earth quaternary systems provided new opportunities for the discovery of high H capacity compounds by incorporating unique features of Mg-bearing phases. When the divalent Mg ion is replaced for two mono-valent alkali ions in known alanate structures, the Mg ion may effectively coordinate with a greater number of Al-H complexes to redistribute charge balance within the structure. For sodium alanates (but not for lithium alanates), such a substitution would result in weight reduction and a marked increase in gravimetric H capacity. In many Mg-bearing aluminum fluoride phases, the Mg ions form unique coordinative environments, e.g. directly bonding with fluoride anions outside of the Al complexes or coordinating as counter-ions with a very large number of neighboring fluoride anions. The Mg-bearing complex hydrides offered

the possible advantage of disproportionation to form binary and ternary Mg intermetallic compounds upon dehydrogenation. The formation of these phases in place of Mg hydride (MgH_2) would decrease the amount of bound hydrogen, and thus, would increase the reversible hydrogen content upon dehydrogenation.

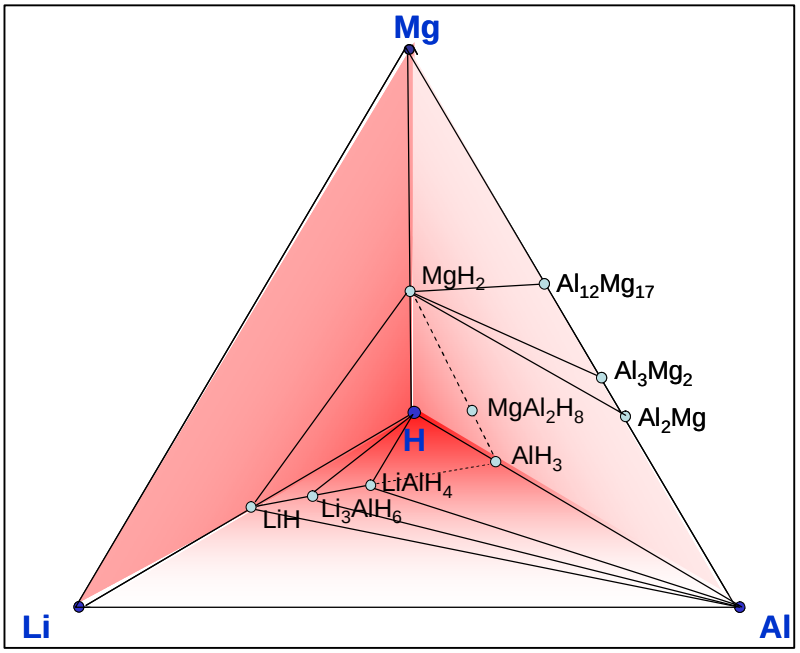

Figure 3: Aerial view of Li-Mg-Al-H quaternary pyramid.

3.1.2 Coupled High Hydrogen Reactions with Complex Hydrides

Following the surveys of the five quaternaries based on the Na-Al-H and Li-Al-H systems, we expanded our original strategy to search out coupled complex hydride reactions with co-reactants to enable the design of low H products upon disproportionation. This expanded strategy, illustrated conceptually in Figure 4, used a triad of first principles modeling, thermodynamic calculations and experimentation to identify, design and refine new reaction pathways for high H reversible capacity. Our atomic-thermodynamic modeling effort was expanded to encompass a larger repertoire of solid-state complex hydride chemistries and hydrogen-retrieval reactions. This expanded strategy built upon our existing capability to search out and discover new phases by comprehensively evaluating all conceivable (known and hypothetical) participating phases and their possible associated reaction pathways, within each multi-order compositional space. We updated our approach to include complex hydride mixtures and reactions with coreactants that can lead to the formation of new products upon decomposition. Such reaction scenarios enabled both the decomposition enthalpy (ΔH) per mole of H_2 generated and the relative stability of reactant and product phases to be adjusted for a given set of temperature and pressure conditions. The result was an even more powerful capability to optimize the overall elemental stoichiometry of a given compositional system to stabilize the most favorable balance of phases that provide access to the largest possible retrievable hydrogen capacity.

First Principles and Thermodynamic Modeling

The thermodynamics of hydride bearing systems were central to the new parallel search strategy, providing fertile ground for integration of our experimental and theoretical synthetic efforts. Within each compositional space, we evaluated existing experimental thermodynamic data in order to identify critical gaps and to develop formulation approaches for high capacity systems. We then applied our coupled atomic-thermodynamic methodology to simulate thermodynamic properties for uncharacterized known phases and for yet-to-be-discovered hypothetical complex hydride phase candidates. Predicted thermodynamic properties were assessed and parameterized, allowing their incorporation within our experimental thermodynamic databases. The supplemented databases were then used to identify the reaction scenarios that leveraged the most hydrogen capacity and to recommend composition targets for synthesis campaigns. Both the thermodynamic results and experimental observations were used to propose new candidate phase models for additional thermodynamic properties simulations. The result was the capability to iteratively refine high hydrogen capacity systems.

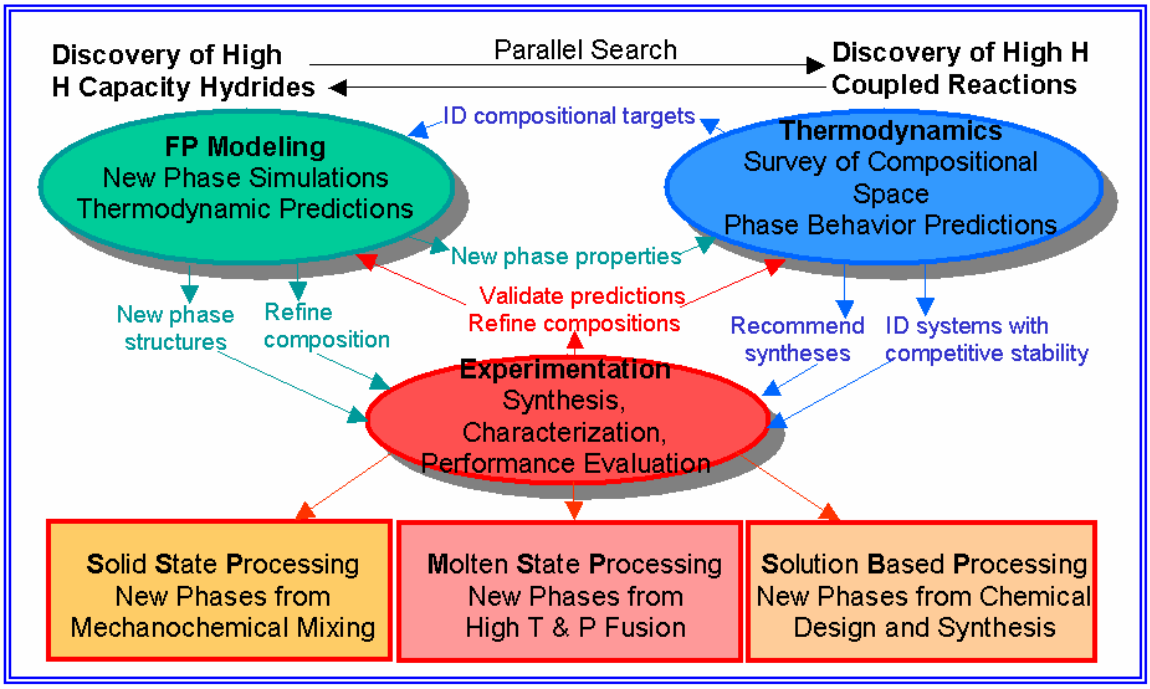

Figure 4: Shematic illustrating parallel search strategy of high H coupled reactions with high H capacity complex hydrides.

3.2 Methodology

3.2.1 Quaternary Survey Approach

Our strategy was to utilize combined atomistic-thermodynamic simulation methodologies to seek out high hydrogen capacity hydride compounds that could reversibly release hydrogen in a single, small reaction enthalpy disproportionation or dehydrogenation step to form predominantly non-hydrogen bearing phases. The combined atomistic-thermodynamic simulations were comprised of five stages, including: 1) model definition, 2) model refinement, 3) candidate phase identification, 4) finite

temperature thermodynamic property predictions and 5) thermodynamic stability predictions, which will be described in detail. Our new protocols iteratively coupled these theoretical methodologies with experimentation to establish a new paradigm for materials exploration.

Our simulations systematically screened candidate complex hydride compositions and structures in the compositional systems evaluated without reference to requisite synthesis conditions and starting reagents. The hierarchical approach used to systematically survey systems of increasing complexity within each compositional space will be described using the founding Na-Ti-Al-H system as an example. Referring to the Na-Ti-Al-H schematic in Figure 2, the trigonal pyramid representing the quaternary space is oriented so that the hydrogen-rich region of interest is closest to the viewer and is symmetrically bounded by the three important ternary surfaces. At the outset, we explored the two surfaces with the Na-Ti-H and Ti-Al-H systems with known binary phases, to complement our existing knowledge of the third Na-Al-H system. In these two systems, we proposed plausible fixed limiting ionic formulae that satisfied a preliminary (lower) minimum criterion of 6 wt% total H, which were derived from substituting the quaternary elements into the stoichiometries of analogous compounds, assuming reasonable oxidation states and/or valences for the constituting elements.

We intentionally wanted to survey as many space groups as possible for each qualifying compound stoichiometry. We developed a catalog of candidate structures for the stoichiometric analogs by conducting an extensive search of crystallographic literature and databases to find complex ternary compound structures: hydrides including boronates, halides, oxides, and to a lesser extent, amides. Structural analogs of covalent oxides, sulfates and their hydrates were not considered. We created models by substituting the Na-Ti-H or Ti-Al-H compositions into the analog compound atomic positions to achieve the desired stoichiometry while maintaining the original analog space group symmetry. The most favorable ternary structures were later used as a basis for simulating quaternary compositions within the trigonal pyramid phase space. We simulated large-scale substitution of the ternary systems with the fourth remaining element, wherever possible, to achieve stoichiometries with greater than 7.5 wt% retrievable hydrogen. The rationale for this approach was that there are relatively few quaternary structural analogs on which to base our simulations and the alloying of line compounds with additional elements can lead compositional ranges for the existence of phases, as opposed to discrete stoichiometries in the ternary system line compounds. We then implemented methodologies to predict thermodynamic potentials and conduct preliminary thermodynamic assessments of potentials of these phases as a function of composition.

3.2.1.1 Model Definition

The multi-pronged, tiered approach employed for the simulation of more than 100 phases within the Na-Ti-Al-H quaternary system (Na-Ti-Al-H) is shown schematically in Figure 5. In this approach, known phase structures were used as templates for the development of potential new phase models, since existing methodologies for the derivation of a wide range of solid-state structures for a given set of elements with a minimal structural basis (i.e. no assigned atomic positions) had the capability to only survey one space group at a time. As shown by the headings in Figure 5, potential candidate phases were developed in increasing order (number of elements) from known phases using three major approaches:

First Principles and Thermodynamic Modeling

1) Isostructural hydride candidate templates
   - -elemental, intermetallic or complex hydride structures
   - -higher order systems from direct cation sublattice substitution
2) Substitution in lower order mixed metal systems
   - -derived from known low-order or intermetallic phases
   - -higher order systems created by interstitial substitution of H
3) Complex analog templates
   - -complex and mixed alkali/alkaline fluorides, boranates
   - -direct 1:1 substitution of cations and/or anions in analogs

Known and proposed phases were theoretically evaluated in tiers of progressively increasing phase order (number of elements within phase). Only energetically favorable VASP-minimized lower order phases were used to develop higher order systems. The simulations concentrated primarily on identifying high hydrogen capacity candidate phases, and did not systematically survey lower hydrogen capacity phases, unless they were chemically related to, or, were a necessary precursor structure to derive the candidate phases.

In the first tier, known unary elemental phases were evaluated both to establish fundamental structures for the derivation of higher order phases and to determine standard state energies for thermodynamic calculations. In the higher tiers, new phases were derived either by substituting quaternary elements into known hydride or analog compound structures, or by substituting quaternary elements onto the lattice or interstitial sites of lower order known phases within the quaternary system. In a number of cases, the latter approach was used to effectively meld the ionic structures of two lower order systems to create a third higher order system. Thus, the theoretical evaluation of the proposed phases necessarily included the fundamental phases from which they were derived. The complete evaluation of the stability and reversibility of a given phase also required the simulation of lower order known phases that could form upon disproportionation and/or dehydrogenation.

In the second tier, the evaluated binary phases included: a) known elemental hydride phases (i.e. TiH_2 and NaH), b) known stable Ti-Al intermetallic phases, and c) proposed metastable Ti-Al (i.e. Al_3Ti $D0_{23}$) and Ti-H (i.e.TiH_3) phases. The justification for the evaluation of low order metastable systems was their possible role as derivative structures for higher order systems. In titanium aluminides, interstitial hydrogenation has been observed to stabilize lesser known metastable systems and to shift phase boundaries to lower temperatures [Ref. 8]. The third tier focused on the Ti-Al-H and Na-Ti-H ternary phases, including: a) Ti-Al-H and Na-Ti-H phases based upon known complex and intermetallic ternary mixed alkali-alkaline earth and alkali-transition metal hydride structures, b) Ti-Al-H phases formed by interstitial hydrogenation of Ti-Al intermetallic phases, and c) $Ti(AlH_4)_n$ [n=1-4] phases formed from analog complex halide and borohydride compounds. The ternary evaluations intentionally focused on a survey of the highest possible hydrogen stoichiometries that could be used to derive high hydrogen capacity compounds. No attempts were made to determine hydrogen solubility limits in the derivative binary phases.

The fourth tier only focused on the evaluation of quaternary substituted favorable ternary phases, as no quaternary complex hydride or analog (non-oxide) compounds are known to exist. The quaternary phases evaluated primarily included favorable Na-Al-H phases highly substituted with Ti and favorable Na-Ti-H phases substituted with Al.

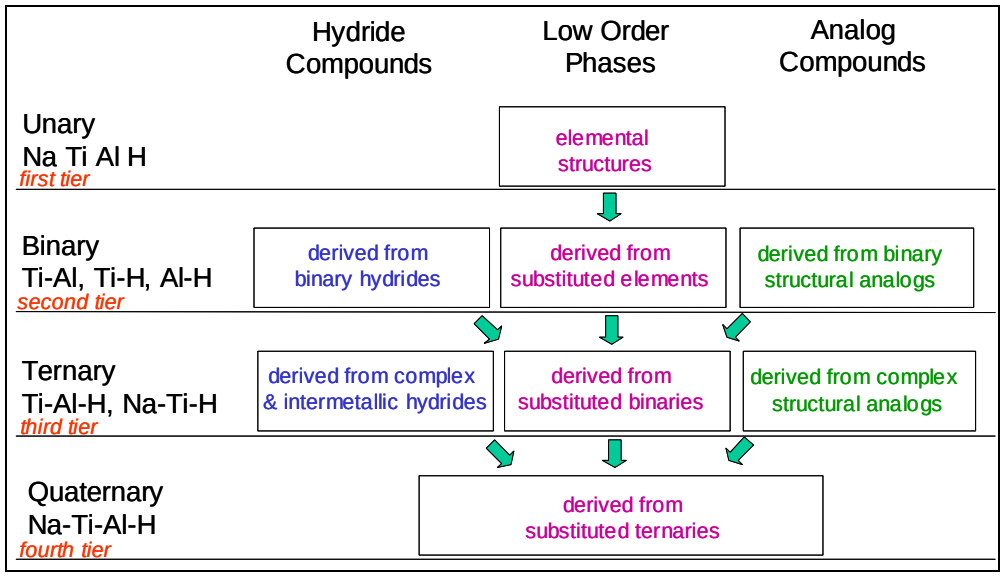

Figure 5: Schematic of model definition within the Na-Ti-Al-H quaternary system.

3.2.1.2 Model Refinement

Atomic simulations were implemented with the Vienna Ab Initio Simulation Package (VASP) code developed by Kresse and Hafner at the University of Vienna [Refs. 9,10,11], which is based upon density functional theory developments of Kohn and Sham [Ref. 12]. Crystalline and molecular atomic structures are represented as periodically repeating geometries with electronic orbitals expanded in a plane-wave basis set. In this way the number of one-electron wavefunctions is equal to the number of electrons in the crystal unit cell. The wavefunctions were described by a finite number of plane waves having wave vectors defined by the reciprocal lattice vectors of the crystal. The VASP code calculates the Kohn-Sham ground state ionic and electronic structure by an iterative band-by-band matrix diagonalization scheme and by charge density mixing. The calculations employed the valence electrons and were explicitly represented with projector augmented wave (PAW) potentials [Ref. 13] using the generalized gradient approximation (GGA) of Perdew and Wang (PW 91) [Ref. 14].

For the simulation of hydride and related phase structures in the Na-Ti-Al-H system, we selected, based upon previous simulations [Refs. 5,6,15,16,17], the hard potentials for Na $\{2s^2\ 2p^6\ 3s^1\}$ and Ti $\{3s^2\ 3p^6\ 3d^2\ 4s^2\}$ which include the next lower electronic level electrons in the valence shell, and the regular potentials for Al $\{3s^2\ 3p^1\}$ and H $\{1s^1\}$. Initial tests were performed on representative ternary candidate structures to optimize parameter values to within a total convergence energy of less than 1 meV per atom. These parameters were then selected for the initial screening of all structures with the Na-Ti-Al-H system. They included a planewave cutoff energy of 780 eV and the Gaussian smearing method energy broadening of 0.2 eV. The k-mesh of each structure was optimized individually to achieve a spacing of 0.5/Angstrom or finer. The ground state geometries were determined by minimizing the Hellman-Feynman forces with the conjugate gradient algorithm, until all the ionic forces were less than 0.005 eV / Å. In order to span as wide a range of energetically accessible crystal structures, full minimization of the cell volume, cell shape and atomic positions were made simultaneously. The structures were relaxed in this manner in a series of calculations

made with progressively increasing precision. A final high accuracy calculation was made to determine the ground state energy of the converged structure.

3.2.1.3 Candidate Identification Criteria

The electronic ground state (gs) heat of formation, $\Delta H_{\text{formation gs electronic}}$, was determined by referencing the ground state electronic energies of VASP-minimized complex hydride and disproportionation model phases with respect to the sum of the VASP-calculated ground state electronic energies of the respective stoichiometric equivalents of the constituent element atoms in their standard state, $\Sigma H_{\text{element gs electronic}}$

Equation 1 $$\mathbf{\Delta H_{formation\ gs\ electronic} = H_{compound\ gs\ electronic} - \Sigma H_{element\ gs\ electronic}}$$

The $\Delta H_{\text{formation gs electronic}}$ determined for stoichiometrically related candidate phases and known phases were systematically compared to evaluate candidate favorability. Only ternary and quaternary candidate phases with a $\Delta H_{\text{formation gs electronic}}$ within 0.1 eV/atom (9.6 kJ/mole*atom) of the $\Delta H_{\text{formation electronic}}$ of relevant known phases as well as the most favorable corresponding competing phases, or lower order disproportionation phases, were down selected for the more computationally intensive finite temperature thermodynamic property prediction by the Materials Design Phonon Module [Ref. 18]. This selection criterion was used to allow inclusion of metastable candidate phases that could possibly be stabilized by vibrational contributions at higher, more practical temperatures. Convex hull methodologies were not required with this approach to distinguish the most favorable candidate ternary and quaternary phases in the Na-Ti-Al-H and other systems.

3.2.1.4 Finite Temperature Thermodynamic Property Predictions

The atomic predictions of finite temperature thermodynamic data were obtained using the lattice dynamics direct method of Parlinski implemented in the Materials Design Phonon module interfaced with the VASP code [Refs. 18,19]. The Phonon module automates a number of steps to determine the thermodynamic functions, including: supercell formation, calculation of forces from systematic atom displacement, transformation of force constants into a dynamical matrix, matrix diagonalization to determine phonon frequencies, and integration over reciprocal space to determine phonon density of states. The vibrational thermodynamic functions as a function of temperature are derived by substituting the integrated phonon density of states into statistical mechanical functions [Ref. 20]. The finite temperature thermodynamic data are determined by summing the phase ground state structure electronic energy and the phonon-calculated zero-point energy (ZPE), with the vibrational energies as a function of temperature. Thermodynamic values are typically referenced to the elements in the standard state. This is accomplished by subtracting the sum of electronic energy, ZPE, and vibrational energy determined at 298 K for the stoichiometric equivalents of the respective constitutive elements of the phase. This methodology is described in detail in references [Refs. 5,16].

The phonon direct method is most suitable for predicting the thermodynamics of stable phase structures with discreet stoichiometrics that have stable (negative) $\Delta H_{\text{formation gs electronic}}$ at the ground state. Since often it is found that there may be a number of energetically equivalent candidate hydride

structures for the same compound at the ground state, the most stable structures can be identified as those lacking imaginary (negative or soft) phonon dispersion bands. These imaginary bands indicate instabilities towards possible displacive transformations to other phase structures. Their presence confounds reliable thermodynamic predictions from lattice dynamics.

The direct approach describes finite displacements in an otherwise perfect crystal, where the displacements are approximated to be harmonic with up to quadratic order analytic terms. The chosen crystal cell has to be large enough, approaching 1000 $Å^3$ in size, to minimize interactions between perturbations in the translational symmetry equivalent copies. Phonon calculations were also executed on molecular structures in asymmetric periodic cells, using only the gamma point frequencies in determining thermodynamic relations. The Phonon module typically executes 10–50 calculations of displaced structures for each phase, depending on the supercell size and symmetry. The typical error in the Phonon module thermodynamic predictions was determined in initial benchmarking studies to be 5-15 kJ/mole. The vibrational contributions predicted with the Phonon module tends to be fairly accurate. The error mainly originates from the exchange-correlation approximation in the VASP ground state electronic enthalpy determination. Computationally-intense determinations of the quasi-harmonic approximation for the volume-dependency of lattice phonons and of the Born effective charges to describe electric field polarization were not implemented in this study because of the limited computational facilities available. However, it has been shown that the corrections for the ZPE-induced lattice expansion and for longitudinal optical-transverse optical (LO/TO) splitting, respectively, do not make a significant impact on reducing the error of the predicted thermodynamics.

3.2.1.5 Thermodynamic Data Assessment and Stability Predictions

The thermodynamic predictions for newly identified candidate phases were first evaluated with respect to other known thermodynamic data. The candidate phases' predicted data of Gibbs free energy as a function of temperature were referenced with respect to the stoichiometric-equivalent sum of the constituent elements' standard state enthalpy values at 298.15 K, following the GHSER referencing convention used in databases for the Thermo-Calc [Ref. 21] and HSC [Ref. 22] programs used in this study. This enabled the direct comparison of predicted data with experimentally measured and assessed thermodynamic data for known, stable phases. The Gibbs free energy as a function of temperature predicted for a given candidate phase were compared to that of the most stable assembly of phases determined by the Thermo-Calc POLY Gibbs energy minimization module to evaluate candidate stability. The Gibbs phase equilibria were calculated using experimentally-derived thermodynamic data parameters both from the previously described assessments [Refs. 5,16,23,24] and the SSUB3 database [Ref. 21]. Only phases that were shown to have lower (more favorable) GHSER (T) than that of the Gibbs energy minimized equilibrium for the equivalent stoichiometry determined for relevant temperature and pressure conditions, were down-selected as stable phases.

Rigorous thermodynamic assessments were conducted in selected cases to incorporate new experimental information and thermodynamic predictions into thermodynamic databases. Assessments involve several components: data selection, thermodynamic model selection and data fitting, and assembly of fit parameters into data files. Thermodynamic assessments involve the simultaneous optimization of empirical model fits to multiple sets of thermodynamic data, such as enthalpies of formation, heat capacities as a function of temperature, equilibria between two or more phases, etc., for stable phases within a specific compositional system. In the final stage of the

assessment, thermodynamic databases are constructed from the optimum parameter values that describe the system phases' referenced Gibbs free energies as a function of temperature, GHSER(T), and may include interaction parameters for varying phase compositions formed by sub-lattice or interstitial substitution. Thermodynamic parameter optimizations are an iterative process of progressive refinement. Appropriately refined databases can be used to calculate equilibria that closely match good quality measured equilibria, which were not included in the original optimization. This demonstrated capability qualifies the use of the database for predictions of thermodynamic properties for related (composition, temperature and pressure) conditions that have not yet been experimentally tested. The combined modeling approach for the progressive refinement and down-selection of candidate phases is illustrated by the modeling flow path and decision criteria in Figure 6.

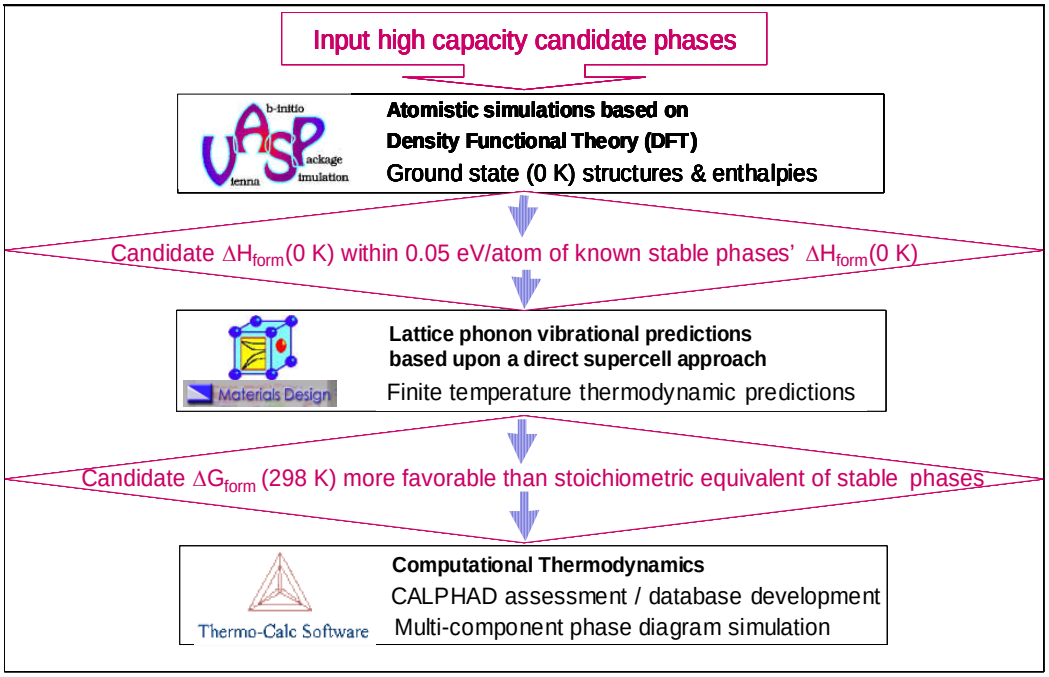

Figure 6: Combined atomic-thermodynamic flowpath.

3.2.2 Refinements for High H Coupled Complex Hydride Reaction Strategy

The expansion to the high H coupled complex reaction strategy required the implementation of additional theoretical methodologies in close integration with experimental and thermodynamic methods. First, a global optimization method was implemented for the refinement of candidate input structures, especially in conjunction with the crystallographic refinement of new phases. Second, thermochemical reaction predictions were implemented for the design of reversible high H capacity reactions to provide guidance for experimental formulation of new systems. Finally, a method was developed to enable thermodynamic optimization of theoretical H capacity within a mutli-dimensional parameter space.

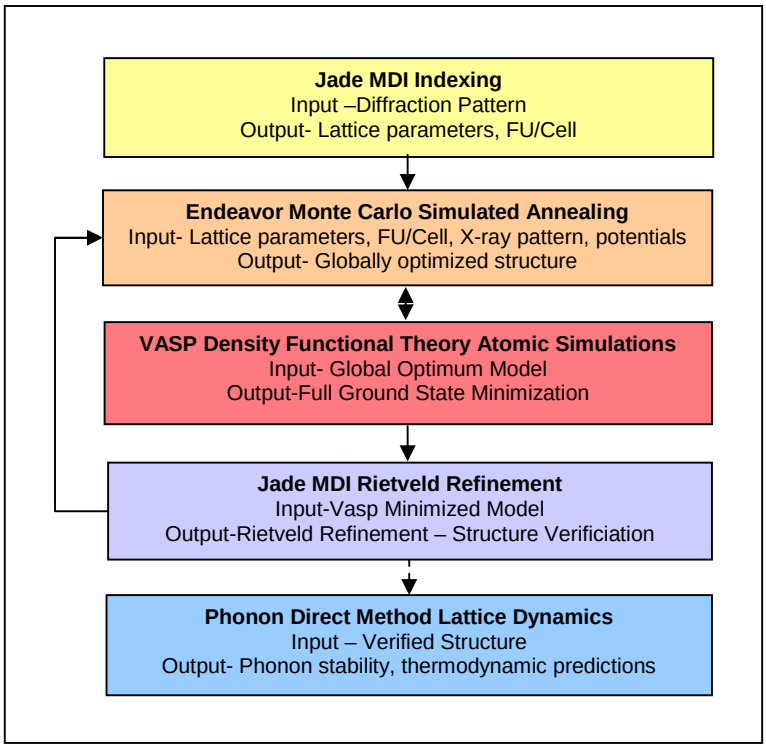

Figure 7: New combined crystallographic analyses and atomic modeling approach to accelerate refinement of crystal structures.

3.2.2.1 Improved Model Structures: Monte Carlo Simulated Annealing Methodology

A new approach has been developed to prepare new candidate input models for virtual screening studies and for crystallographic Rietveld refinements, as shown schematically in Figure 7. This approach can be used to integrate atomic simulations and experimental structural analyses to accelerate the identification and resolution of new crystallographic structures. This new linkage was first envisioned in a joint collaboration plan developed with Sandia National Laboratories to support the development of high capacity titanium borohydride compounds [Ref. 25]. The approach employs an additional methodology, Monte Carlo simulated annealing, implemented with the Endeavor code [Ref. 26]. Input models are globally optimized with this code to find the best atomic positions that (simultaneously) match given crystallographic X-ray diffraction data (and) or minimize the potential energy of the crystal structure. The simulated annealing samples both atomic displacements and exchanges over a large hypersurface with many local minima, to eventually converge on a global minimum structure [Ref. 27]. This new methodology was interfaced at the front end of our original simulation protocol shown in Figure 6, where the new methodology can be used to iteratively refine new structures to improve the reliability of thermodynamic predictions.

3.2.2.2 Thermochemistry Design of Reversible Reactions

The HSC Chemistry program [Ref. 22] was used to propose and evaluate reaction pathways for new high H candidate systems. First, thermodynamic data are established for candidate phases, co-reactants, and products, by supplementing with thermodynamic predictions wherever necessary. In order to identify new candidate high H capacity systems, new reactions are systematically evaluated in terms of reaction energetics and H exchange between dehydrogenation and rehydrogenation. The most

thermoneutral reactants with the largest H capacity are used to create input conditions for equilibrium survey calculations. These calculations, based on the Gibbs minimization method, are used to identify which phases will predominate in H exchange reactions, especially where there may be many possible competing reactions for consideration. The identification of the most stable phases is used to propose the most likely candidate reactions, which can be further evaluated. The goal is to identify reactions which have the minimum number of steps and reduce the likelihood of formation of harmful side-products.

3.2.2.3 Thermodynamic Optimization Tool

The final stage is to optimize the system composition to find the best stoichiometry that gives the highest reversible H capacity. A new Matlab tool was developed for the TC MATLAB Toolbox [Ref. 28] interface and Thermo-Calc thermodynamic software [Ref. 21] to calculate the equilibrium reversible hydrogen content over a selected compositional space and temperature/pressure conditions. The tool can be used with established and/or user-developed thermodynamic databases to determine the optimum elemental stoichiometry for the highest theoretical reversible hydrogen capacity. Equilibrium and phase diagram calculations can be made to determine the most stable fully hydrogenated reactant and dehydrogenated product phases that correspond to the optimum elemental stoichiometry. Thermochemical simulations can then be made to deduce the predominant reaction pathways and to project the equilibrium dehydrogenation pressure temperature dependency. This tool completes the methodology development for the virtual design of high capacity, reversible thermodynamic reactions.

3.2.2.4 Overview of Theoretical Methodologies

To summarize our progress, we have implemented a broad array of coupled theoretical methodologies that are closely integrated with experimental and thermodynamic methods, as schematically shown in Figure 8. New candidate input structures are globally optimized to match both crystallographic information and to minimize structure potential energy. Candidate structures are then minimized at the ground state with DFT. In certain cases, global optimization and minimization can be conducted iteratively to refine new crystal structures. Finite temperature thermodynamic predictions are made for stable ground state structures, enabling the inclusion of hypothetical phases in thermodynamic surveys. Assessments are conducted to validate and incorporate predicted thermodynamic data alongside experimental data in thermodynamic databases, enabling phase diagram predictions for a range of composition, temperature and pressure conditions. Thermochemistry methods are used to survey and design new coupled reactions that exchange high H between species. Once a target chemistry is identified, the optimum theoretical hydrogen capacity can be designed thermodynamically to guide experimental development.

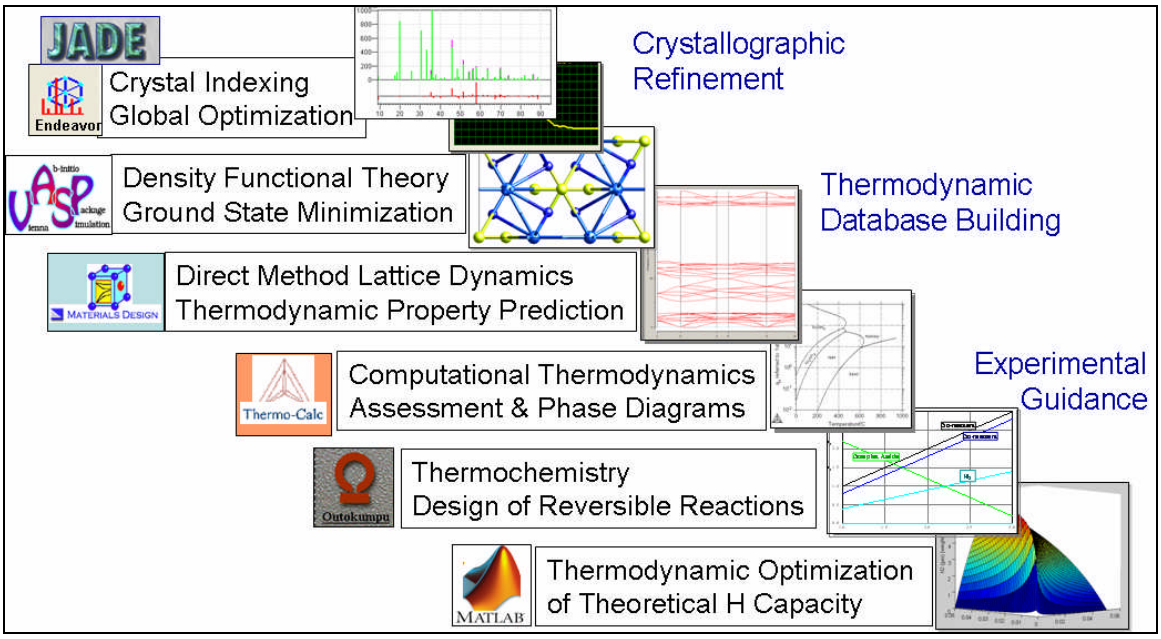

Figure 8: Array of computational methodologies for virtual discovery and design of high hydrogen capacity systems.

3.3 Results and Discussion

This section presents an overview of the extensive virtual survey of high capacity candidate hydrides and related phases conducted for this project, emphasizing the continuous improvement and implementation of new simulation methodologies. The approach taken and the survey scope evolved throughout the execution of the program both in response to the knowledge gained from our findings and recommendations from our reviewers and colleagues in the hydrogen storage research community. Out of necessity, many of the important findings from this project already published in the open literature are presented in brief. The reader is encouraged to consult the cited references for a more detailed presentation of results.

3.3.1 Funding Year 1 Atomic-Thermodynamic Modeling

3.3.1.1 Literature Survey

To prepare for our virtual surveys, we conducted extensive scientific literature surveys on binary hydrides, intermetallic and complex hydride ternary hydrides, and their respective relevant disproportionation products. From the most illuminating references [Refs. 29,30,31,32,33,34,35], we surveyed common structure-property observations and rules for their stable existence that were derived from complex hydride crystallographic, spectroscopic, and thermochemical characterizations, as summarized in Table 4. These observations include: the structural correlation of certain complex hydride stoichiometries to specific ternary halide or oxide compounds with analogous stoichiometries, typical bond distances within various types of hydride complexes, and geometrical relationships for interactions between neighboring metallic cations and between neighboring hydrogen atoms. The rules for complex hydride existence are not universal; they were developed for specific complex hydride subclasses that exhibit similar types of bonding behavior and stoichiometries. For example,

there are discrete stoichiometries with limiting ionic formulae observed for all complex compounds, electron rules for the formation of different covalent transition metal hydride complex geometries [Refs. 30,31], and heat of formation ranges for stable existence of complex transition metal hydrides [Ref. 29]. Since there are multiple exceptions to these established observations and rules, they were only used to guide, not to bound our search for high capacity phases with heretofore unknown characteristics.

Table 4: Solid-state hydride classes and characteristics from literature review [Refs. 29,30,31,32,33,34,35].

Compound Class	Compositions	Examples	Characteristics
Complex Covalent Hydrides, $Aa^{[+Z]}(NH_x)_n^{[-Y]}$ where a=(n*Y)/Z	A = AK,AE, TM, NT N = B, Al, Ga	$Mg(AlH_4)_2$ $Zr(BH_4)_4$	Stoichiometric, covalent complex of non-TM bonded to H, stabilized by counter ions
Complex Ternary TM Hydrides $A_a^{[+1,2]}(B_mH_h)^{[-a*1,2]}$	A= AK, AE, some RE B = TM	K_3PtH_6 $CaMgNiH_4$	Central complex follows 18 electron rule, dehydrided binary phase not stable.
Complex Alkali, Alkaline Earth & TM Halides $A_a^{[+1,2]}(B_mX_h)^{[-a*1,2]}$	A= AK, AE, NT B = A, NT, TM X = F, Cl	$MgAl_2Cl_8$ Na_2TiH_6 Na_3AlF_6	Many binary and ternary hydrides are isostructural, often equivalent H and F ionic radii.
Complex Alkali/ Alkaline Earth Hydrides $A_aB_bH_{[a+2b]}$	A = AK B = AE, some RE	$NaMgH_3$ $SrLiH_3$	Ionic coordination proportional to relative ionic radii, binary hydrides not isostructural
Interstitial TM & Laves Hydrides, $TMA_aTMB_bH_h$	TMA=some TM or RE TMB= any TM	$LaNi_5H_6$ $FeTiH_6$	Nonstoichiometric H substituted in stable intermetallic phases
AK= alkali AE = alkaline earths TM = transition metals NT = non-transition metals RE = rare earths			

3.3.1.2 Benchmarking of Thermodynamic Predictions

The over-riding objective of the first year was to develop theoretical and assessment methodologies for constructing thermodynamic databases jointly from both experimentally measured and predicted thermodynamic properties. This new capability would then be used as a tool to identify potential high hydrogen capacity hydride phases and to evaluate their phase stability over a wide range of temperature and pressure conditions. In this manner, the combined atomic-thermodynamic methodologies would be used to guide experimentation and to supplement thermodynamic measurements that may be difficult or impossible to execute in the laboratory. The latter includes the evaluation of candidate phases that have yet to be identified experimentally, and the prediction of pressure-composition isotherms and van't Hoff P vs. T relationships that are labor and time intensive to measure in the laboratory. In the first year, these new combined methodologies were first exercised by benchmarking predicted thermodynamic properties of known phases against those calculated using

experimentally-based thermodynamic data parameters [Refs. 5,16,23]. These comparisons made for known phases were then used to estimate the error of thermodynamic predictions of hypothetical candidate phases simulated within the three quaternary systems. These methodologies were then used in the remainder of the program to scout new quaternary systems that have the potential to yield high H complex hydrides and to develop new thermodynamic parameters for compositional phase spaces that encompass these successful new candidates. The thermodynamic parameters enable virtual evaluation of the complex hydride phase behavior over a wide range of temperature and pressure conditions.

The predicted referred Gibbs free energies of formation as a function of temperature, GHSER (T), were determined for each of the known sodium alanate complex hydrides and disproportionation products, to enable direct comparison with assessed experimental data parameterized in the Thermo-Calc thermodynamic database. An example comparison is shown in Figure 9 for the predicted and experimentally measured GHSER (T) versus temperature for sodium aluminum tetra-hydride, $NaAlH_4$ [Ref. 5]. The predicted $GHSER_{NaAlH4}$ (T) values were within 9 kJ/Mole of the composite experimental values [Refs. 2,36,37,38] over the temperature range of 300 – 450 K. The predicted and measured dissociation pressures from the van't Hoff relationship for the first $NaAlH_4$ disproportionation reaction:

Equation 2 $$\mathbf{NaAlH_4 = {}^{1}/_{3}Na_3AlH_6 + {}^{2}/_{3}Al + H_2}$$

are shown in Figure 10. The predicted dissociation pressures were calculated using the GHSER (T) determined from the lattice dynamics of the three solid state phases in Equation 2, and the $GHSER_{H2}$ (T) in the Thermo-Calc PURE database. The agreement between the predicted and composite measured dissociation pressures is excellent, due to the cancellation of errors of the predicted $GHSER_{NaAlH4}$ and $GHSER_{Na3AlH6}$ values in the van't Hoff relationship. Additional plots comparing thermodynamic experimental data and first principles predictions in the Na-H and Na-Al-H systems can be found in [Refs. 5,16]. These references also show the extensive phase diagram predictions that are possible from the assessments of the combined experimental-first principles thermodynamic datasets.

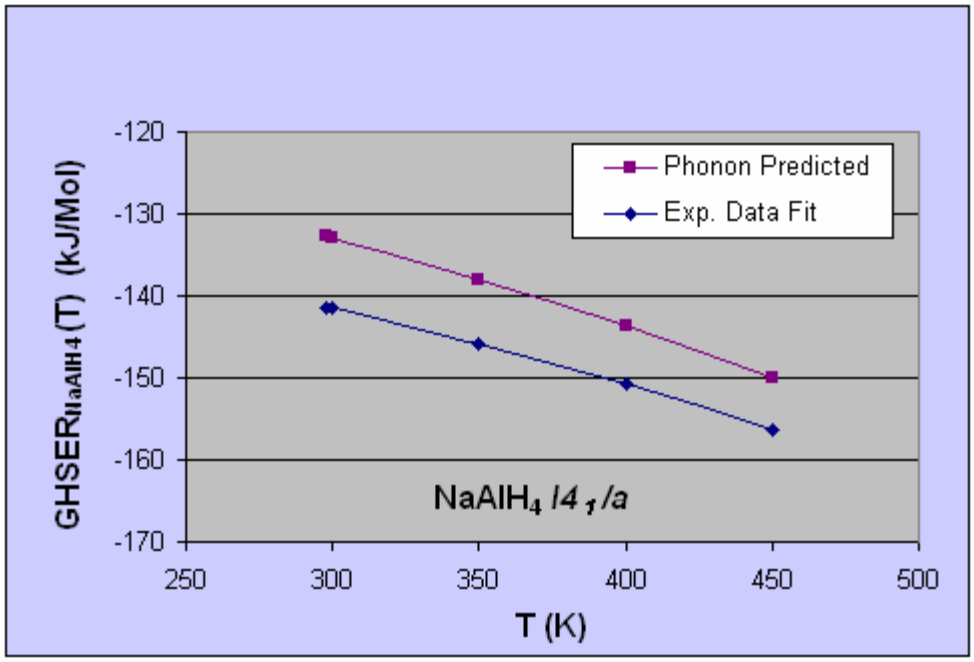

Figure 9: The comparison of $GHSER_{NaAlH4}$ (T) predicted with Phonon direct method lattice dynamics [Refs. 18,19] of the ground-state VASP minimized $NaAlH_4$ $I4_1/a$ phase, compared with that calculated with Thermo-Calc using assessed fits from [Ref. 5] to experimental measurements published in references [Refs. 2,36,37,38].

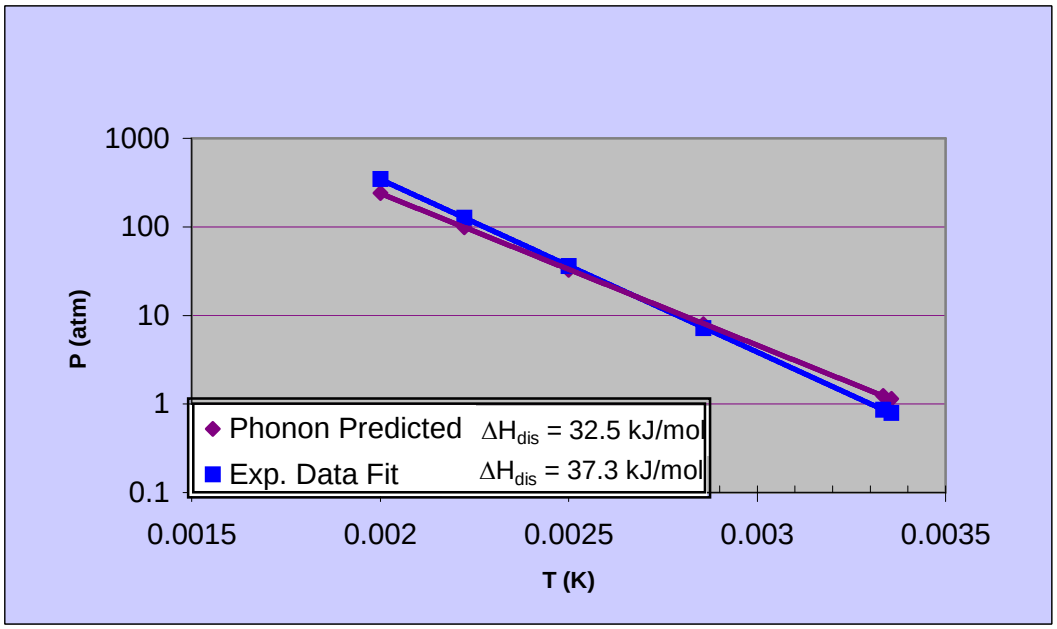

Figure 10: The comparison of predicted and measured dissociation pressures for the first $NaAlH_4$ disproportionation reaction, $NaAlH_4 = {}^1/_3Na_3AlH_6 + {}^2/_3Al + H_2$. The dissociation pressure predictions are described in the text. The measured values are a composite fit from [Ref. 5] to the experimental data in references [Refs. 2,36,37,38]. The disproportionation enthalpies, ΔH_{dis}, are determined from the slopes of the lines.

3.3.1.3 Na-Ti-Al-H Candidate Hydride Simulations

To build the Na-Ti-Al-H quaternary system, the candidates were refined in increasing order, yielding down-selected candidates to derive progressively higher order systems. The simulations first focused on developing precursor phases in the Ti-Al, Ti-H, Na-H, and Al-H binaries. Unlike the other two possible Na-Ti and Na-Al binaries that were not evaluated, these four binaries exhibited significant co-solubilization and intermediate phase formation over their binary compositional ranges. In the Ti-Al binary system, a large number of stable, metastable, and hypothetical phases with varying stoichiometry in the $\leq$ 50 % Ti binary region were evaluated to determine the relative phase stability at 0 K. The calculated ground state heats of formation for the various Ti-Al phases are shown in Figure 11. The most stable phases were down-selected as templates for candidates in the higher order Ti-Al-H ternary, to be formed by interstitial hydrogen substitution. Simulations of the other three binaries focused primarily on simulating known phases at the ground state and hypothetical lattice stability phases to develop parameters for the further refinement of thermodynamic assessments.

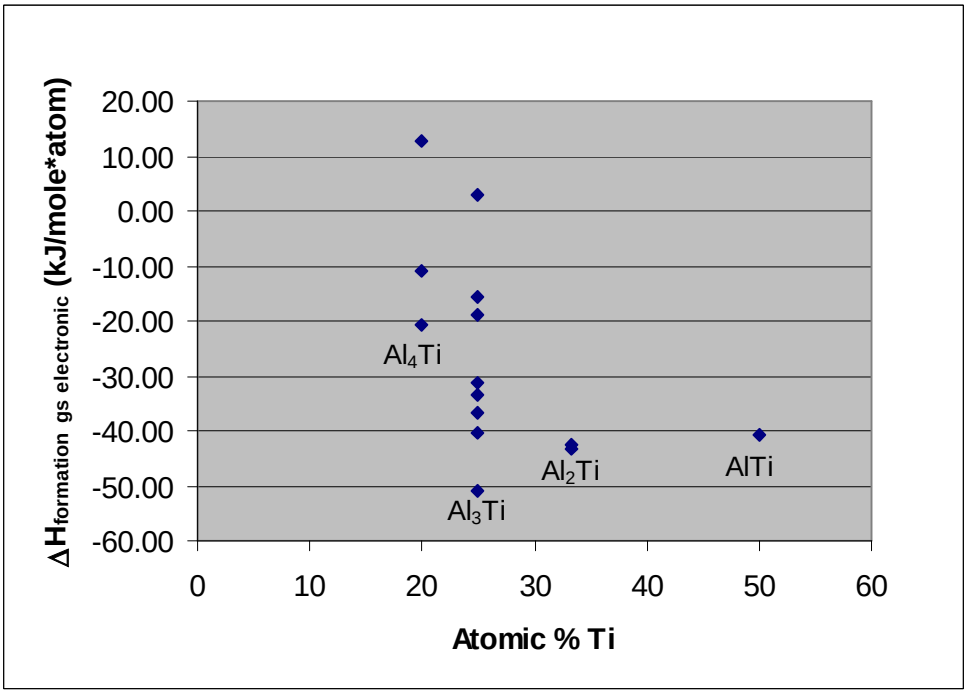

Figure 11: Ground state enthalpies of formation, $\Delta H_{formation\ gs\ electronic}$, for candidate binary Ti-Al intermetallic structures.

The next tier of simulations explored the Ti-Al-H, Na-Al-H, and Na-Ti-H ternary faces that share the common high hydrogen vertex in the Na-Ti-Al-H system. The candidates' theoretical reversible gravimetric hydrogen content was defined as:

Equation 3 $\quad$ **wt% $H_{Rev\ Theor} = (N_H - N_{Na})$/ Hydride Formula Weight**

where N_H and N_{Na} were the number of H and Na atoms in the candidate hydride formula. Here, only the Na atoms were assumed to combine with H upon complete dehydrogenation and all Ti was assumed to be incorporated into a Ti-Al intermetallic phase ($TiAl_3$ is the most favorable phase) upon complete dehydrogenation and would not be available to sequester hydrogen. Candidate phases were not simulated within the basal Na-Ti-Al ternary opposite this vertex. The Ti-Al-H candidates were derived either by interstitial hydrogenation of Ti-Al intermetallic structures, or, by direct sub-lattice substitution on the complex analog templates. Both approaches offered the possibility of discovering high hydrogen capacity compounds, akin to the reported, but unsubstantiated $Ti(AlH_4)_4$ compound. The simulation results for a wide range of interstitially H-substituted known and candidate $Ti-Al_x$ stoichiometries, where x ranged from 1 to 4, are shown in Figure 12, compared to predictions for the known stable sodium alanate and TiH_2 phases. Most of the candidates did not have favorable (negative) $\Delta H_{formation\ gs\ electronic}$ values. Interstitial hydrogenation of the Ti-Al phases exhibited a nearly linear decreasing favorability with increasing wt% $H_{Rev\ Theor}$.

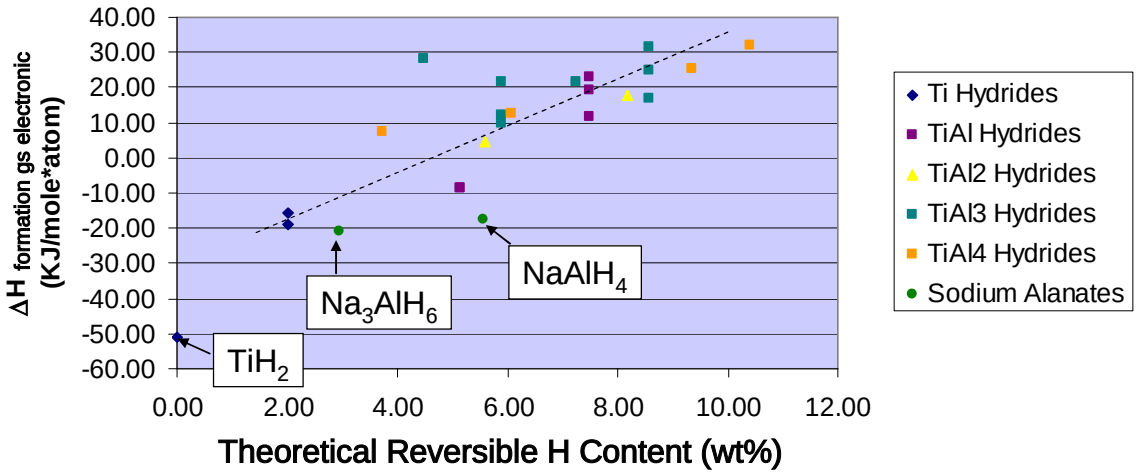

Figure 12. Ground state enthalpies of formation, $\Delta H_{formation\ gs\ electronic}$, for candidate Ti-Al hydrides formed by H interstitial substitution in known and hypothetical Ti-Al intermetallic phases.

The Ti-Al-H complex analog approach sampled a wide range of compound structures to represent the $Ti(AlH_4)_x$ stoichiometries, where x ranged from 2 to 4. These candidates corresponded to a wt% $H_{Rev\ Theor}$ range of 7.2-9.4, respectively. Figure 13 shows that a number of these later candidate phases had $\Delta H_{formation\ gs\ electronic}$ in the –5 to –10 kJ/mole∗atom range, indicative of weak favorability with a high driving force for disproportionation. None of these structures were down-selected for further refinement as a ternary phase or as templates for quaternary systems. The only new candidate phase evaluated in the Na-Al-H ternary was $Na_5Al_3H_{14}$, derived from the fluoride analog compound. The two major approaches used to evaluate phases in the Na-Ti-H system were isostructural complex hydride and complex analog templates. Several Na-Ti-H compound Na_2TiH_6 stoichiometries were simulated to have $\Delta H_{formation\ gs\ electronic}$ in the –21 to –29 kJ/mole∗atom range. These compound predictions are also shown in Figure 13. Although these compounds did not have potential for high

hydrogen capacity, they could be used as templates for higher capacity quaternary systems formed by partially substituting Al for Ti.

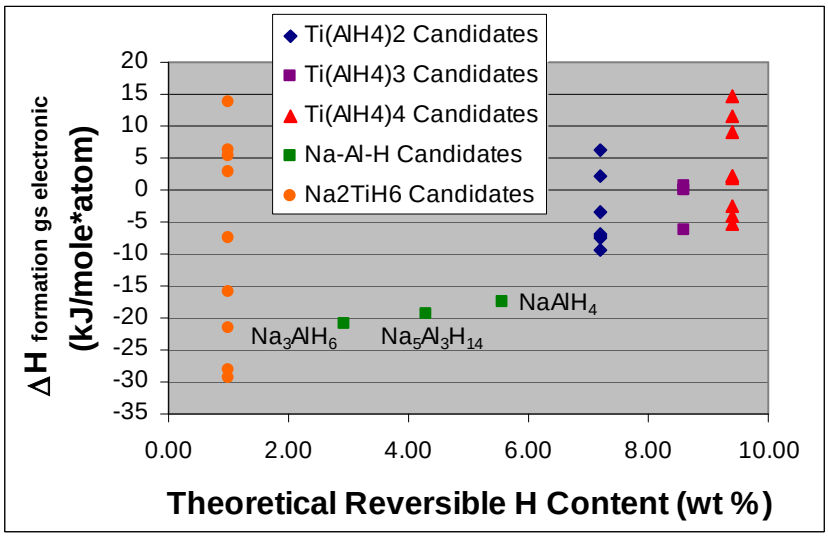

Figure 13: Ground state enthalpies of formation, $\Delta H_{\text{formation gs electronic}}$, for candidate Ti-Al-H, Na-Al-H and Na-Ti-H ternary phases.

Several approaches were also trialed for proposing new quaternary Na-Ti-Al-H candidate phase models, including candidate derivation from structures of other known complex or intermetallic hydride phases, direct or interstitial substituted lower-order phases, and non-hydride analog compounds. Since there are relatively few solved structures of complex hydride analog compounds formed from four elements in the crystallographic literature, quaternary hydride models were mainly formed by substituting a fourth element into one or more sublattices of known ternary hydride phases. The creation of ternary and quaternary complex hydrides from substitution of lower order phases only revealed stable candidates for lower H capacity phases that were outside of our range of interest in this contract. The most fruitful approach so far, was to utilize other analog compounds as templates for new complex phases. This approach was especially successful for virtually resolving structures of known phases [Ref. 24], and for the case of fluoride analogs, has an established solid-state basis. Many isostructural fluoride and hydride phases are known to exist, where F and H ions occupy equivalent sublattices, respectively, and the sublattice spatial arrangements are the same for each ion type. This equivalency is attributed to the similar radii of fluoride and hydride ions that are often found in corresponding local coordinative environments [Ref. 30]. An example of an iso-structural complex phase pair are the high temperature orthorhombic *Immm* β-Na_3AlF_6 cryolite and β-Na_3AlH_6 phases. Further justification for using fluoride analogs as templates was based directly on our synthetic observations that iso-structural fluoride/hydride mixed complex phases are formed by metathesis reactions from fluoride and hydride precursor compounds. The use of fluoride analogs to develop new hydride models essentially surveys compositional phase space by employing virtual metathetical reactions.

The best Na-Ti-Al-H quaternary candidates were derived mainly from isostructural hydrides and complex fluoride analogs. The wt% $H_{\text{Rev Theor}}$ of the candidates ranged from 4.3 to 7.3, encompassing a range of compositions for each of the doped candidates. Figure 14 shows that although most all

candidates yielded favorable negative $\Delta H_{formation\ gs\ electronic}$, overall the favorability tended to decrease with increasing hydrogen content. The most favorable candidates with $\Delta H_{formation\ gs\ electronic}$ comparable to the known sodium alanate phases had less than 5 wt% $H_{Rev\ Theor}$. Finite temperature predictions were made for several of these latter candidate phases, first to further method development for candidate stability evaluation, and, second to evaluate possible templates for other quaternary systems containing lighter elements that would have the potential to yield higher hydrogen capacity.

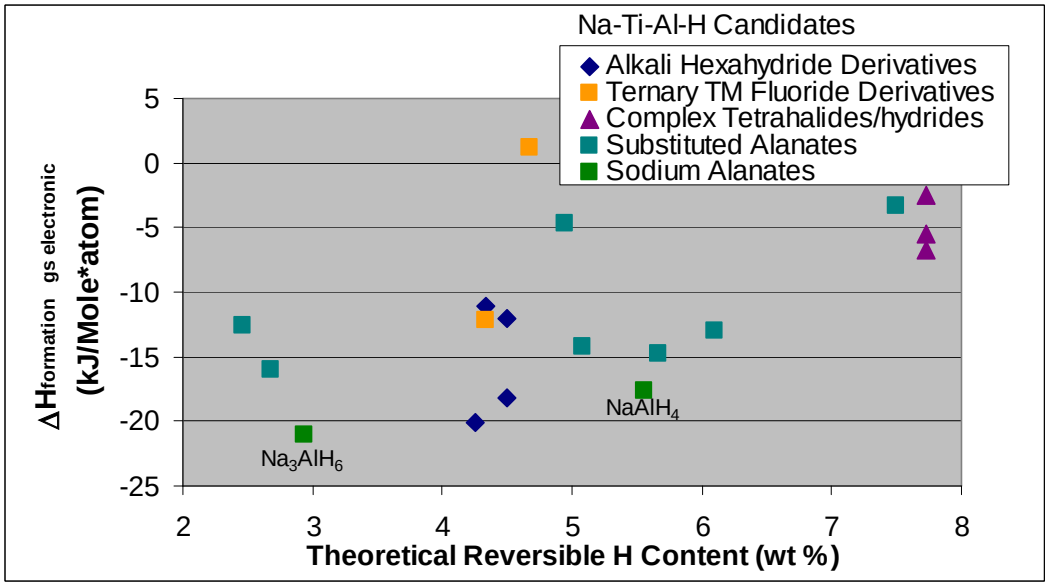

Figure 14: Ground state enthalpies of formation, $\Delta H_{formation\ gs\ electronic}$, for candidate Na-Ti-Al-H quaternary phases.

3.3.1.4 Li-Ti-Al-H and Na-Li-Al-H Candidate Hydride Simulations

The simulated quaternary phases for the Li-Ti-Al-H system built on the approaches taken and the results for the Na-Ti-Al-H system. The Li-Ti-AlH $\Delta H_{formation\ gs\ electronic}$ are plotted versus the theoretical H content in Figure 15. Several of the quaternary Li-Ti-Al-H phases were predicted at the ground state to be more favorable, but did not offer increased capacity compared to the corresponding Li-Al-H phases.

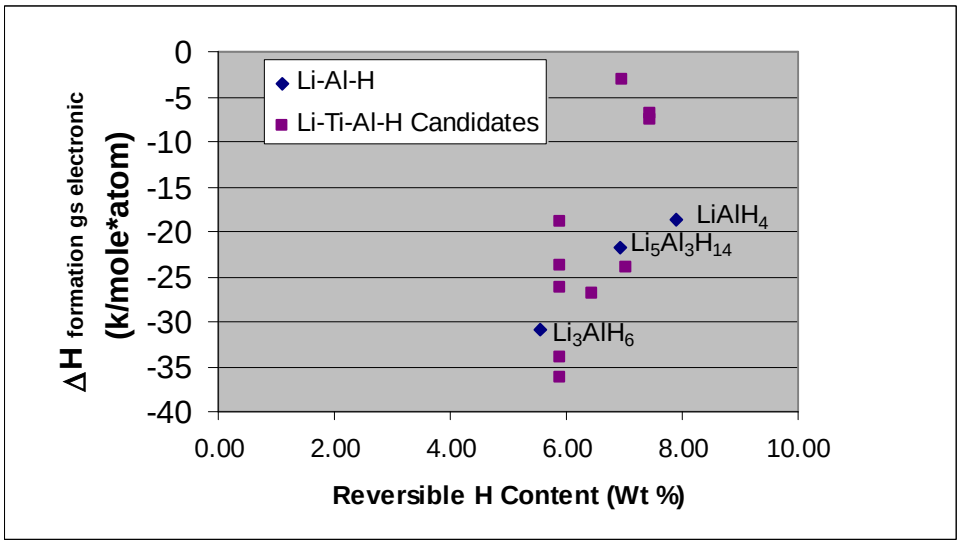

Figure 15: Ground state enthalpies of formation, $\Delta H_{\text{formation gs electronic}}$, for candidate Li-Ti-Al-H quaternary phases.

Extensive surveys were conducted on the Na-Li-Al-H and other mixed alkali quaternary systems, in collaboration with Ole M. Løvvik of the University of Olso, and the Institute for Energy, Norway. From the results summarized in Ref. 40, it was determined that no new Na-Li-Al-H candidate phases for stable existence were identified other than the known Na_2LiAlH_6 phase with 3.5 wt% $H_{\text{Rev Theor}}$. The comparison of the predicted thermodynamic properties for this phase with those determined from experimental measurements is made in Ref. 41. The predicted dissociation enthalpy for the first Na_2LiAlH_6 disproportionation reaction

Equation 4 $$^2/_3Na_2LiAlH_6 \rightarrow {}^4/_3NaH + {}^2/_3LiH + {}^2/_3Al + H_2$$

was 6-9 kJ/mol smaller than the measured values [Refs. 42,43].

3.3.1.5 Assessment of Na-Ti-Al-H, Li-Ti-Al-H and Na-Li-Al-H Candidate Hydrides

Complex hydride phase candidates with theoretically reversible gravimetric hydrogen capacities of 5.9 % or higher, as well as associated phases, were evaluated within the three Na-Ti-Al-H, Li-Ti-Al-H, and Na-Li-Al-H systems. The predicted candidate phases' GHSER(T) values were compared to the Thermo-Calc Gibbs energy minimized equilibrium of known phases at relevant temperature and pressure conditions. One such comparison is shown in Figure 16 for the favorable complex hydrides (wt% $H_{\text{Rev Theor}}$): Na_4TiAlH_{12} (4.5), $Na_6Ti_2AlH_{18}$ (4.3), and $Na_8Ti_3AlH_{24}$ (4.3). Although these candidates do not have significant H capacity, the comparison of their stability with the predicted equilibrium of phases determined with established thermodynamic databases provides a clear illustration of candidate evaluation for down-selection. In this case, the predicted equilibrium of NaH, TiH_2, Na_3AlH_6 and gas phases are more stable by over 10 kJ/mole∗atom over the isopleth composition range, having the Na and H mole fractions fixed at 0.22 and 0.66, respectively, at 298 K and 1 atm. None of these candidate phases were shown to have lower (more favorable) GHSER(T) than that of the Gibbs energy minimized equilibrium for the equivalent stoichiometry determined for

relevant conditions, the criteria for down-selection as stable phases. However, the predicted thermodynamic properties of a number of stable, uncharacterized, associated phases in these systems were successfully assessed and incorporated into the database. This latter activity signifies successful completion of the combined modeling first-year objective for database construction.

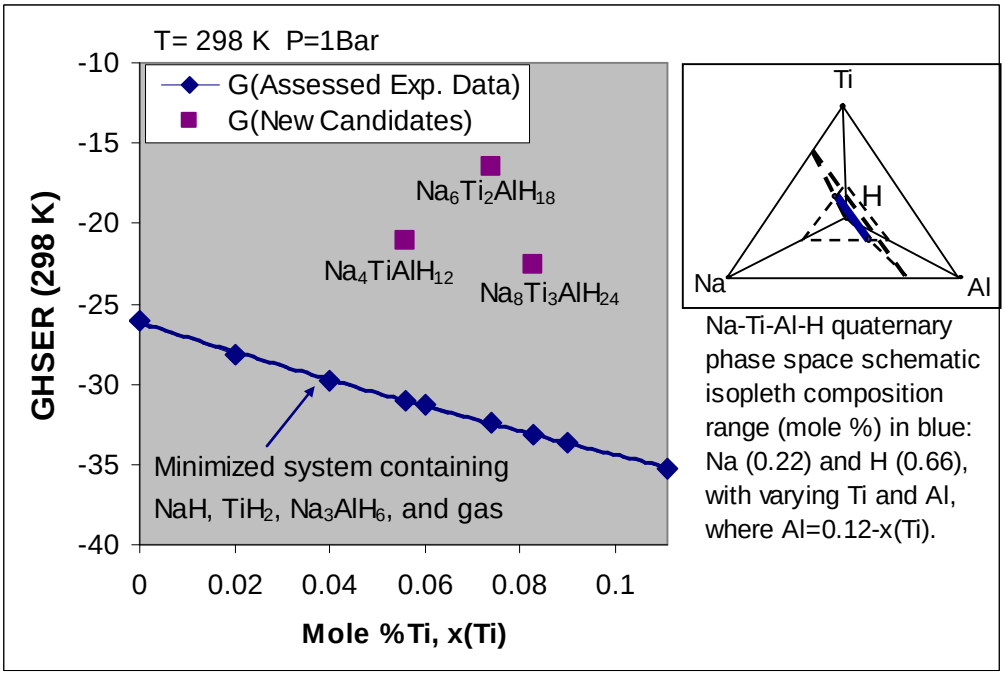

Figure 16: Na-Ti-Al-H quaternary Ti-Al isopleth comparing GHSER (298 K, 1 bar) values for newly predicted Na-Ti-Al-H complex hydride candidates with the Gibbs energy minimized phases determined with the Thermo-Calc Poly program with the combined SSUB3 [Ref. 21] and Na-Al-H [Ref. 5] databases for the composition range in mole %: 0.22 Na, 0.66 H, with 0.12 (Ti+Al) and Al=0.12-x(Ti).

The thermodynamic assessment of selected experimentally characterized and predicted phase data within the Na-Ti-Al-H quaternary system is detailed in reference [Ref. 44]. This enabled the thermodynamic modeling of Ti solubility within the $NaAlH_4$, Na_3AlH_6, and NaH phases, and the coexistence of Ti-bearing phases with the Na-Al-H system using sub-lattice models. This included the predicted thermodynamic properties of the hypothetical $NaTiH_4$ and Na_3TiH_6 compounds, as well as their mixing properties with $NaAlH_4$ or α-Na_3AlH_6. A repulsive interaction is predicted by the first principle calculations when Ti is dissolved in $NaAlH_4$ or α-Na_3AlH_6 which becomes stronger when increasing the temperature. If Ti is present, decomposition of $NaAlH_4$ and α-Na_3AlH_6 can lead to formation of $TiAl_3$ and/or TiH_2.

3.3.1.6 Thermodynamic Optimization of the Na-Li-Al-H quaternary

An investigation was conducted on the Na-Li-Al-H system to demonstrate the utility of coupling experimental and theoretical methodologies for material optimization [Ref. 41]. Of interest was the development of mixed hydride systems that could leverage the high capacity of the lithium alanates

and the reversibility of the sodium alanates. A database of the predicted thermodynamic properties of all known phases in the Na-Li-Al-H quaternary system was created, including the recently evaluated Na_2LiAlH_6 phase [Refs. 42,43,45,46]. Thermodynamic calculations with this database were used to elucidate the most favorable reactions for synthesis and disproportionation of the intermediate Na_2LiAlH_6 phase. The two most favorable competing disproportionation reactions are shown in Figure 17. The disproportionation to the elemental hydrides, as given in $^2/_3Na_2LiAlH_6 \rightarrow {}^4/_3NaH + {}^2/_3LiH + {}^2/_3Al + H_2$ releases the most hydrogen. A less desirable Na_2LiAlH_6 disproportionation step releasing less H_2 was predicted to predominate below 87°C.

Equation 5 $$^2/_3Na_2LiAlH_6 = {}^4/_9Na_3AlH_6 + {}^2/_3LiH + {}^2/_9Al + {}^1/_3H_2$$

In this latter pathway, another reaction step would be required to fully release all of the hydrogen within the system. Experimental observations corroborated the occurrence of this reaction occurring at lower temperature [Ref. 41].

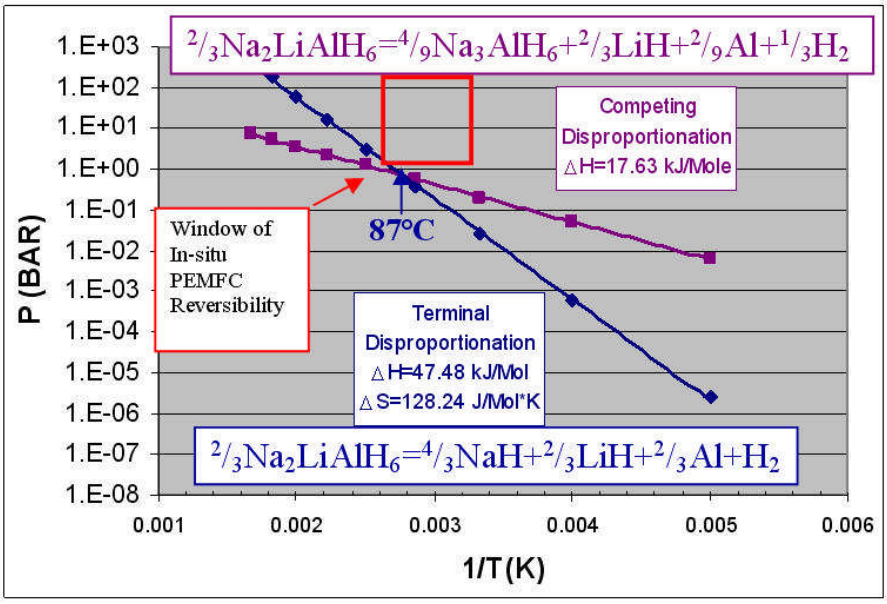

Figure 17: The predicted van't Hoff plot showing the relationship two competing Na_2LiAlH_6 disproportionation reactions.

Gibbs free energy minimization and phase diagram calculations were conducted to identify the composition, temperature and pressure conditions for optimum H capacity within the Na-Li-Al-H system. A theoretical reversible 5.2 wt%$H_{Rev\ Theor}$ was predicted for the starting stoichiometry {2Na : 1Li : 2Al : 9H} corresponding to a $2NaAlH_4$:1LiH mixed hydride composition. This mixture would disproportionate at ambient temperature and pressure to release 2.6 wt%$H_{Rev\ Theor}$.

Equation 6 $$^4/_3NaAlH_4 + {}^2/_3LiH \rightarrow {}^2/_3Na_2LiAlH_6 + {}^2/_3Al + H_2$$

This is essentially a destabilized disproportionation reaction that has a lower $\Delta G_{disproportionation}$ below 100°C and a smaller $\Delta H_{disproportionation}$ per mole H_2 dissociated, compared to that for $NaAlH_4$ alone. Upon heating above 100°C, a second disproportionation is predicted to follow the reaction to release the remaining 2.6 wt%$H_{Rev\ Theor}$ (including the extra Al atom).

3.3.2 Funding Year 2 Atomic-Thermodynamic Modeling

3.3.2.1 Na-Mg-Al-H and Li-Mg-Al-H Candidate Hydride Simulations

The wt%$H_{Rev\ Theor}$ of quaternary complex hydrides in the Na-Mg-Al-H and Li-Mg-Al-H systems will be dependent upon the change in dehydrogenation products formed with varying conditions. A lower wt% H_2 limit can be projected for the formation of both alkali and alkaline earth hydrides upon dehydrogenation at lower temperatures. A higher wt% H_2 limit can be projected when all of the Mg is incorporated in intermetallic phases upon disproportionation at higher temperatures. Numerous fluoride and other complex analog models were used as templates to survey for possible existence of quaternary hydride phases in each of the Na-Mg-Al-H and Li-Mg-Al-H systems with atomic simulations. Thermodynamic predictions were made of quaternary complex hydride candidates, numerous binary and ternary lower order phases, including many known Al-Mg and Al-Li phases and line compounds, and lesser-known Li-Al-Mg alloys and compounds. The ternary hydride phases, both known and proposed phases for $Mg(AlH_4)_2$, $NaMgH_3$, and $Li_xMg_yH_z$ compositions have also been predicted, as well as the elemental hydride phases. This enabled the determination of candidate phase stability under different temperatures and pressure.

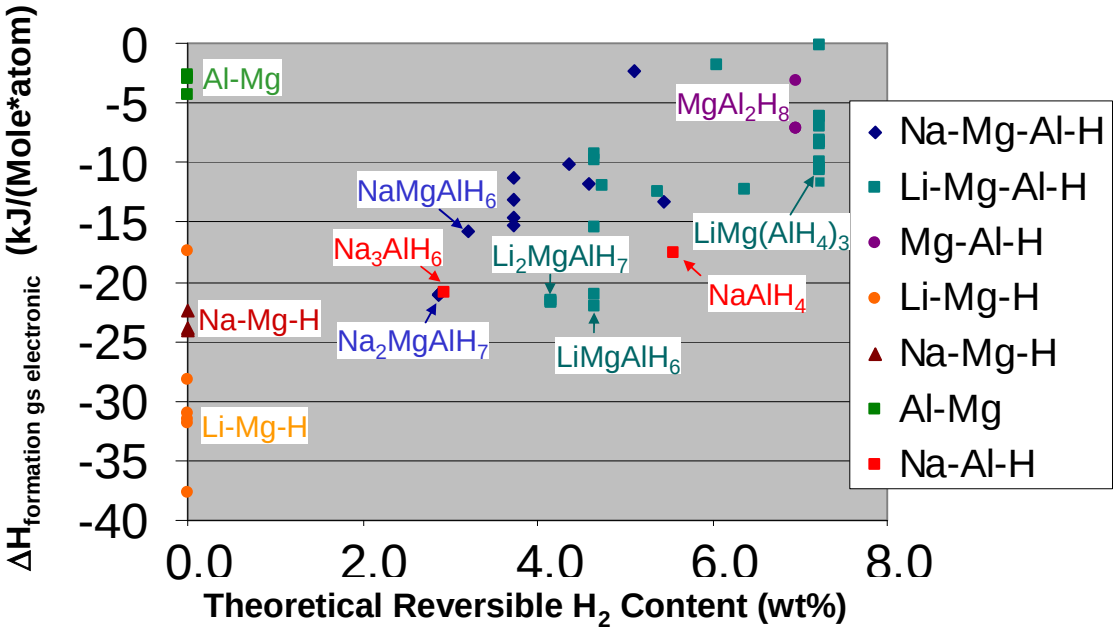

Figure 18: Ground state $\Delta H_{formation\ gs\ electronic}$ for candidate Na-Mg-Al-H and Li-Mg-Al-H quaternary phases for the lower limit wt% $H_{Rev\ Theor}$. Many symbols actually consist of multiple superimposed data points for candidate phases having nearly identical enthalpies. The stoichiometries of the most favorable phases are labeled.

The ground state electronic heat of formation, $\Delta H_{formation\ gs\ electronic}$, for quaternary candidate structures in the Na-Li-Mg-Al-H quinary system are plotted versus the lower limit $wt\%H_{Rev\ Theor}$ in Figure 18. Also shown for comparison are some lower order related phases. Many of the candidates' electronic $\Delta H_{formation\ gs\ electronic}$ were comparable in stability to the corresponding values determined for the sodium alanates. Despite the overall trends of decreasing stability with increasing H_2 content, there were many ground state stable Li-Mg-Al-H candidates with significant $wt\%H_{Rev\ Theor}$.

3.3.2.2 Thermodynamic Optimization of the Li-Mg-Al-H and Na-Mg-Al-H Quaternaries

A large number of favorable candidate phase structures were identified for the $AkMgAlH_6$ and Ak_2MgAlH_7 stoichiometries, where Ak is either Na or Li, that had heats of formation, $\Delta H_{formation\ gs\ electronic}$ more negative than -20 kJ/mole*atom. Such values were competitive with those that have been determined for the well-known alkali alanate phases. The former compound has been synthesized by solution-based processing in our program and also by mechanochemical preparation in another laboratory [Ref. 47], but did not yet have a crystallographically-refined structure. For this reason, we experimentally and theoretically sought to identify the most stable $LiMg(AlH_4)_3$ structure, in order to enable thermodynamic predictions to be made for this phase.

Thermodynamic calculations were made in order to access the total theoretical reversible hydrogen capacity of our newly identified favorable candidate structures. Thermodynamic property predictions were made for selected $AkMgAlH_6$ and Ak_2MgAlH_7 phases, as well as other favorable known and hypothetical lower-order phases in the Li-Mg-Al-H and Na-Mg-Al-H systems, using direct method lattice dynamics. These latter known phases included $Mg(AlH_4)_2$, $NaMgH_3$, pure alkali alanate, elemental hydride phases, and various Mg-Al intermetallic phases. The latter hypothetical favorable candidate phases included Li_6MgH_8, Li_2MgH_4, and Li-Mg-Al alloy phases. The predicted thermodynamic properties were parameterized and compiled into a thermodynamic database, and were used along with the COST507 database [Ref. 48] to identify the composition, temperature and pressure conditions for the optimum hydrogen capacity within both quaternary systems. For brevity, only the results for the Li-Mg-Al-H system, with the greater potential for high H capacity will be presented. Our major question was whether it would be possible to form intermetallic Al-Mg or Li-Mg-Al phases upon complete dehydrogenation of the complex quaternary $AkMgAlH_6$ and Ak_2MgAlH_7 phases, partially or fully in place of forming the elemental hydride phases. This would result in significantly higher theoretical reversible hydrogen capacities for these hypothetical compounds. The ternary isopleth for the Li-Mg-Al-H elemental stoichiometry {1Li : 1Mg : 1Al : 6H}, shown in Figure 19, predicts the stable existence of the $LiMgAlH_6$ phase at -23°C, 100 bar pressure, and $3x10^{-3}$ hydrogen activity over a range of compositions (higher pressures were necessary to predict stable existence at room temperature). Upon lowering the pressure to 1 bar at 25°C, the $LiMgAlH_6$ phase decomposes to the elemental hydride phases to release 4.7 wt%H.

Equation 7 $\mathbf{LiMgAlH_6 \rightarrow LiH + MgH_2 + Al + {}^3/_2H_2}$

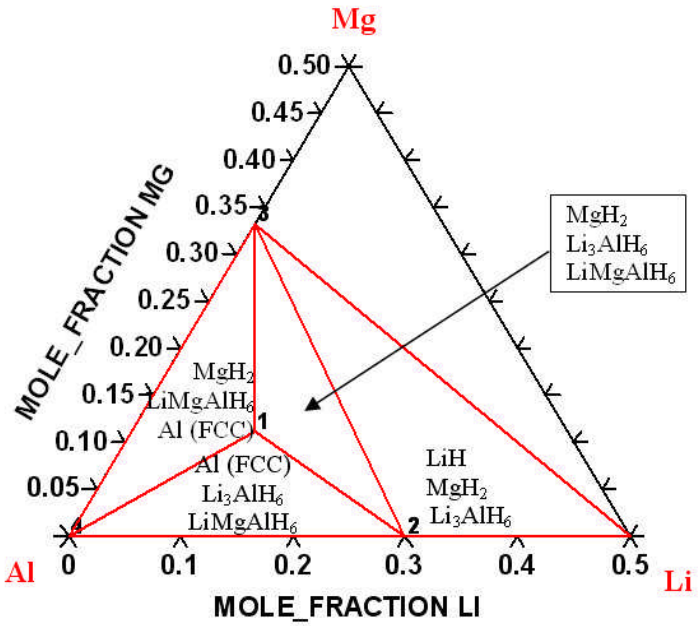

Figure 19: Ternary isopleth for Li-Mg-Al-H quaternary system at constant $3x10^{-3}$ H activity, -23°C temperature and 100 bar pressure showing distribution of phases with varying composition.

If the hydrogen activity is lowered further, akin to the evacuation of H_2, various Al-Mg and in some cases, Al-Li intermetallic phases are predicted to form, in place of the elemental hydride phases. The change in disproportionation phases with decreasing H mole-fraction at 25°C and 100 bar is shown in Figure 20. If starting from the fully hydrided $LiMgAlH_6$ phase, the H mole-fraction is decreased to 0.25 under these conditions and the corresponding disproportionation reaction would be

Equation 8 $\mathbf{LiMgAlH_6 \rightarrow 0.25LiH + 0.04Al_3Mg_2 + 0.01Al_{12}Mg_{17}\ (+{}^5/_2H_2\ evacuated)}$

resulting in the release of 7.7 wt%H. In the Mg-Al binary phase diagram at 1 bar pressure, Al_3Mg_2 and $Al_{12}Mg_{17}$ are stable over narrow composition ranges from 100°C up to melting at 450°C [Ref. 49]. The formation of an intermetallic phase similar to Al_3Mg_2 has been observed experimentally during the decomposition of $LiMg(AlH_4)_3$ above 250°C [Ref. 47], signifying the possibility of an even higher H capacity. Thus, these combined atomic-thermodynamic predictions have projected a theoretical upper bound for Li-Mg-Al-H complex alanates to have the potential for H capacities that meet or exceed the project target.

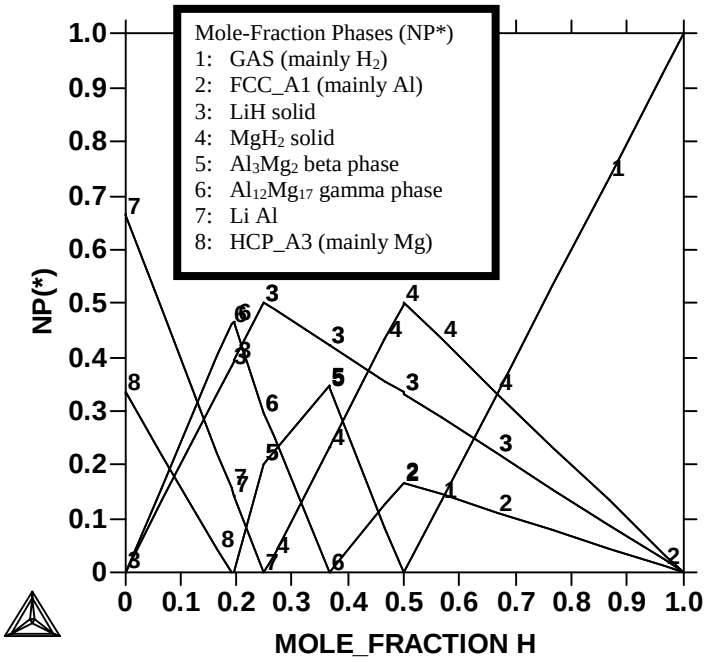

Figure 20: The mole-fraction of disproportionation phases with increasing H mole-fraction at 25°C and 100 bar with a constant stoichiometry {1Li : 1Mg : 1Al } calculated with COST507 database [Ref. 48].

Thermodynamic modeling of the Na-Mg-Al-H system showed that the best quaternary candidate phases were not stable under reasonable temperature and pressure conditions. The phase diagram in Figure 21 shows that only the ternary $NaMgH_3$ phase was predicted to co-exist with the sodium alanate phases at 298 K and 100 bar.

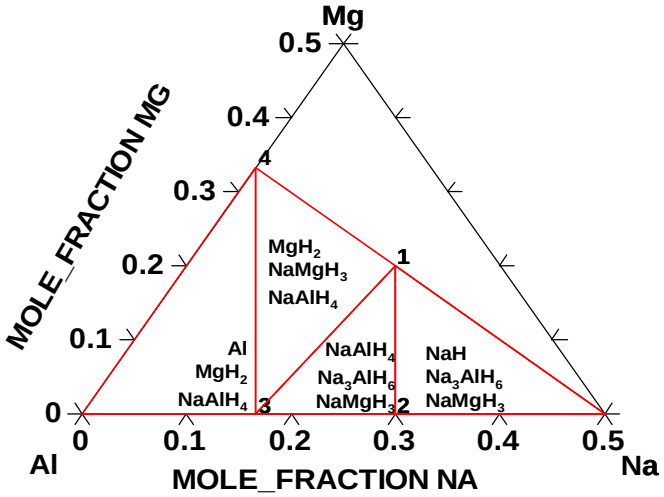

Figure 21: Na-Mg-Al isothermal ternary section calculated at 298 K and 100 bar with H activity of 3.9×10^{-3} bar, showing distribution of phases with varying composition.

Although the Na-Mg-Al-H system does not have potential for high H capacity, the thermodynamic modeling of reactions with the $NaMgH_3$ phase enabled insight into the modification of $NaAlH_4$ decomposition. A van't Hoff plot of the possible reactions in the Na-Mg-Al-H system is shown in Figure 22. The addition of MgH_2 to $NaAlH_4$ may promote the single step dehydrogenation reaction to form $NaMgH_3$ below 52°C.

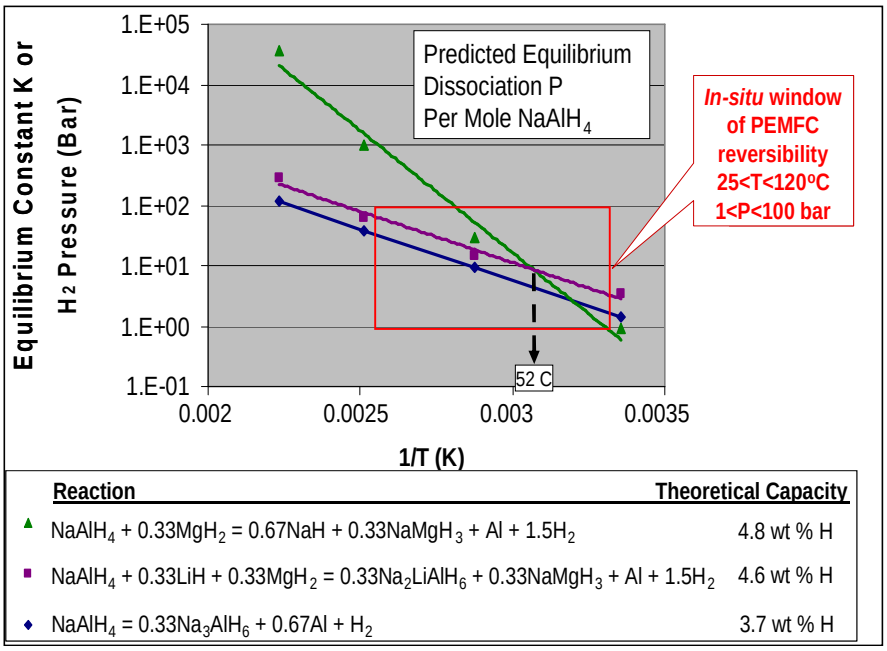

Figure 22: Van't Hoff plot showing the dehydrogenation reactions predicted for the most stable phases in the Na-Mg-Al-H system.

3.3.2.3 Refinement of Li-Mg-Al-H Phase Structures

Atomic modeling was used in conjunction with experimentation to further refine the structures and thermodynamic predictions of two unique phases in the Li-Mg-Al-H system: $LiMg(AlH_4)_3$ and $LiMgAlH_6$ [Refs. 50,51]. The best ground state candidate structures were previously identified for $LiMg(AlH_4)_3$ and were used as preliminary input for the refinement of crystallographic structure. Our collaborators at the Institute for Energy (IFE) in Norway, Hendrik Brinks and Hilda Grove, refined the monoclinic structure for this compound from powder neutron diffraction and high resolution synchrotron radiation powder x-ray diffraction analytical results. We evaluated the refined structure with respect to other possible candidates simulated with the structural analog approach. There are relatively few known analog quaternary complex compounds, none of which are hydrides, which have a ratio of one or two counterions to three complex functional groups that could function as templates for the derivation of the $LiMg(AlH_4)_3$ structure. Therefore, additional quaternary complex halide and oxide compound structures with closely related stoichiometries were also used as templates. Additional approaches to derive candidate structures, including the substitution of Li in $Mg(AlH_4)_2$ and Mg in $LiAlH_4$ were also employed, as well as the use of the Endeavor program Monte Carlo simulated annealing [Ref. 26] to globally optimize atomic positions. The refined $LiMg(AlH_4)_3$ structure developed in this study was predicted to have the lowest, most stable $\Delta H_{formation\ gs\ electronic}$

compared to the other most favorable candidate structures derived from the structural analog approach [Ref. 50].

Comparison of experimental and modeling results have confirmed the likelihood of the existence of best candidate trigonal $P32_1$ structure simulated for the $LiMgAlH_6$ intermediate phase [Ref. 51]. This structure was also identified in parallel in separate studies by our collaborators [Ref. 52]. Following desorption of the $LiMg(AlH_4)_3$ phase for several hours at 100 ºC, unidentified peaks were detected by x-ray diffraction. The 2θ positions of many of these peaks were found to be equivalent to those in the simulated x-ray pattern determined for the trigonal $LiMgAlH_6$ structure [Ref. 51]. This validation serves both to confirm the important reaction mechanism for $LiMg(AlH_4)_3$ and to validate the structures for generating thermodynamic predictions. First principles thermodynamic predictions were made with these refined structures to improve our thermochemical predictions.

3.3.2.4 Strategy Expansion

The newly expanded "coupled complex reaction strategy" implemented during the course of the second year, mandated the inclusion of a broader range of chemistries for the effective identification, design, and refinement of reversible high capacity complex hydrides and co-reactants, and low capacity disproportionation products, using our integrated atomic-thermodynamic-experimental approach. To accomplish this, the atomic-thermodynamic surveys were expanded to include the Na-Li-Al-H, Na-Mg-Al-H, Li-Mg-Al-H, Li-Mg-(Na)-N-(Al)-H, Li-Mg-(Na)-B-(Al)-H, and Li-Mg-(Na)-(Al)-B-N quaternary compositional systems. These systems were then merged into the higher order septenary system: Li-Mg-Na-Al-B-N-H, schematically illustrated in Figure 23. This multi-order extension in compositional space outfitted our palette for designing coupled complex reactions using a combination of established thermochemical formulation methods. In addition, a new thermodynamic methodology was developed for optimizing the H capacity and reversibility of newly designed coupled complex reactions. The following sections highlight our progress in the survey, reaction design, and thermodynamic optimization of coupled complex reactions within this septenary system.

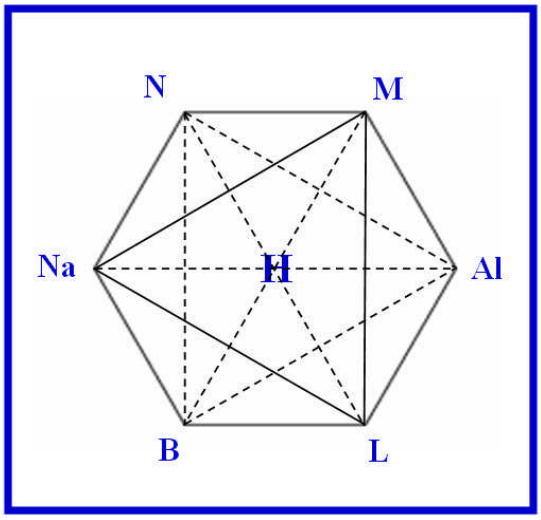

Figure 23: Schematic of high capacity septenary compositional system.

3.3.2.5 Survey of Li-Mg-Na-Al-B-N-H Septenary System

During the second-half of the second year, atomic-thermodynamic surveys concentrated on rapidly building a database of simulated finite thermodynamic properties for phases within the Li-Mg-(Na)-N-(Al)-H, Li-Mg-(Na)-B-(Al)-H, and Li-Mg-(Na)-(Al)-B-N systems. These systems included both known and hypothetical amides-imides, borohydrides, and their disproportionation products, such as complex boron-nitrides, elemental borides and nitrides. These simulations first concentrated on over 40 known phases within these three systems. For structurally-defined known phases, a higher priority was given to systems which have not yet been thermodynamically characterized. For known phases with incomplete or no known structural information, analogous systems were utilized as templates to create candidate structure phases. The best candidate(s) for each phase were then input into Phonon lattice dynamics calculations for prediction of finite temperature thermodynamic values. These predicted values were integrated into thermodynamic databases to facilitate design of new high capacity coupled reactions. A tabulation of all the possible permutations of multi-order systems up to and including quinaries with H in the Li-Mg-Na-Al-B-N-H septenary system is shown in Figure 24, with the subsystems having known compound formation colored in red. Many subsystems shown in magenta remain to be investigation for potential hydrides, co-reactants and/or disproportionation products.

The expansion of our virtual surveys to the nitrogen- and boron-based chemistries called for additional benchmarking of our predictive accuracy. The well-known lithium amide system was selected for this validation. A ternary isothermal section for the Li-N-H system in Figure 25 shows the relative stability of the lithium amide ($LiNH_2$), imide (Li_2NH), and hydride (LiH) phases, as well as the gaseous decomposition products predicted at 25°C (298 K) and 100 bar. From this diagram, it can be clearly seen how the change in composition dramatically affects the stability of the decomposition products, especially how the ammonia formation can be eliminated through the thermodynamic optimization of the elemental system stoichiometry. As a benchmark, the change in enthalpy upon dehydrogenation for the reaction: $LiNH_2 + LiH = Li_2NH + H_2$, was predicted to be 79.92 kJ/mol. This value compares well with the experimental value of 66 kJ/mol determined by Chen et al. [Ref. 53], and the theoretical value of 73.6 kJ/mol determined by Herbst and Hector [Ref. 54].

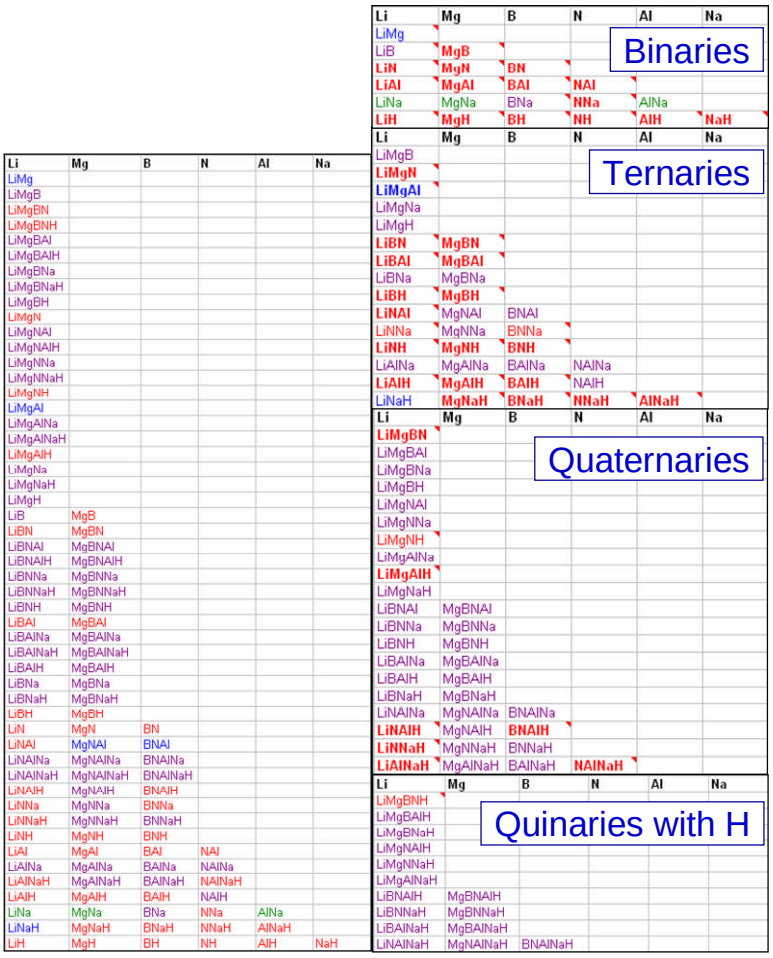

Figure 24: All possible permutations of multi-order systems up to and including quinaries with H in the Li-Mg-Na-Al-B-N-H septenary system.

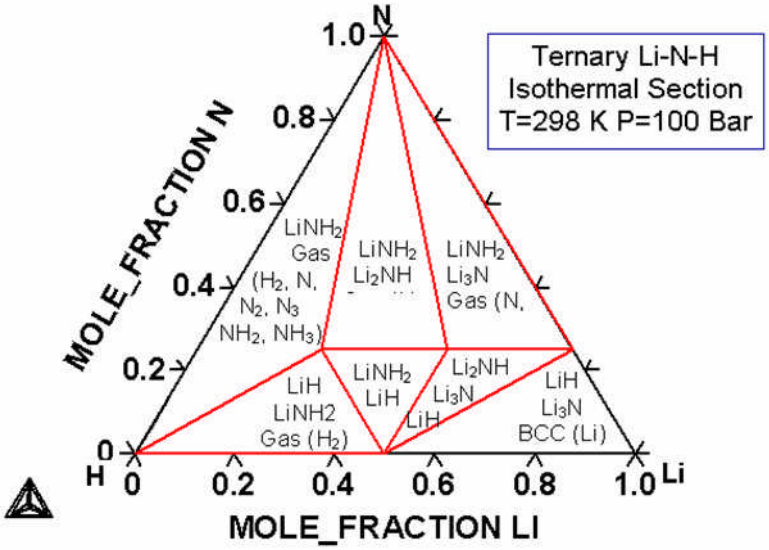

Figure 25: Benchmarking of atomic-thermodynamic predictions for the Li-N-H system.

3.3.2.6 Reaction Design and Thermodynamic Optimization

One high capacity strategy was to mix complex hydrides combining Al and N, Al and B, or B and N centered complexes. However, the dehydrogenation of these mixtures can lead to the very exothermic formation of favorable products of AlN, AlB, or BN-bearing compounds, rendering the reverse hydrogenation reactions to be thermodynamically impractical. Alternatively, our new strategy and expanded survey enables the design of reversible high capacity coupled reactions with more stable co-reactants, and less stable products, to effectively balance or tune the dehydrogenation reaction. Reaction design was accomplished by systematically examining complex hydride reactions with co-reactants, iteratively utilizing both thermochemical reaction and Gibbs energy minimization equilibria calculations. The reaction H capacity is determined from the most favorable reaction products and the reversibility is determined from the change in free energy or enthalpy upon dehydrogenation.

Once a new potential chemistry was identified from the reaction design surveys, the composition was optimized to maximize reversibility, H capacity, simplify discharge/recharge reactions, and/or eliminate side-products. This was done by simulating the change in phase stability within the multidimensional space formed by varying composition, temperature, and pressure. The composition and parameters are converged to maximize the H reversibility within the "in-situ window of reversibility" for polymer electrolyte membrane fuel cell (PEMFC) operation (25-120°C and 1-100 bar).

The dehydrogenation of the $LiNH_2$ to release up the 6.5 - 8.7 $wt\%H_{Rev\ Theor}$ by forming the Li_2NH or Li_3N products, respectively, presents a challenge because the decomposition reactions are endothermic and accessible only at high temperatures. In addition, these reactions involve multiple possible intermediates, are kinetically impeded, and are subject to forming NH_3 and other side-products. A new reversible dehydrogenation reaction that was optimized for $LiNH_2$ using our thermochemical reaction design approach is illustrated in Figure 26. An isobaric temperature thermochemical survey shown on the left hand side revealed a significant change in H content for reactions of $LiNH_2$ with the BN and LiH co-reactants to form the Li_3BN_2. Thermodynamic optimization was conducted to find the best stoichiometry that would generate the largest $wt\%H_{Rev\ Theor}$ at the temperature and pressure conditions closest to PEMFC operation. The van't Hoff plot of reaction with the optimized 3Li:1B:2N:4H stoichiometry with 6.3 $wt\%H_{Rev\ Theor}$

Equation 9 $$\mathbf{{}^1/_2LiNH_2 + {}^1/_2BN + LiH = {}^1/_2Li_3BN_2 + H_2}$$

is shown on the right hand side of Figure 26. Here, the co-reactants effectively shifted the dehydrogenation reaction to just below the "in-situ window of reversibility", yielding a predicted single step H_2 dissociation with an 1 bar equilibrium pressure at 135°C, with minimal formation of ammonia. It is important to remember that this prediction is an upper bound for what thermodynamically could be possible in the absence of kinetic limitations.

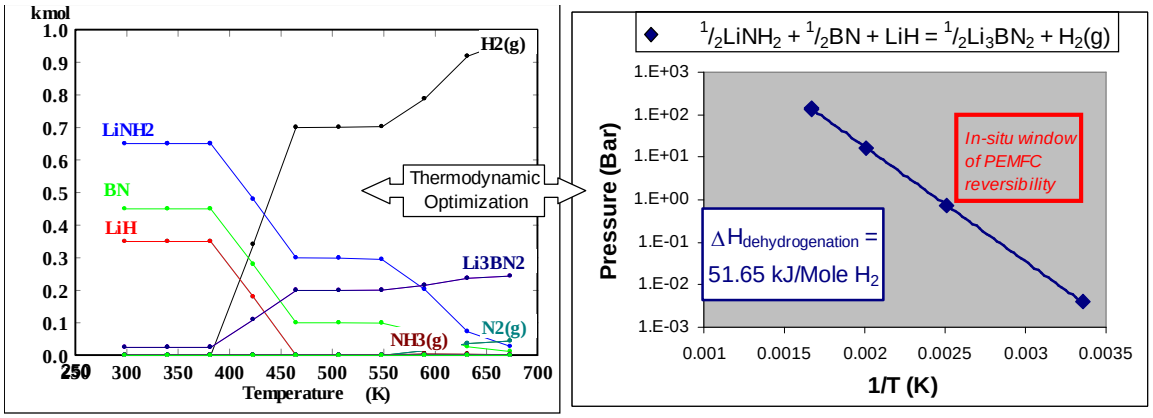

Figure 26: Example of thermodynamically designed and optimized reaction for H_2 storage with $LiNH_2$, BN and LiH reactants.

The example above gives evidence for implementation of the thermodynamic optimization tool. An expanded schematic for the virtual design of reversible, high capacity reactions is shown in Figure 27 based on this lithium amide reaction. Our approach to designing balanced reactions is through thermodynamic predictions, equilibrium studies, and optimization. We start with establishing thermodynamic data for candidate phases, co-reactants, and products, supplementing with first-principles finite T thermodynamic predictions wherever necessary. In order to identify new candidate systems, we employ an iterative approach of proposing reactions, then evaluating the reaction thermodynamics and hydrogen exchange for the reaction. For interesting reactions, we then employ equilibrium survey calculations, to determine for the many possible competing reactions which phases will predominate in hydrogen exchange reactions. We look for conditions, whereby changing composition, T or P, H evolves from being entrained in a solid phase to gaseous state. Once we find such an exchange, we extract the best possible reaction scenario, and scope out a candidate composition range for thermodynamic optimization. We also seek reactions that have a minimum number of steps and which minimize the formation of harmful side-products. Finally, we thermodynamically optimize the composition of our system to find the best stoichiometry that gives the highest hydrogen capacity. Shown in Figure 27 is a surface formed over a compositional range for a model system from the difference in H pressure between relevant high T, low P conditions and low T, high P conditions. We are able to predict phase diagrams and predict the equilibrium of phases for the thermodynamically optimized stoichiometry. From there we can back out the reaction, and determine the dissociation pressure. Shown in the van't Hoff plot on the right is a designed reaction for $LiNH_2$ with co-reactants that is predicted to exhibit intermediate dehydrogenation behavior, falling just below the window for PEMFC desorption.

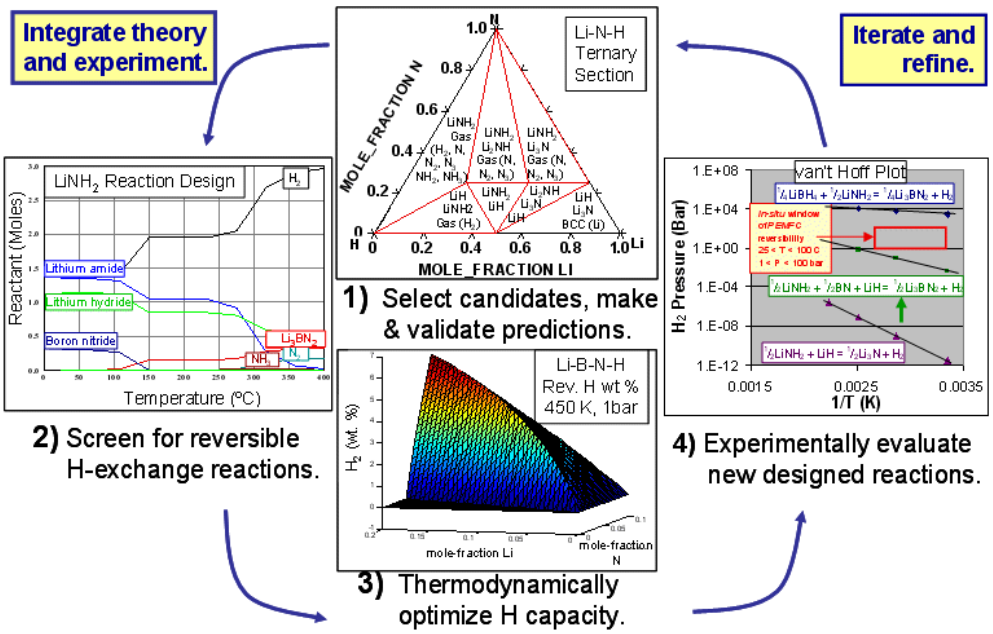

Figure 27. Schematic showing progression of modeling methodologies to design the reaction of $LiNH_2$ with co-reactants to increase the dehydrogenation pressure closer towards 1 bar at 100°C, including: 1) thermodynamic mapping of phase behavior for Li-N-H system and co-reactants, 2) thermochemical screening of reactions with co-reactants to search for reversible hydrogen exchange, 3) thermodynamic optimization of the best candidate compositional system, 4) prediction and evaluation of dissociation behavior.

3.3.3 Funding Year 3 Atomic-Thermodynamic Modeling

3.3.3.1 Borohydride Systems - Simulation of Disordered Structures

The decision to selectively focus on borohydride systems was prompted by the challenges identified in the H storage community with the reversibility and side-products of amide-based systems. Our first principles atomic modeling of the borohydride systems followed several parallel paths. First, baseline finite temperature thermodynamic property predictions were established for the known structures of $LiBH_4$ and $NaBH_4$ compounds and for the candidate structures for the lesser known compounds $Mg(BH_4)_2$, $Al(BH_4)_3$ and $Ti(BH_4)_4$. These thermodynamic property predictions enabled a preliminary assessment of designed borohydride reactions with other co-reactants (at that time, this was more of an approximation for the lesser known borohydrides) that served to guide experimental efforts. In a second path, modeling was used in an attempt to identify the structures of the newly synthesized Mg and Zr borohydride complexes with organic ligands. The structures of these complexes could not be obtained from the multiple overlapping peaks in the x-ray pattern indicative of an amorphous structure. Since there are very few known quaternary crystal structures to serve as templates for input models, especially for quaternary complexes with ligand adducts, and there was limited structural experimental information available for verification of modeling results, these systems were difficult to model with our established methodology for crystallographic simulations. This inspired us to turn

to molecular dynamic simulated anneals for the refinement of amorphous or locally ordered hydride phases. It made sense to implement this methodology in a third path, a new initiative to integrate simulations with solid-state (UTRC) and solution-based (Albemarle) syntheses to explore alkali borohydride destabilization through metal dopant substitution. This new approach showed great utility for screening doped compositions, elucidating doping mechanisms, and providing insights into experimental results. The following sections will highlight our approach and results for this third path.

The newly implemented atomic scale modeling approach combined VASP density functional theory elevated temperature molecular dynamics (MD) simulations with ground state minimizations to search out and refine low symmetry doped alkali borohydride structures. The MD served to impart kinetic energy to the structures that enabled: 1) energy barriers for crystallographic rearrangement to be overcome at moderate temperatures, sampling a larger configurational space for the development of input models for ground state minimization, and 2) the melting (amorphitization) of structures and progressive annealing into lower energy (more stable) configurations by slowly decreasing the simulation temperature. In the first phase, we used the former MD approach coupled with ground state minimizations to quickly screen dopant element substitution in the alkali or boron sublattices in the $LiBH_4$ and $NaBH_4$ crystals, using a doped stoichiometry for a charge-neutral structure with the dopant atom formal charge in the most stable oxidation state (for example: if Ti^{+3} was substituted for Li^{+1} in $4LiBH_4$, then altogether 3 Li^{+1} ions were removed from the input model). Initial ground state minimizations were conducted to identify the most favorable of all possible configurations. The best configuration was then annealed in a MD run for several picoseconds (10^{-12} seconds), where each step was ~ a fentosecond ($1x10^{-15}$ seconds) in duration, at an intermediate temperature near the melting point until an equilibrium energy oscillation was achieved. In some cases, less stable structures actually fell apart and/or became less favorable in the MD run. In other cases, significantly lower energy structures were formed, where the additional kinetic energy enabled local energy barriers to be overcome. Thus, the MD was used to quickly evaluate the stability of a doped structure with respect to decomposition. The MD output structures were fully minimized to determine the ground state energies and $\Delta H_{\text{formation gs electronic}}$. Further screening was done on the most favorable down-selected dopant/substitution site combinations to evaluate variation of dopant oxidation state/stoichiometry (only for TM dopants) and variation of dopant loading level to identify maximum solubility in the lattice. The best candidate structures were selected for experimental evaluation. For the most promising amorphous experimental systems, the second MD approach described above was appropriate. The melting and simulating annealing runs typically were 20 picoseconds or longer in total duration, and were conducted for systematically varying volumes. These rigorously refined structures could be directly compared with experimental results.

3.3.3.2 Quaternary Borohydride Survey

Our first principles atomic modeling survey assessed the stabilities and structures of the high H-discharging quaternary alkali metal borohydride systems newly discovered by solution-based processing and solid-state processing, and the candidacy of hypothetical compositions for future experimental evaluation. The thermodynamic properties of known and lesser-known ternary borohydride systems were benchmarked to set the stage for the survey. The alkali borohydride $NaBH_4$ $F\bar{4}3m$ and $LiBH_4$ *Pmna* structures were substituted with an additional element to survey a wide range of quaternary compositions. These included the substitution of 25 mole% metal (M): alkali (Na or Li), Mg, Al, Sc and Ti on the Li or Na sublattices (introducing alkali vacancies as necessary to maintain

compound charge neutrality), and of Al and Ti on the B sublattices. These quaternary systems have a theoretical maximum H capacity of 4.9 -12.3 wt% $H_{Rev\ Theor}$, assuming their full decomposition to binary hydrides and elements, such as: LiH, NaH, MgH_2, the most stable transition metal hydrides, Al and/or B upon dehydrogenation.

The ternary borohydride stability predictions set the foundation for assessing the relative stability of the quaternary phases. The benchmarking of the ternary alkali borohydride predictions, given in Table 5, gave us confidence to use the well-known $NaBH_4$ and $LiBH_4$ structures as the basis for our quaternary borohydride survey. The other ternary compounds: $Mg(BH_4)_2$, $Al(BH_4)_3$, and $Ti(BH_4)_4$, had been synthetically reported in the literature, but were not structurally known at that time. The values given for these latter compounds are for the most stable structures identified from ground state surveys of possible candidate structures. These predictions essentially bound the lower limit for ternary hydride stability.

Table 5: Ground-state predictions of ternary borohydride compounds.

Metal Borohydrides	Space Group	Predicted $\Delta H_{formation\ gs\ electronic}$ kJ/Mol*atom	Calculated Volume Å^3/atom
$NaBH_4$	$P4_2/nmc$	-33.88	9.33
$LiBH_4$	*Pnma*	-34.69	8.91
$Mg(BH_4)_2$	*Pc*	-22.94	9.38
$Al(BH_4)_3$	$P3_11_2$	-11.98	10.68
$Ti(BH_4)_4$	$P4_2/nmc$	-14.46	12.04

The metal quaternary constituents have a dramatic impact on quaternary alkali borohydride stability, as shown in Table 6 for a wide range of compound stoichiometries. Overall, the quaternary lithium borohydrides were more stable than the quaternary sodium borohydrides. The most stable compositions were substituted with other alkali (25 mole% Na in $LiBH_4$ and 25 mole% Li in $NaBH_4$), and were very close in stability to the corresponding ternary phases. The other most stable phases included the substitution of Mg on the $LiBH_4$ Li sublattice with the requisite additional vacancy formation, and the substitution of Al on the B sublattices of $LiBH_4$ and $NaBH_4$. The substitutions of 25 mole% Ti or Sc on the Li sublattice (with the concomitant formation of two vacancies to simulate a +3 transition metal charge) or Ti on the B sublattice were of similar magnitude in stability. The 25 mole% substitution level selected for the preliminary screening is rather high, and all heats of substitution are endothermic, indicating that the substituent solubility limits were exceeded. The relaxations were limited by the relatively few degrees of freedom for the doped high symmetry structure based on the $F\bar{4}3m$ $NaBH_4$ isomorph (this structure was selected for convenience; it is slightly less stable than the $P4_2nmc$ structure). Although the 700 K MD temperature was below that of the $NaBH_4$ melting point, all of the doped compositions became less stable from the MD anneals.

Table 6: Simulated heats of formation and atomic volumes for quaternary alkali metal borohydride systems.

Quaternary Compound Formula	Ak = Li		Ak = Na	
	$\Delta H_{formation\ gs\ electronic}$ kJ/Mol*atom	Volume Å^3/atom	$\Delta H_{formation\ gs\ electronic}$ kJ/Mol*atom	Volume Å^3/atom
(Ak)Al(BH_4)$_4$	-15.45	9.87	3.03	7.73
(Ak)Ti(BH_4)$_4$	-14.03	10.78	-2.21	7.69
(Ak)Sc(BH_4)$_4$	-23.34	12.19	-16.95	8.06
(Ak)$_2$Mg(BH_4)$_4$	-28.05	11.00	-22.07	8.68
(Ak)$_3$Li/Na(BH_4)$_4$	-34.17	9.95	-30.72	9.26
(Ak)$_4$AlH_4(BH_4)$_3$	-28.07	10.82	-24.80	10.94
(Ak)$_4$TiH_4(BH_4)$_3$	-21.48	9.16	-10.88	11.46

The resulting ionic and electronic structures were analyzed, and excellent correlations were found between stability and electronic properties, which were used as the basis for further formulation development. For example, the correlation between the quaternary compound heats of formation and the metal substituent redox potential for the most favorable metal oxidation state is shown in Figure 28. In general, it may be concluded that the lower the redox potential for the metal substituent, the more stable the substituted quaternary alkali metal borohydride.

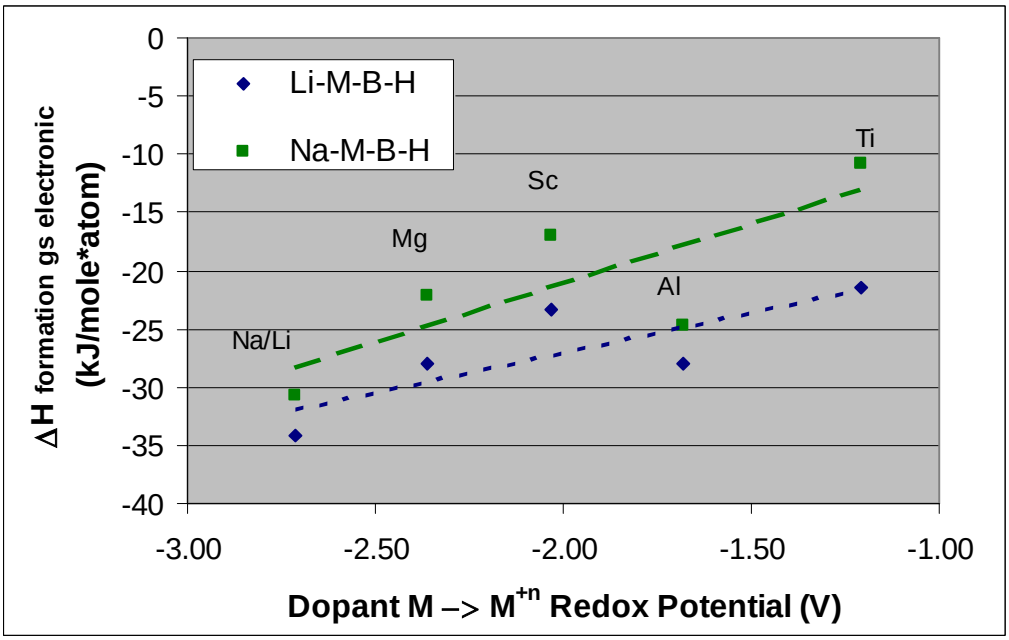

Figure 28: Correlation plot between quaternary compound simulated $\Delta H_{formation\ gs\ electronic}$ in Table 6 and the M substituent standard state redox potential for the most favorable M oxidation state.

For the quaternary systems formed with Al and Ti substituents on the alkali B sublattices, varying compositions were simulated to determine if there was a possible compositional range where quaternary compositions would be more stable than corresponding ternary alkali borohydrides. The heats of formation for varying Al and Ti substitution in $NaBH_4$ and $LiBH_4$ are plotted in Figure 29. The substitution of low concentrations of Al in $LiBH_4$ is predicted to be more stable than $LiBH_4$.

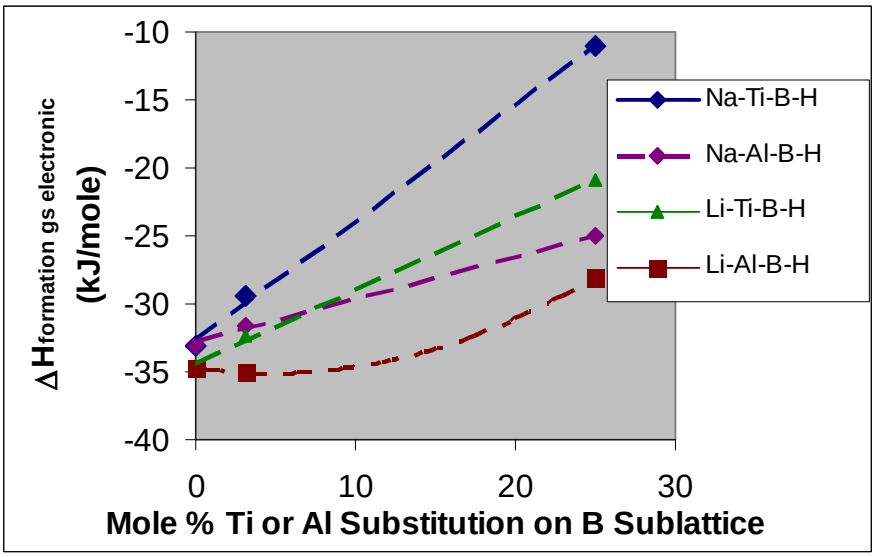

Figure 29: Ground state enthalpies of formation, $\Delta H_{formation\ gs\ electronic}$, for varying Al and Ti substitution in $NaBH_4$ and $LiBH_4$.

3.3.3.3 Atomic Scale Simulation of $Mg(BH_4)_2*2.2NH_3$ Ligand Complex

Atomic modeling was used to investigate the range of possible structures that could be formed with the $Mg(BH_4)_2*2.2NH_3$ complex synthesized by Albemarle (Section 5.3) and the change in possible decomposition reaction mechanisms with structure. Although synthesis of the complex $Mg(BH_4)_2$ without ligands has been reported, its stability and structure had not yet been substantiated. A recent atomic modeling study surveyed possible $Mg(BH_4)_2$ crystal structures and found the most favorable structure to be that derived from the substitution of $Mg(BH_4)_2$ stoichiometry on the $CdAl_2Cl_8$ *Pmc*2_1 structural analog lattice sites [Ref. 57]. We surveyed a number of candidate structure types for this compound, including several structures not covered by Ref. 57. We found a number of structures that were very similar in stability, but none as stable as that derived from $CdAl_2Cl_8$. However, we found that the input and minimized symmetry for this structure was *Pc*, not *Pmc*2_1 as was stated in Ref. 57. The calculation results are shown in Table 7.

Table 7: Simulation results for candidate $Mg(BH_4)_2$ structures.

MgB_2H_8 Structural Analog	Reference (ICSD #)	Input Model Space group / Pearson	$\Delta H_{formation\ gs\ electronic}$ (kJ/mole*atom)
$CdAl_2Cl_8$	62037	*Pc* mP22	-23.68
$MgAl_2Cl_8$	62046	C_2/c mS44	-22.94
$MgAu_2F_8$	65287	P_12_1/C_1 mP22	-21.76
$UPbSe_2O_8$	280839	*Pc* mP44	-21.75
$BaMn_2O_8$	27087	*Fddd* oF88	-21.43
BeB_2H_8	10315	$I4_1CD$ tI176	-21.20

This most favorable $Mg(BH_4)_2$ *Pc* model was used as the starting point for developing models for the $Mg(BH_4)_2*2NH_3$ complex (2 NH_3 groups were used instead of 2.2, because fractional numbers are atomically difficult to represent). Several approaches were used to simulate varying possible NH_3 complexing interactions. First, NH_3 groups were added to obtain the $Mg(BH_4)_2*2NH_3$ stoichiometry, and the structure was minimized while maintaining the *Pc* symmetry. The NH_3 groups in this structure were in the outer coordination sphere and were not directly associated with the Mg ion. The $Mg(BH_4)_2$ formed 2-dimensional staggered layers, where each Mg was tetrahedrally bonded to $4BH_4^-$ groups and each BH_4^- complex was associated with 2 Mg ions. The $Mg(BH_4)_2$ layers were intercalated with the NH_3 molecules. Next, in order to explore other possible interactions of NH_3 with Mg, the symmetry was "broken" by displacing one of the atoms slightly. Molecular dynamics was conducted, thermalizing the model at 400 K for 1.3 picoseconds (1000 steps). The model was then minimized, with the result that one of the two NH_3 groups became directly bonded to Mg. Here, the $Mg(BH_4)_2$ sheets were broken up into chains and each Mg was bonded to $3BH_4^-$ groups and 1 NH_3 group. There were two types of BH_4^- groups in this structure, one shared between two Mg ions and one bonded as a pendant group to one Mg. Two pendant BH_4^- and NH_3 groups, and two shared BH_4 groups were arranged tetrahedrally around each Mg ion. Finally, to simulate the possible direct bonding of two NH_3 to each Mg, the second NH_3 was moved closer to each Mg. Molecular dynamics and minimizations were conducted as before. The result was a crystal structure containing distinct

tetrahedral $Mg(BH_4)_2(NH_3)_2$ complexes that were not bridge-bonded to other complexes. The complexes are shown in Figure 30, and the $\Delta H_{formation\ gs\ electronic}$ are given in Table 8. The stability of the $Mg(BH_4)_2*2NH_3$ compound was found to increase with the lowering of the dimensionality of $Mg(BH_4)_2$ network bonding and with the increasing inclusion of the NH_3 group in the inner-coordination sphere.

Table 8. Simulation results for proposed $Mg(BH_4)_2*2NH_3$ complex structures.

$Mg(BH_4)_2*2NH_3$	NH_3 Bonding Description	$\Delta H_{formation}$ (kJ/mole*atom)
	2 NH_3 bonded to Mg	-33.31
	1 NH_3 bonded to Mg	-30.74
	No NH_3 directly bonded	-27.49

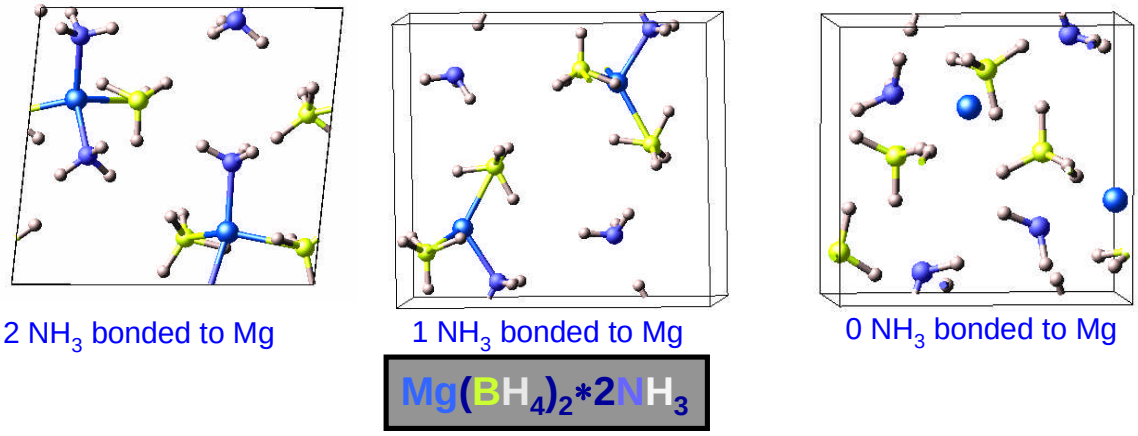

Figure 30: The $Mg(BH_4)_2*NH_3$ complexes with varying NH_3 in inner coordination sphere.

The predictions provided insight into $Mg(BH_4)_2$ stabilization by complexation with NH_3. The proposed disruption of the $Mg(BH_4)_2$ inter-complex bonding by NH_3 may also provide an explanation for the kinetic enhancement of decomposition that was observed experimentally. The predicted ground state electronic reaction enthalpies, $\Delta H_{dehydrogentaion}$, are shown in Table 9 for the decomposition of $Mg(BH_4)_2$ and $Mg(BH_4)_2*2NH_3$ complexes. These give an indication of relative reaction trends, but are not corrected for vibrational contributions. The ground state predictions show that the $Mg(BH_4)_2$ decomposition reactions to MgH_2 or Mg have similar enthalpies per H_2 molecule generated. The ground state decomposition enthalpies for the $Mg(BH_4)_2*2NH_3$ complex varied with the incorporation of NH_3 into the complex. The first reaction for $Mg(BH_4)_2*2NH_3$ "hydride-mechanism" decomposition to form MgH_2 is more endothermic than the $Mg(BH_4)_2$ reaction, and becomes decreasingly endothermic with the decrease in stability of the complex (2 → 0 NH_3 directly bonded). On the other hand, the second reaction "amine-borane mechanism" for $Mg(BH_4)_2*2NH_3$ decomposition, is predicted to be only slightly endothermic at the ground state and becomes almost thermally neutral with decreasing NH_3 bonding to Mg.

Table 9: Predicted electronic reaction enthalpies, $\Delta H_{dehydrogentaion}$, for various decomposition reactions.

Ground State Reactions	No. NH_3 Groups Bonded to Mg		
	2	1	0
	$\Delta H_{decomposition}$ (kJ/mole*H_2)		
$Mg(BH_4)_2$ --> MgH_2 + 2B + $3H_2$	64.35	-	-
$Mg(BH_4)_2$ --> Mg +2B + $4H_2$	65.13	-	-
$Mg(BH_4)_2$*$2NH_3$ --> MgH_2 + 2B + $2NH_3$ + $3H_2$	115.06	98.81	78.18
$Mg(BH_4)_2$*$2NH_3$ -->1/3Mg_3BN_3 + BN+ 2/3B + $7H_2$	25.16	18.20	9.36

4 Solid State Processing

4.1 Summary

Solid state processing has been used to investigate the high hydrogen capacity alanate and borohydride classes of materials described above. The primary composition systems are listed in Table 3 along with the other methods which have been applied for those systems. A total of nine compositional systems were studied in the search for high capacity materials. The project started with the investigation of mixed Am (alkaline metal) and Ae (alkaline earth metal) alanates with and without transition metals. The research focus was later shifted to borohydrides for their potential of higher storage capacity. In this section, the techniques and results for solid state synthesis are presented.

4.2 Experimental

The starting materials, NaH (95%), LiH (95%) MgH_2 (90%), $LiBH_4$ (>90%), transitional metals and hydrides were purchased from the Aldrich Co. and other commercial sources. AlH_3 was obtained utilizing a proprietary method. Detailed characterization of this aluminum hydride is described in Ref. 58. The X-ray diffraction pattern of this material shows only AlH_3, with no detectable impurities (Figure 31). Solid state NMR (by the California Institute of Technology) confirms that the material does not contain trapped H_2 gas and only a trace amount of elemental Al is present in the sample (Figure 32). Commercial grade $NaAlH_4$ (98%) was obtained from Albemarle having only Na_3AlH_6 and Al, products of dehydrogenation, as "impurities" detected by XRD examination. All solid materials were used in the as-received condition without further purification. The chemicals were stored, measured and transferred under high purity N_2 environment inside a glove box with oxygen content < 25 ppm.

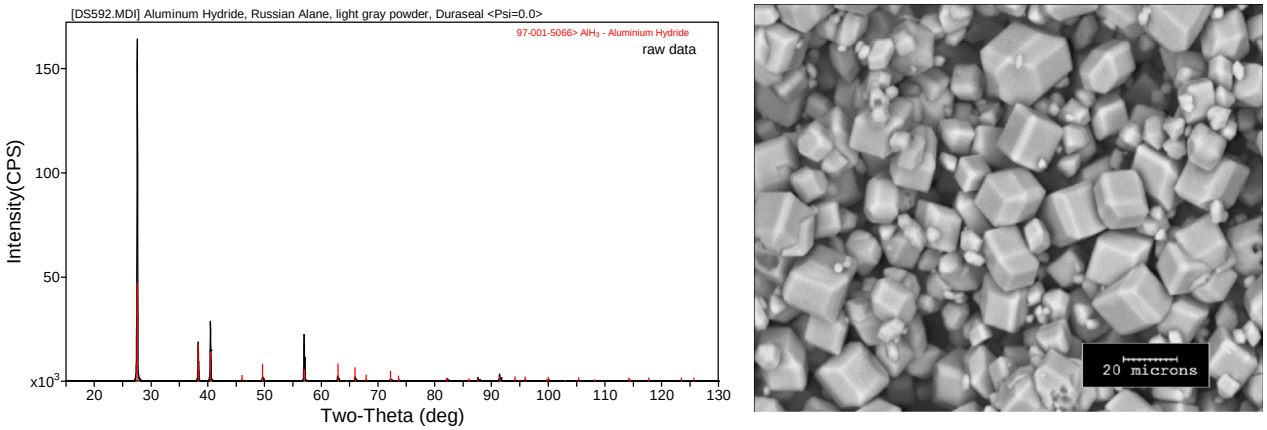

Figure 31: XRD and SEM characterization of AlH_3.

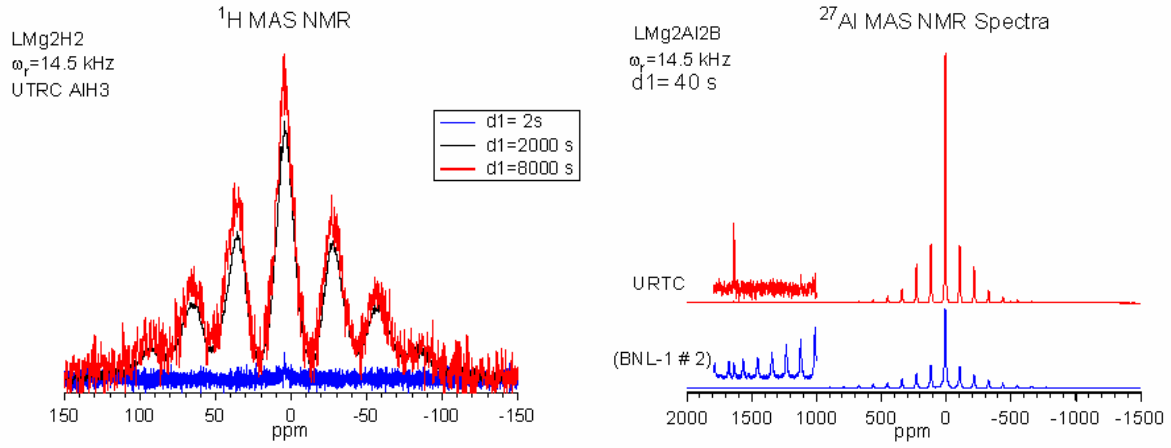

Figure 32: Solid state NMR of AlH_3.

The new complex alanate materials were synthesized by mixing simple hydrides, such as NaH, LiH, MgH_2, AlH_3 and transition metals or metal hydrides in a mortar and pestle for 15 min at various molar ratios. Approximately 10 g of the mixtures were ball milled in a high energy SPEX mill in an N_2 environment for 3 hours. Immediately after ball milling, approximately 1g of the samples were transferred into a sample holder of a modified Sievert's apparatus (Advanced Materials Co.). The samples were hydrided under 190-195 bar hydrogen for 20 hours each at 60, 80, 100 and 120˚C respectively and followed by XRD analysis.

XRD analyses were performed on a Rigaku D/Max-b, Model RU-200B diffractometer equipped with a rotating Cu anode, or a Scintag X1 Advanced Diffraction System equipped with a Cu anode housed in a glove box. Samples for the Rigaku were mounted on a glass sample holder and covered with a layer of DuraSeal™ sealed with a ring of silicone grease in the glove box. Differential Scanning Calorimetry (DSC) measurements were conducted on TA Instruments 2910 (Albemarle) or 2920 (UTRC). The sample pans were made of gold plated stainless steel (Swiss Institute for Safety and Security) or Al, and the sample heating rate was 10˚C/min. Thermal Gravimetric Analysis - Mass Spectrometry (TGA-MS) was conducted using a TA 2950, coupled with Pfeiffer Omnistar Mass Spectrometer GSD 300 through heated capillary tubing.

4.3 Results

4.3.1 Alanates

The syntheses of mixed alkaline and alkaline earth salts of aluminum hydride from simple hydrides were attempted by the solid synthesis method described in the experimental section. This method of synthesis was chosen due to its high energy mechanical alloying effect. In addition, this method is simple to implement, and therefore it can serve as a screening method for a large collection of compositions. Table 10 lists alanate compositions studied using this method, including key reactions derived based on XRD analysis. A few examples are reported in the following sections in detail. The appendix of Section 10.1 provides additional composition evolution results for a larger set of materials.

Table 10: Compositions of mixed alanates prepared by SSP.

Compositions		Mole ratio	Main Reactions
Basic Alanates			
1	$NaH:LiH:AlH_3$	1:1:1	$NaH + LiH + AlH_3 \Rightarrow LiH + NaAlH_4$
			$2NaAlH_4 + LiH \Rightarrow Na_2LiAlH_6 + Al + 3/2H_2$
2	$NaH:MgH_2:AlH_3$	1:1:1	$NaH + MgH_2 + AlH_3 \rightarrow MgH_2 + NaAlH_4$
			$MgH_2 + NaAlH_4 \Leftrightarrow NaMgH_3 + Al + 3/2H_2$
3	$LiH:MgH_2:AlH_3$	1:1:1	$LiH + MgH_2 + AlH_3 \Rightarrow MgH_2 + LiAlH_4$
			$LiAlH_4 \Rightarrow 1/3Li_3AlH_6 + 2/3Al + H_2 \Rightarrow LiH + Al + 3/2H_2$
4	$NaH:LiH:MgH_2:AlH_3$	1:1:1:1	$NaH + LiH + AlH_3 \Rightarrow 1/3Na_2LiAlH_6 + 1/3NaAlH_4 + 1/3Al + 2/3LiH + 1/2H_2$
			$NaH + MgH_2 + LiH + AlH_3 \Rightarrow 1/2MgH_2 + 1/4Na_2LiAlH_6 + 1/2NaMgH_3 + 3/4Al + 3/4LiH + 9/8H_2$
5	$NaH:LiH:AlH_3:Na_2O$	1:1:1:0.2	$NaH + LiH + AlH_3 \rightarrow NaAlH_4 + Na_2LiAlH_6 + Al + H_2$
6	$NaH:LiH:AlH_3:NaOH$	1:1:1:0.2	$NaH + LiH + AlH_3 \rightarrow NaAlH_4 + Na_2LiAlH_6 + Al + H_2$
Ti Addition			
7	NaH:Ti:Al	1:1:1	$NaH + Ti + Al + 3/2H_2 \rightarrow 1/3TiH_{1.5} + 2/3TiH_2 + NaAlH_4$
8	NaH:Ti:Al	2:1:1	$NaH + Ti + Al + 3/2H_2 \rightarrow 1/3TiH_{1.5} + 2/3TiH_2 + NaAlH_4$
9	$NaH:TiCl_2:Al$	3:1:1	$3NaH + TiCl_2 + Al + 3/2H_2 \rightarrow 2NaCl + 1/2Al + NaH + TiH_2 + 1/6Al3Ti$
10	$NaH:TiCl_2:AlH_3$	3:1:1	$2NaH + TiCl_2 \rightarrow 2NaCl + TiH_2$, $AlH_3 \rightarrow Al + 3/2\ H_2$
11	$NaH:TiH_2:AlH_3$	1:1:1	$NaH + TiH_2 + AlH_3 \rightarrow TiH_2 + NaAlH_4$
12	$NaH:LiH:TiH_2:AlH_3$	1:1:1:1	$NaH + LiH + AlH_3 \Rightarrow 1/3NaAlH_4 + 1/3Al + 1/3Na_2LiAlH_6 + 2/3LiH + 1/2H_2$
			$2NaAlH_4 + LiH \Rightarrow Na_2LiAlH_6 + Al + 3/2H_2$
13	$NaH:MgH_2:TiH_2:AlH_3$	1:1:1:1	$NaH + MgH_2 + TiH2 + AlH3 \Rightarrow 1/2MgH_2 + TiH_2 + 1/2NaAlH_4 + 1/2NaMgH_3 + 1/2Al + 3/4H_2$
			$NaAlH_4 + MgH_2 \Rightarrow NaMgH_3 + Al + 3/2H_2$
Ni Addition			
14	$LiH:Ni:AlH_3$	1:1:1	$LiH + Ni + AlH_3 \Rightarrow 1/3Li3AlH_6 + Al + Ni$
15	$NaH:Ni:AlH_3$	1:1:1	$NaH + Ni + AlH_3 \Rightarrow NaAlH_4 + Ni$
16	$MgH_2:Ni:AlH_3$	1:1:1	$MgH_2 + Ni + AlH_3 \Rightarrow MgH_2 + Ni + Al$
17	$LiH:MgH_2:Ni:AlH_3$	1:1:1:1	$LiH + MgH_2 + Ni + AlH_3 \Rightarrow MgH_2 + Ni + Al + Li_3AlH_6$
18	$NaH:MgH_2:Ni:AlH_3$	1:1:1:1	$NaH + MgH_2 + Ni + AlH3 \Rightarrow MgH_2 + Ni + NaAlH_4$
Co Addition			
19	$LiH:Co:AlH_3$	1:1:1	$LiH + AlH_3 + Co \Rightarrow 1/3Li_3AlH_6 + 2/3Al + Co$
20	$NaH:Co:AlH_3$	1:1:1	$NaH + Co + AlH_3 \Rightarrow NaAlH_4 + Co$
21	$MgH_2:Co:AlH_3$	1:1:1	$MgH_2 + Co + AlH_3 \Rightarrow MgH_2 + Co + Al + 3/2H_2$
22	$LiH:MgH_2:Co:AlH_3$	1:1:1:1	$LiH + MgH_2 + Co + AlH_3 \Rightarrow MgH_2 + Co + Al$
23	$NaH:MgH_2:Co:AlH_3$	1:1:1:1	$NaH + MgH_2 + Co + AlH_3 \Rightarrow MgH_2 + Co + NaAlH_4$

Fe Addition			
24	$LiH:Fe:AlH_3$	1:1:1	$LiH + Fe + AlH_3 \Rightarrow 1/2LiAlH_4 + 1/6Li_3AlH_6 + 1/3Al + Fe$
25	$NaH:Fe:AlH_3$	1:1:1	$NaH + Fe + AlH_3 \Rightarrow NaAlH_4 + Fe$
26	$MgH_2:Fe:AlH_3$	1:1:1	$MgH_2 + Fe + AlH_3 \Rightarrow MgH_2 + Al + Fe$
27	$LiH:MgH_2:Fe:AlH_3$	1:1:1:1	$LiH + MgH_2 + Fe + AlH_3 \Rightarrow MgH_2 + Fe + Al$
28	$NaH:MgH_2:Fe:AlH_3$	1:1:1:1	$NaH + MgH_2 + Fe + AlH_3 \Rightarrow MgH_2 + Fe + NaAlH_4$
Cr Addition			
29	$LiH:Cr:AlH_3$	1:1:1	$LiH + Cr + AlH_3 \Rightarrow LiAlH_4 + Cr$
30	$NaH:Cr:AlH_3$	1:1:1	$NaH + Cr + AlH_3 \Rightarrow NaAlH_4 + Cr$
31	$MgH_2:Cr:AlH_3$	1:1:1	$MgH_2 + Cr + AlH_3 \Rightarrow MgAlH_4 + Cr$

4.3.1.1 Na-Li-Mg-Al-H

In the Na-Li-Mg-Al-H (1:1:1:1) system (Composition #4), XRD examination of the samples after hand mixing did not show evidence of chemical reactions, although the LiH signal was absent in mixtures containing LiH. It is suspected that the LiH signal, which should not be masked by any of the other constituents, is absorbed by one or more of the other compounds present. After SPEX milling, several reaction products were detected by XRD, including $NaAlH_4$, $LiNa_2AlH_6$, $NaMgH_3$, and Al (Figure 33).

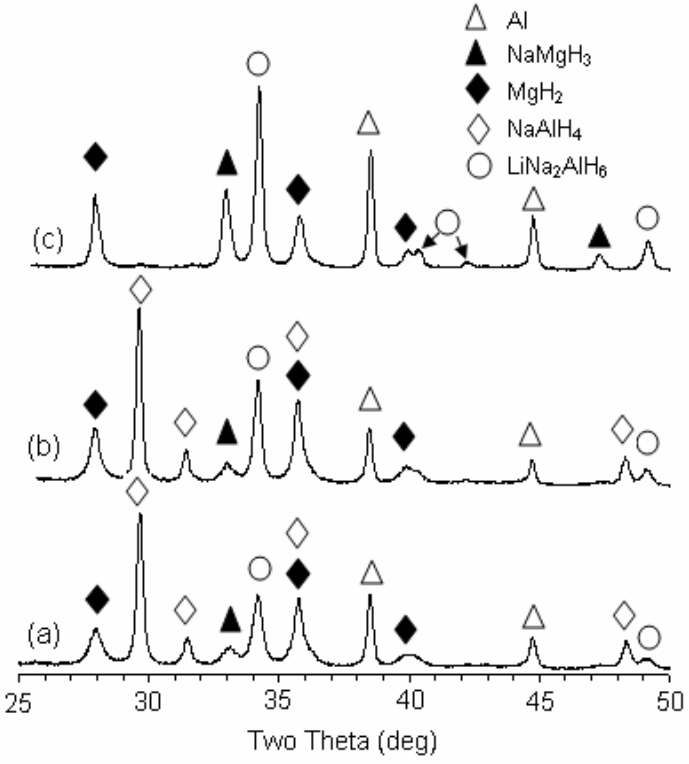

Figure 33: XRD of (a) SPEX milled for 3 hours, (b) 80˚C and (c) 120˚C hydriding at 195 bar hydrogen pressure for 20 hours.

This observation suggests that the following reaction occurred during the milling process:

Equation 10: $2AlH_3 \rightarrow 2Al + 3H_2$

Equation 11: $NaH + AlH_3 \rightarrow NaAlH_4$

Equation 12: $LiH + 2NaH + AlH_3 \rightarrow LiNa_2AlH_6$

Equation 13: $NaH + MgH_2 \rightarrow NaMgH_3$

Upon heat-treatment, the sample composition remained unchanged below 100˚C. At temperatures greater than 100˚C, the signal of $NaAlH_4$ decreased substantially. Signals from the $LiNa_2AlH_6$, $NaMgH_3$ and Al phases increased, indicating Equation 14 and Equation 15 may occur at this temperature.

Equation 14: $2NaAlH_4 + LiH \rightarrow LiNa_2AlH_6 + Al + 3/2H_2$

Equation 15: $NaAlH_4 + MgH_2 \rightarrow NaMgH_2 + Al + 2H_2$

In this system, NaH appears to be the most reactive among alkali and alkaline earth hydrides. It can form binary complex hydrides with AlH_3 and MgH_2 respectively, and ternary complexes with LiH plus AlH_3. Among the complex hydrides formed, $LiNa_2AlH_6$ and $NaMgH_3$ are the most stable. The existence of $LiNa_2AlH_6$ and $NaMgH_3$ [Refs. 59,60,61] has been reported in the literature. No $LiAlH_4$, Li_3AlH_6, Na_3AlH_6 and mixed lithium magnesium aluminum hydride phases were observed, indicating they were less stable than the $LiNa_2AlH_6$ and $NaMgH_3$ under this reaction environment. It could also be due to their formation being kinetically impeded.

In order to further understand thermodynamic stability without the interference of varying kinetics, first principles thermodynamic property predictions were utilized to generate data for equilibrium thermochemical calculations. Below 87ºC, the LiH destabilization of $NaAlH_4$ to form the Na_2LiAlH_6 intermediate phase (Equation 14) with the release of only 2.6 weight % H_2, is predicted to predominate. At higher temperatures, the $NaAlH_4$ decomposition reaction to the intermediate phase, Na_3AlH_6, with the release of 3.7 weight % H_2 is predicted to predominate, even in the presence of LiH. In contrast, the MgH_2 destabilization of $NaAlH_4$ to form $NaMgH_3$ (Equation 15) is predicted to predominate above 52ºC, leading to the release of 4.8 weight % H_2. These predictions confirm the above experimental observations that Na_2LiAlH_6 and $NaMgH_3$ are predominate phases at higher temperatures.

4.3.1.2 Li-Mg-Al-H

The initial synthesis attempts of Li-Mg-Al-H compounds were performed with solid state methods. A reaction mixture containing LiH, MgH_2 and AlH_3 (1:1:1) (Composition #3) was hand mixed and SPEX milled for 3 hours. The SPEX milling resulted in the formation of $LiAlH_4$. Upon heat-treatment to 60°C under 190-195 bar of hydrogen, $LiAlH_4$ dissociated to Al and Li_3AlH_6. Further heating above 100°C in hydrogen dissociated the Li_3AlH_6 to LiH and Al. The MgH_2 did not react. No mixed lithium

magnesium aluminum hydride phase formed using the solid state method with simple hydride precursors.

In this study, $LiMg(AlH_4)_3$ was prepared by Albemarle using the solution based method described in Section 5.2. The as-synthesized compound was tested for isothermal hydrogen desorption at 100 and 150˚C (Figure 34). At 100˚C, 4.0 wt% H_2 was released at a slow rate. The desorption rate increased significantly at 150˚C, with 6.9-7.0 wt% H_2 released. An additional 1.8 wt% H_2 was released at 340˚C, yielding a total capacity of 8.7-8.8 wt% H_2.

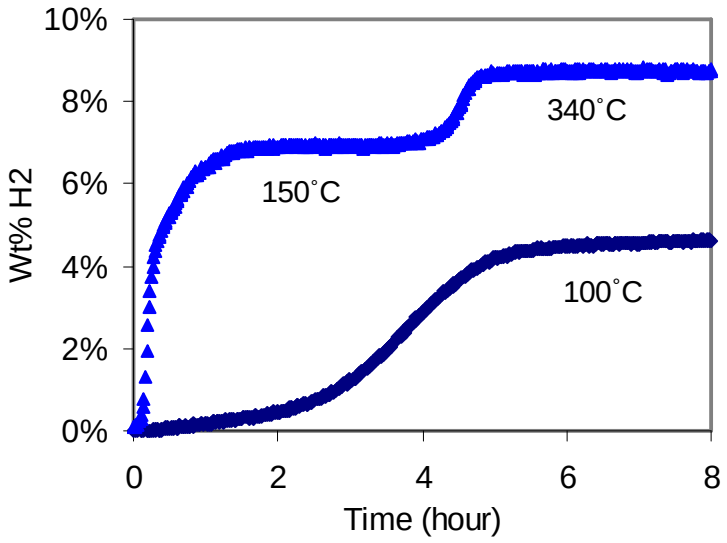

Figure 34: Hydrogen desorption of $LiMg(AlH_4)_3$ at 100˚C, 150˚C and 340˚C.

The XRD characterization of the dehydrogenated $LiMg(AlH_4)_3$ indicated that the phase composition varied with desorption temperature (Figure 35) and desorption time. After 5 hours of desorption at 100˚C, XRD showed the presence of Al and an unknown compound, proposed to be an intermediate $LiMgAlH_6$ phase based on the H_2 weight % released (Equation 16). This hypothesis was corroborated by the identification of a VASP-minimized $LiMgAlH_6$ hexagonal candidate structure whose simulated powder pattern closely matched the unknown XRD peaks. Desorption at 150˚C for 24 hours resulted in the formation of MgH_2 and additional Al (Equation 17). Note that small amounts of LiH cannot be determined by XRD in the presence of Al. Increasing the temperature to 340˚C caused the appearance of Al_3Mg_2 via Equation 18.

Equation 16: $\mathbf{100^{\circ}C: LiMg(AlH_4)_3 \rightarrow LiMgAlH_6 + 2Al + 3H_2}$

Equation 17: $\mathbf{150^{\circ}C: LiMgAlH_6 \rightarrow LiH + MgH_2 + Al + 2H_2}$

Equation 18: $\mathbf{340^{\circ}C: 2MgH_2 + 3Al \rightarrow Al_3Mg_2 + 2H_2}$

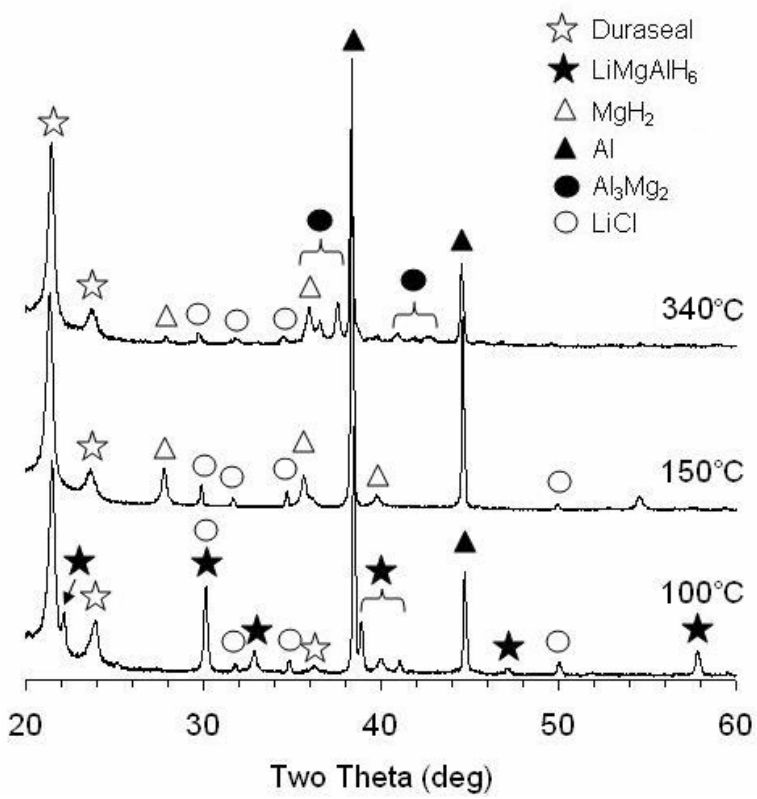

Figure 35: XRD of decomposition products of $LiMg(AlH_4)_3$ at 100˚C, 150˚C and 340˚C.

Thermal analyses and first principles thermodynamic predictions confirmed the likelihood of these reactions. When $LiMg(AlH_4)_3$ was heated at 10ºC/min in a DSC, an exothermic reaction began at 140ºC with a latent heat of -5.5 KJ/mol-H_2 (Equation 16), immediately followed by an endothermic reaction with a latent heat of 13.1 KJ/mol-H_2 (Equation 17). Results from the first principles thermodynamic modeling confirmed their exothermic (Equation 16) and endothermic nature (Equation 17). The reaction heat for Equation 17 agrees with the value reported by Mamatha [Ref. 62].

The reverse hydrogen absorption of Equation 17 was experimentally tested using both undoped and 2% $TiCl_3$ doped $LiMg(AlH_4)_3$. The doping was achieved by 15 minutes of SPEX milling. After being discharged at 150˚C for more than 5 hours, the samples were charged under 190 bar of hydrogen at 80 and 100˚C for a total of 24 hours. No absorption was observed. The material is not rechargeable under these conditions.

4.3.1.3 Am-Ae-Tm-Al systems

Synthesizing mixed alkaline (Na, Li) or alkaline earth (Mg) and transition metal alanates using solid state processing method was also investigated. Transition metals investigated included Ti, Ni, Co, Fe and Cr. In the case of Ti, various precursors: Ti metal, $TiCl_2$, and TiH_2, were studied in the Na-Ti-Al system. When Ti metal was used as the precursor, a 75% decrease in observed Ti appeared to occur. It was later determined that the loss in Ti signal strength was due to absorption by the metallic aluminum. It is hypothesized that the lack of Ti signal, widely reported in the literature as occurring in catalyzed $NaAlH_4$ samples, is due in part to absorption with elemental aluminum, which is widely

present after reduction during the catalyzation. Furthermore, upon SPEX milling, significant amounts of elemental sodium are apparent, resulting from reduction by Ti. Thermal exposure at 200 bar H_2 transforms much of the remaining Ti metal to TiH_2. Higher temperature exposures increase both TiH_2 and Na_xAlH_y concentrations. It is concluded that the introduction of Ti through the elemental route is not effective to alternate phase formation.

In the case of $TiCl_2$ as a precursor, the primary product of SPEX milling is NaCl with Al_3Ti and TiH_2. No unidentified peaks or significant shifts in peak locations were observed. It is thus concluded that the utilization of halides as cation precursor materials is inappropriate.

TiH_2 was also tested for the synthesis of transition metal alanates using the SSP method. The XRD results of the $NaH:TiH_2:AlH_3$ (1:1:1) material indicate that the primary products are TiH_2 and $NaAlH_4$ at all temperatures studied. No new phases were generated. One interesting feature resulting from this experiment is the tentative observation at 100°C of a second $NaAlH_4$ phase having a higher 2θ than the JFIZ database indicates. This split is manifest in all of the $NaAlH_4$ peaks and is consistent with a lattice dilation of 0.13% in the *a* and *b* directions. Figure 36 shows this split peak effect in both the (103) and (004) peaks. This is not a solitary observation, but has been observed in a number of instances in the past.

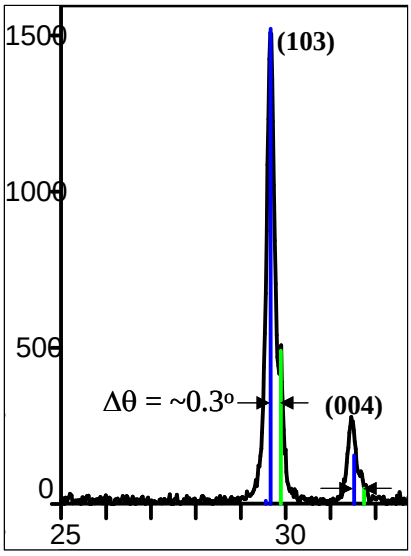

Figure 36: Illustration of raw XRD data for $NaAlH_4$ showing split peaks in the (103) and (004) peaks.

No new phases that contain transition metals were formed with the addition of other transition metals, including Ni, Co, Fe and Cr. Based on these results, it is concluded that SSP is not a suitable method to synthesize transition metal alanates. It was subsequently discovered by our partners at Albemarle and other researchers that transition metal alanates are thermodynamically unstable. Our attention was then transitioned to the development of borohydride based materials for their high hydrogen capacity.

4.3.2 $Mg(BH_4)_2$ and $Mg(BH_4)_2$*2.2NH_3

$Mg(BH_4)_2$ has a theoretical capacity of 14.93 wt% if all hydrogen is released. SSP was used to synthesis $Mg(BH_4)_2$ by SPEX milling $LiBH_4$ and $MgCl_2$ at a 2:1 mole ratio for 6 hours. The XRD characterization showed the formation of the by-product LiCl (Figure 37). A small amount of $LiBH_4$ remains in the sample. Only a trace amount of crystalline $Mg(BH_4)_2$ was detected. TGA-MS analysis showed that the material starts to release hydrogen around 150ºC. The release of hydrogen peaks circa 300ºC (Figure 38).

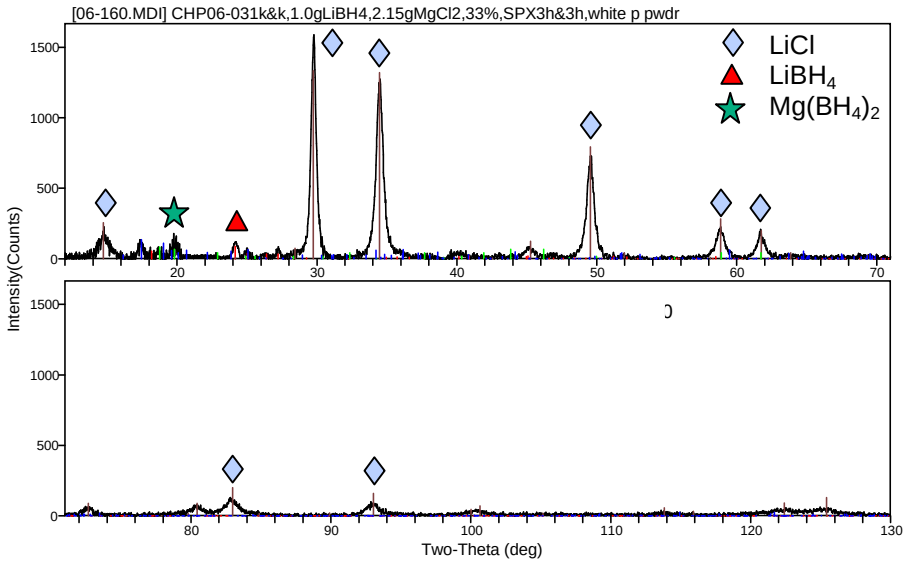

Figure 37: XRD of reaction products of $LiBH_4$ and MgH_2 at 2:1 mole ratio.

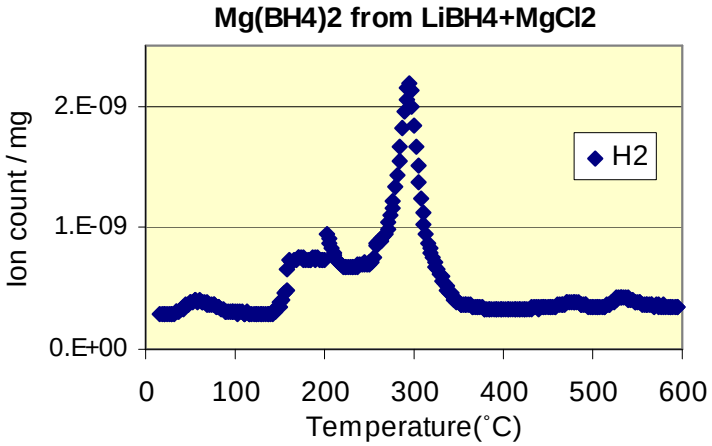

Figure 38: TGA-MS of $Mg(BH_4)_2$ from $LiBH_4$ and MgH_2 by SSP.

In order to purify the reaction mixture and remove the LiCl by-product, a solvent is needed to dissolve $Mg(BH_4)_2$. It was found that $Mg(BH_4)_2$ easily forms adducts with organic ligands in tetrahydrofurane (THF) solution. A $Mg(BH_4)_2$*3THF sample was prepared by our partners at SRNL (Section 6.10). Samples were also synthesized with another aprotic ligand, trimethyl amine (TMA), to form $Mg(BH_4)_2$*TMA by Albemarle using SBP. Both ligands do not contain protonic hydrogen, and therefore can not react with BH_4^-. Figure 39 shows that for both samples, the H_2 started to release below 100˚C; at the same time, the ligands started to volatilize. These results indicate that the incorporation of a N or O containing ligand destabilized the magnesium borohydride structure and significantly lowered the H_2 releasing temperature. In $Mg(BH_4)_2$*3THF, most of the THF released before 300˚C, accompanied by some H_2 release. The remaining $Mg(BH_4)_2$ decomposed in the neighborhood of 300˚C, releasing additional H_2. $Mg(BH_4)_2$*TMA, on the other hand, decomposed in two stages, each stage releasing H_2 and the ligand. This can be attributed to two different types of adduct structures, one of which is much less stable than the other.

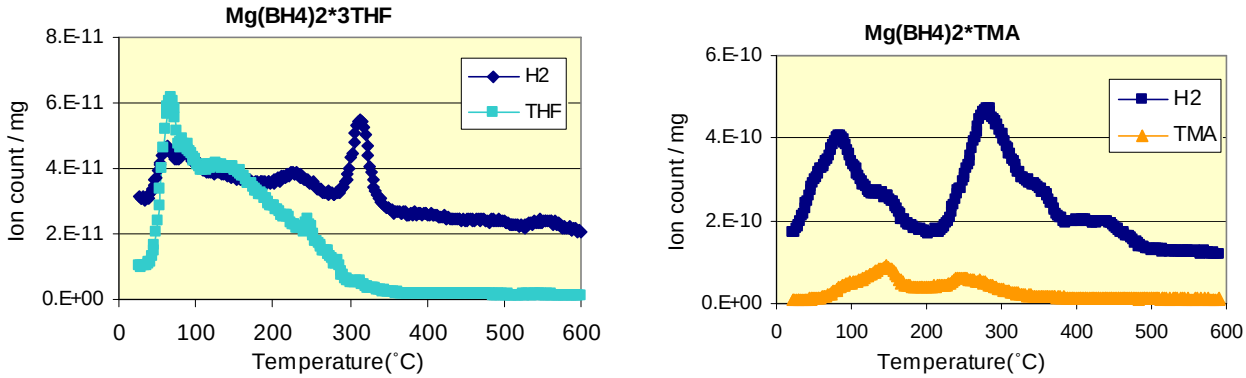

Figure 39: TGA-MS of $Mg(BH_4)_2$*3THF and $Mg(BH_4)_2$*TMA.

$Mg(BH_4)_2$*2.2NH_3 (Material A) was synthesized by Albemarle using solution based processing for its additional capacity from NH_3 if all the hydrogen is released as H_2 gas. Figure 40 shows the DSC and TGA-MS of the as-synthesized material.

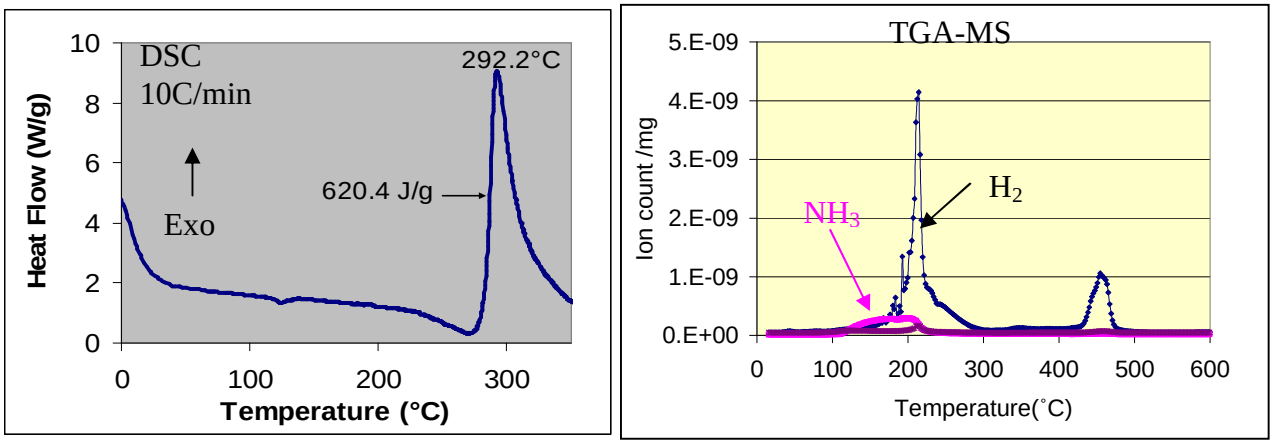

Figure 40: DSC and TGA-MS of $Mg(BH_4)_2$*2.2NH_3 (Material A).

DSC analysis showed an exothermic event around 292˚C, generating a significant amount of heat (620.4J/g). TGA-MS showed two hydrogen peaks at 214˚C and 450˚C. In addition to hydrogen, a significant amount of ammonia was also released at temperatures between 100˚C to 220˚C. Compared with the THF ligand, NH_3 decomposes at a higher temperature; however, most ammonia is liberated before hydrogen release reaches its peak (214˚C).

Ammonia is an undesirable impurity for fuel cells. Two approaches were taken to reduce the generation of ammonia to acceptable levels. The first was to heat the samples at 160˚C in vacuum for 24 hours to remove NH_3 ligands. Figure 41 shows the DRIFT spectra of the as–synthesized and the heated sample. It can be seen that after heating, the peak intensity of N-H bond decreased significantly, indicating the removal of NH_3. However, the signal for the B-H bond was reduced, suggesting that partial decomposition of BH_4^- occurred during heating. TGA-MS analysis of the heated sample (Figure 42) shows the temperature of H_2 releasing peak increased from the original temperature, 214˚C to 256˚C. However, no NH_3 was detected in the gas phase. DSC analyses of the as–synthesized and vacuum heated $Mg(BH_4)_2*2.2NH_3$ are shown in Figure 40 and Figure 43. The as–synthesized material shows an exothermic event around 292˚C, generating a significant amount of heat (620.4J/g). The vacuum heated sample has significantly different thermal events than the as–synthesized one. It shows two relative small exothermic peaks (at 135˚C and 240˚C), followed by an endothermic event at 271˚C. The above characterization indicates that the low temperature H_2 release in the as–synthesized material could be caused by the release of NH_3 ligands. It could also be initiated by the reaction between BH_4^- and NH_3. After being heated at 160˚C in vacuum, a significant amount of the NH_3 was removed. The remaining NH_3 reacted with BH_4^- upon further heating during the TGA-MS analysis, forming boron nitride without releasing NH_3. In the sealed pan DSC analysis for the as–synthesized $Mg(BH_4)_2*2.2NH_3$, all the NH_3 was trapped in the sealed pan, and then reacted with BH_4^-, resulting a large exothermic peak. In the vacuum heated material, a significant amount of NH_3 was removed prior to the analysis in sealed pan. The DSC showed only two small exothermic peaks, resulting from the reaction of residual NH_3 with BH_4^-. The endothermic peak at 271˚C is due to the decomposition of unreacted $Mg(BH_4)_2$.

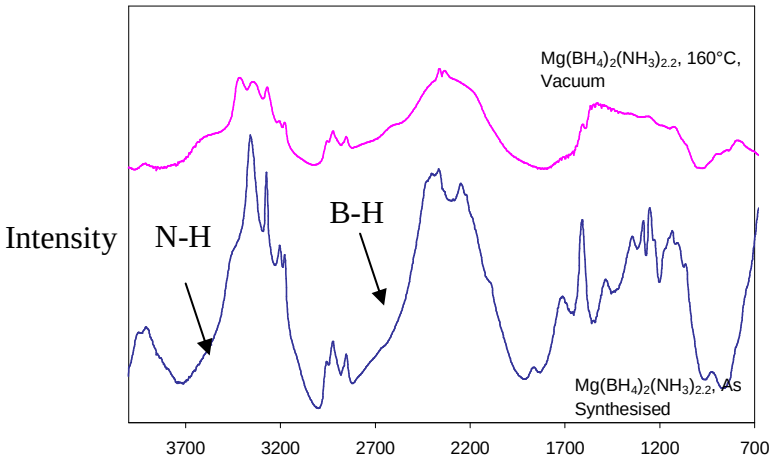

Figure 41: DRIFT spectra of the as-synthesized $Mg(BH_4)_2*2.2(NH_3)$ (Material A) and the sample after heating at 160°C in vacuum for 24 hours.

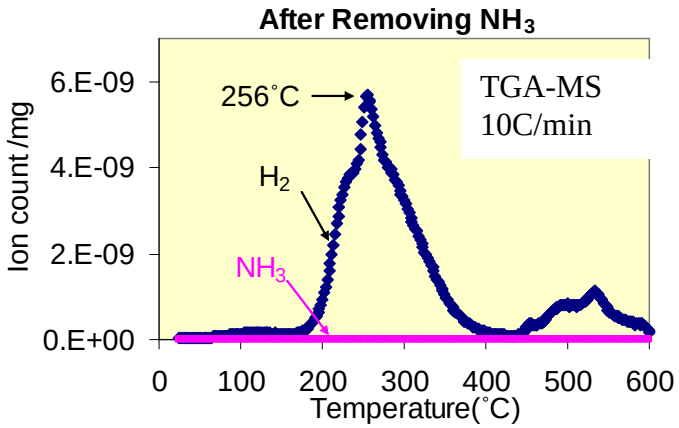

Figure 42: TGA-MS of $Mg(BH_4)_2$*2.2(NH_3) (Material A) after being heated at 160°C in vacuum for 24 hours.

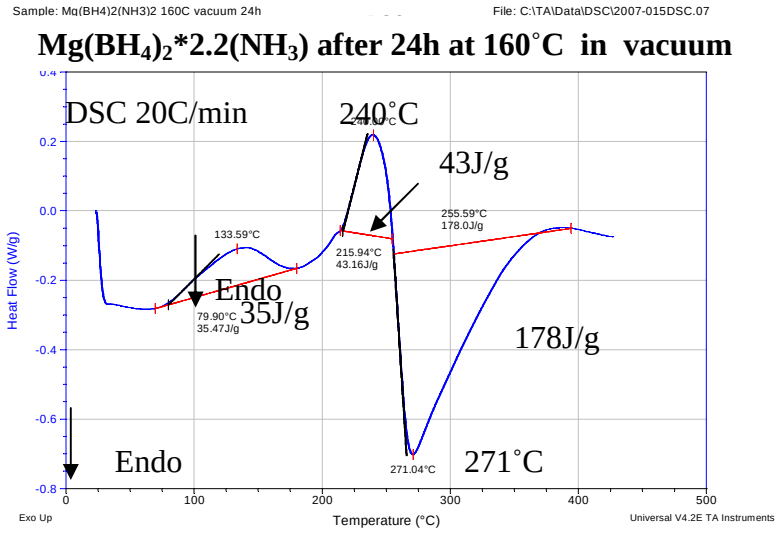

Figure 43: DSC analysis of $Mg(BH_4)_2$*2.2 NH_3 after heating at 160°C in vacuum for 24 hours.

Another approach is to mechanically mix a co-reactant with $Mg(BH_4)_2$*2.2NH_3. This designed reaction has the potential of releasing >8 wt% H_2. Figure 44 shows the DSC and TGA-MS results. Two exothermal peaks were observed at 194˚C and 245˚C in the DSC analysis. Compared with the as-synthesized $Mg(BH_4)_2$*2.2NH_3, the designed reaction contains multiple reaction steps, which onset at lower temperatures than that of the original material. More importantly, the total heat of the reactions was significantly reduced, indicating a less exothermic system. The TGA-MS showed three hydrogen peaks at 128˚C, 238˚C, and 444˚C. No ammonia was detected. This indicated that the introduction of a co-reactant can significantly reduce ammonia generation. For the designed reaction, isothermal desorption testing showed that >7.5wt% hydrogen was released at temperatures up to 350˚C. The dehydrided material was tested for rehydriding under 195 bar hydrogen at 100-300˚C. No hydrogen absorption was observed, indicating the system is not reversible.

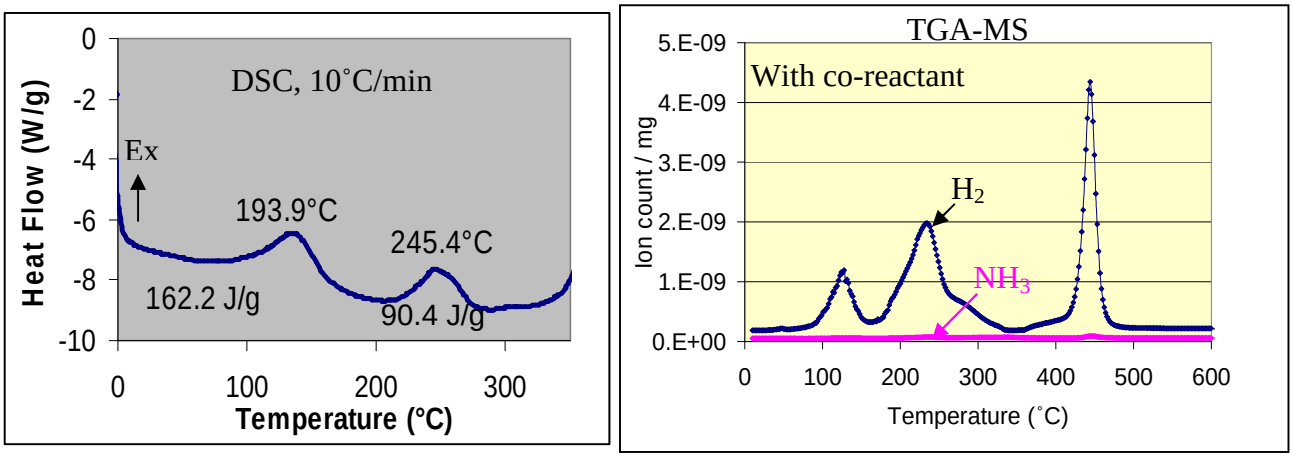

Figure 44: DSC and TGA-MS of $Mg(BH_4)_2$*2.2NH_3 (Material A) with co-reactant.

It was later found that the nature of the $Mg(BH_4)_2$*2.2NH_3 ligand-stabilized borohydride complex synthesized by solution based processing changed with synthesis conditions and/or with aging. Depending on the synthesis conditions, the compound could have two different dissociation mechanisms, one of which involves the release of NH_3 and has a theoretical hydrogen capacity of 9 wt% (Equation 19, Equation 20 and Equation 21). The results in Figure 40 indicate that Material A follows this decomposition mechanism.

Equation 19: **100-200˚C: $Mg(BH_4)_2$*2NH_3 = $Mg(BH_4)_2$+2NH_3↑ (endotherm)**

Equation 20: **200-250˚C: $Mg(BH_4)_2$ = MgH_2+2B+3H_2(g) (small endotherm)**

Equation 21 **430-470˚C: MgH_2 = Mg+H_2 (endotherm)**

The second mechanism is an amine-borane (NH_3-BH_3) like dissociation reaction, possibly forming MgH_2 and BN. This mechanism releases 16 wt% H_2:

Equation 22: **150-280˚C: $Mg(BH_4)_2$*2NH_3 = MgH_2+2BN+6H_2 (exotherm)**

Equation 23: **480-520˚C: MgH_2 = Mg+H_2 (endotherm)**

Figure 45 shows the TGA-MS of $Mg(BH_4)_2$*2.2NH_3 for another batch (Material B) synthesized under slightly different conditions, with minimal NH_3 release, but increased H_2 evolution following mainly the second mechanism. Section 3.3.3.3 describes the atomic modeling investigation of possible structures that could be formed with the $Mg(BH_4)_2$*2.2NH_3 complex and the change in possible decomposition reaction mechanisms with structure.

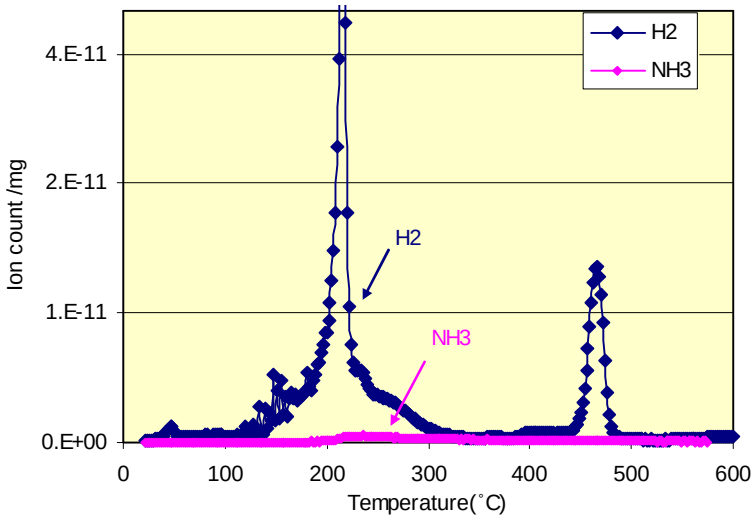

Figure 45: TGA-MS of $Mg(BH_4)_2$*2.2NH_3 (Material B).

4.3.3 $Zr(BH_4)_4(H_2NC_2H_4NH_2)_2$

$Zr(BH_4)_4(H_2NC_2H_4NH_2)_2$ contains 8.8 wt% H_2 from combined N-H/B-H hydrogen ligands. It was synthesized by Albemarle using the SBP method (Section 5.6). The material was tested for isothermal hydrogen desorption at 100˚C and 150˚C for 10 hours under 0-1 bar of hydrogen at UTRC. Figure 46 shows the desorption curves of this compound. This compound showed rapid desorption kinetics at both temperatures, releasing 3.3 wt% H_2 at 100˚C and 5.9 wt% at 150˚C. The color of the material changed from ivory to brown at 100˚C and then to dark brown or black at 150˚C. In order to investigate the fate of the organic ligand, $H_2NC_2H_4NH_2$, the desorbed materials were analyzed for residual $–CH_2$-CH_2- containing species in the solid material using DRIFTS.

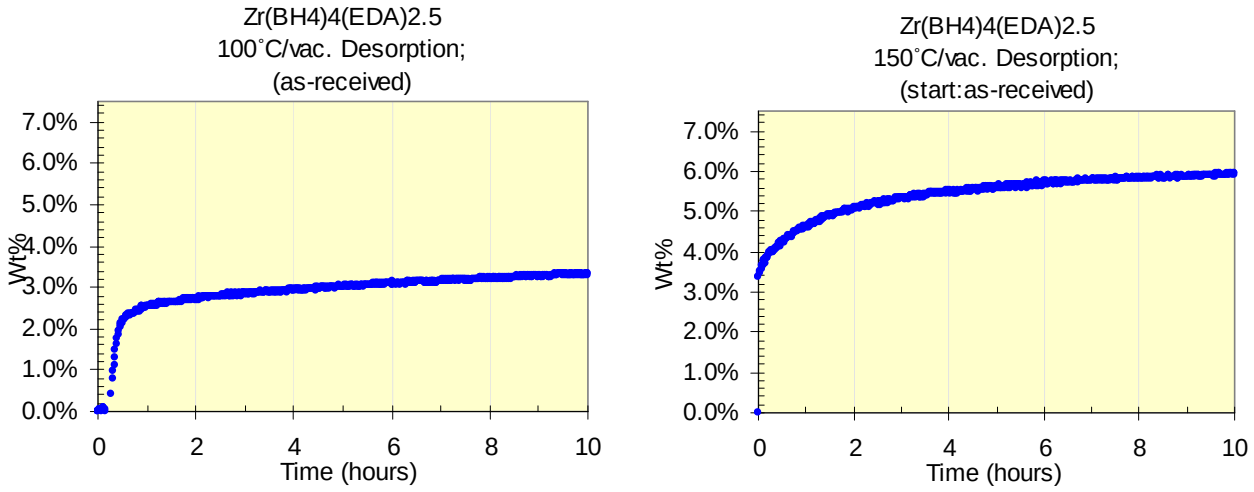

Figure 46: Hydrogen desorption of $Zr(BH_4)(H_2NC_2H_4NH_2)_2$ at 100˚C and 150˚C.

DRIFTS (Diffuse Reflectance Infrared Fourier Transform Spectroscopy) is an FTIR technique, which allows the sample to be mounted in a nitrogen-filled sealed cell. It measures the FT-IR spectra of the species on powder surfaces. This technique was developed first at Albemarle and then at UTRC to evaluate non-crystalline hydride materials that can not be characterized by XRD. The first complex examined by this technique was $Zr(BH_4)_4(H_2NC_2H_4NH_2)_2$. The DRIFTS spectra for this compound under various H_2 discharge and charge conditions are shown in the Figure 47.

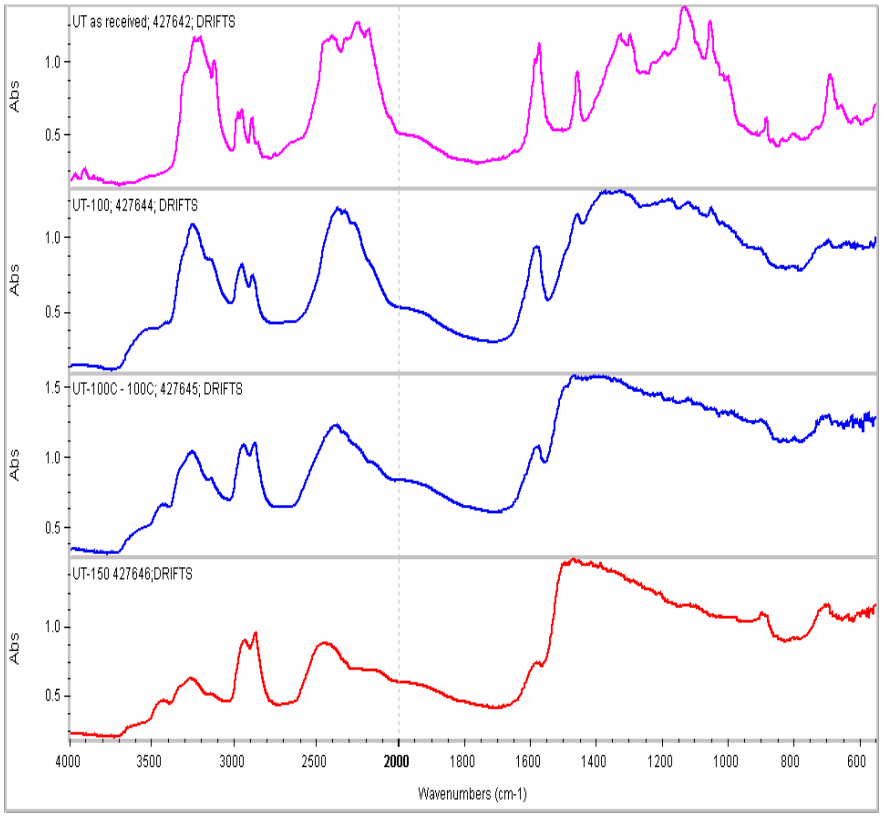

Figure 47: DRIFTS results for $Zr(BH_4)_4(H_2NC_2H_4NH_2)_2$ under various conditions.

From top to bottom:
Magenta - untreated sample
Blue - after hydrogen discharge at 100°C
Blue - after hydrogen discharge at 100°C and 60 bars H_2 at 100°C
Red - after hydrogen discharge at 150°C

While the results are semi-quantitative, the following conclusions can be drawn:

- After hydrogen discharge at 100°C, the N-H (3100-3500cm^{-1} or 1550-1600cm^{-1}) and B-H (2000-2500cm^{-1}) frequencies were reduced but did not disappear completely, indicating partial dehydrogenation under these conditions. This is consistent with a weight loss of 5.9 wt% (full discharge: 8.8%).
- The C-H (2800-3000cm^{-1}) frequencies, on the other hand, stayed constant, indicating little or no loss of the ethylenediamine ligand throughout the processing.

- There is no evidence of hydrogenation under the hydrogen charging conditions (100°C, 68 bar H_2).

It is clear that DRIFTS is a powerful tool for studying non-crystalline hydrogen storage materials. In combination with PCI or any other thermo-physical instrumentation, it allows the determination of the origin of weight loss. No hydrogen absorption was observed at 100˚C and 68 bar H_2 pressure; $Zr(BH_4)_4(H_2NC_2H_4NH_2)_2$ appears to be irreversible.

4.3.4 Am-Tm-B-H system

The mixed alkali metal and transition metal borohydride system (Am-Tm-B-H) is an extension of the Am-Tm-Al-H system in our original proposal. Alkali metal borohydrides ($LiBH_4$ and $NaBH_4$) are very stable hydrides and require desorption temperatures higher than 500 – 600ºC. Transition metal borohydrides ($Ti(BH_4)_3$, $Zr(BH_4)_4$, $Sc(BH_4)_3$) are unstable at room temperature. Partial substitution of transition metal in alkali metal borohydrides could potentially combine their distinctively different thermodynamic behaviors, forming new stable systems with intermediate desorption temperatures.

The syntheses of $NaTi(BH_4)_4$, $NaSc(BH_4)_4$ and $LiSc(BH_4)_4$ were attempted by ball milling of $NaBH_4$ or $LiBH_4$ and $TiCl_3$ or $ScCl_3$ at 4:1 or 5:1 mole ratios. In the case of $NaBH_4$ reacting with $TiCl_3$ at a 4:1 mole ratio, the following reactions may occur during milling:

Equation 24: $$\mathbf{NaBH_4+TiCl_3=TiCl_2BH_4+NaCl}$$

Equation 25: $$\mathbf{NaBH_4+TiCl_2(BH_4)=TiCl(BH_4)_2+NaCl}$$

Equation 26: $$\mathbf{NaBH_4+TiCl(BH_4)_2=Ti(BH_4)_3+NaCl}$$

Equation 27: $$\mathbf{NaBH_4+ Ti(BH_4)_3=NaTi(BH_4)_4+NaCl}$$

The XRD analysis of the reaction products after 3 hours of SPEX milling (Figure 48) shows that all of the $NaBH_4$ reacted with the $TiCl_3$. However, NaCl is the only major identifiable phase as a reaction product. All the other reaction products or intermediates are amorphous. Similar amorphous products were observed by other researchers [Ref. 63]. Multiple compositions in Na-Tm-B-H and Li-Tm-B-H systems were synthesized using SSP. The Tm included Sc, Ti(III), Ti(II), and a mixture of Ti(III) and Al (III). Figure 49 shows the XRD of the SPEX milled Na-Tm-B-H samples without removing the reaction by-product NaCl. It can be seen that $NaBH_4$ partially reacted with the transition metal chloride, $TiCl_2$ after 0.5 hours of SPEX milling, forming NaCl. After 1 hour of milling, most of the $NaBH_4$ has reacted with $TiCl_2$.

In the reaction mixtures of $NaBH_4$ with $TiCl_3$, including $4NaBH_4+TiCl_3$, $5NaBH_4+TiCl_3$, $6NaBH_4+TiCl_3/AlCl_3$, no $NaBH_4$ was observed after 3 hours of SPEX milling. NaCl was the only product observed by XRD. This indicates that the formed Na-Ti-B-H complexes are likely to be amorphous. In the $4NaBH_4+ScCl_3$ reaction mixture, there is only a small amount of NaCl formed. A set of broad peaks was observed, which was labeled as Na-Sc-B-H. These peaks are slightly shifted from the original $NaBH_4$. This could be due to the lattice parameter change caused by the substitution of Sc.

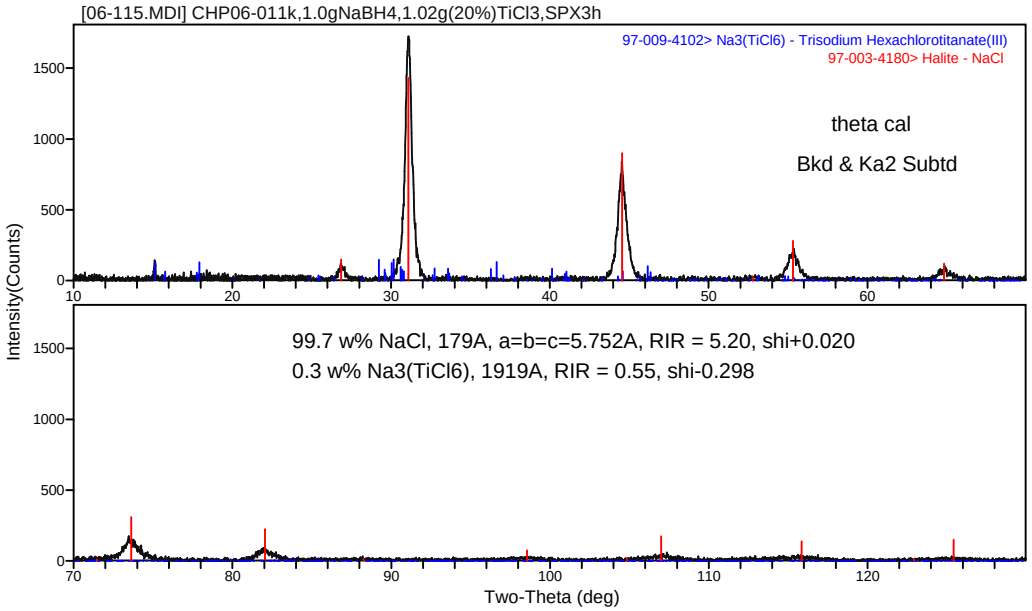

Figure 48: XRD of the reaction products of $NaBH_4$ and $TiCl_3$ at a 4:1 mole ratio after 3 hours of SPEX milling.

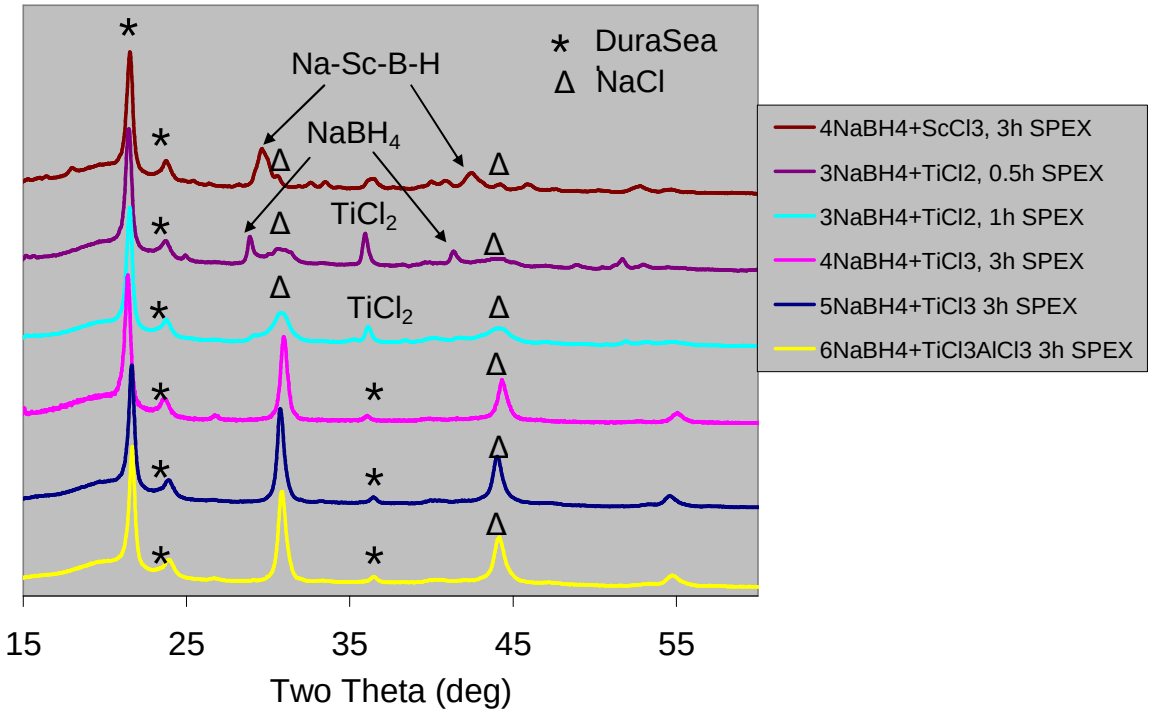

Figure 49: XRD analysis of Na-Tm-B-H materials without removal of the NaCl by-product.

TGA-MS analysis of the reaction products after 3 hours of SPEX milling (Figure 50) shows that the hydrogen release temperature is decreased in Ti or Sc substituted $NaBH_4$, compared with that of $NaBH_4$. The $NaBH_4$-$ScCl_3$ system has the lowest H_2 release temperature. However, it has also been observed that the total amount of H_2 released is significantly lower for the Ti doped system, especially for the $4NaBH_4+TiCl_3$ system. It is suspected that part of the Ti^{3+} might be reduced to Ti during ball milling. Based on observations by our collaborators at Albemarle, the freshly synthesized $NaTi(BH_4)_4$ (using the solution based method) has a clear blue color. It slowly turned to gray and then black at room temperature due to the reduction of Ti. Our material had black color immediately after milling, indicating partial reduction of Ti. The Ti is not detected by XRD, so it could be amorphous or nano-sized particles. The TGA-MS results also indicate that a trace amount of diborane (B_2H_6) was released during desorption along with hydrogen.

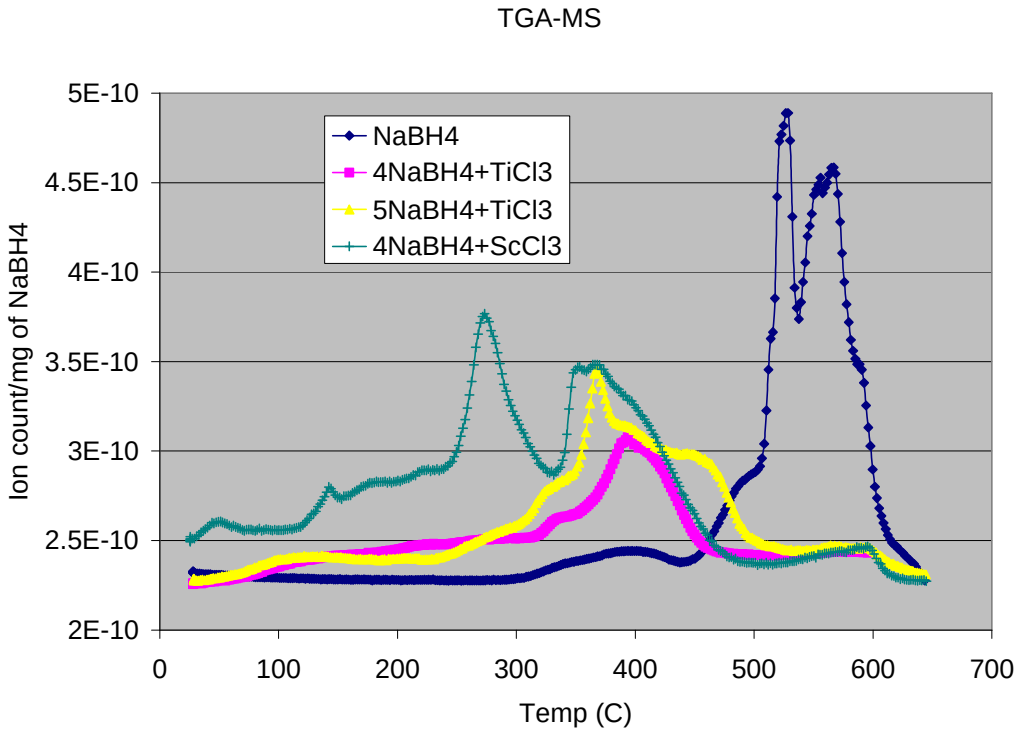

Figure 50: TGA-MS analysis of transition metal substituted $NaBH_4$.

Hydrogen desorption tests using a PCI apparatus were performed on these transition metal substituted sodium borohydrides without removing the NaCl. Figure 51 shows the results for the $4NaBH_4+ScCl_3$, $3NaBH_4+TiCl_2$ and $5NaBH_4+TiCl_3$ systems at 400˚C or 500˚C. The $4NaBH_4+ScCl_3$ composition released more than 9 wt% of H_2 at 500˚C when not including the weight of NaCl by-product.

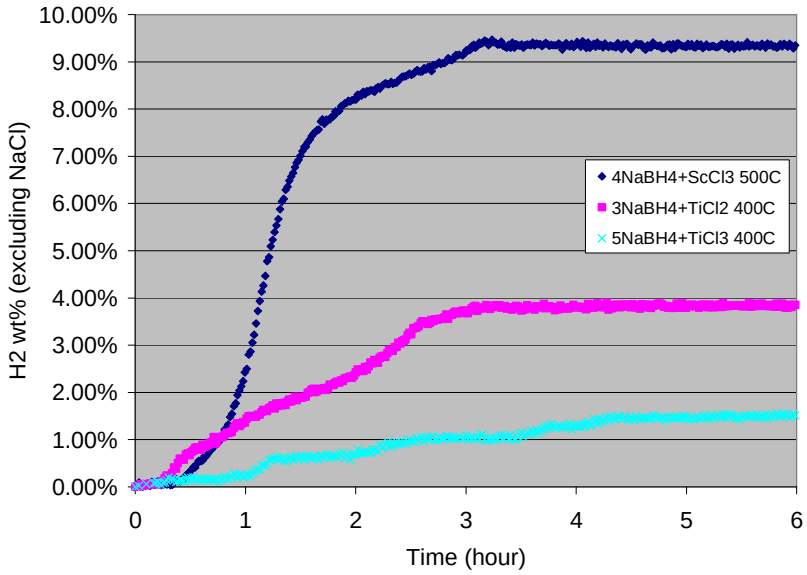

Figure 51: Hydrogen desorption for the Na-Tm-B-H system.

Several materials in the Li-Tm-B-H system were also synthesized and evaluated for their hydrogen desorption properties. Figure 52 shows the desorption curves of the Li-Tm-B-H system where the times to reach the peak test temperature of 400˚C are given in the figure caption. The Li-Sc-B-H system released up to 12 wt% hydrogen when not including the weight of LiCl. The undoped $LiBH_4$ released less than 2 wt% hydrogen. Compared with $LiBH_4$, the Sc substituted material showed greater than 6 times improvement in hydrogen releasing capacity. The Li-Ti-B-H composition, however, released less than 2 wt% hydrogen at 400˚C. One possible cause is kinetics. The Sc substituted borohydride has much faster kinetics than $LiBH_4$ with or without substitution. Another possible reason is that $LiBH_4$ or $NaBH_4$ can reduce Ti(III) during SPEX milling, producing Ti, B and releasing hydrogen or borane. Outgas in the milling vials was observed. This reaction could significantly reduce hydrogen content stored in the material after milling. Scandium, on the other hand, could not be reduced by $AkBH_4$. It remained as Sc(III) during the milling process, possibly substituted in the lattice of $NaBH_4$ and $LiBH_4$. This substitution significantly reduced the hydrogen releasing temperature of alkaline borohydride and enhanced kinetics.

Although the Sc containing mixed borohydrides had good kinetics in desorption, they only absorbed approximately 2 wt% hydrogen during recharging at 220°C and 195 bar. Increasing absorption temperature did not increase absorption capacity. This limited absorption capacity could be due to the formation of stable (either kinetically or thermodynamically) boron containing products or intermediates under high temperature during desorption. The possible desorption/absorption reactions in Ak-Tm-B-H system are shown in the following reactions:

Equation 28: $\mathbf{AkTm(BH_4)_4 <=> AkH + Tm + 4B + 15/2H_2}$

Equation 29: $\mathbf{AkTm(BH_4)_4 => AkH + TmB_2 + 2B + 15/2H_2}$ **(irreversible)**

If the system forms TmB_2, the reaction will not be reversible since TmB_2 is thermodynamically stable. If elemental boron is formed as a major reaction product, the reaction could be reversible with catalyzation. Due to the amorphous nature of the reaction products, we were unable to identify the reaction products in our system.

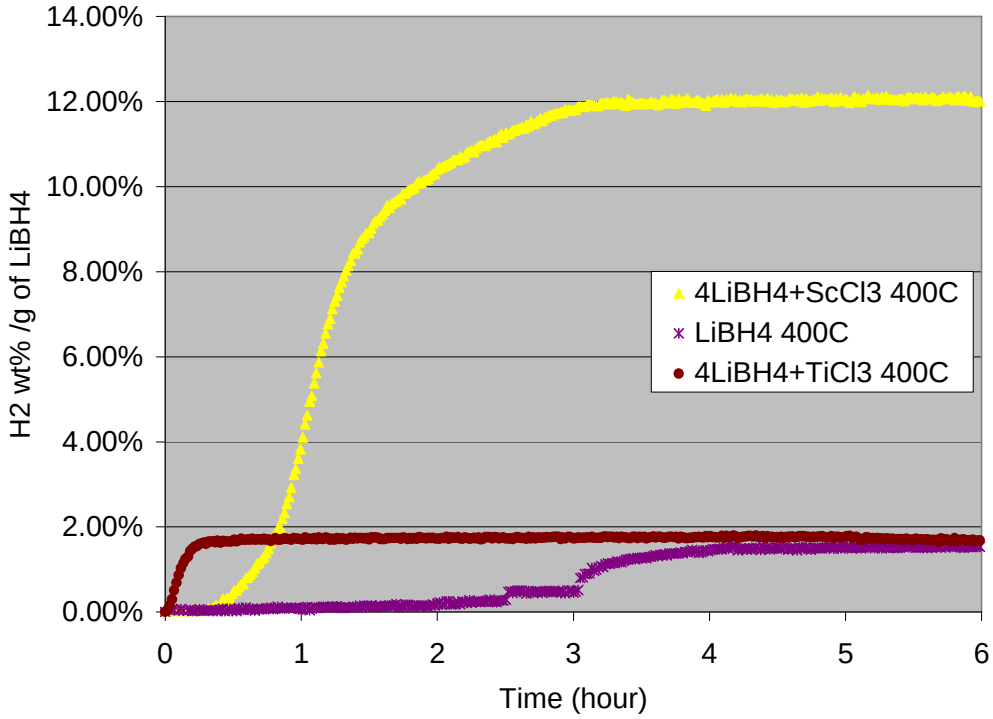

Figure 52: Hydrogen desorption of the Li-Tm-B-H system. The time to reach the peak test temperature of 400°C was 3.4 hr for $LiBH_4$+$ScCl_3$; 4.5 hr for $LiBH_4$; 0.7 hr for $LiBH_4$+$TiCl_3$.

Attempts were also made to reduce the desorption temperature to form less stable desorption products. Studies were performed on a variety of $LiBH_4$ based compositions detailed in Table 11. The initial attempt was to use a titanium oxychloride complex, $[TiCl_3OTiCl_3{\cdot}2DME]_x$, which was synthesized by Albemarle to replace titanium chloride as a synthesis precursor. It could also assist in the formation of less stable desorption products. Since scandium is much more expensive than titanium, we focused on improving titanium containing mixed borohydrides. The $[TiCl_3OTiCl_3{\cdot}2DME]_x$ was milled with $NaBH_4$ for 30 and 60 minutes to synthesize Na-Ti-B-H material. It appears that the Ti was again reduced in this case, since the color of the material changed to black, indicating the formation of metallic Ti. It could be due to the fact that the number of oxygen per titanium is not enough to prevent it from being reduced. Figure 53 shows the TGA-MS analysis of the resulting products at 30 and 60 min SPEX milling time. The dark blue and pink traces represent the H_2 ion counts as function of temperature. The yellow trace is the signal from organic ligand (DME) at 30 min milling time. The results indicated that the milling process generated a new composition which has a much lower hydrogen desorption temperature than the original $NaBH_4$. Also, the product dissociates during prolonged milling. The ligand remained in the reaction product and released upon heating in the 50ºC to 200ºC temperature range.

Table 11: $LiBH_4$ compositions studied.

System	Composition	Testing
$LiBH_4$+TM	$8NaBH_4$+ $[OTiCl_2 \cdot DME]_x$	TGA-MS
	$6LiBH_4$+$TiOCl_2$	DSC, TGA, PCT
	$6LiBH_4$+$TiCl_3$	DSC, TGA, PCT
	$6LiBH_4$+$TiCl_3/FeCl_3$	DSC, TGA
$LiBH_4$	$LiBH_4$+3%$TiOCl_2$	DSC, TGA
	$LiBH_4$+3%$TiCl_3$	DSC, TGA
	$LiBH_4$+3%$TiCl_3/FeCl_3$	DSC, TGA
$LiBH_4$+MgH_2	$LiBH_4$+MgH_2+4%$TiOCl_2$	DSC, TGA, PCT
	$LiBH_4$+MgH_2+2%$TiOCl_2$	DSC, TGA
	$LiBH_4$+MgH_2+3%$TiCl_3$	DSC, TGA
	$LiBH_4$+MgH_2+3%TiCl3/$FeCl_3$	DSC, TGA
$LiBH_4$+Si	$4LiBH_4$+Si+4%$TiOCl_2$	DSC

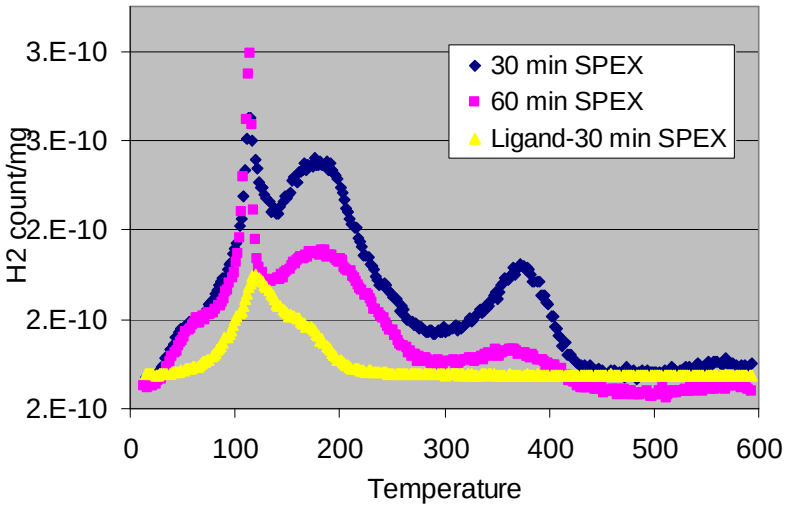

Figure 53: TGA-MS of the reaction products of $8NaBH_4$ + $TiCl_3OTiCl_3 \cdot 2DME$. Yellow / bottom trace is for ligand counts.

Subsequent examinations were conducted by reacting $LiBH_4$ with high levels of $TiOCl_2$, $TiCl_3$ and $TiCl_3/FeCl_3$. $TiOCl_2$ is an improved titanium oxy-chloral complex, which does not contain organic ligands. Results for the $TiOCl_2$ composition are given in Figure 54 and Figure 55. The DSC data shows a significant exotherm peaking at 175°C. The desorption kinetics and capacity measurements indicate a reversible capacity for the indicated conditions of nominally 2 wt%, far below the initial

desorption of 7 wt%. Desorption/absorption testing of the $6LiBH_4+TiCl_3$ gave similar capacity upon cycling of approximately 2 wt%. The evaluations indicate that the high level of these additives caused exothermic dehydrogenation and reduced reversibility.

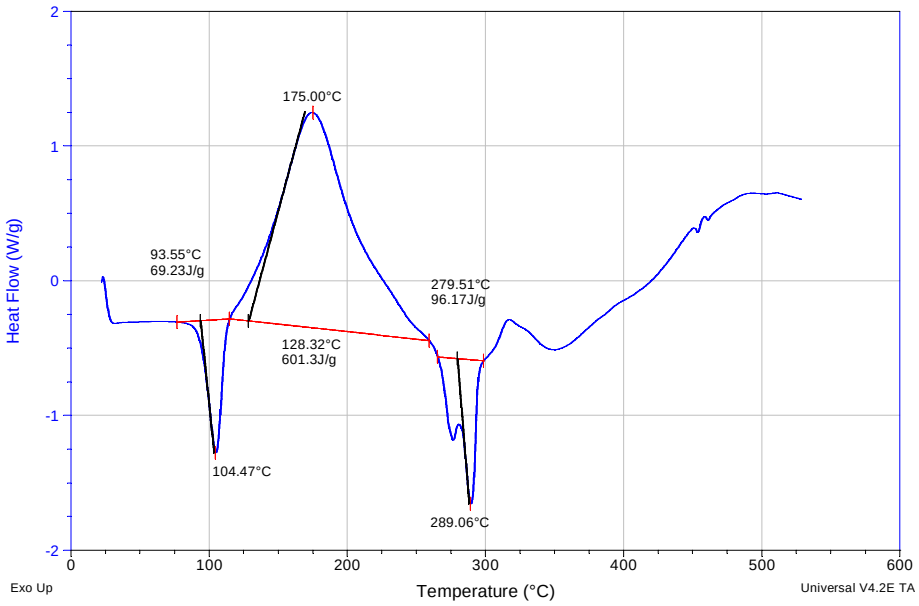

Figure 54: DSC characterization of $6LiBH_4+TiCl_2O$.

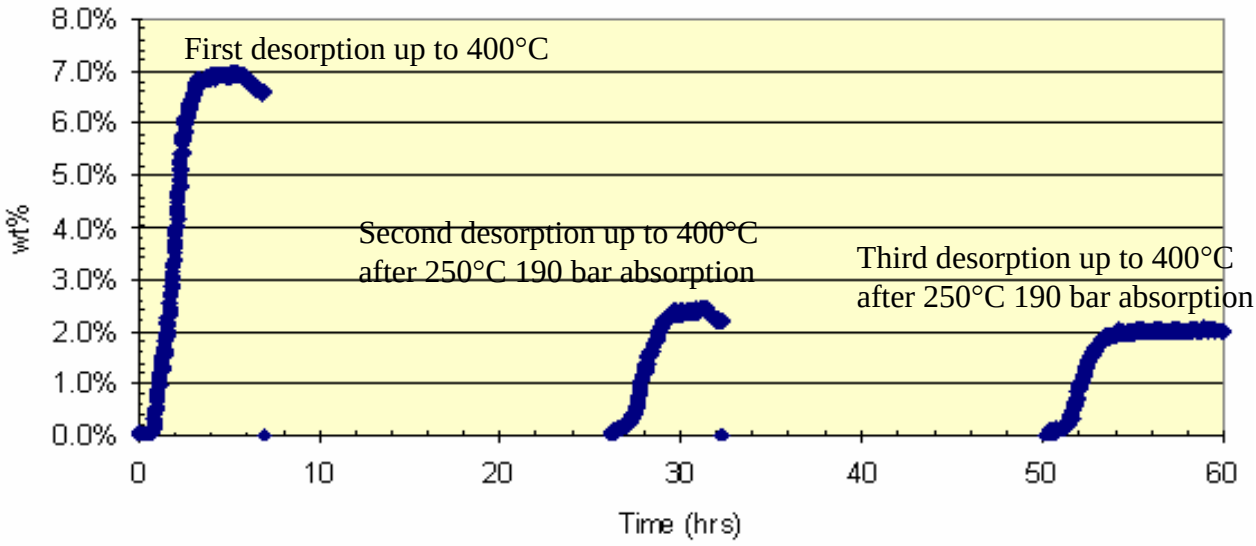

Figure 55: Sievert's apparatus / PCT desorption measurements for $6LiBH_4+TiCl_2O$.

The levels of the $TiOCl_2$, $TiCl_3$ and $TiCl_3/FeCl_3$ additions were decreased to reduce the potential / level of the exothermic reaction. DSC results of these compositions indicated that the exothermicity was reduced, but PCT testing was not conducted as these materials foamed upon desorption and clogged the PCT apparatus. The inclusion of MgH_2 along with the above additives was also examined. A baseline DSC trace for $2LiBH_4+MgH_2$ is shown in Figure 56. The behavior and

performance of $2LiBH_4+MgH_2+4\%TiOCl_2$ are plotted in Figure 57 and Figure 58. Compared with the DSC data for $2LiBH_4+MgH_2$, the second primary endotherm is composed of two valleys and the temperature of the third primary endotherm has been reduced from 377°C to 335°C. The capacity for temperatures up to 400°C is seen to be above 6 wt% for the second desorption cycle.

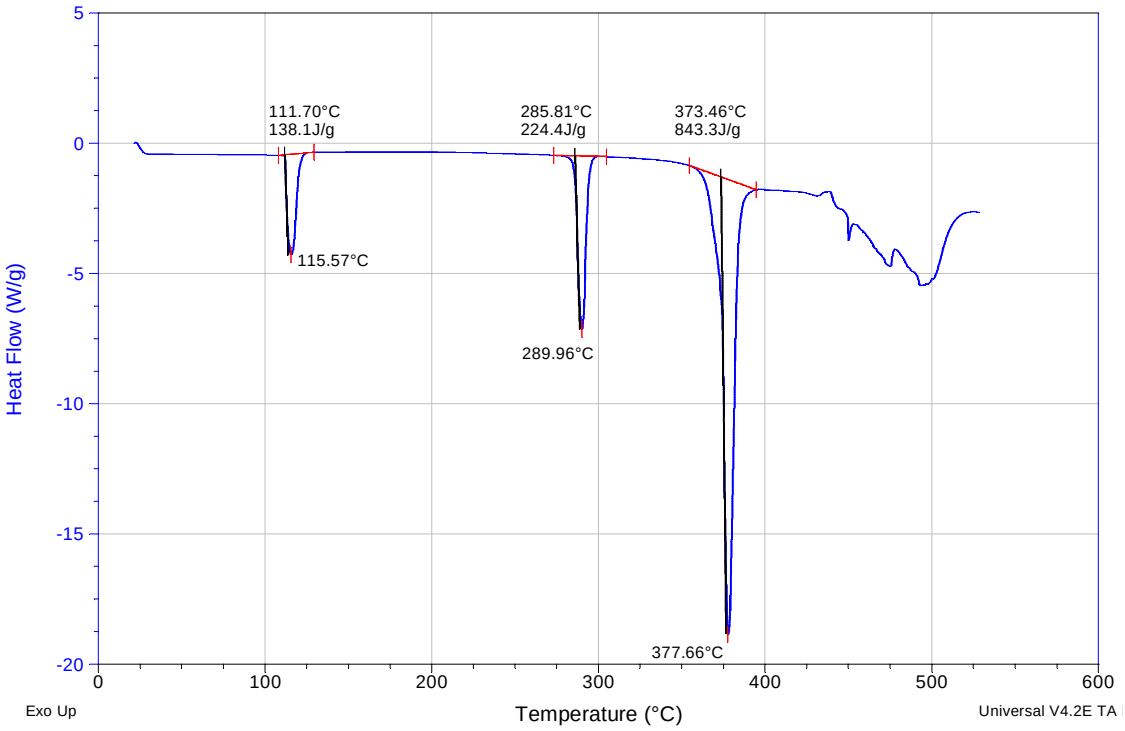

Figure 56: DSC characterization of $2LiBH_4+MgH_2$.

$NaTi(BH_4)_4$*DME synthesized by Albemarle using the solution based method (Section 5.8) was also tested for hydrogen desorption and absorption. When tested at 150˚C for desorption, the compound released approximately 1.5 wt% hydrogen. It absorbed approximately 1% H_2 at 150˚C and 190 bar H_2 pressure. This result indicates that the reversibility of borohydrides can be increased if the temperature for desorption and reabsorption is low enough to prevent the formation of stable boron decomposition compounds. Currently, there are still some issues with this compound. It is not stable at room temperature, and the presence of the organic ligand, DME, decreases its H_2 capacity significantly. Possibilities exist for increasing its reversibility and stability using nano-framework structures.

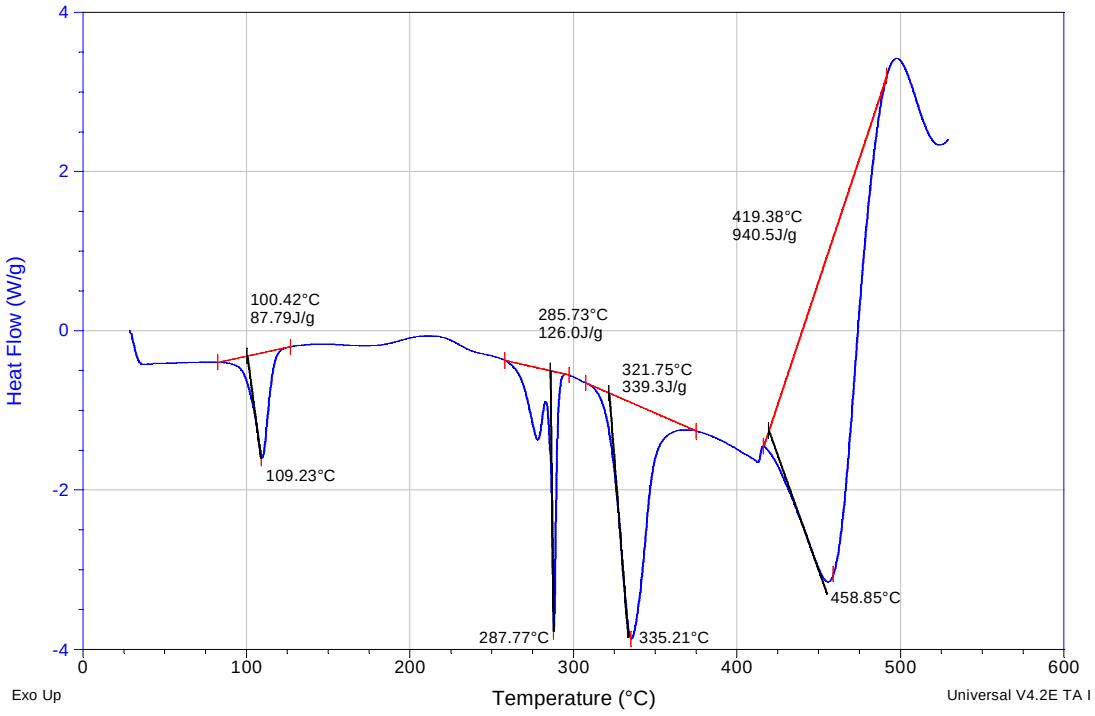

Figure 57: DSC characterization of $2LiBH_4+MgH_2+4\%TiOCl_2$.

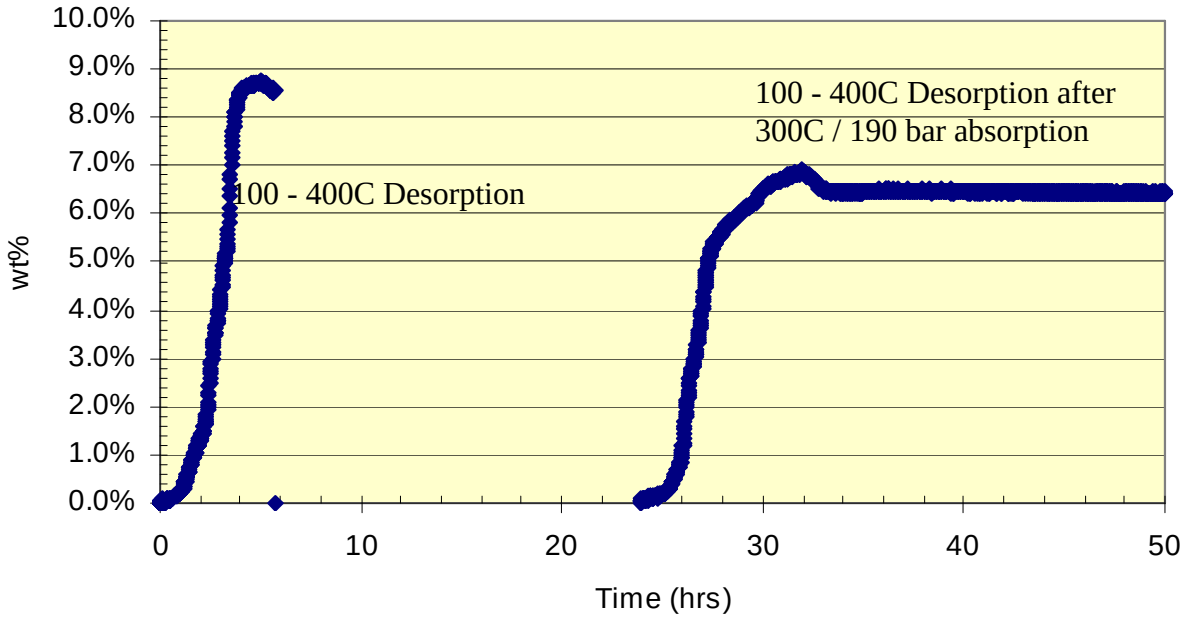

Figure 58: Sievert's apparatus / PCT desorption measurements for $2LiBH_4+MgH_2+4\%TiOCl_2$.

5 Solution Based Processing

In this project, Albemarle Corporation has applied the approach of solution based processing (SBP) which offers potential benefits in the following areas:

- Greater control of process variables
- Homogeneity (*i.e.* more uniform distribution of metal dopants)
- Possible separation of reaction by-product (i.e. NaCl…etc)
- Ease of scale up production

Table 12 summarizes the majority of the important complexes studied in the program. Complexes **4-10** are new compounds synthesized. Complexes **5-10** involve the strategy of ligand-stabilized transition metal compounds whose hydrogen discharge temperatures fall in the commercially viable range. With the exception of complex **1**, complex **8** is the only one showing some limited signs of reversibility.

Table 12: Summary of complexes studied and their properties.

Complexes Studied		Anticipated Dehydrided Products	Theoretical Max H%	Observed Hydrogen Discharge T (^oC)*
1	**Ti-doped $NaAlH_4$**	NaH + Al	5.6%	110°C
2	**$LiMg(AlH_4)_3$**	LiH + Mg + 3Al	8.9%	160°C
3	**$Mg(BH_4)_2(NH_3)_2$**	Mg + 2BN	16.0%	180°C
4	**$Mg(BH_4)_2(NMe_3)$**	Mg + 2B + NMe_3	7.1%	80°C
5	**$Zr(BH_4)_4(NH_3)_8$**	Zr + 4BN + $4NH_3$	9.8%	80°C
6	**$Zr(BH_4)_4(H_2NC_2H_4NH_2)_2$**	$Zr(BNC_2H_4NB)_2$	6.0%	100°C
7	**$NaTi(BH_4)_4(NH_3)_6$**	NaH + Ti + 4BN	13.9%	100°C
8	**$NaTi(BH_4)_4$•DME**	NaH + Ti + 4B + DME	6.9%	60°C
9	**$Na_2O[Ti(BH_4)_4DME]_2$**	2NaH +OTi_2 +8B +2DME	6.6%	85°C
10	**$NaOTi(BH_4)_3$•DME**	NaH + OTi + 3B + DME	5.0%	80°C

* Data were obtained from the DSC/TGA thermal analyses. They are onset temperatures for the first discharge which is followed by second or third discharges at much higher temperatures such as MgH_2 at 480^{o}C.

5.1 Complex 1: Ti-Doped $NaAlH_4$

The Ti-doped $NaAlH_4$ (SAH) samples were prepared by reacting $NaAlH_4$ with varying mol% of $TiCl_3 \bullet THF_3$ in THF at -5^oC. The highly pure titanium complex (Aldrich sells a 85% pure material) was freshly prepared using an Albemarle patented procedure [Ref. 64]. The reaction was monitored by gas evolution measurement. Similar reactions between β-$TiCl_3$ and SAH in ether or toluene have been reported in Ref. 65. They found the H_2 evolution to be around 1.5-2.0 mol H_2 / mol Ti and thus suggest reduction of Ti(+3) to Ti(0).

Interestingly, very different gas evolution results were obtained in our case as shown in Table 13. Much more hydrogen was evolved from our system, around 6 mol H_2 /mol Ti.

Table 13: Gas evolution results of the reactions between $TiCl_3THF_3$ and $NaAlH_4$ at varying Ti : Al ratios.

Mole ratios of Ti : Al	2 : 100	4 : 100	10 : 100	33 : 100
Mole H_2 per mole Ti	7.7	6.7	6.4	5.7

Figure 59 below shows the evolution of hydrogen with time during the first two hours of titanium doping reaction (10 mol%) for both $LiAlH_4$ and $NaAlH_4$. The reaction was carried out in THF and during those two hours the temperature increases from -5^oC to ambient. We found that $LiAlH_4$ releases H_2 earlier at lower temperatures than $NaAlH_4$ but, eventually, it maintains the same pattern of releasing six mole equivalents of H_2 per mole of Ti.

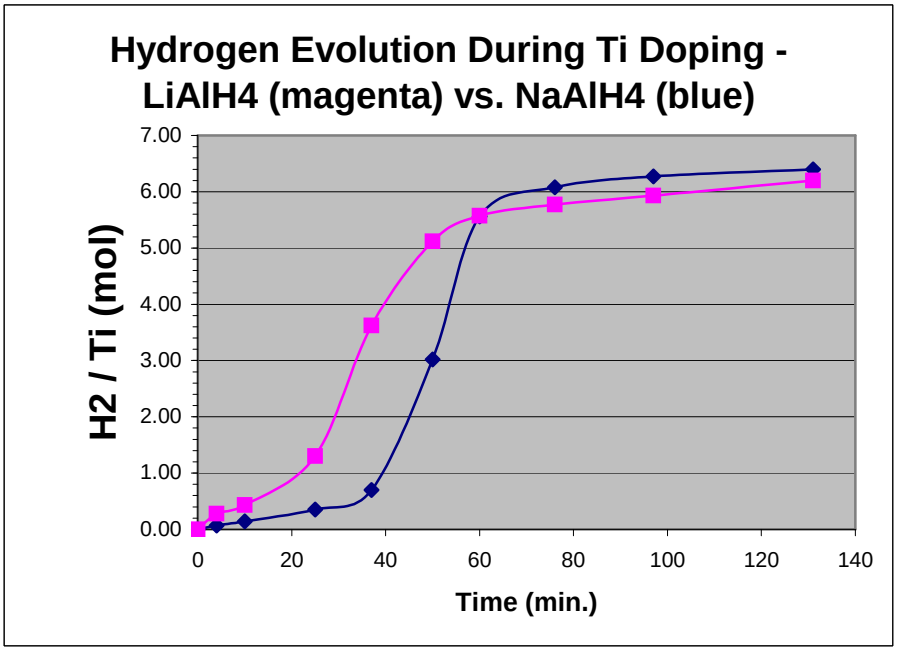

Figure 59: Hydrogen release for titanium doped $LiAlH_4$ and $NaAlH_4$.

Our gas evolution results strongly suggest the doping reaction involves a 12-electron redox reaction per mole of Ti (6 moles of H_2 evolved, see Equation 30 and Equation 31 below), thus, reinforcing the $TiAl_3$ theory proposed by Graetz *et al.* in Ref. 66. The results also raise a possibility that previous solution based preparations of Ti-doped SAH done by Bogdanovic and others might have been incomplete.

Equation 30 $\mathbf{TiCl_3 + 3NaAlH_4 \rightarrow Ti(AlH_4)_3 + 3NaCl}$ **--------- (1)**

Equation 31 $\mathbf{Ti(AlH_4)_3 \rightarrow TiAl_3 + 6H_2}$ **--------- (2)**

Figure 60 to Figure 62 shows the DSCs of Albemarle's commercial $NaAlH_4$, and 4% Ti-doped $NaAlH_4$ via the solution process and through ball milling, respectively. Interestingly, Figure 61 and Figure 62 clearly show a different product composition was formed from solution processing.

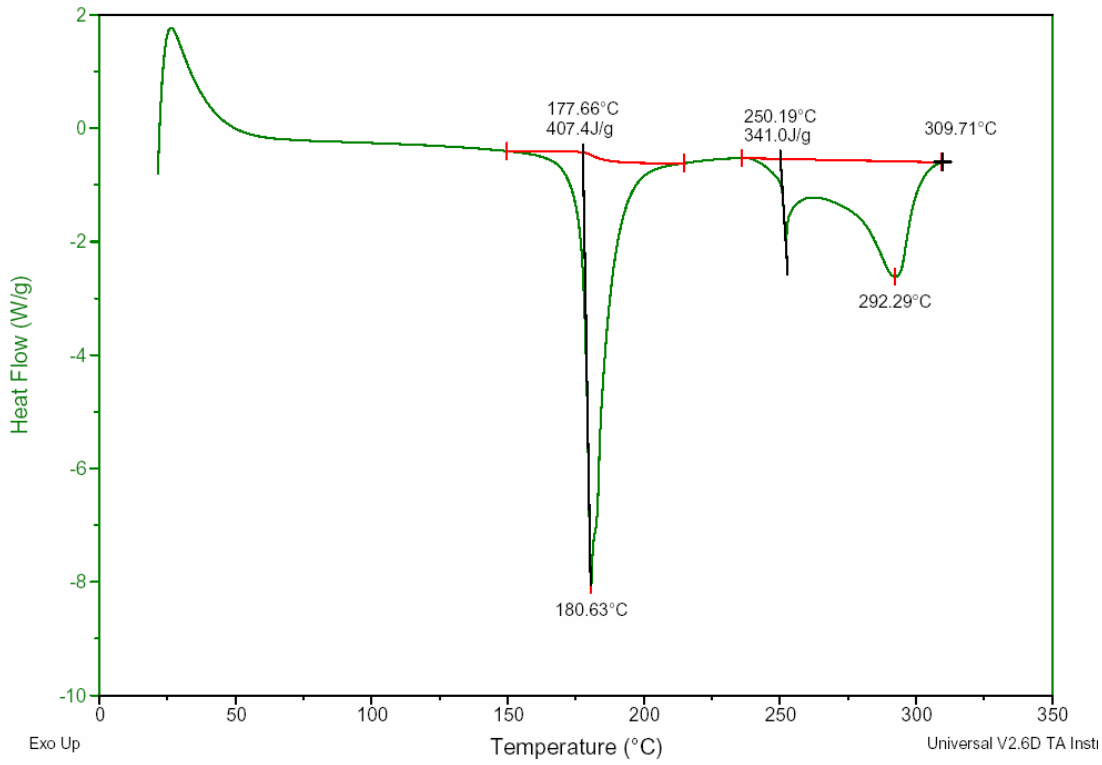

Figure 60: DSC of Albemarle $NaAlH_4$.

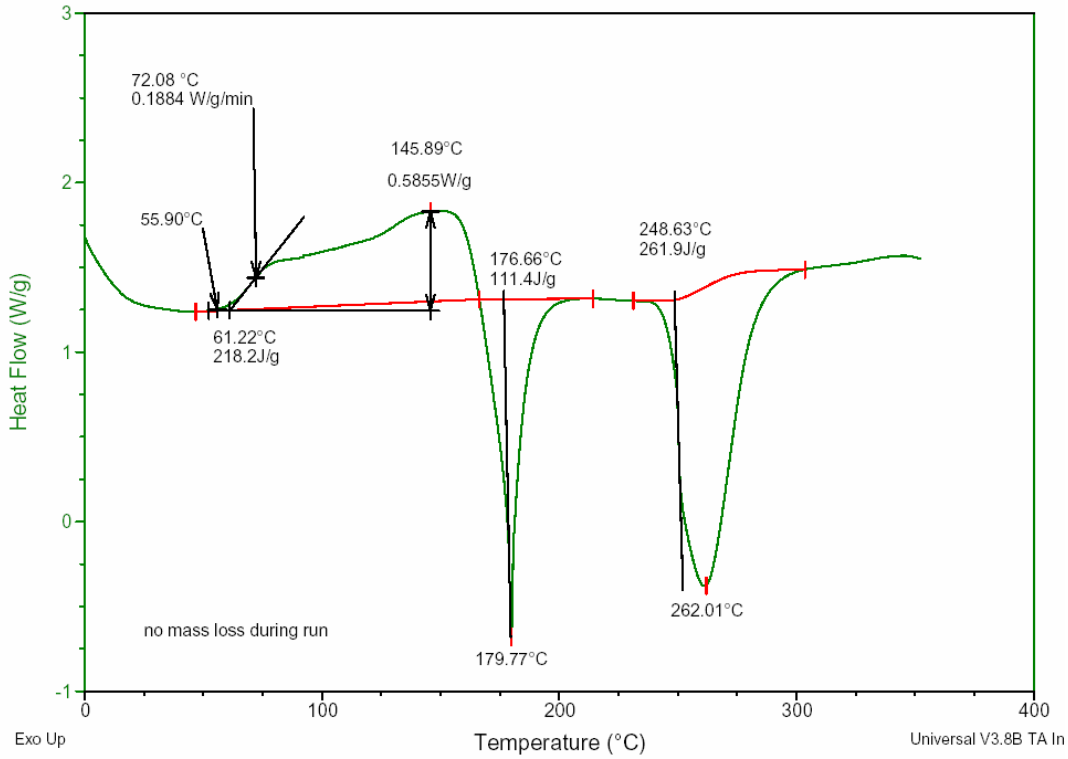

Figure 61: DSC of 4% Ti-doped $NaAlH_4$ via solution process.

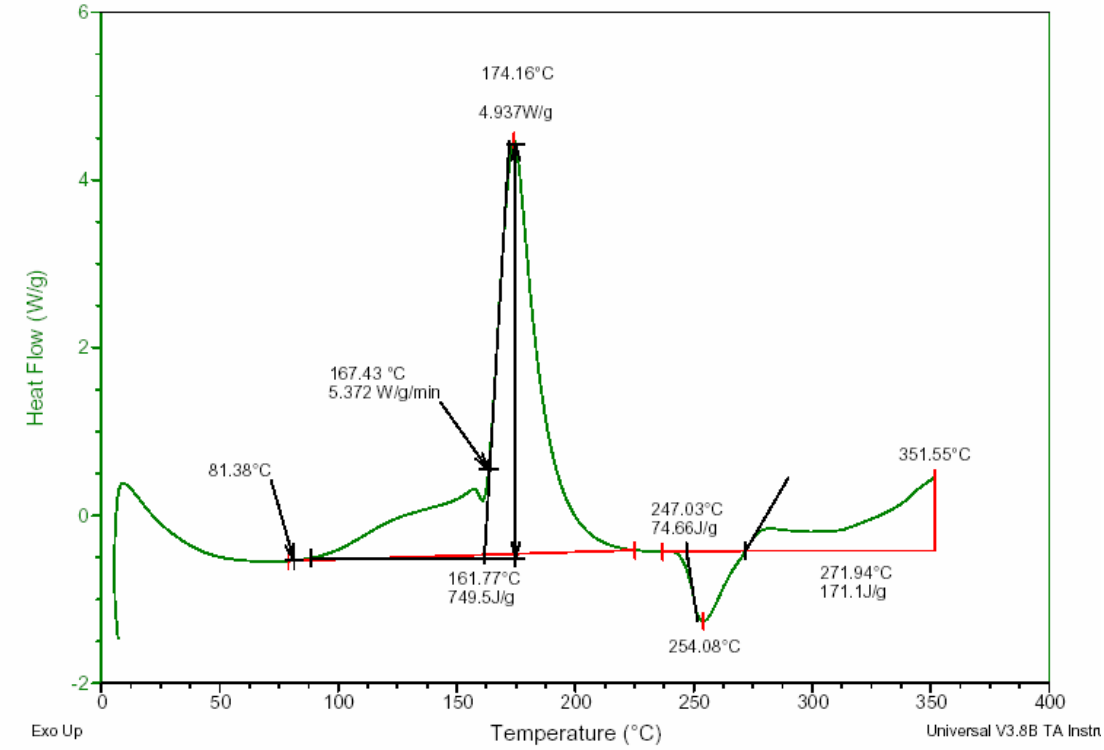

Figure 62: DSC of 4% Ti-doped $NaAlH_4$ via ball-milling.

5.2 Complex 2: $LiMg(AlH_4)_3$

This Li-Mg-Al-H quaternary compound has a theoretical maximum H wt% of 8.9%, assuming LiH, Mg, and Al as the depleted products. This compound has been successfully synthesized by a three-step process in the literature [Ref. 67] as outlined below. Reactions of Equation 32 and Equation 33 were carried out in Et_2O. The reaction of Equation 34 was carried out in Et_2O/toluene at 80°C. Use of $NaAlH_4$ in Equation 33 was critical in producing a chloride-free product.

Equation 32 $$MgCl_2 + 3LiAlH_4 \rightarrow \{LiCl \bullet LiMg(AlH_4)_3\} + LiCl \quad (1)$$

Equation 33 $$\{LiCl \bullet LiMg(AlH_4)_3\} + NaAlH_4 \rightarrow \{LiAlH_4 \bullet LiMg(AlH_4)_3\} + NaCl \quad (2)$$

Equation 34 $$\{LiAlH_4 \bullet LiMg(AlH_4)_3\} \rightarrow LiMg(AlH_4)_3 + LiAlH_4 \quad (3)$$

To support detailed characterization by IFE, the analogous deuterium compound, $LiMg(AlD_4)_3$, was successfully synthesized from $LiAlD_4$. The elemental analyses for both of these compounds are shown in Table 14 below.

Table 14: ICP results of $LiMg(AlH_4)_3$ and $LiMg(AlD_4)_3$.

	Li%	Mg%	Al%	Na%
$LiMg(AlH_4)_3$				
theory	5.58	19.6	65.1	0
found	5.50	19.1	63.9	1.12
$LiMg(AlD_4)_3$				
theory	5.09	17.8	59.4	0
found	5.27	17.4	58.3	0.60

The XRD pattern for $LiMg(AlH_4)_3$ is shown in Figure 63. The DSC/TGA data are given in Figure 64 and Figure 65, respectively. Refer to Section 4.3.1.2 for more characterization data and discussion.

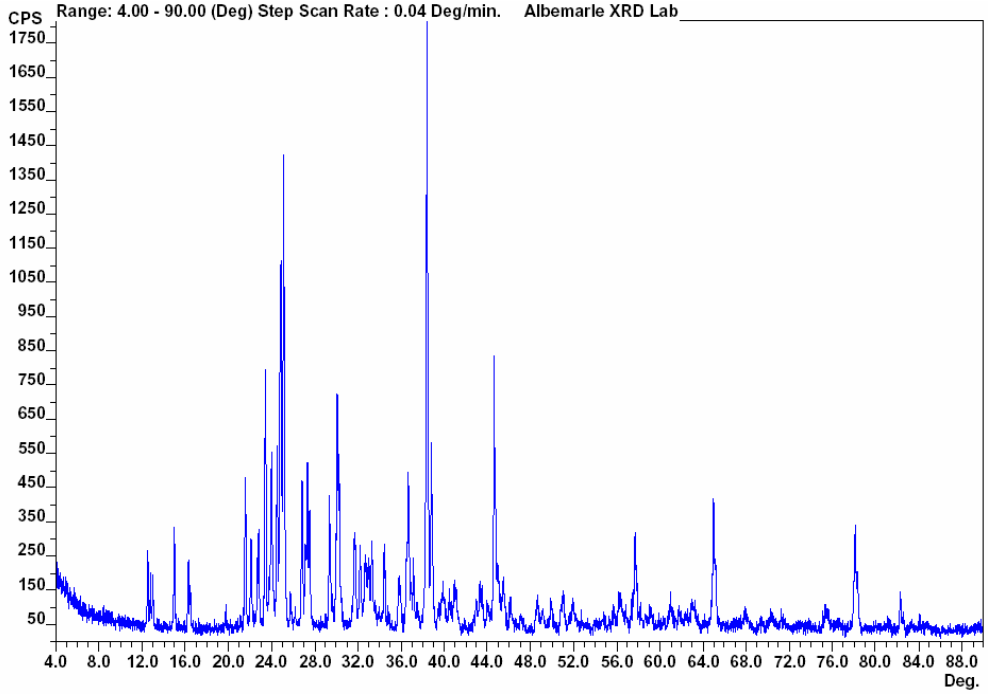

Figure 63: XRD of $LiMg(AlH_4)_3$.

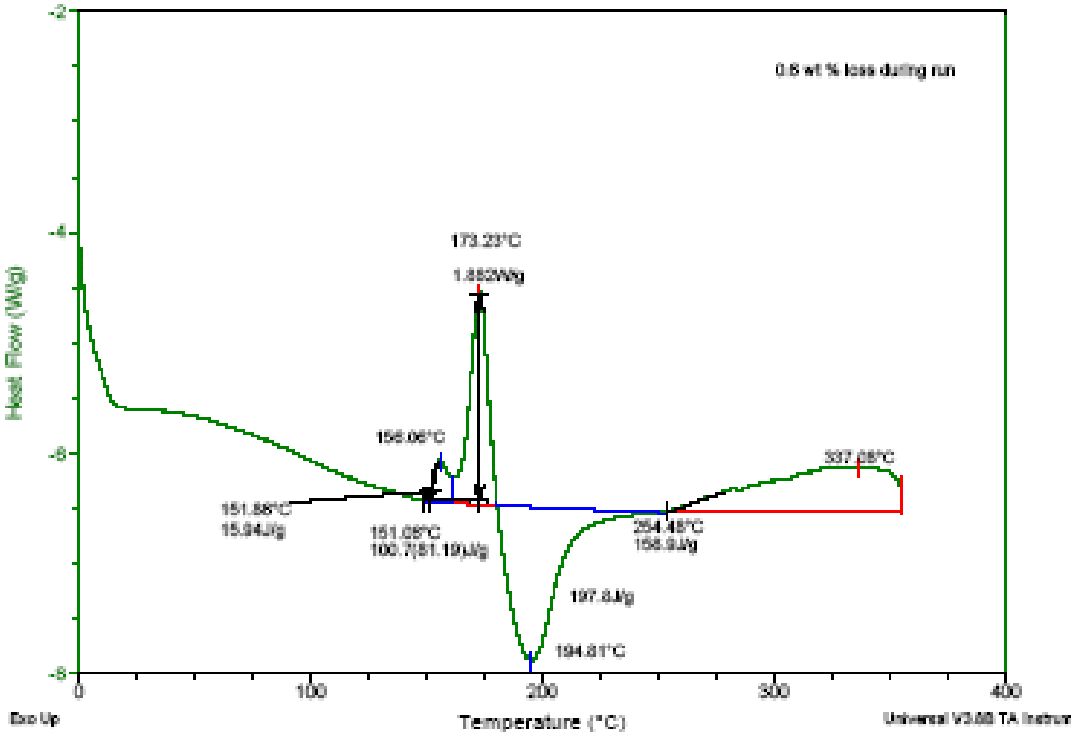

Figure 64: DSC of $LiMg(AlH_4)_3$.

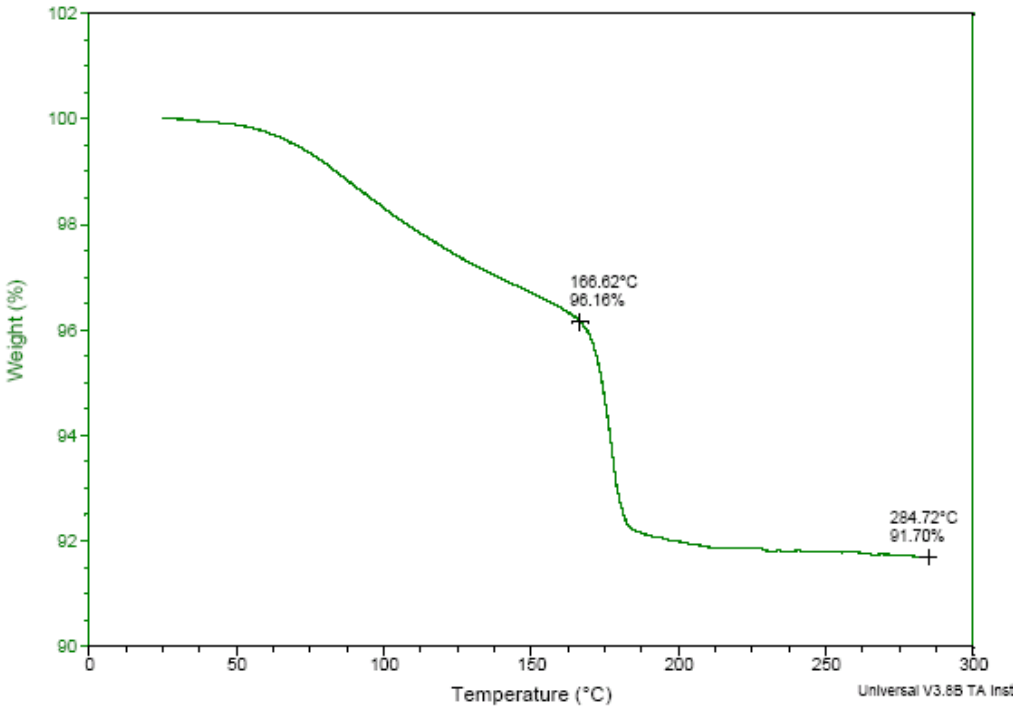

Figure 65: TGA of of $LiMg(AlH_4)_3$.

Bogdanovic *et al.* [Ref. 68] also reported the synthesis of $LiMg(AlH_4)_3$ by way of ball milling based on the reaction below

$$MgCl_2 + 3LiAlH_4 \rightarrow LiMg(AlH_4)_3 + 2LiCl$$

In this work, separation of $LiMg(AlH_4)_3$ from LiCl was accomplished using a wet chemical separation method. Dehydrogenation of the material was also reported. Interestingly, the XRD analysis suggested that the bulk of the material was mostly amorphous. It should be noted that the mixture $LiMg(AlH_4)_3$ + 2LiCl was used in the dehydrogenation study. No reverse hydrogenation reactions were mentioned.

The synthesis of the corresponding sodium analog, $NaMg(AlH_4)_3$, was not successful after a few attempts. This turns out to be consistent with the calculation showing its formation being thermodynamically unfavorable according to Ref. 69.

5.3 Complex 3: $Mg(BH_4)_2(2NH_3)$

This magnesium borohydride ammonia complex has a theoretical maximum H wt% of 16.0%, assuming Mg and BN as the hydride-depleted products. It represents an interesting alternative to ammonia borane, $BH_3{\bullet}NH_3$, which has received considerable interest as a hydrogen storage material. The compound can be prepared by a three-step procedure according to a literature report as outlined below [Ref. 70].

Equation 35 $$\mathbf{MgCl_2 + 2NaBH_4 \rightarrow Mg(BH_4)_2{\bullet}Et_2O + 2NaCl} \quad \mathbf{(1)}$$

Equation 36 $Mg(BH_4)_2 \bullet Et_2O + 6NH_3 \rightarrow Mg(BH_4)_2 \bullet 6NH_3 + Et_2O$ **(2)**

Equation 37 $Mg(BH_4)_2 \bullet 6NH_3 \rightarrow Mg(BH_4)_2 \bullet 2NH_3 + 4NH_3$ **(3)**

The reactions of Equation 35 and Equation 36 were carried out in Et_2O. In Equation 37, the hexa-ammonia complex is converted to the di-ammonia complex by heating at 100°C under vacuum for 7 hours.

The XRD patterns of $Mg(BH_4)_2 \bullet 6NH_3$ and $Mg(BH_4)_2 \bullet 2NH_3$ are shown in Figure 66 and Figure 67, respectively.

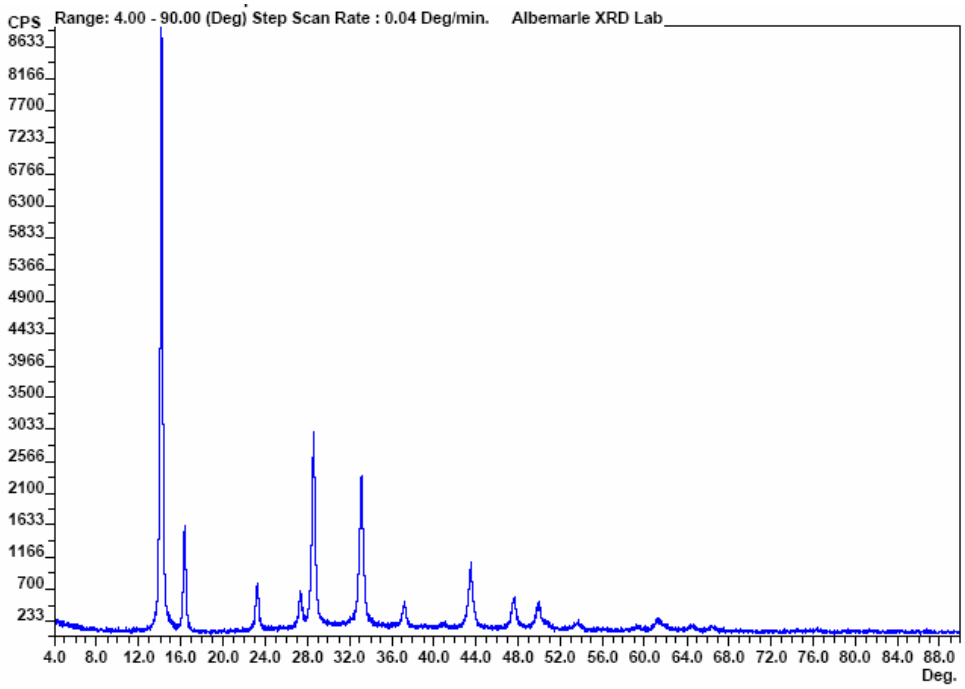

Figure 66: XRD pattern of $Mg(BH_4)_2 \bullet 6NH_3$.

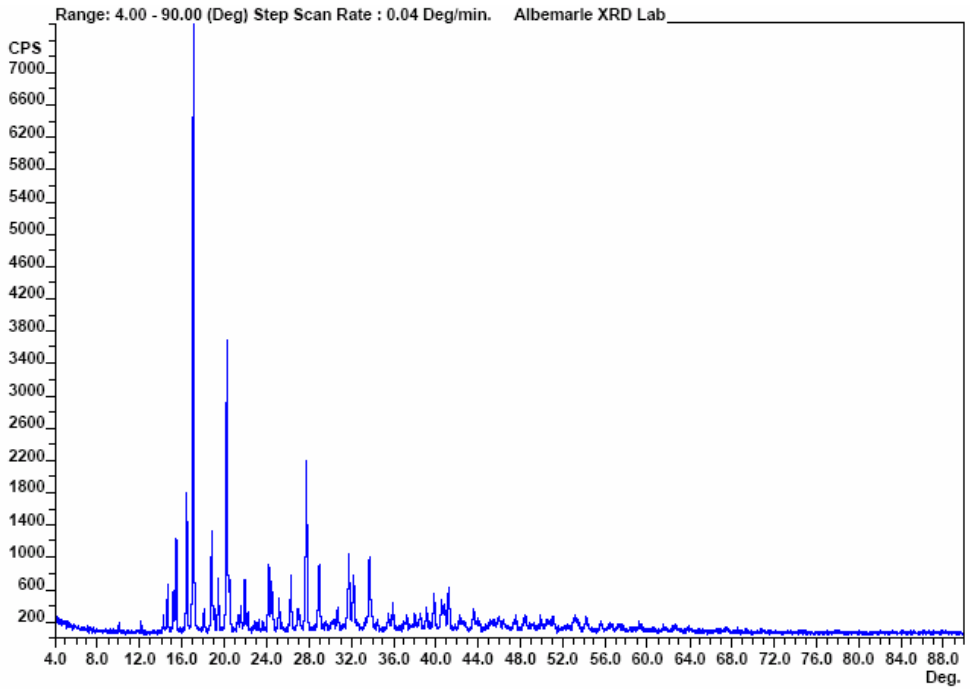

Figure 67: The XRD pattern of $Mg(BH_4)_2 \bullet 2NH_3$.

Interestingly, two distinct forms of the di-ammonia complex seem to exist based on thermal analyses. One has two ammonia molecules loosely bound, consistent with the "solvate" formulation of $Mg(BH_4)_2 \bullet 2NH_3$ and another has the two ammonias tightly bound, more consistent with the formulation of $Mg(NH_3)_2(BH_4)_2$. The two forms have drastically different thermal behaviors during hydrogen discharge, as shown in Figure 68 to Figure 71.

$Mg(BH_4)_2 \bullet 2NH_3$ (Metal Hydride Mechanism)

$$Mg(BH_4)_2 \bullet 2NH_3 \longrightarrow Mg(BH_4)_2 + 2NH_3$$

$$Mg(BH_4)_2 \longrightarrow MgH_2 + 2B + 3H_2$$

$$MgH_2 \longrightarrow Mg + H_2$$

$Mg(NH_3)_2(BH_4)_2$ ($BH_3 \bullet NH_3$-like Mechanism)

$$Mg(NH_3)_2(BH_4)_2 \longrightarrow MgH_2 + 2BN + 6H_2$$

$$MgH_2 \longrightarrow Mg + H_2$$

Table 15 summarizes the expected weight loss and thermal characteristics predicted by the two hydrogen discharge mechanisms exhibited by $Mg(BH_4)_2(NH_3)_2$, which are in total agreement with the TGA data (Figure 69 and Figure 71, respectively) . The two sets of corresponding DSC data are shown in Figure 68 and Figure 70. Figure 70 shows an endotherm at 61°C likely due to melting of

$Mg(NH_3)_2(BH_4)_2$, which is not seen in Figure 68 consistent with a more ionic nature of $Mg(BH_4)_2 \bullet 2NH_3$. The exotherm at 232°C in Figure 70 corresponds to 70.3 kJ/mol.

Table 15: The properties of two forms of $Mg(NH_3)_2(BH_4)_2$.

	Theoretical Total Weight Loss in TGA	Thermal Events in Open System (TGA)
$Mg(BH_4)_2 \bullet 2NH_3$ **Metal hydride mechanism**	52.2%	1. Ammonia evaporation: endothermic 2. Hydrogen discharge (B-H): endothermic 3. Hydrogen discharge (Mg-H): endothermic
$Mg(NH_3)_2(BH_4)_2$ **$BH_3 \bullet NH_3$-like mechanism**	16.0%	1. Hydrogen discharge (H-BN-H): exothermic 2. Hydrogen discharge (Mg-H): endothermic

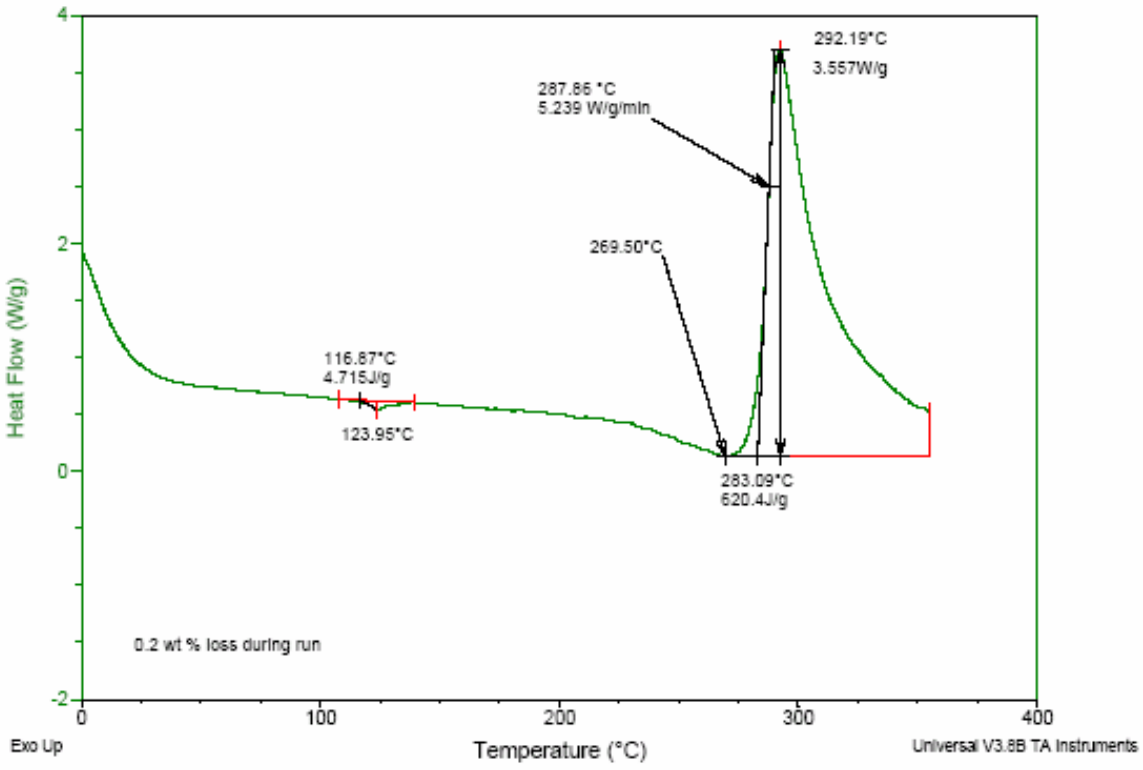

Figure 68: DSC of $Mg(BH_4)_2 \bullet 2NH_3$.

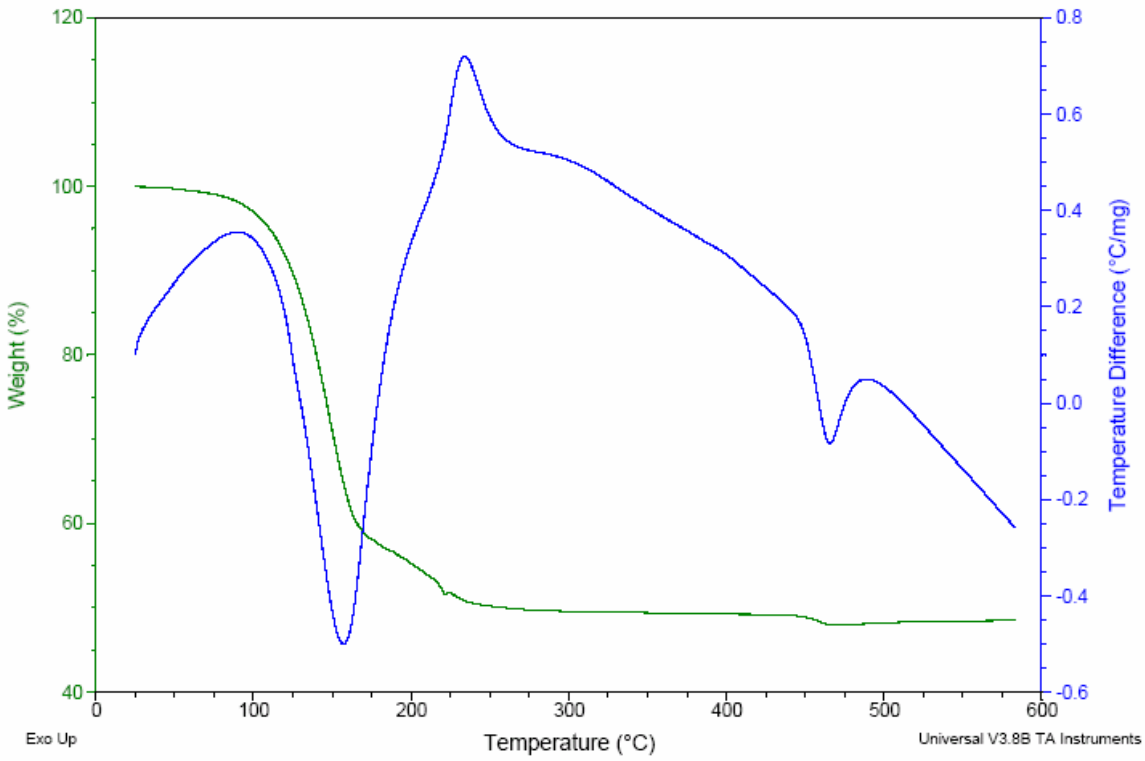

Figure 69: TGA-DTA of $Mg(BH_4)_2 \cdot 2NH_3$ showing metal hydride characteristics.

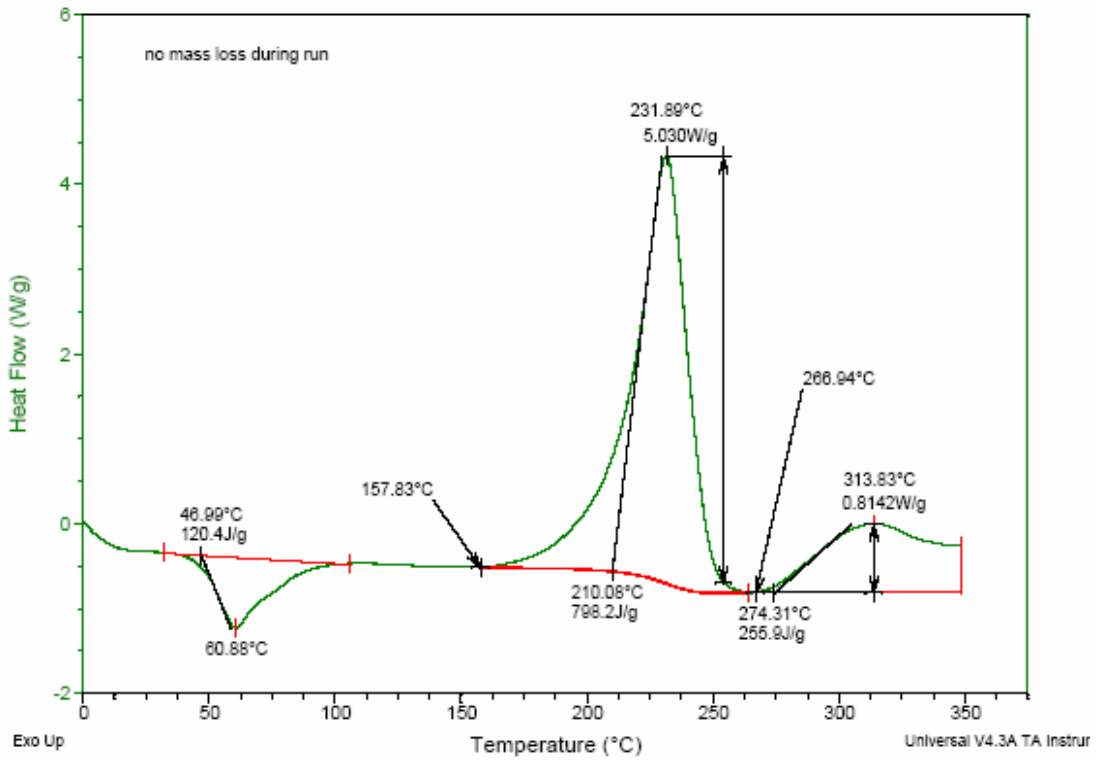

Figure 70: DSC of $Mg(NH_3)_2(BH_4)_2$.

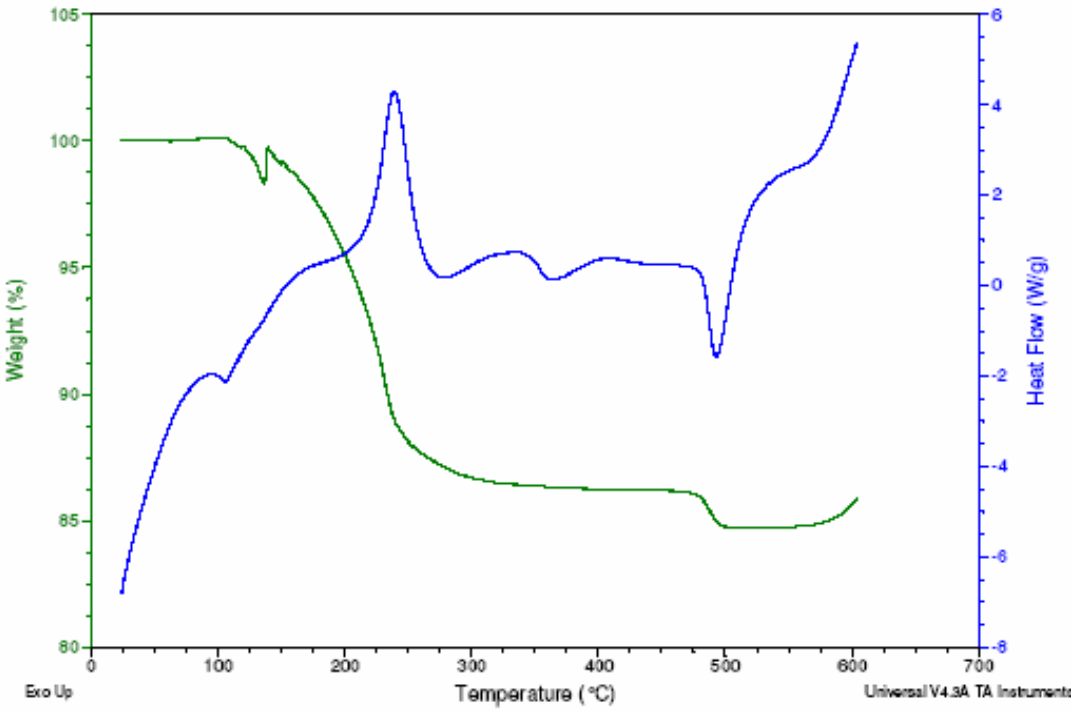

Figure 71: TGA-DSC of $Mg(NH_3)_2(BH_4)_2$ showing $BH_3 \bullet NH_3$-like characteristics.

It is not clear what causes these two types of the di-ammonia complexes to form. It is speculated that the likely cause is the manner in which the reaction of Equation 37 is carried out. The hexa to di-ammonia reaction, performed at 90-110°C under vacuum, is sometimes accompanied by melting of the solids but sometimes not, with no apparent pattern. Notice that in the two DSC data sets shown above, one has a melting endotherm at 60.9°C (Figure 70) and the other has none (Figure 68). Conceivably, factors such as the temperature profile and vacuum strength could influence the reaction.

It also should be mentioned that we have synthesized a sample of $Mg(BH_4)_2(NH_3)_2$ that shows a weight loss of around 28%, suggesting a roughly 50/50 ratio of the two forms.

In Konoplev's article [Ref. 70], the IR data of BH_4^- in both the hexa and di-ammonia complexes are reported. The results suggest the hexa-ammonia complex has the formulation of $[Mg(NH_3)_6](BH_4)_2$ where the BH_4^- anions are in the outer coordination sphere, whereas the di-ammonia complex has the BH_4^- anions directly coordinated to the Mg. The transition of inner and outer sphere ligands is certainly a poorly understood process which must have a significant bearing on the observed chemistry.

5.4 Complex 4: $Mg(BH_4)_2(NMe_3)$

The trimethylamine complexes of $Mg(BH_4)_2$ were synthesized specifically to rule out the possibility of the hydrogen release via a $BH_3 \bullet NH_3$-like mechanism. The synthesis was carried out in a similar fashion as that of the ammonia complex, i.e.:

$$MgCl_2 + 2NaBH_4 + \text{excess } NMe_3 \longrightarrow Mg(BH_4)_2(NMe_3)_2 + 2NaCl$$

$$Mg(BH_4)_2(NMe_3)_2 \longrightarrow Mg(BH_4)_2(NMe_3) + NMe_3$$

The first reaction was carried out in toluene at 60°C. Carrying out the reaction above 60°C resulted in production of grayish materials, likely a result of some decomposition. After filtration and removal of excess NMe_3, the toluene filtrate showed by H^1-NMR to contain roughly a 1:1 ratio of BH_4 and NMe_3, indicating the formation of a di-amine complex. In the case of NH_3, the initial product was a hexa-ammonia complex, $Mg(BH_4)_2(NH_3)_6$. One of the trimethylamine ligands in $Mg(BH_4)_2(NMe_3)_2$ is labile at room temperature under vacuum. By contrast, four of the six ammonias in $Mg(BH_4)_2(NH_3)_6$ are labile, but only when heated to around 100°C under vacuum. The monoamine complex was analyzed by ICP to contain 21.3% Mg (theory: 21.5%).

The monoamine complex indeed exhibits very different thermal properties in DSC and TGA from those of $Mg(BH_4)_2(NH_3)_2$. The DSC of the complex (Figure 72) shows small exo- and endotherms at low temperatures (101°C and 128°C respectively), likely due to a partial hydrogen release and evaporation of the amine. A prolonged endotherm follows at temperatures of >240°C. The TGA-DSC (Figure 73) shows two gradual weight losses, one between 80-200°C and another between 200-300°C. The total of the two weight losses was >50% and are roughly thermally neutral as shown by the accompanying DSC. Interestingly, the TGA-MS carried out by UTRC shows the complex begins to release hydrogen at temperatures as low as 60°C. Thus, the first weight loss in the TGA must be the combination of hydrogen discharge and NMe_3 evaporation. This result indicates a dramatic reduction of the hydrogen discharge temperature from ~320°C for $Mg(BH_4)_2$ to <100°C in $Mg(BH_4)_2(NMe_3)$. ***Thus, we have unambiguously demonstrated the use of simple nitrogen ligands to destabilize $Mg(BH_4)_2$ which otherwise would only discharge hydrogen at an impractical temperature range.***

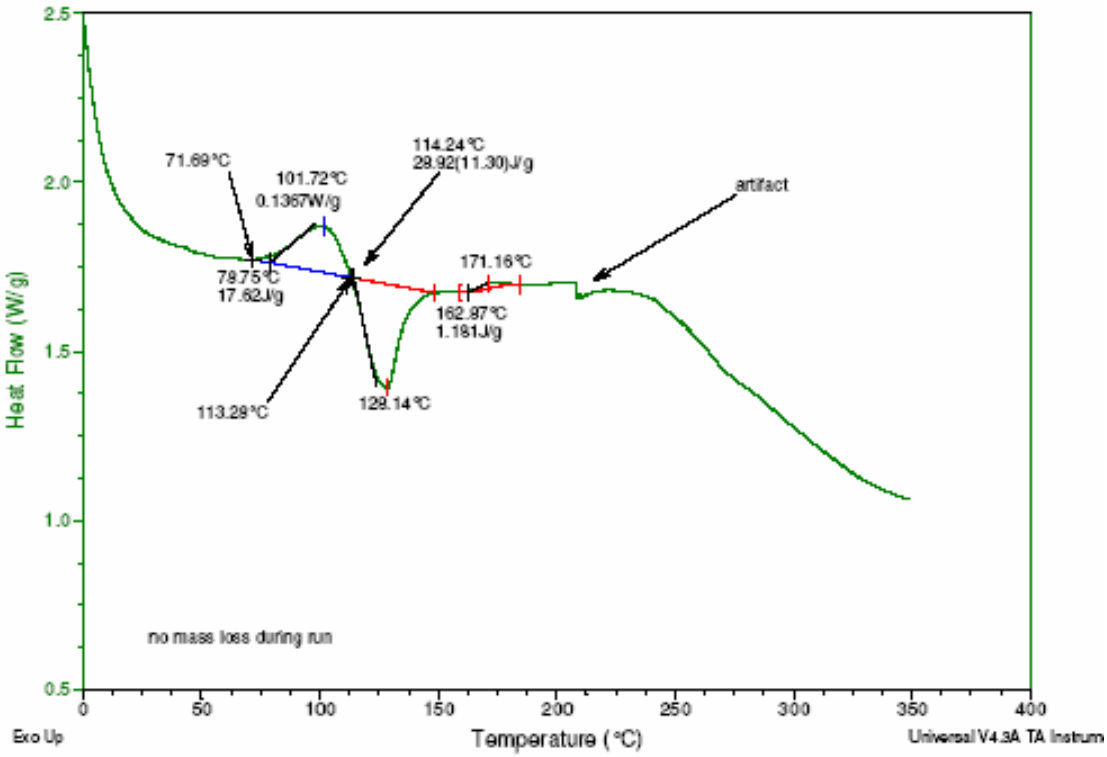

Figure 72: DSC of $Mg(BH_4)_2(NMe_3)$.

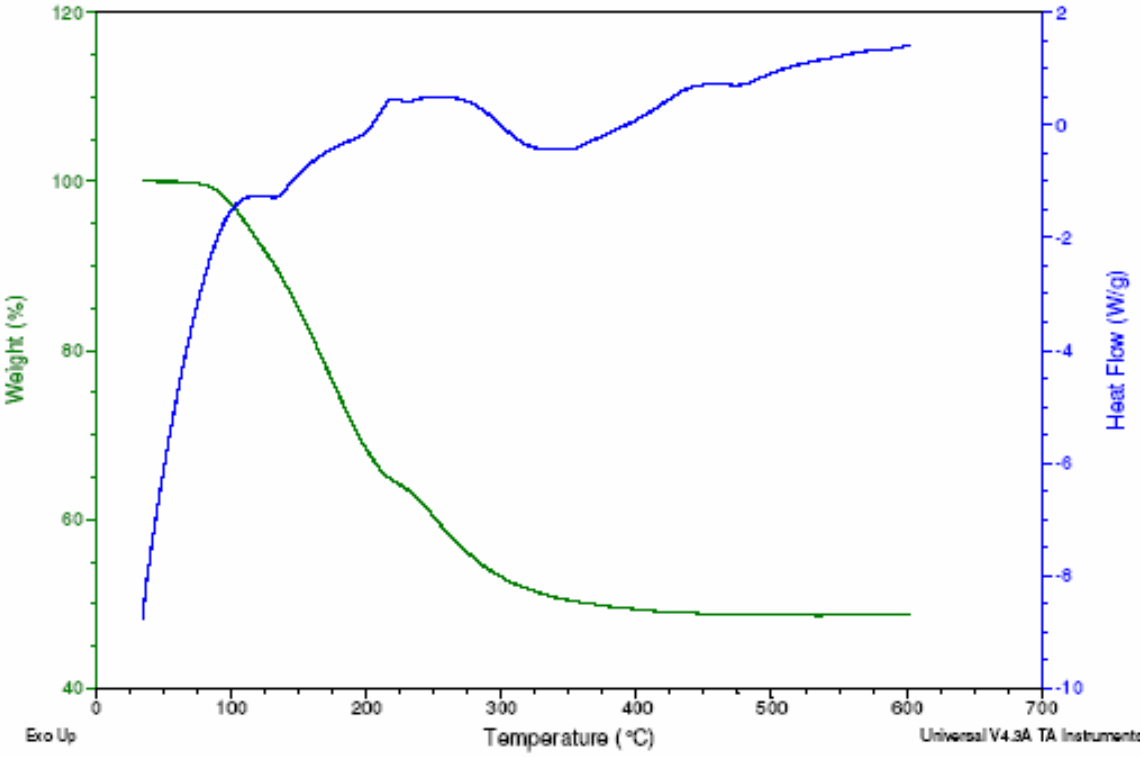

Figure 73: TGA-DSC of $Mg(BH_4)_2(NMe_3)$.

5.5 Complex 5: $Zr(BH_4)_4(NH_3)_8$

Some group 4 metal complexes of tetrahydroborate are known. They are usually characterized by high theoretical hydrogen content but thermally unstable as shown in Table 16.

Table 16: Group 4 transition metal complexes of tetrahydroborate.

Group 4 metal	Known Borate*	H %	Thermal Stability
Ti	$Ti(BH_4)_3 \cdot Et_2O$	13.1% (no ether)	unstable at –20°C
Zr	$Zr(BH_4)_4$	10.7%	unstable at ambient T
Hf	$Hf(BH_4)_4$	6.8%	unstable at ambient T

* For Ti, see Ref. 71.
* For Zr and Hf, see Ref. 72.

Our approach to improve the thermal properties of these materials was to form complexes with polar molecules that could stabilize the dehydrogenation process via filling the open metal coordination sites. A particularly useful polar group is ammonia, which not only provides for this coordination, but also can be a source of hydrogen as well.

We decided to focus our initial efforts on $Zr(BH_4)_4$ which is typically much more stable than its Ti analogs and surprisingly volatile, thus easily separable from LiCl by distillation. The ammonia complex of Zr borohydride was prepared by a two-step process:

$$ZrCl_4 + 4LiBH_4 \longrightarrow Zr(BH_4)_4\uparrow + 4\,LiCl$$

$$Zr(BH_4)_4 + NH_3\,(\text{excess}) \longrightarrow Zr(BH_4)_4 \bullet 8NH_3$$

The product from reaction of $Zr(BH_4)_4$ with ammonia turns out to be an octa-ammonia complex, $Zr(BH_4)_4 \cdot 8NH_3$, obtained in excellent yield (92%). This complex is thermally stable at room temperature. ***Thus, the concept of stabilizing the metal borate complex via ammonia coordination was confirmed.***

Confirmation of an octa-ammonia complex was obtained by elemental analysis using ICP (theory: Zr 31.8%, B 15.1%; found: Zr 31.7%, B 15.4%) and ^{1}H-NMR. Figure 74 shows the ^{1}H-NMR spectrum (both ^{11}B-coupled and decoupled) of $Zr(BH_4)_4 \cdot 8NH_3$ in DMSO-D_6. The integration of the resonances indicated the presence of two types of BH_4 groups in a three (δ-0.5 to 0.3 ppm,) : one (δ1 to 2 ppm) ratio as well as three types of ammonia (16 BH_4 protons and 24 NH_3 protons).

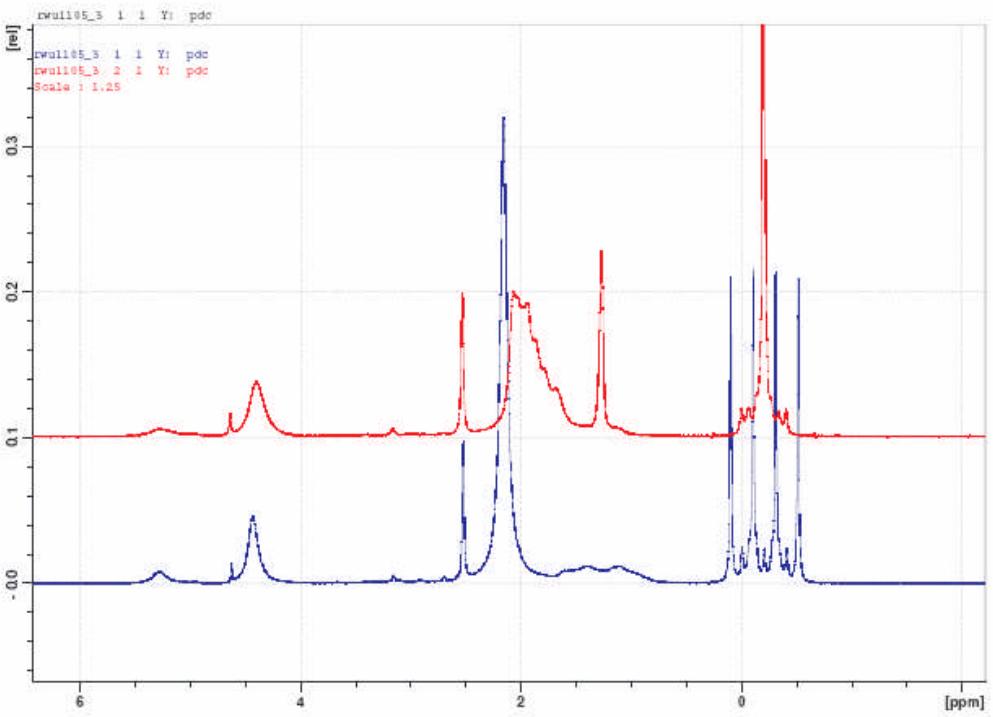

Figure 74: ^{11}B Decoupled (red / upper) and coupled (blue / lower) spectra of $Zr(BH_4)_4$▪$8NH_3$.

The XRD pattern of $Zr(BH_4)_4$▪$8NH_3$ is shown in Figure 75.

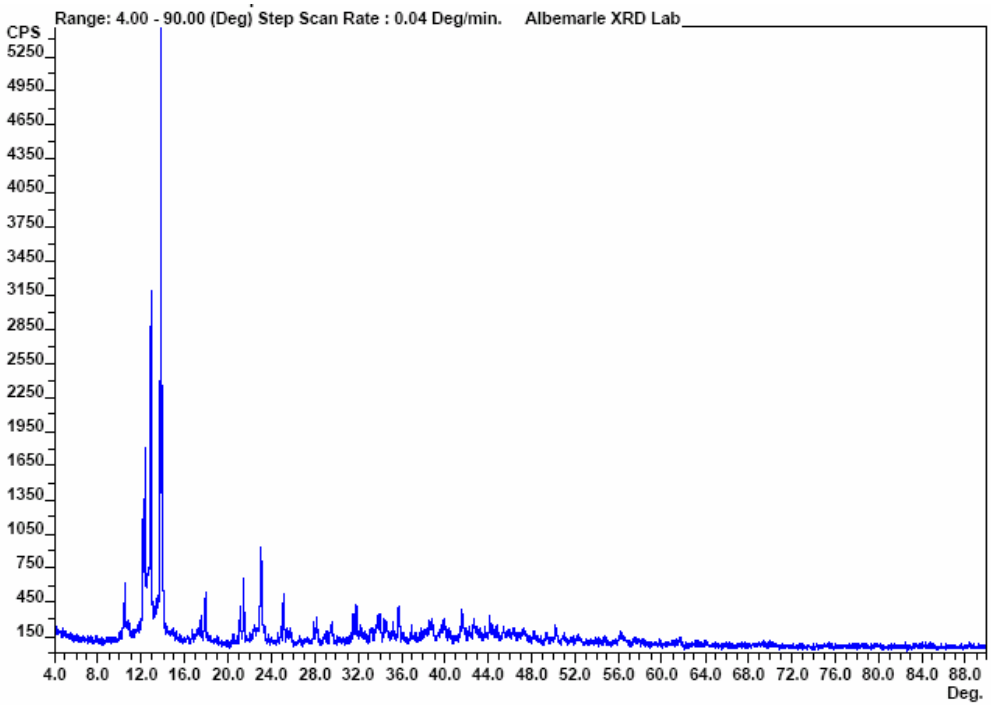

Figure 75: XRD pattern of $Zr(BH_4)_4$▪$8NH_3$.

The DSC and TGA-DTA of this complex are shown in Figure 76 and Figure 77, respectively. The DSC shows a single exotherm at 147°C with a heat release of 286 kJ/mol. Such a heat release is much larger than the 70.3 kJ/mol in $Mg(NH_3)_2(BH_4)_2$. Assuming both complexes operating via the same $NH_3 \bullet BH_3$-like mechanism, the Zr complex must have a much more complete hydrogen discharge than the Mg complex. The 34% weight loss in the TGA at around the same temperature could be accounted for by a combined loss of 4 ammonias (24%) and 28 hydrogens (10%). A small endotherm at 100-110°C suggests dissociation and evaporation of ammonia.

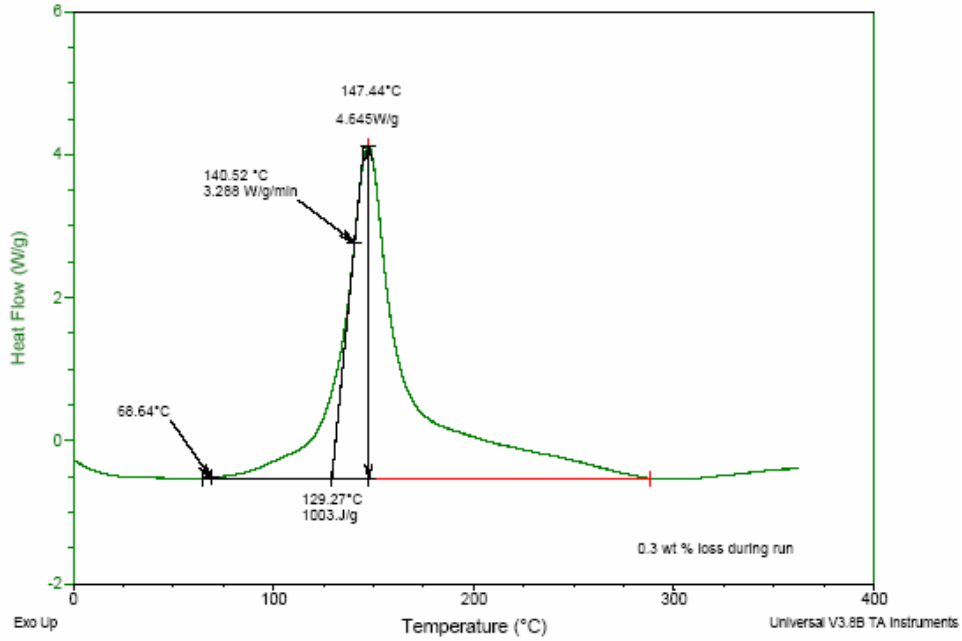

Figure 76: DSC of of $Zr(BH_4)_4 \bullet 8NH_3$.

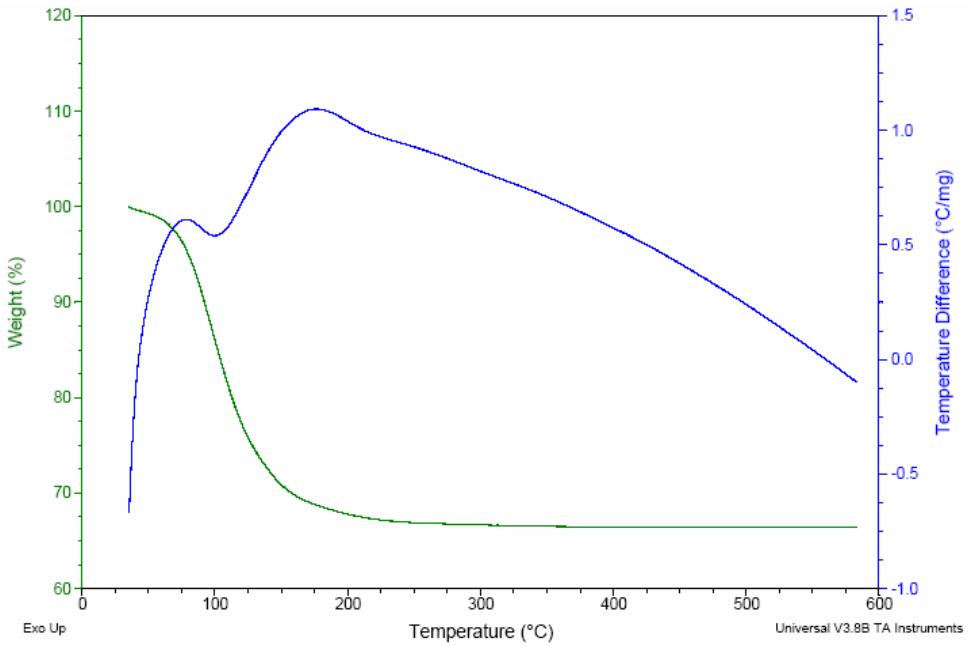

Figure 77: TGA-DTA of $Zr(BH_4)_4 \bullet 8NH_3$.

5.6 Complex 6: $Zr(BH_4)_4(H_2NC_2H_4NH_2)_2$

The TGA analysis of $Zr(BH_4)_4 \cdot 8NH_3$ indicates four out of eight ammonia molecules are "loose", which can present a hazard to the PEM fuel cell. To address this problem, we opted to use the less volatile ethylenediamine (ED, bp 118°C) in place of ammonia. Thus, reaction of $Zr(BH_4)_4$ with two equivalents of ED in Et_2O resulted in an instant precipitation of a white solid with an empirical formula of $Zr(BH_4)_4(ED)_{2.5}$ (ICP: Zr=30.2%; B=14.7%). The material is apparently a mixture of coordination complexes $Zr(BH_4)_4(ED)_x$, where x = 1,2,3..etc. The starting complex, $Zr(BH_4)_4$, is absent since it is highly soluble in Et_2O and would have been removed by filtration. The H^1-NMR of the material in DMSO showed two types of BH_4^- anion and a myriad of resonances assignable to N-H. A small amount of solvent Et_2O was also detected (<1 wt%), which cannot be removed by vacuum drying at room temperature. In contrast, there is no coordinated Et_2O detected in $Zr(BH_4)_4 \cdot 8NH_3$.

The thermal analyses results of the ethylenediamine complex are shown in Figure 78 and Figure 79. The DSC (Figure 78) shows at least three exothermic peaks at temperatures below 225°C with an onset temperature of 86°C. The size of the total exotherm, 261.5 J/g, is roughly a quarter of that for $Zr(BH_4)_4 \bullet 8NH_3$. This reduced exotherm is beneficial in thermal management and should in principle render more favorable thermodynamics. At temperatures of >225°C, some additional exothermic events of unknown nature begin to occur.

The ethylenediamine complex, $Zr(BH_4)_4(ED)_{2.5}$, has a maximum hydrogen content of 8.7 wt% consistent with the TGA results (Figure 79) which shows a weight loss of about 7.5 wt% at temperatures up to 238°C. Further weight loss occurs as the temperature is increased. Again, the nature of this high temperature phenomenon is unknown at this time. Throughout the temperature range, the weight loss follows a gradual profile which is consistent with $Zr(BH_4)_4(ED)_{2.5}$ being a mixture as discussed earlier.

Ethylenediamine complexes, $Zr(BH_4)_4(ED)_x$ where x is 2.1 or 3.7, have also been synthesized. Unfortunately, none of these complexes show reversible hydrogen discharge/re-charge under practical real-world conditions.

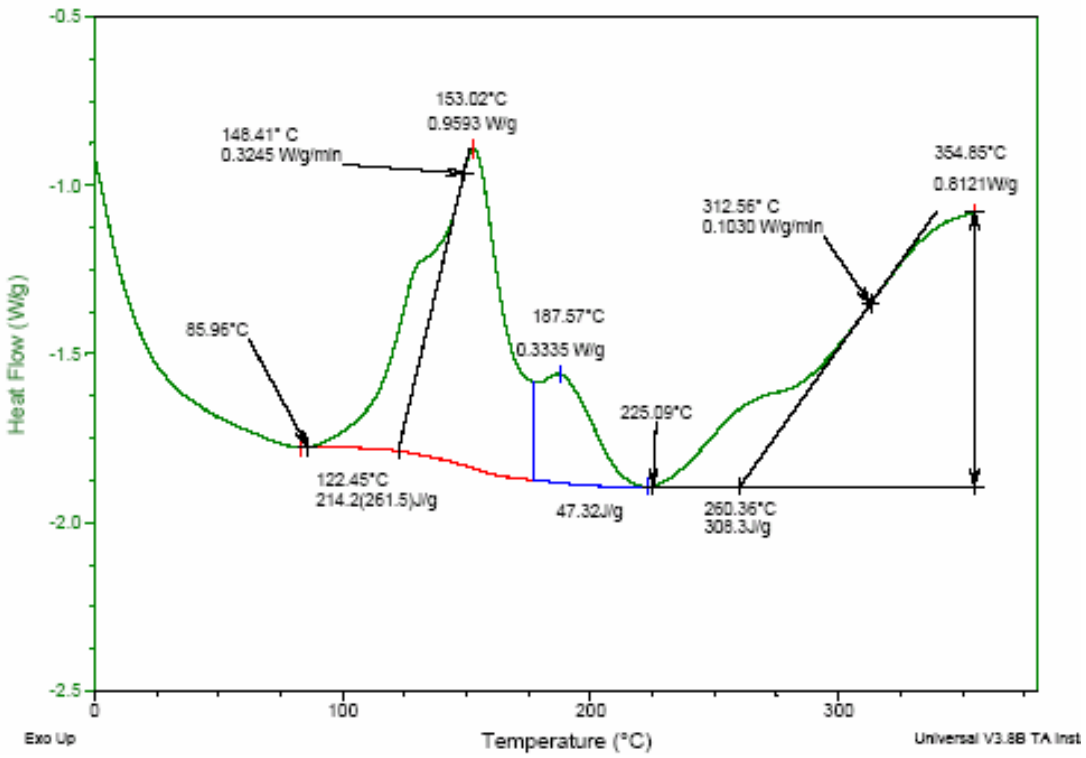

Figure 78: DSC of of $Zr(BH_4)_4(ED)_{2.5}$.

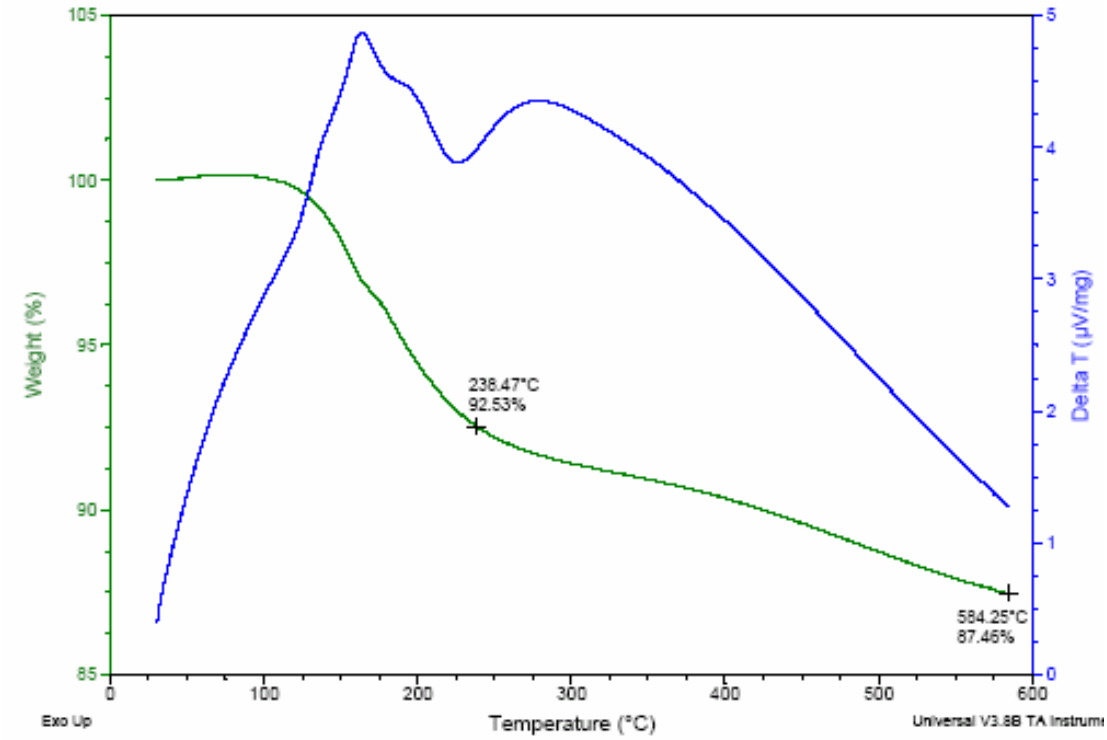

Figure 79: TGA-DTA of $Zr(BH_4)_4(ED)_{2.5}$.

5.7 Complex 7: $NaTi(BH_4)_4(NH_3)_6$

In preparing the titanium analog of $Zr(BH_4)_4(NH_3)_8$, we encountered a number of obstacles. First, the known precursor complex, $Ti(BH_4)_3 \cdot Et_2O$, unlike $Zr(BH_4)_4$, is thermally unstable (at > -20ºC) and appears to be sensitive to nitrogen as well. Additionally, $Ti(BH_4)_3 \cdot Et_2O$ is also much less distillable than $Zr(BH_4)_4$, thus making the literature preparation method rather impractical. We noticed from the literature that the 1,2-dimethoxyether (DME) complex of $Ti(BH_4)_3$, prepared by $Ti(BH_4)_3 \cdot Et_2O$ + DME, is much more thermally stable. We have thus designed a modified synthesis of $Ti(BH_4)_3 \cdot DME$ using $NaBH_4$ instead of $LiBH_4$ and DME as the solvent instead of Et_2O. The modified method requires no distillation of the product, and its product is indeed thermally stable at room temperature for at least a couple of days. We proceeded to prepare its corresponding ammonia complex. The product from the ammonia reaction is a purple solid and appeared to be thermally stable at room temperature as well. Its H^1-NMR in DMSO reveals the absence of DME and is strikingly similarly to that of $Zr(BH_4)_4 \bullet 8NH_3$. Surprisingly, the ICP analysis suggested the isolated purple material was an ionic compound, $NaTi(BH_4)_4 \cdot (NH_3)_6$ (ICP: Na 9.81%; Ti 21.1%; B 19.6%).

Equation 38 $\mathbf{TiCl_4(DME) + 5NaBH_4 \longrightarrow NaTi(BH_4)_4 \bullet DME + 4\,NaCl + BH_3/H_2 \uparrow}$

Equation 39 $\mathbf{NaTi(BH_4)_4 \bullet DME + NH_3\ (excess) \longrightarrow NaTi(BH_4)_4(NH_3)_6}$

The thermal analyses results of $NaTi(BH_4)_4(NH_3)_6$ are shown in Figure 80 and Figure 81. The DSC of this titanium compound (Figure 80) is strikingly similar to that of $Zr(BH_4)_4(NH_3)_8$, showing one single exotherm peaking at ~170ºC. Figure 82 shows the overlay of the two DSC data sets. It is interesting that the titanium complex is slightly more stable thermally than the zirconium complex in the closed DSC system, undoubtedly due to the ionic nature of the Ti complex versus the neutral Zr complex. The exotherm amounts to 220 kJ/mol, compared to 286 KJ/mol for $Zr(BH_4)_4(NH_3)_8$.

The TGA-DTA for $NaTi(BH_4)_4(NH_3)_6$ (Figure 81) shows a weight loss of 32%, indicating about 3 ammonias out of 6 that are loosely bound as has previously been observed in $Zr(BH_4)_4(NH_3)_8$. Interestingly, the weight loss is accompanied by an endotherm, not exotherm, as shown by the DTA graph. This strongly suggests the hydrogen discharge pathway of $NaTi(BH_4)_4(NH_3)_6$ in an open system such as TGA is less NH_3BH_3-like (known to decompose exothermically) and more like $NaTi(BH_4)_4$ whose decomposition, like most of the metal hydrides, is endothermic.

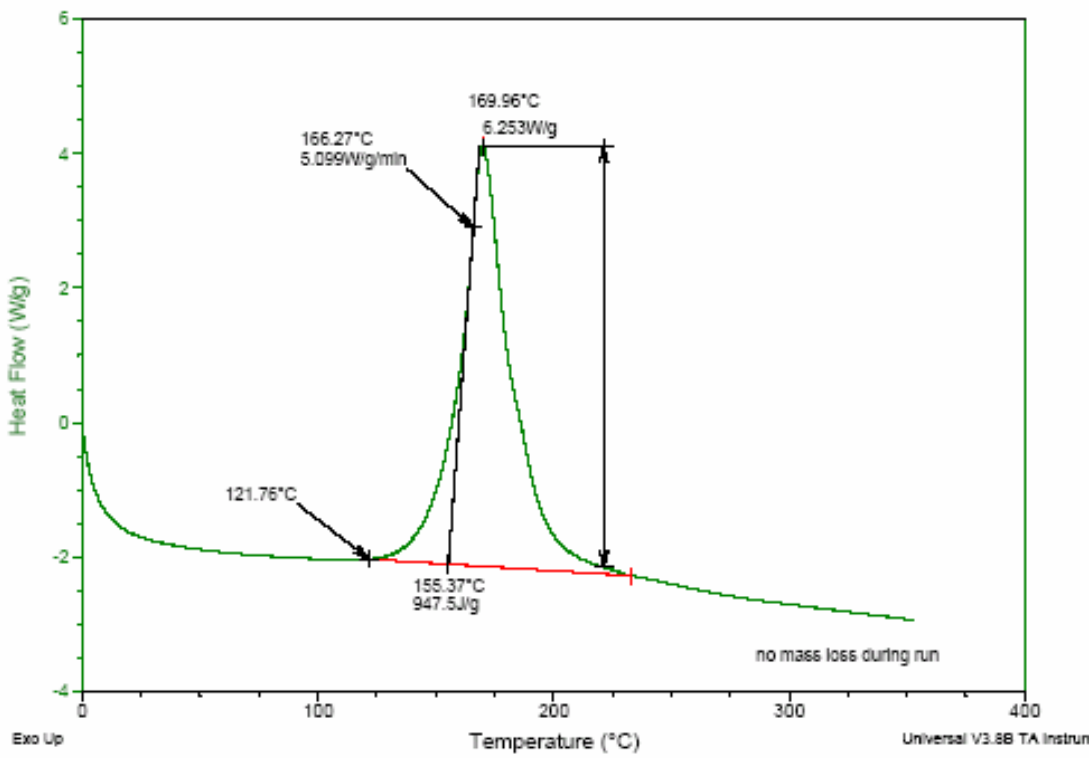

Figure 80: DSC of $NaTi(BH_4)_4(NH_3)_6$.

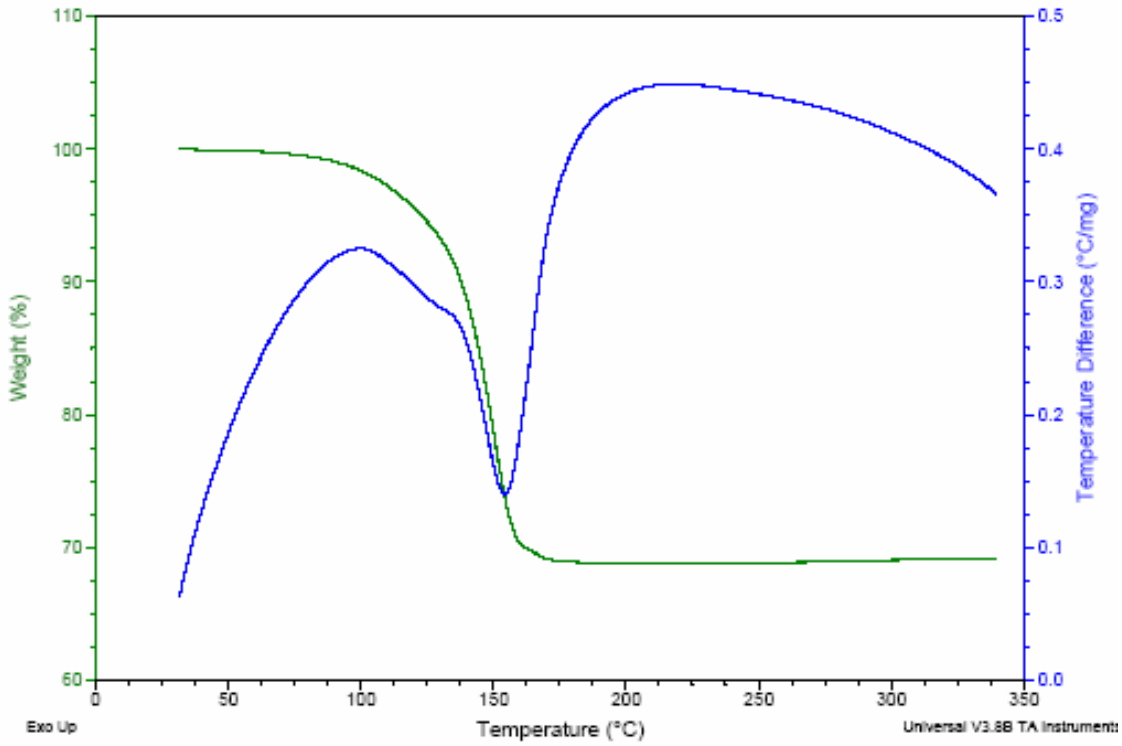

Figure 81: TGA-DTA of $NaTi(BH_4)_4(NH_3)_6$.

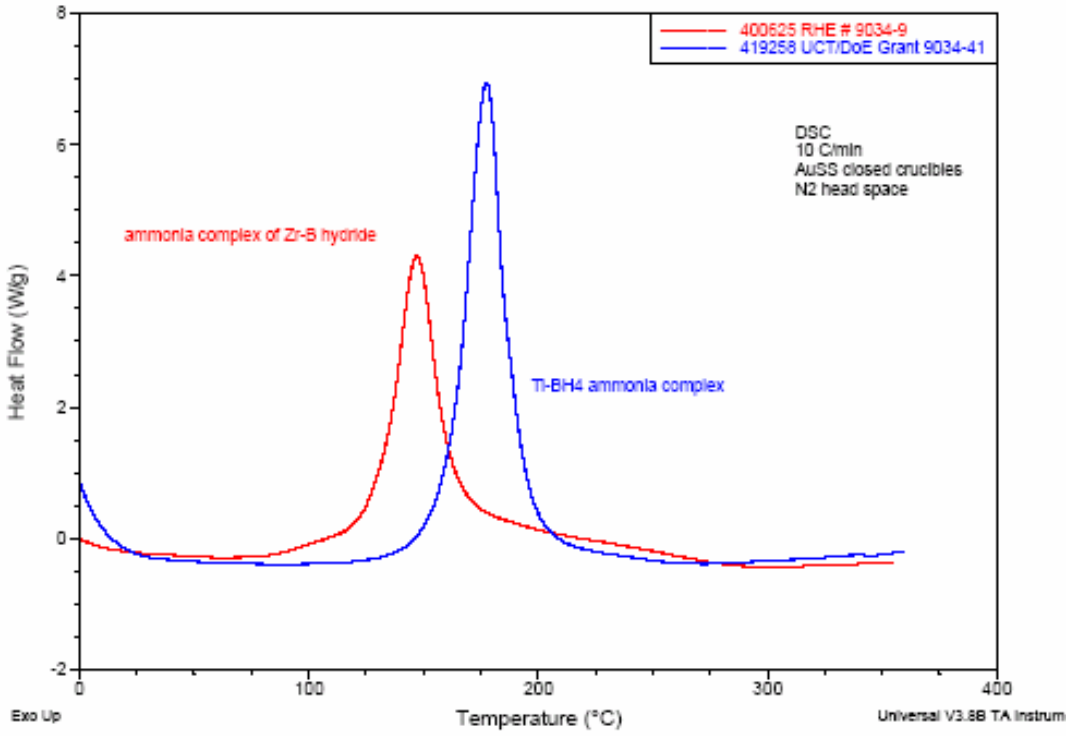

Figure 82: Overlay of DSC data for $Zr(BH_4)_4(NH_3)_8$ (red / left peak) and $NaTi(BH_4)_4(NH_3)_6$ (blue / right peak).

5.8 Complex 8: $NaTi(BH_4)_4DME$ (DME=1,2-dimethoxyethane)

The reaction of $TiCl_4$ and $NaBH_4$ in DME first produces $NaTi(BH_4)_4(DME)_3$ which can be easily converted to $NaTi(BH_4)_4DME$ by applying vacuum at room temperature. The yield was nearly quantitative. During the reaction, the titanium center was reduced from an oxidation state of VI to III. The tri-DME complex is known [Ref. 73], whereas the mono-DME complex has not been previously reported. The $NaTi(BH_4)_4$•DME is a blue compound, containing 7.3 wt% of B-H hydrogen. It is unstable at room temperature and slowly decomposes into a dark gray compound.

The thermal analyses of $NaTi(BH_4)_4$•DME produced the results of Figure 83 and Figure 84 below. The DSC shows an initial endotherm at ~100°C immediately followed by two exotherms at ~110°C. The endotherm is likely due to evaporation of DME and/or hydrogen discharge. The occurrence of endotherms that immediately follow is interesting. It is speculated that it arises from re-coordination of DME to the Ti or B center after hydrogen discharge. If true, the intermediates have apparently been stabilized (thus, endothermic) by the presence of DME. There is another big exotherm at >200°C. The TGA-DTA shows a weight loss of about 44%, consistent with loss of the DME ligand (~41%) and some hydrogen. The DTA curve shows the weight loss being accompanied by an endotherm, typical of a metal hydride.

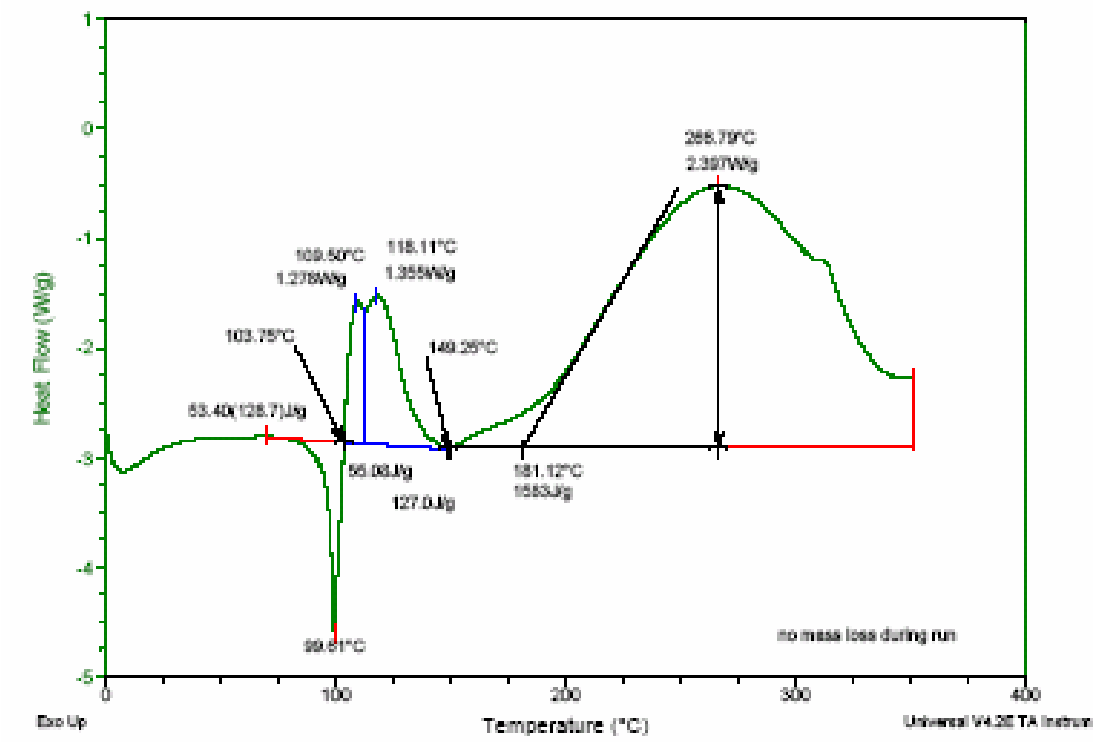

Figure 83: DSC of $NaTi(BH_4)_4$•DME.

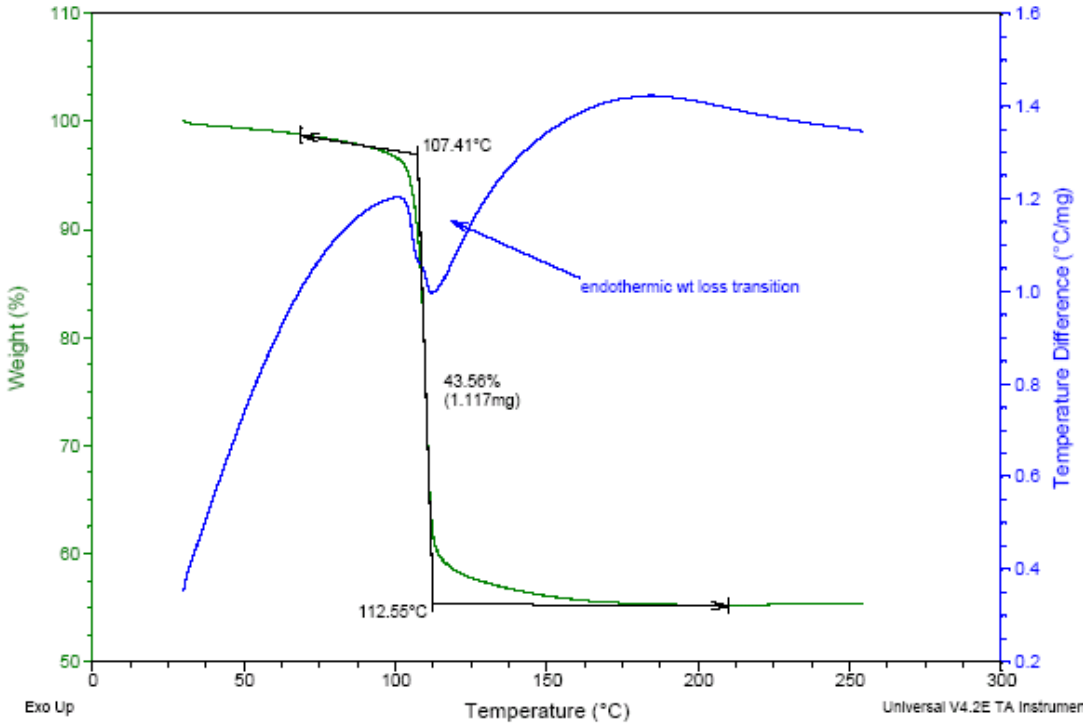

Figure 84: TGA-DTA of $NaTi(BH_4)_4$•DME.

To study the reversibility of hydrogen charge and discharge of $NaTi(BH_4)_4$·DME, we have successfully employed an analytical technique called DRIFTS (Diffuse Reflectance Infrared Fourier Transform Spectroscopy). This technique allows the sample to be mounted in a sealed cell under dry nitrogen. The IR-active frequencies in this complex include: B-H frequencies at 2000-2500 cm^{-1} and C-H/O-C frequencies at 2800-3000 and 800-1500 cm^{-1}. Figure 85 below shows the three overlay DRIFTS spectra before and after hydrogen charge and discharge conditions. The following observations can be made from the spectra:

- The material after hydrogen discharge at 60°C changed color from blue to black but still contain some residual B-H absorbances, suggesting at least one of the four boron-hydrides still remains.
- The reverse reaction did indeed occur at temperatures as low as 20°C, as evidenced by the increased B-H frequencies. This observed hydrogen recharge, however, is small compared to the original complex and the material remains black.
- The DME ligand is crucial for the reverse hydrogen reaction to occur. $NaTi(BH_4)_4$·DME releases DME after hydrogen discharge. If DME were allowed to escape from the system, then the reverse reaction would not occur. Consistent with this observation, the overlay spectra show a direct correlation between DME and B-H absorbances: the more DME, the higher B-H absorbances.

Thus, the hydrogen sorption/desorption kinetics of $NaTi(BH_4)_4$·DME is rather interesting. The DRIFTS study shows the complex is able to discharge most of its hydrogen at 60°C, turning from blue to black, and recharge some of hydrogen back at a temperature as low as 20°C. These observations suggest significant improvement from Ti-doped $LiBH_4$, which requires >350°C and 650°C for the respective reactions to occur [Ref. 74].

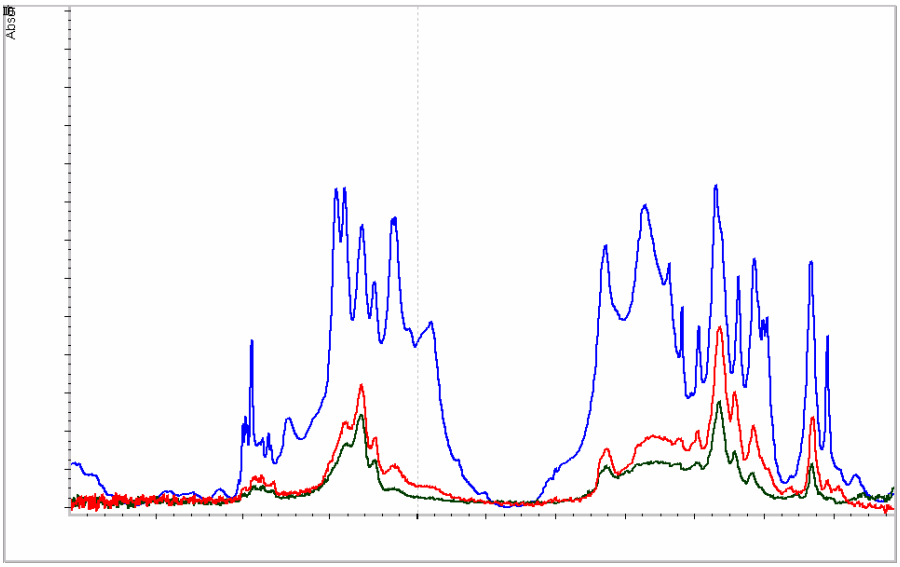

Figure 85: The overlay DRIFTS spectra of $NaTi(BH_4)_4$·DME before and after hydrogen discharge; Top: $NaTi(BH_4)_4$·DME before hydrogen discharge; Middle: after 60°C hydrogen discharge and 20°C recharge; Bottom: after 60°C hydrogen discharge.

5.9 Complexes 9 and 10: $Na_2O[Ti(BH_4)_4DME]_2$ and $NaOTi(BH_4)_3DME$

During the study of its hydrogen sorption/desorption kinetics, we found $NaTi(BH_4)_4$•DME has the three following issues:

1. Thermally unstable at room temperature
2. DME reduces gravimetric H%
   - $NaTi(BH_4)_4$•DME, 7.3% H
   - $NaTi(BH_4)_4$, 12.4% H
3. Ti(III) ↔ Ti(0) or Ti(II) not reversible (a key challenge)

These three issues were addressed in this study, *vide infra*.

A key challenge of $NaTi(BH_4)_4$•DME is the fact that the redox cycle of the titanium center is not reversible. While a completely reversible hydrogen sorption/desorption cycle dictates that the titanium center has a low barrier between various oxidation states, the current Na/Ti/B/H system appears to favor the titanium center in the reduced state(s).

One strategy to coerce the titanium center to be more able to re-oxidize is to incorporate an oxide ligand into the Na/Ti/B/H system. We choose to use water as a source of oxygen. Since a direct hydrolysis of $NaTi(BH_4)_4$▪DME failed to yield the right products, we had to carry out a partial hydrolysis of $TiCl_4$(DME) which gives two oxy titanium chloride intermediates, depending on the hydrolysis ratio, as shown below. Table 17 summarizes the properties of these two intermediates along with $TiCl_4$(DME).

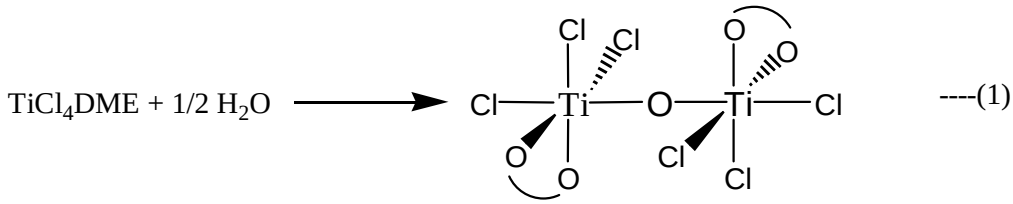

$TiCl_4DME + H_2O \longrightarrow$ **$[OTiCl_2DME]_x$** ----(2)

x = 2 or higher

Table 17: Properties of oxy titanium chloride precursors.

	$TiCl_4$(DME)	**$O[TiCl_6DME]_2$**	**$[OTiCl_2DME]_n$**
O/Ti ratio	0	0.5	1.0
Ti wt%	17.1%	19.0%	21.3%
Color	Orange	Yellow	White
Solubility in DME	High	Medium	Very low

This hydrolysis reaction (1) produces the intended product $O(TiCl_3DME)_2$ in >90% yield (ICP: found 19.3% Ti; theory 19.0%). Three analogous compounds of the type, $(\mu\text{-}O)[TiCl_3L]_2$ have been structurally characterized by single crystal X-ray determination: where L= $MeSC_2H_4SMe$ [Ref. 75] or two Me_2S [Ref. 76] or two THF [Ref. 77].

Reaction (2) in which one equivalent of water was added, also proceeded quite smoothly giving a white product with the indicated empirical formula in essentially quantitative yield. While being in excellent agreement with the ICP analysis, the $[OTiCl_2{\cdot}DME]_x$ was likely a mixture of dimer, oligomers, or even polymers. The DME ligand in $[OTiCl_2{\cdot}DME]_x$ cannot be removed with high vacuum at room temperature. At elevated temperatures, however, two transformations were observed. One was the anticipated evaporation of DME and the other was sublimation of some small amounts of yellow Ti-containing material. The yellow materials are likely to be low-oxygen, low molecular weight species such as $TiCl_4{\cdot}DME$ monomer or $O[TiCl_3{\cdot}DME]_2$ dimer from reaction (1). These yellow species form during heating and are likely generated from some kind of disproportionation. At 100^{o}C, both transformations start to occur but at a very slow rate. At 130^{o}C, removal of DME was close to completion after just one and a half hours. The resulting white product lost roughly 8% of Ti via sublimation of the yellow species mentioned above. It should be noted that the attempt to remove DME in $O[TiCl_3{\cdot}DME]_2$ under similar conditions resulted in sublimation of the dimer without loss of DME.

Thus, we have demonstrated that when a sufficient amount of oxide ligand was added to the quaternary Na/Ti/B/H system, the bonding between the titanium center and the DME ligand was weakened and it is now possible to prepare DME-free $[OTiCl_2]_x$. The oxy titanium chloride, $OTiCl_2$, is known in the literature. However, it was always made as an aqueous solution. To our knowledge, we have made the $OTiCl_2$ in the anhydrous form for the first time***. The anhydrous $OTiCl_2$ represents an interesting alternative dopant in the research of Ti-doped metal hydrides.***

Table 18 summarizes the use of these oxy precursors for the preparations of their corresponding BH_4^- complexes. In the subsequent reactions with $NaBH_4$, these new oxo-bridged precursors immediately exhibit a markedly different behavior from that of $TiCl_4DME$. There was no reduction of Ti(IV) when treated with $NaBH_4$. The titanium centers in complexes **9** and **10** remain as Ti(IV). Apparently, the oxo ligand renders the Ti(IV) center to be more resistant to reduction. This modification partially address the issue #3, vide supra, and represents one step in the right direction in the rational design of the fully reversible hydrogen storage media based on Ti.

Another change that occurs in these oxide containing complexes is that both complexes **9** and **10** are now more thermally robust than $NaTi(BH_4)_4{\cdot}DME$. Clearly, the introduction of the oxide ligand stabilizes the complexes and alleviates the issue #1, vide supra.

As can be seen from Table 18, the yield of complex **10** was moderate (40-50%). This is because the reaction in DME produced roughly a 50:50 DME soluble and insoluble composition, as shown in the scheme below. The soluble half was the DME-containing salt, $NaOTi(BH_4)_3{\cdot}DME$. The insoluble part, on the other hand, was DME-free but co-precipitates with the by-product NaCl, which was also insoluble in DME. It is not clear if the DME-free products were neutral $OTi(BH_4)_2$ or ionic $NaOTi(BH_4)_3$ or a combination of both. Thus, this was yet another sign of solvate-free yet thermally

robust complex being formed as a result of incorporating an oxide ligand. So far, the DME-free products have not been tested since the issue of their separation from NaCl has not been resolved.

Table 18: Comparison of reaction products w/ $NaBH_4$.

	$TiCl_4DME$	$O[TiCl_3DME]_2$	$[OTiCl_2DME]_x$
O/Ti ratio	0	0.5	1.0
Isolated products w/ $NaBH_4$	$NaTi(BH_4)_4DME$	$Na_2O[Ti(BH_4)_4DME]_2$ **9**	$[NaOTi(BH_4)_3DME]_x$ **10**
Isolated yields	>95%	70-80%	40-50%
Oxidation state of Ti	Ti(III)	Ti(IV)	Ti(IV)
Stable at 25°C	No	Yes	Yes

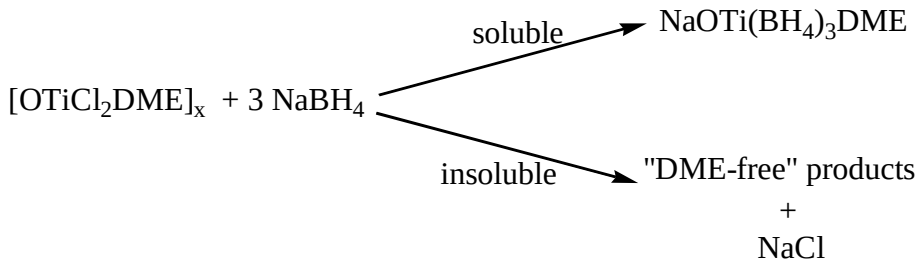

The complexes **9** and **10** were tested for both hydrogen discharge and recharge reactions. They both discharged hydrogen around 80°C. Unfortunately, however, we have not found conditions up to 100°C / 1000 psi in which hydrogen uptake is observed.

5.10 Solution Based Processing Conclusions

During the duration of the program we have synthesized seven novel organometallic complexes as possible reversible hydrogen storage candidates. In addition, three new oxy titanium precursors were also synthesized, including the anhydrous $OTiCl_2$ as an interesting alternative dopant to $TiCl_3$ commonly used. All of the new complexes discharge hydrogen at very mild temperatures, although none of them show full reversibility. A number of new concepts have been demonstrated, especially in the use of a coordinating ligand. Thus, ammonia, ethylenediamine, and DME have been used to stabilize the BH_4^- complexes of Ti and Zr. On the other hand, NH_3 and NMe_3 appear to destabilize $Mg(BH_4)_2$ allowing it to release hydrogen at a much lower temperature. The latter is in our opinion particularly noteworthy and should be pursued further.

6 Molten State Processing

6.1 Overview

The unique Molten State Processing (MSP) technique was developed and applied at the Savannah River National Laboratory (SRNL) to provide a wider range of temperatures and pressures in the search for novel storage compounds. These conditions promote high atomic mobility, in some cases enabling liquid state mixing of substitutional species and possible alteration of mixed metal alanate and other hydride stoichiometry. The SRNL MSP approach produces operating conditions that allow materials to interact and combine, leading to a higher potential for successful fusion over traditional ball milling and chemical processing techniques. In addition to the formation of new complexes, the process was found to enhance kinetics.

Structural characterization and physical property analyses were employed to identify newly synthesized complex hydride phases. X-ray diffraction and PCT system testing were the primary methods. The MSP apparatus developed is shown in Figure 86, with the central component being a high pressure, elevated temperature reactor vessel.

Figure 86: SRNL Molten State Processing apparatus.

Table 19 gives an overview for the majority of novel compositions examined in the effort. As previously discussed, the initial objective was to explore materials of the class, $Na_yM_{+ix}(AlH_4)_{y+ix}$ based on NaH, AlH_3, transition metal or rare earth (M) hydrides. The pure transition metal alanates (e.g. Ti, Fe, Mn, Cu, …etc.), are only stable at very low temperatures. In the latter stages of the project, novel borohydrides were also examined using both MSP as well as limited solvent assisted synthesis at SRNL. The processing and characterization of the various material systems are described in more detail in the sections below.

Table 19: Overview composition matrix for majority of MSP.

Compounds	mol ratios	prep cond	MSP cond	BM Results	MSP Results
MgCl2:LiBH4	1:2	Spex BM 60 min THF		$Mg(BH_4)_2(THF)_3$	
MgB2:LiBH4	1:2	Spex BM 60 min THF		Extremely hard material stuck To vial walls	
MgB2:H2 100 psi	1:~0.1	Frit BM 60 min		SM + Mg, MgO,(both in SM) NiCrFe (rxn w/SS vessel)	
MgB2:LiBH4:H2 100 psi	3:1:~0.1	Frit BM 114 min		SM + NiCrFe (rxn w/ss vessel)	
MgB2:H2 100 psi	1:~0.1	Frit BM 114 min		SM + NiCrFe (rxn w/ss vessel)	
NaAlH4:LiAlH4:Cr	1:1:1	Spex BM 60 min	170-4500-2h	SM + Al	LiNa2AlH6, NaAlH4, Al, Cr, NaH?
NaAlH4:LiAlH4:Mn	1:1:1	Spex BM 60 min	190-4500-2h	SM + Al	LiNa2AlH6, Al, Mn, NaH?
NaAlH4:LiAlH4:Mn	1:1:1	Spex BM 60 min	170-4500-2h	SM + Al	LiNa2AlH6, Al, Mn, NaH?
NaAlH4:LiAlH4:MgH2:VHx	1:1:1:1	Spex BM 60 min	170-4500-2h	SM + Al	VH0.81, LiAlH4, MgH2, Al, LiAn2AlH6, NaMgH3
NaAlH4:LiAlH4:MgH2:Cr	1:1:1:1	Spex BM 60 min	170-4500-2h	SM + Al	MgH2, Al, LiAn2AlH6, NaMgH3, Cr, Al, NaH?
NaAlH4:LiAlH4:MgH2:Cr	1:1:1:1	Spex BM 60 min	60-4500-3h	SM + Al	SM + Al, Li3AlH6
NaAlH4:LiAlH4:MgH2:Cr	1:1:1:1	cold ball mill	60-4500-3h	SM	SM + Al, Li3AlH6
NaAlH4:LiAlH4:MgH2:Cr	1:1:1:2	Spex BM 60 min		SM + Al	
NaAlH4:LiAlH4:MgH2:Cr	1:1:1:4	Spex BM 60 min		NaAlH4, MgH2, Cr, Al, Li3AlH6	
NaAlH4:LiAlH4:MgH2:Cr	1:1:2:2	Spex BM 60 min		SM + Al	
NaAlH4:LiAlH4:MgH2:Cr	1:1:2:1	Spex BM 60 min		SM + Al	
NaAlH4:LiAlH4:MgH2:Mn	1:1:1:1	Spex BM 60 min	170-4500-2h	MnH0.07!, NaAlH4, MgH2, LiAlH4, Al	MgH2, Al, LiAn2AlH6, NaMgH3, Mn, Al, NaH?
NaAlH4:VHx	1:1	Spex BM 60 min	190-4500-2h	n/a - outgasses	
NaAlH4:Cr	1:1	Spex BM 60 min	190-4500-2h	SM	Na3AlH6, NaAlH4, Cr
NaAlH4:Mn	1:1	Spex BM 60 min	190-4500-2h	SM	SM + Na3AlH6
LiAlH4:VHx	1:1	Spex BM 60 min			
LiAlH4:Cr	1:1	Spex BM 60 min	170C 2h	SM + Al	SM + Al, Li3AlH6
LiAlH4:Mn	1:1	Spex BM 60 min		SM + Al	Mn, Al
LiAlH4:KH:TiCl3	1:2:0.04	BM 40 min		LiAlH4, KAlH4, K3AlH6	KAlH4, K3AlH6, KCl
LiAlH4:MgH2:TiCl3	1:1:0.04	BM 40 min		MgH2, Li3AlH6, Al, LiCl, Mg	MgH2, Al, LiCl
LiAlH4:CaH2:TiCl3	1:1:0.04	BM 40 min		SM, Li3AlH6, Al	CaH2, Al, LiCl, LiH
LiAlH4:Mg2NiH4	1:1			MgH2, Mg2NiH, Mg2NiH0.3, Al1.1Ni0.8	
NaAlH4:Mg2NiH4	1:1			SM, NaMgH3, Mg2NiH0.3	
NaAlH4:Mg2NiH4:TiCl3	1:1:0.04	mortar pestle		SM, MgH2, Mg2NiH0.3	
NaAlH4:Mg2NiH4:TiCl3	1:1:0.04	BM 40 min		SM, Al, NaMgH3, Mg2NiH0.26	
Mg2NiH4:NaH	1:1.2	mortar pestle		SM, MgH2, Mg2NiH.26	
Mg2NiH4:LiH	1:9.9	BM 40 min		SM, MgH2, Mg2NiH.26	

6.2 Na_2LiAlH_6

Initial MSP development and application focused on the synthesis of known alanate compounds including Na_2LiAlH_6. Temperature Programmed Desorption (TPD) studies were conducted to assess hydrogen desorption kinetics of the MSP synthesized materials.

A stoichiometric mix of $NaAlH_4$ and LiH designed to produce Na_2LiAlH_6 was prepared and placed in the high temperature \ pressure cell. After holding at 3000 psi H_2 pressure and 190°C for ~1 hour, XRD analysis was performed on the material, with the pattern shown below in Figure 87. The desired compound, Na_2LiAlH_6 was identified by comparison to library spectra (orange lines), along with residual starting materials.

$$NaH + LiH + NaAlH_4 \rightarrow Na_2LiAlH_6$$

The XRD peaks showed slight shifts indicating that perhaps the product was Li-rich.

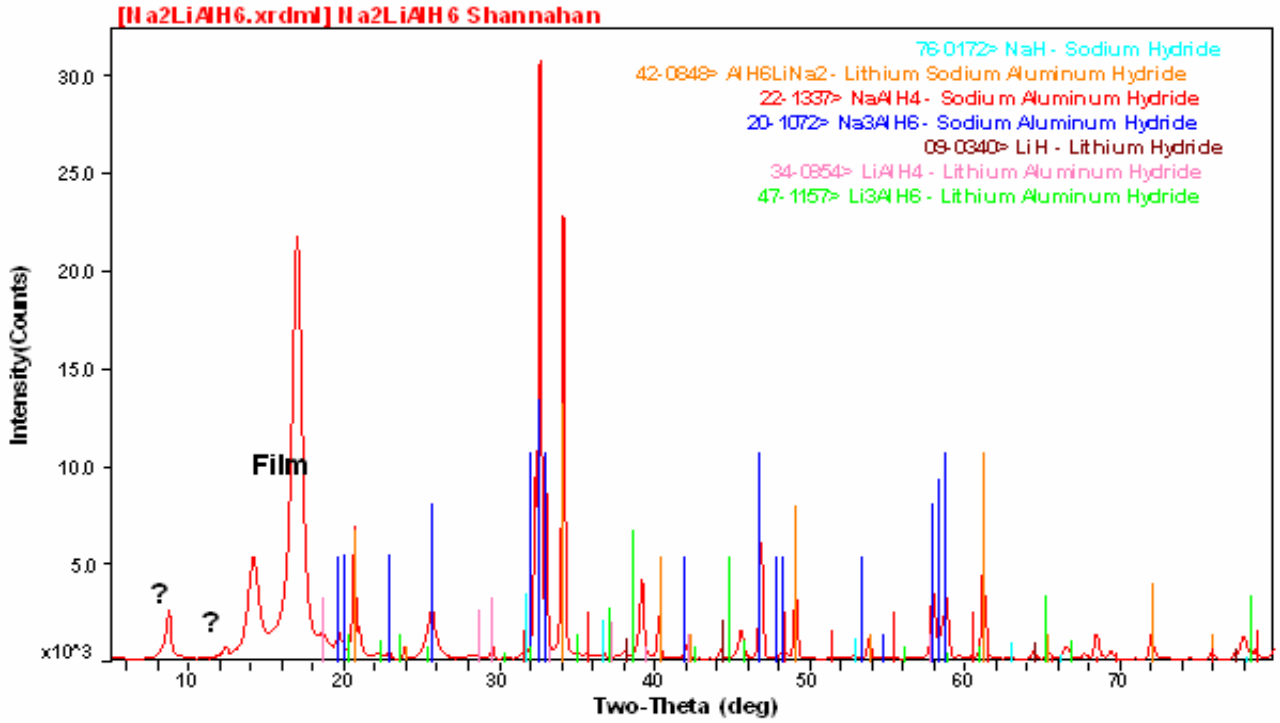

Figure 87: XRD results of MSP $NaAlH_4$/LiH indicating the presence of Na_2LiAlH_6.

A second attempt was made with the melt held at temperature for ~5 hours. A mixture was obtained which was still only partially enriched in Na_2LiAlH_4. A TPD experiment was performed at a temperature ramp rate of 5°C/min. As can be seen in Figure 88**,** the material begins to dehydrogenate at ~175°C.

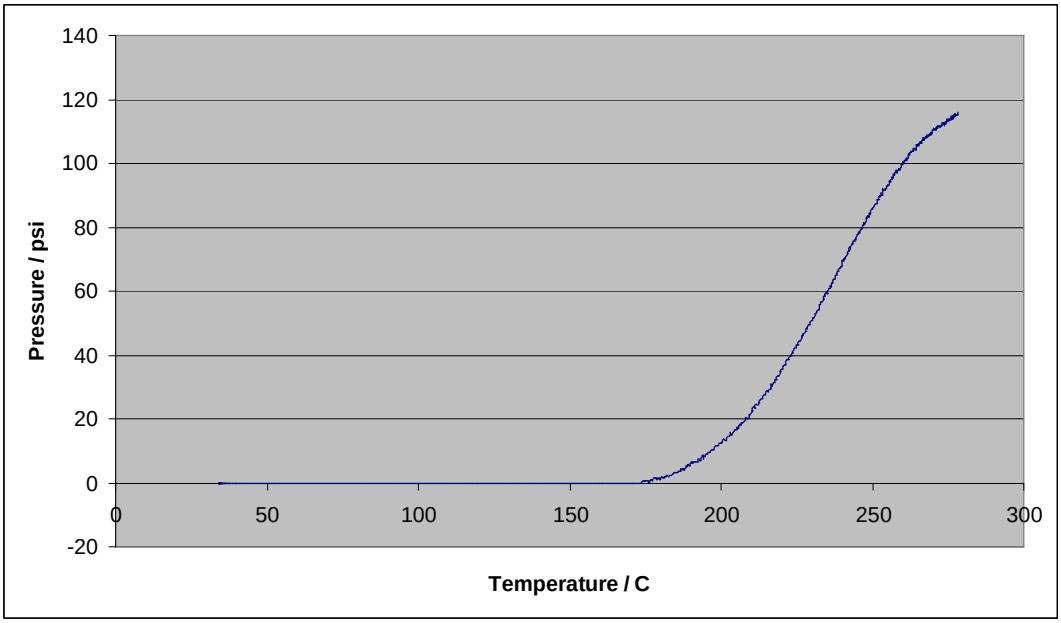

Figure 88: TPD results for $NaAlH_4$/LiH MSP material.

6.3 Catalyzed $NaAlH_4$

Additional efforts were conducted to produce a composite complex hydride similar to that formed through standard practice with conventional metal hydrides. Titanium hydride (TiH_2) was mixed with $NaAlH_4$ and melt processed. The first attempt used uncatalysed $NaAlH_4$ and ball-milled TiH_2. The chemicals were ball-milled and then processed at 190°C and 3,000 psi for 2 hours. A TPD run was made on this material up to 270°C which showed that no pressure producing gas evolved, and the XRD of the desorbed material showed sodium hydride, titanium hydride, traces of Na_3AlH_6, aluminum, and possibly traces of aluminum hydride and Ti_2O_3 as seen in Figure 89. Thus, the material had desorbed during the melt processing.

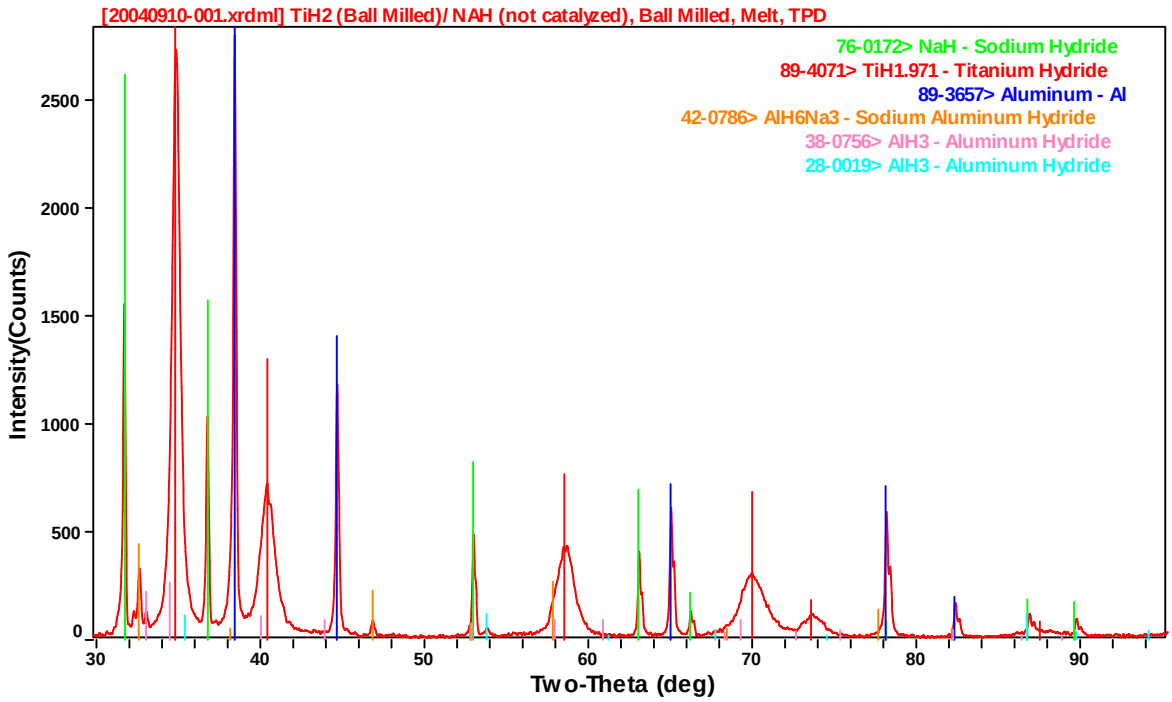

Figure 89: XRD results following processing of NaAlH4/TiCl3 at 190°C/3kpsi/2hrs.

A second attempt used a ball-milled mixture of titanium-butoxide catalyzed $NaAlH_4$ and ball-milled TiH_2. It also was heated for 2 hours at 190°C and 3,000 psi. Initially the sample was cooled to room temperature, with final cooling to ~-40°C with dry ice while still at 3,000 psi in order to retain any metastable compounds which may have formed. The pressure was removed and the material allowed to return to room temperature. No pressure rise was observed during heating to ambient temperature, indicating that no metastable phases dehydrided. The XRD results of this melt processed material showed TiH_2, NaH, Al, and traces of $NaAlH_4$ and Na_3AlH_6. A subsequent TPD to ~300°C showed no pressure increase, similarly indicating that no significant desorption had occurred.

In a third attempt to melt process TiH_2 and $NaAlH_4$, excess aluminum was added. All chemicals were hand-milled only in this experiment. The mixture was melted at 190°C and 3,000 psi for 2 hours; then the pressure was increased at temperature to 4,900 psi and held for 2 hours. The XRD of this material showed only NaH, Al, and TiH_2. A subsequent TPD produced no pressure.

The conclusion from these experiments is that the TiH_2 is a very efficient decomposition catalyst, as the melt processing did not produce substantial quantities of hydrogenated alanates. The possible detection of alane in the first set of experiments (Figure 89, ≈ 52 deg.) is intriguing.

6.4 MgH_2 / $NaAlH_4$ and Mg_2NiH_4 / $NaAlH_4$

Additional MSP synthesis experiments were conducted on combinations of MgH_2, Mg_2NiH_4 and $NaAlH_4$. Four mixtures of MgH_2 / $NaAlH_4$ and two mixtures of Mg_2NiH_4 / $NaAlH_4$ were prepared and examined. The four MgH_2 : $NaAlH_4$ mixtures had a mole ratio of ~4.4:1 with the addition of ~0.7 mole % $TiCl_3$. The two mixtures of Mg_2NiH_4 : $NaAlH_4$ were prepared with a mole ratio of 1:1. $TiCl_3$

was added in an effort to catalyze the hydrogenation and dehydrogenation steps. Three processing techniques were used to combine the powders: Hand Mixed (HM), Hand Shaken (HS) and Ball Milled (BM). Hand Shaken refers to hand shaking the starting materials in a ball mill vial with no balls, and Ball Milling was conducted in a SPEX mill for one hour. Melt processing was conducted at 150°C and 200 bar for 2 hours.

Table 20 and Table 21 give the trial identifiers, the molar ratios of MgH_2 / $NaAlH_4$ and Mg_2NiH_4 / $NaAlH_4$ respectively, the mole % of $TiCl_3$, the processing methods and the resulting XRD pattern Figure numbers.

Table 20: Summary of MgH_2/ $NaAlH_4$ compositions. HM = Hand Mixed; HS = Hand Shaken; BM = Ball Milled.

Trial	MgH_2 / $NaAlH_4$	m/%$TiCl_3$	Processing	XRD
1a	4.3	0.70	HM	Figure 90
2a	4.4	0.76	HS	Figure 91
3a	4.4	0.83	HS	Figure 92
4a	4.2	0.85	BM	Figure 93

Table 21: Summary of Mg_2NiH_4 / $NaAlH_4$ experiments.

Trial	Mg_2NiH_4 / $NaAlH_4$	%$TiCl_3$	Milling	XRD(Milled)	XRD(Melt)
1b	1.0	4.2	HS	Figure 97	-
2b	1.0	4.2	BM	Figure 98	Figure 99

TPD experiments consisted of heating the specimen at a rate of 5°C/min from ambient to 250°C with continuous pressure monitoring in a modified Sievert's apparatus.

All four XRD patterns of the MgH_2 / $NaAlH_4$ compositions (Figure 90 to Figure 93) show strong reflections for Al, MgH_2, and $NaMgH_3$, and moderately strong reflections for Mg and NaCl, with the exception of Figure 93 where the Mg reflection is weak. Semi-quantitative analysis was not available to further analyze the relative proportions of the products.

TPD experiments were conducted on compositions 3a and 4a and were followed by rehydrogenation attempts. Mixture 3a had a subsequent TPD run conducted, whereupon it was removed and sampled for XRD (Figure 95). This XRD showed strong reflections for MgH_2, Al, and $NaMgH_3$ and moderate reflections for Mg and NaCl. The first TPD to 220°C produced no noticeable hydrogen release above baseline, and the second TPD to 245°C likewise showed no significant H_2 release.

The XRD pattern of the ball milled and melted product from mixture 4a in Figure 93 showed traces of $NaAlH_4$. Subsequent TPD gave limited H_2 evolution starting at ~80°C and continuing up to 280°C. This limited hydrogen release was most likely due to remaining $NaAlH_4$. This sample was removed, rehydrogenated and analyzed again in the XRD of Figure 96. These results showed strong reflections for Al, MgH_2, and $NaMgH_3$, moderate reflections for Mg and NaCl, and possibly a trace of $NaAlH_4$.

Mixture 1b had strong $NaAlH_4$ reflections and moderate Mg_2NiH_4, $Mg_2NiH_{0.3}$, and MgH_2 reflections. This material had two TPD-rehydrogenation cycles performed on it, followed by a final XRD as shown in Figure 100. The TPD experiments did not produce any significant hydrogen desorption (the first went to 250°C, the second to 260°C). The XRD results showed strong reflections for Al, $NaMgH_3$, Mg_2NiH_4, $Mg_2NiH_{0.3}$, and NaCl, with moderate reflections for $NaAlH_4$ and MgH_2.

Mixture 2b's XRD taken after ball milling 40 minutes showed strong reflections for $NaAlH_4$, Al, MgH_2, Mg, Mg_2NiH_4, and NaCl, with moderate peaks for Na_3AlH_6. The XRD of the melted product had strong reflections for $NaMgH_3$, Mg_2NiH_4, and NaCl, with moderate peaks for $NiAl_3$ alloy, and possibly a trace of MgH_2 present. Mixture 2b also had two TPD experiments conducted on it (separated by a rehydrogenation), but was sampled for XRD after the second TPD. The first TPD (to 230°C) produced an anomalous sharp desorption occurring over the rage 170-190°C. The second TPD to 240°C produced no desorption. The XRD after the second TPD is given in Figure 101.

In all cases, after the melt processing, the compound $NaMgH_3$ was detected in appreciable quantities. When examining the MgH_2 / $NaAlH_4$ mixtures, the other major products were Al and unreacted MgH_2, with moderate peaks observed for Mg and NaCl in most cases. When the Mg_2NiH_4 / $NaAlH_4$ mixtures were examined, the situation was somewhat more complicated as several Mg_2NiH_x compounds could be observed, along with Al, MgH_2 and $NaMgH_3$ as major products. In one experiment $NiAl_3$ was also observed.

The compound $NaMgH_3$ seems to be quite easy to form, showing up in almost all the XRDs obtained. However, it does not seem to evolve hydrogen at low temperatures (<~280°C). The XRDs from the Mg_2NiH_3 experiments are quite complicated and might mask several other minor compounds. The X-ray cross section of Mg and Ni are quite similar for the Cu K-alpha source in use, and this makes it difficult to distinguish the Mg compounds from Mg-Ni compounds. It is unclear at this point why the Mg_2NiH_3 / $NaAlH_4$ mixture 2b showed an anomalous TPD. The XRD of the melted mixture did show $NiAl_3$ alloy, which had not been observed before.

The various milling methods (hand, ball, none) do not seem to impact the results strongly. The melt processing step seems to equalize all the possible variations, which is, in part, the benefit of the melt processing method.

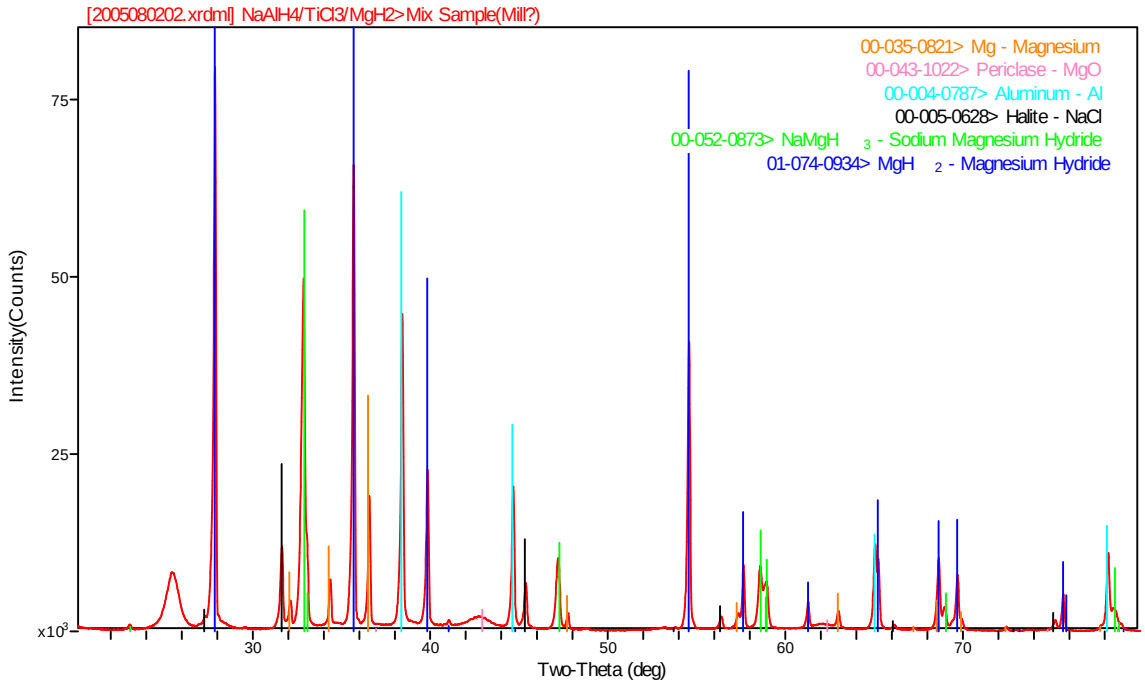

Figure 90: XRD analysis of Hand Mixed/MSP $MgH_2/NaAlH_4/TiCl_3$.

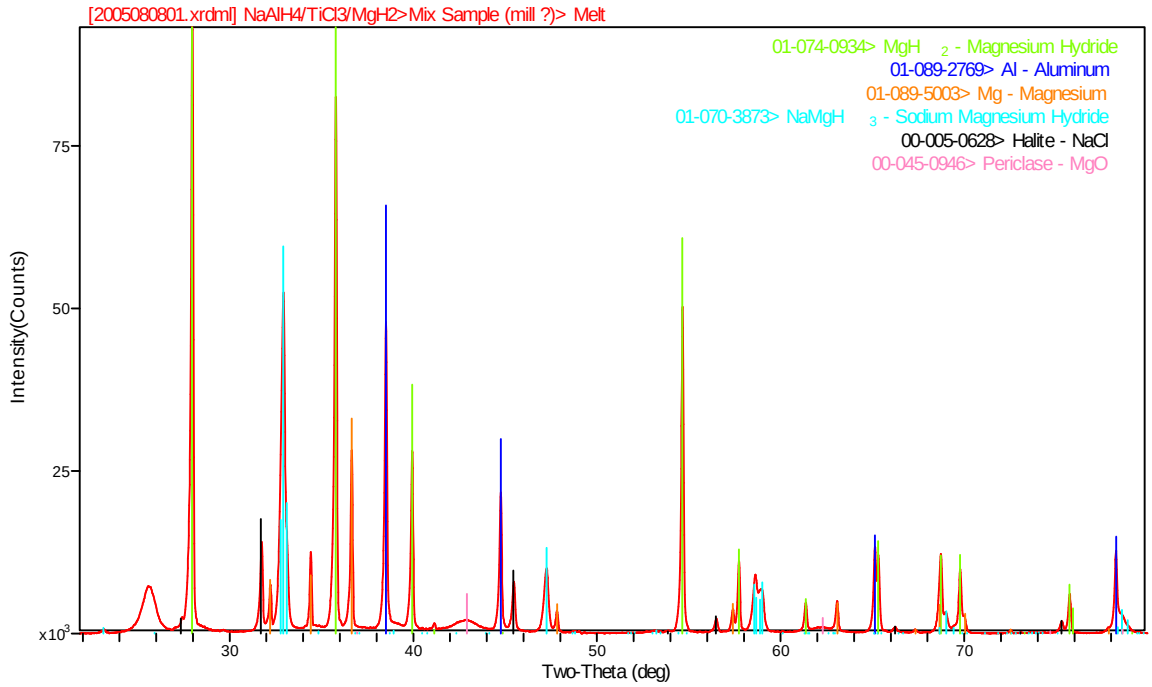

Figure 91: XRD Analysis of Hand Shaken/MSP $MgH_2/NaAlH_4/TiCl_3$.

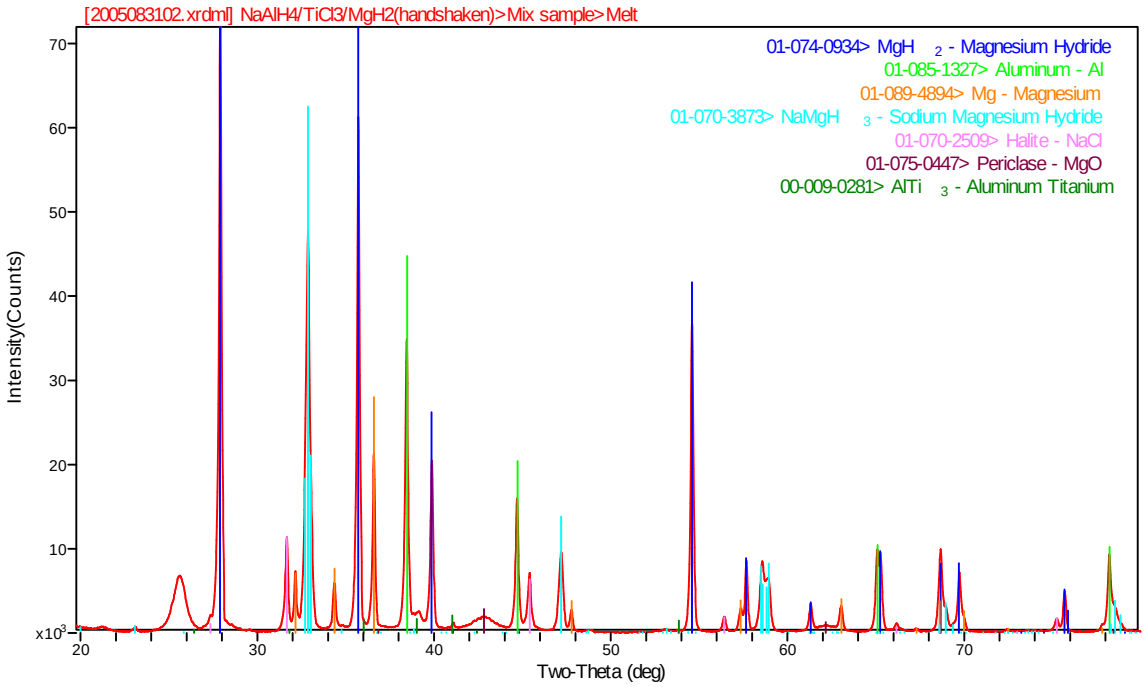

Figure 92 XRD Analysis of Hand Shaken/MSP $MgH_2/NaAlH_4/TiCl_3$.

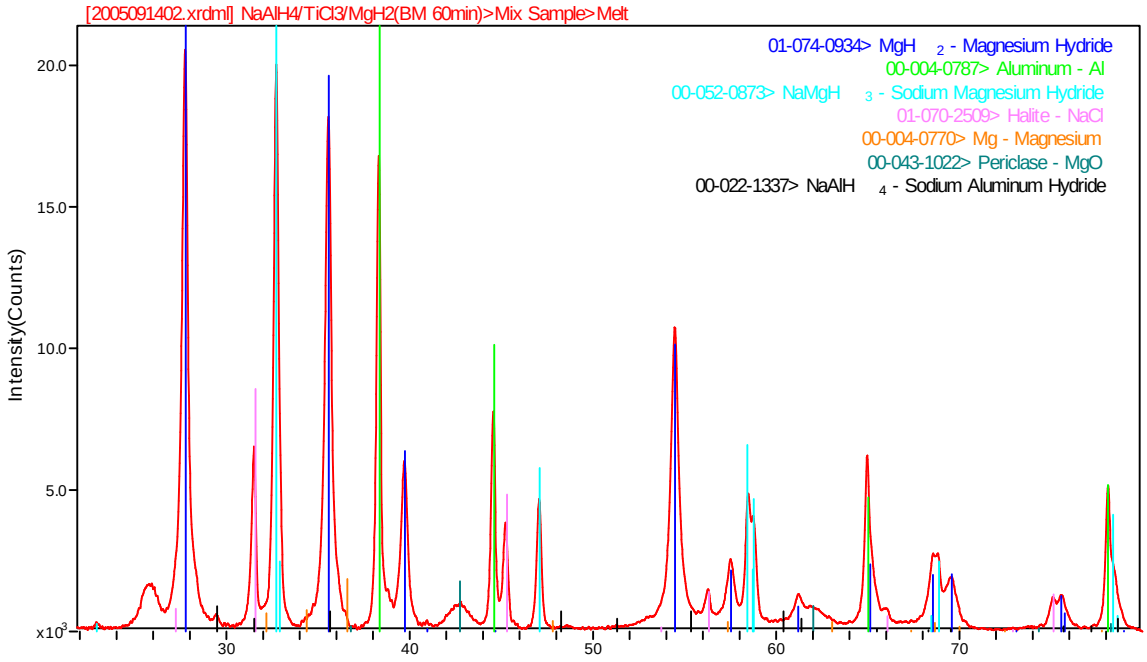

Figure 93 XRD Analysis of Ball Milled/MSP $MgH_2/NaAlH_4/TiCl_3$.

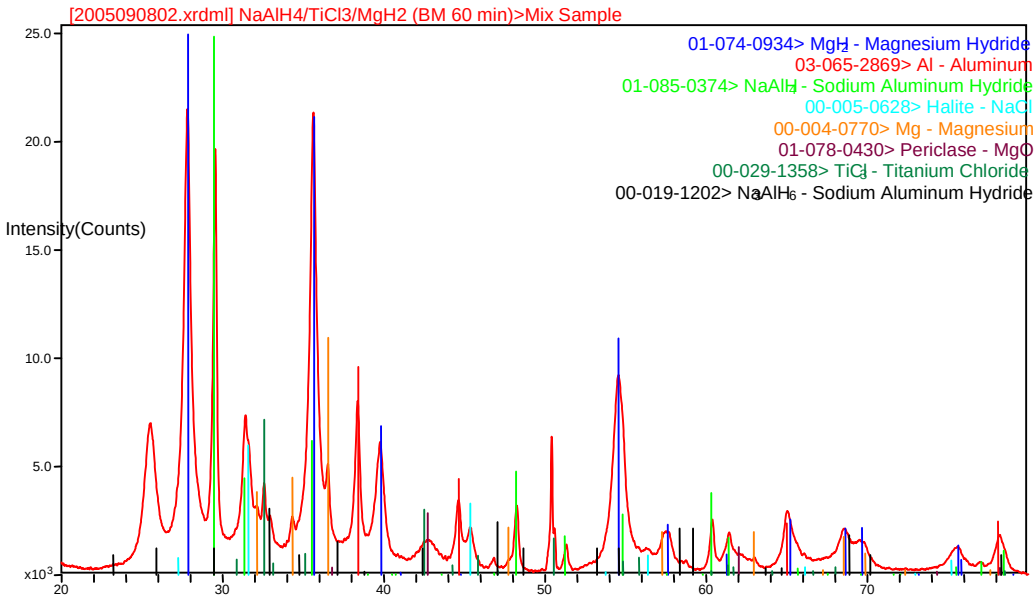

Figure 94: XRD analysis of ball milled only MgH_2 / $NaAlH_4$.

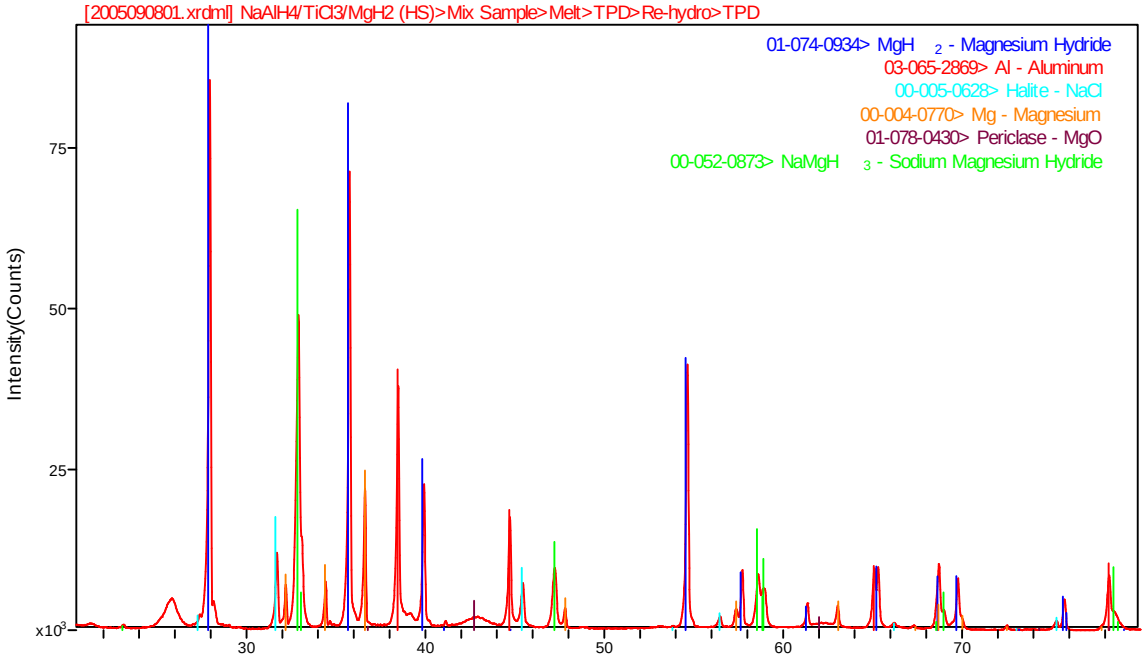

Figure 95 XRD analysis of mixture 3a after TPD run.

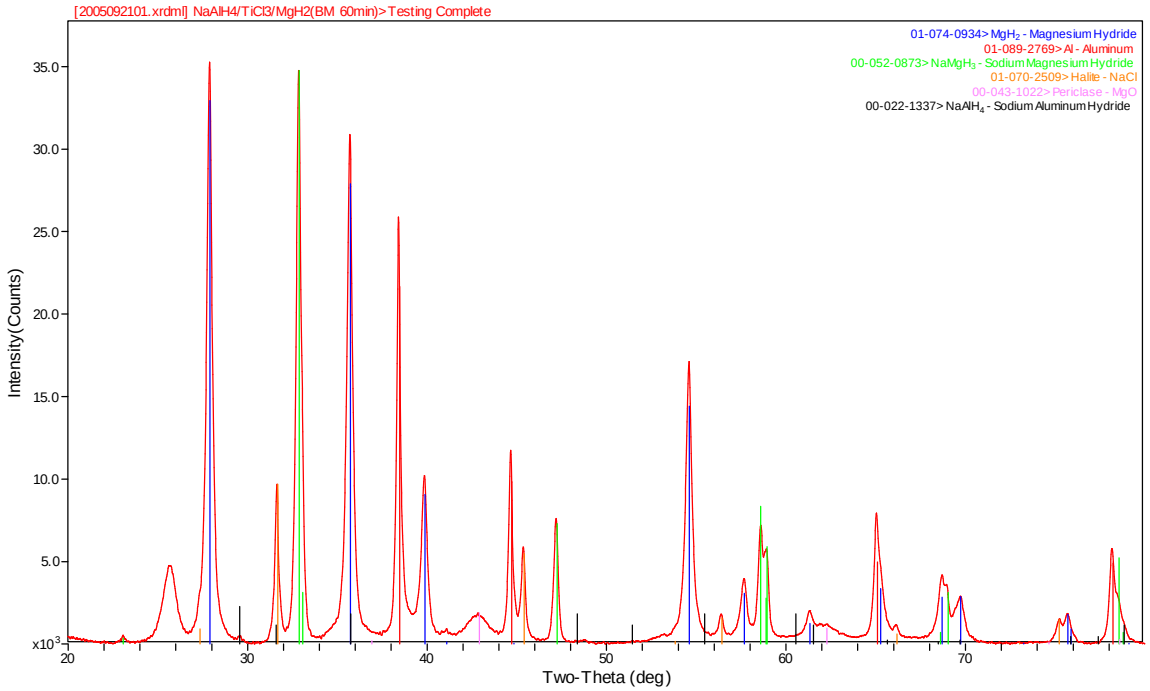

Figure 96: XRD analysis of mixture 4a after MSP, TPD and rehydrogenation.

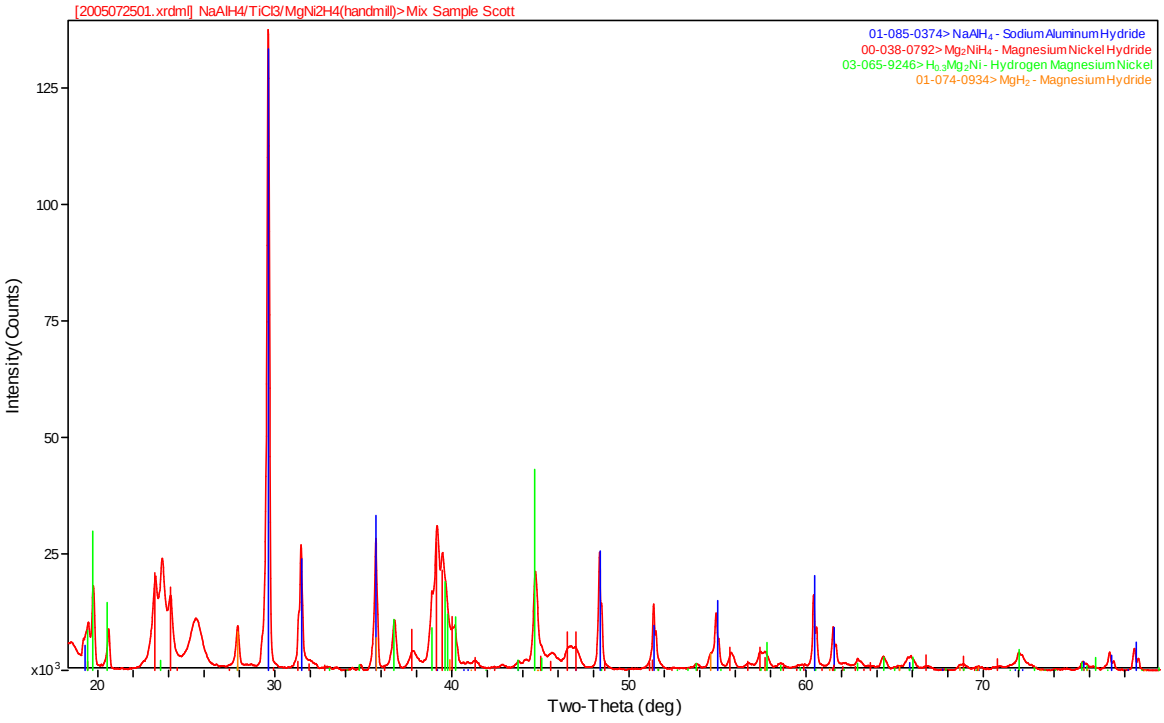

Figure 97: XRD analysis of Hand Mixed $Mg_2NiH_4/NaAlH_4$.

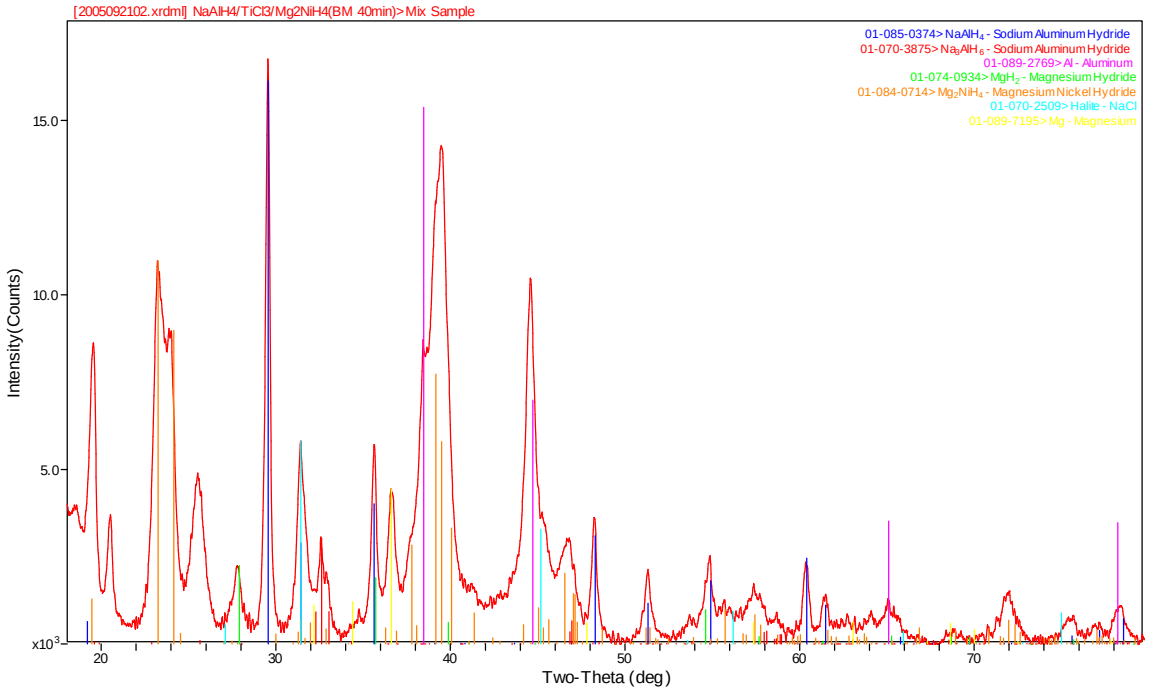

Figure 98: XRD Analysis of Ball Milled $Mg_2NiH_4/NaAlH_4$.

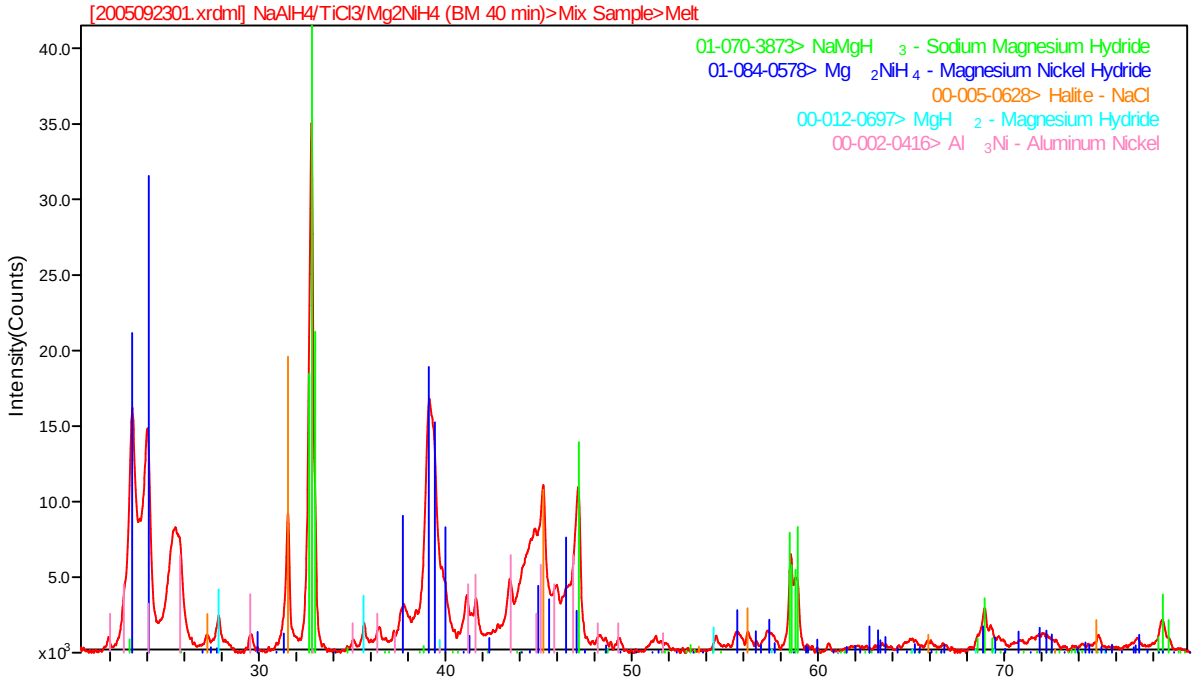

Figure 99: XRD analysis of Ball Milled / MSP $Mg_2NiH_4/NaAlH_4$.

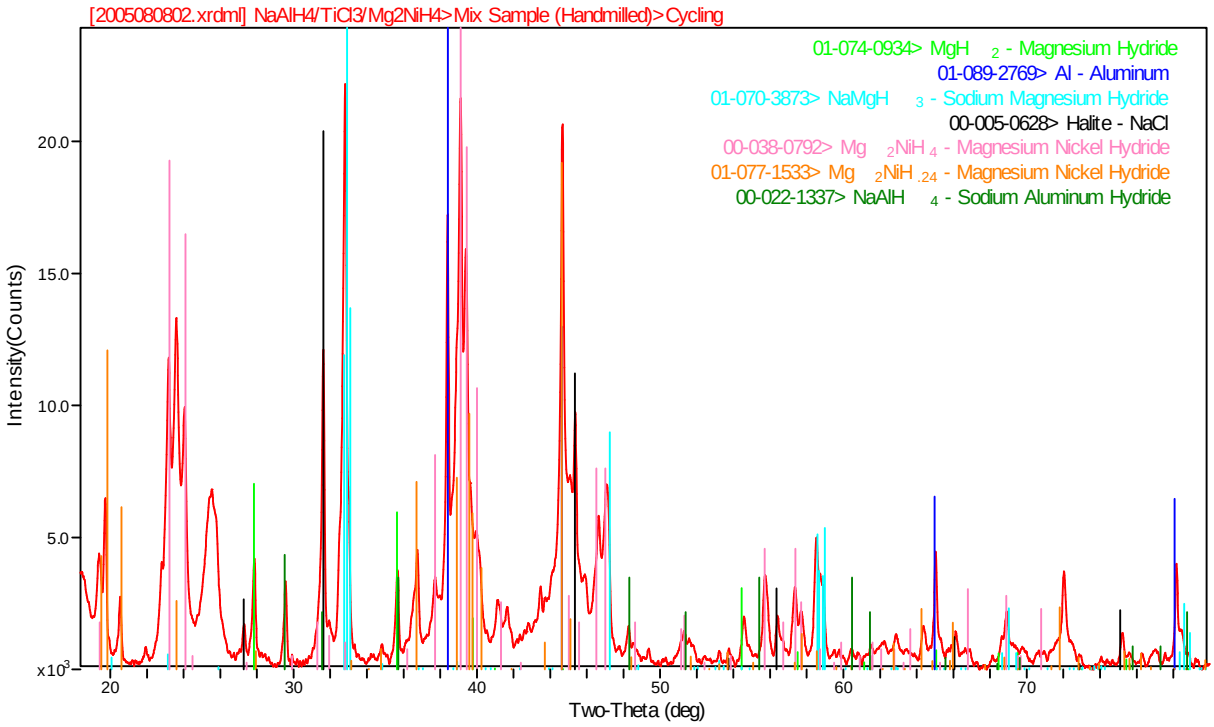

Figure 100: XRD analysis of mixture 1b after two dehydride/hydride cycles.

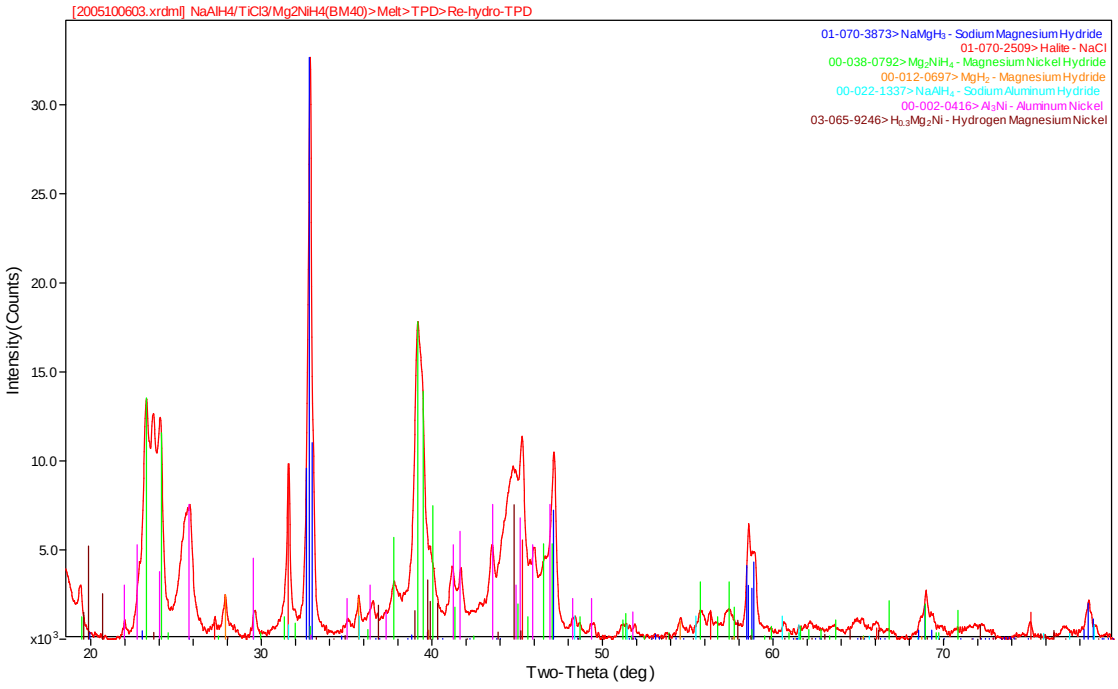

Figure 101: analysis of mixture 2b after two dehydride/hydride cycles.

6.5 *$NaAlH_4$ + MgH_2 + (TiH_2 or Fe)*

Sodium aluminum hydride reactions with the mixtures containing MgH_2 + TiH_2 and MgH_2 + Fe were studied. A nominal 1:1 molar mixture of MgH_2 and TiH_2 was prepared by SPEX milling for 60 minutes. An XRD of the mixture showed no reaction. A quantity of 1.430 grams of this mixture was combined with 1.012 grams of $NaAlH_4$ and 0.114 grams of $TiCl_3$, and ball milled for 40 minutes (Figure 102). The sample was melted and an XRD sample obtained (Figure 103). A 1.042 gram sample of the melt processed material was thermally desorbed with no change in composition observed (Figure 104).

A nominal 1:1 molar mixture of MgH_2 and Fe (Sigma-Aldrich 99.99+%) was prepared by placing 1.605 grams of MgH_2 (SRNL prep) and 3.415 grams of Fe into a ball mill vial using in this case only 4 balls (2 large, 2 small) vs. the normal 5 (2 large, 3 small) and ball milled for 60 minutes. A quantity of 1.004 grams of $NaAlH_4$, 0.114 grams of $TiCl_3$ and 1.530 grams of the MgH_2:Fe mixture were placed were ball milled for 40 minutes (Figure 105). The material was melted (Figure 106) and thermally desorbed, similarly showing little change in composition (Figure 107).

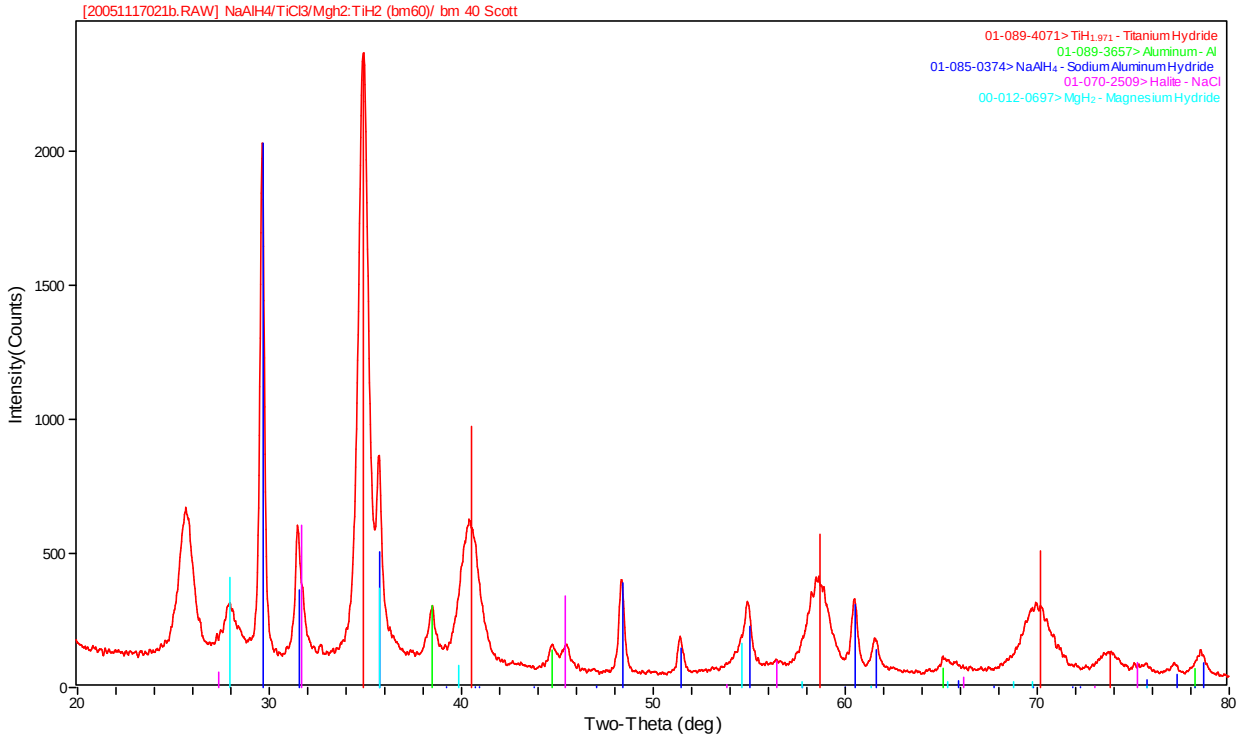

Figure 102: Ball milled $NaAlH_4$ / $TiCl_3$ / MgH_2 / TiH_2 mixture.

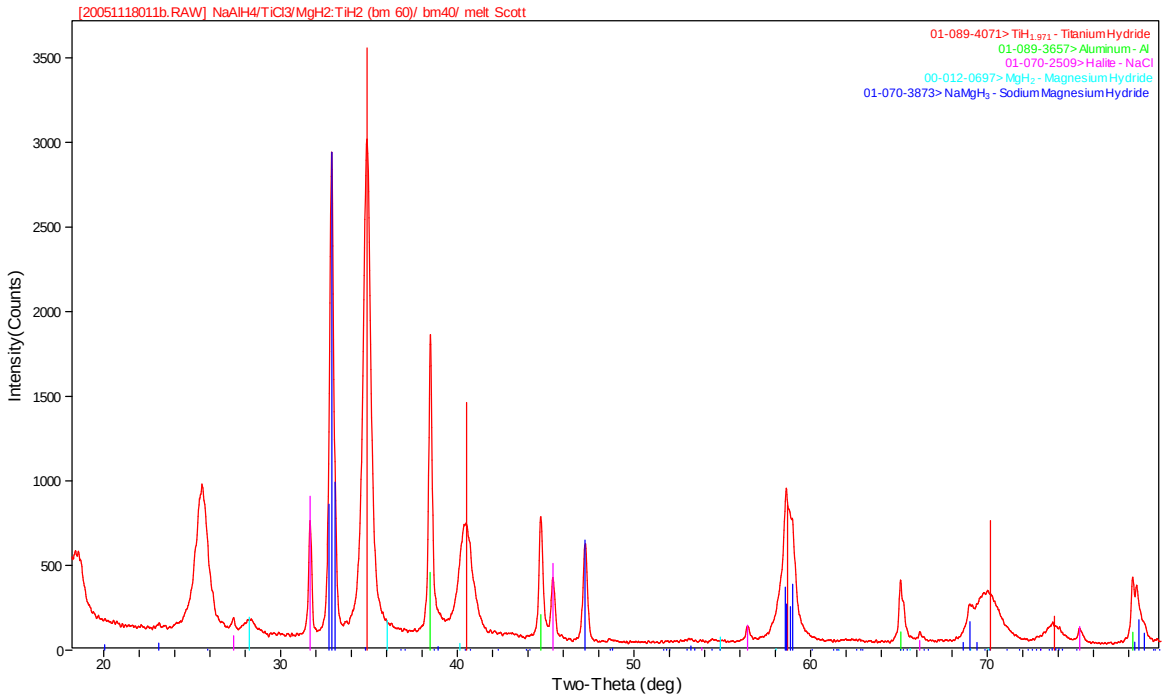

Figure 103: Melt processed $NaAlH_4$ / $TiCl_3$ / MgH_2 / TiH_2 mixture.

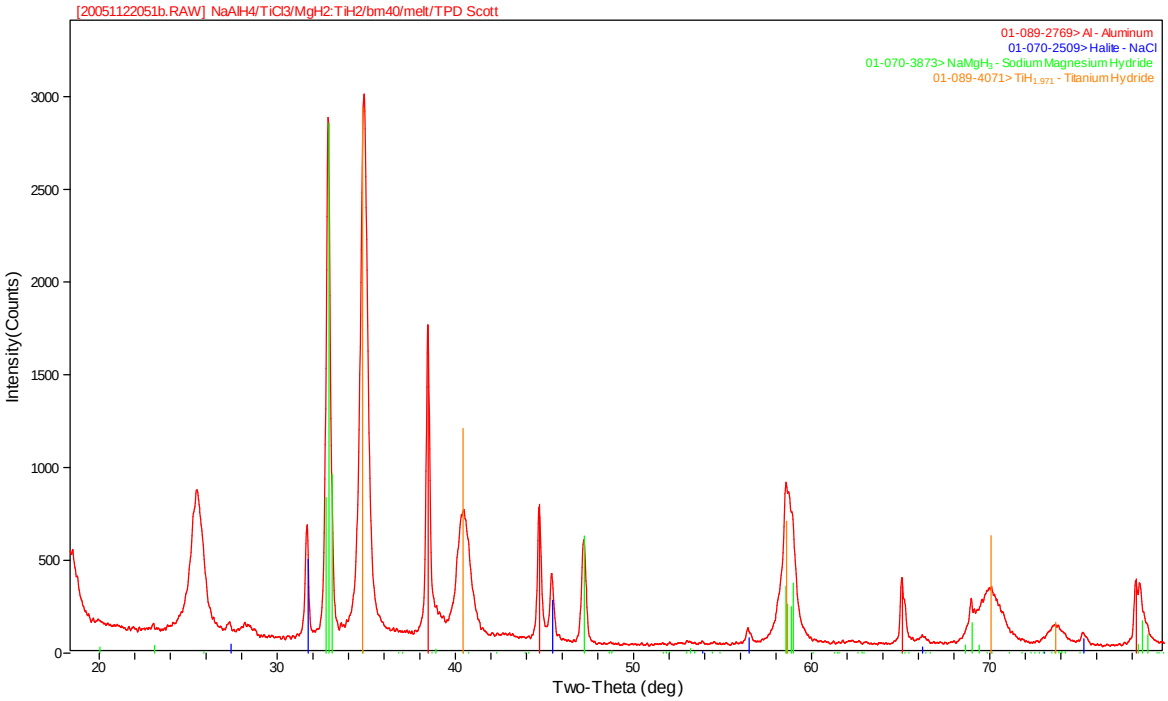

Figure 104: Desorbed melt processed $NaAlH_4$ / $TiCl_3$ / MgH_2 / TiH_2 mixture.

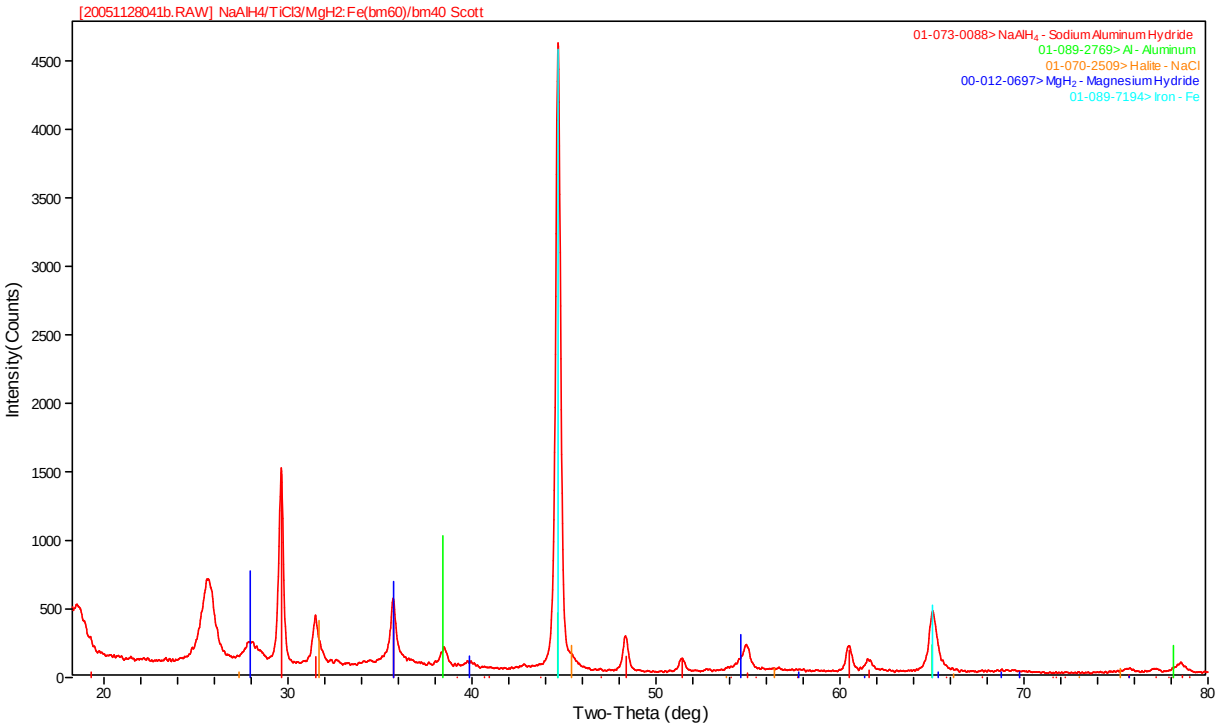

Figure 105: Ball milled $NaAlH_4$ / $TiCl_3$ / MgH_2 / Fe mixture.

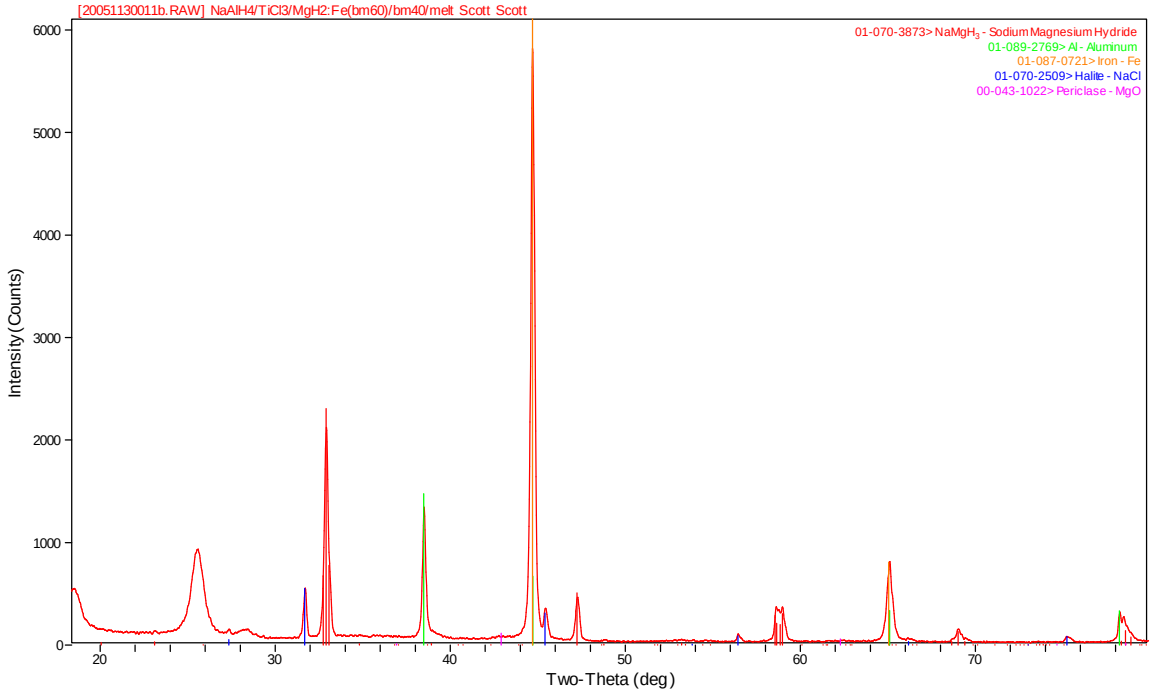

Figure 106: Melt processed $NaAlH_4$ / $TiCl_3$ / MgH_2 / Fe mixture.

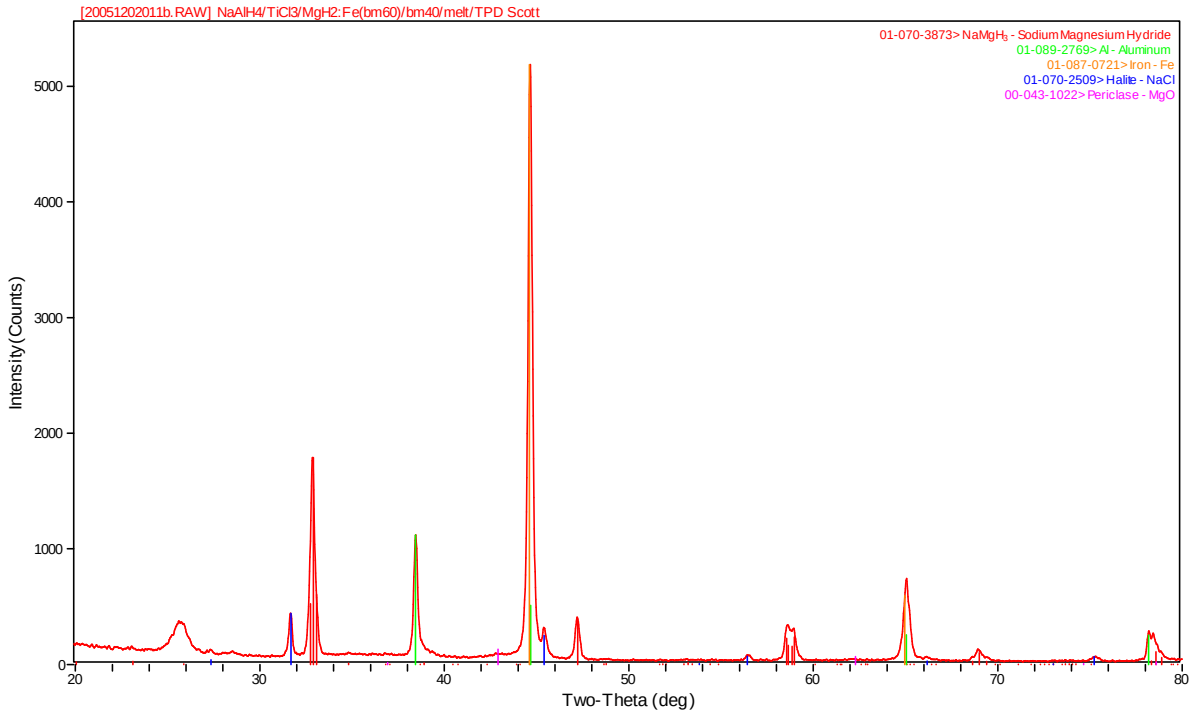

Figure 107: Desorbed melt processed $NaAlH_4$ / $TiCl_3$ / MgH_2 / Fe mixture.

6.6 NaH + (MgH_2 or Mg_2NiH_4)

Quantities of 1.420 grams of NaH and 1.576 grams of MgH_2 were ball milled for 60 minutes, which induced the formation of some $NaMgH_3$. This mixture was *not* melted and only a thermal desorption was conducted which produced little change in composition (Figure 108).

A mixture containing 0.531 grams of NaH and 2.046 grams of Mg_2NiH_4 (SRNL prep) was ball milled for 40 minutes (Figure 109). This mixture was *not* melt processed before a thermal desorption was conducted (Figure 110). During this TPD, a pressure of 75 psi developed at 320°C, which represents a minor desorption from the Mg_2NiH_4.

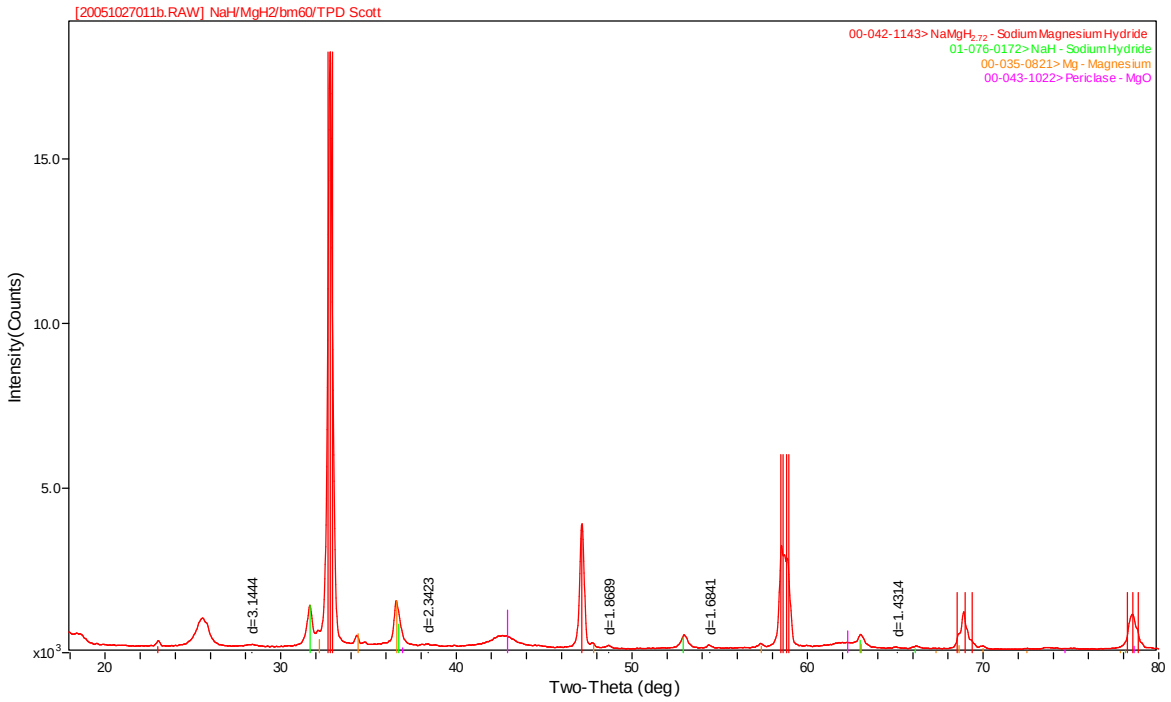

Figure 108: Ball milled and desorbed NaH / MgH_2 mixture.

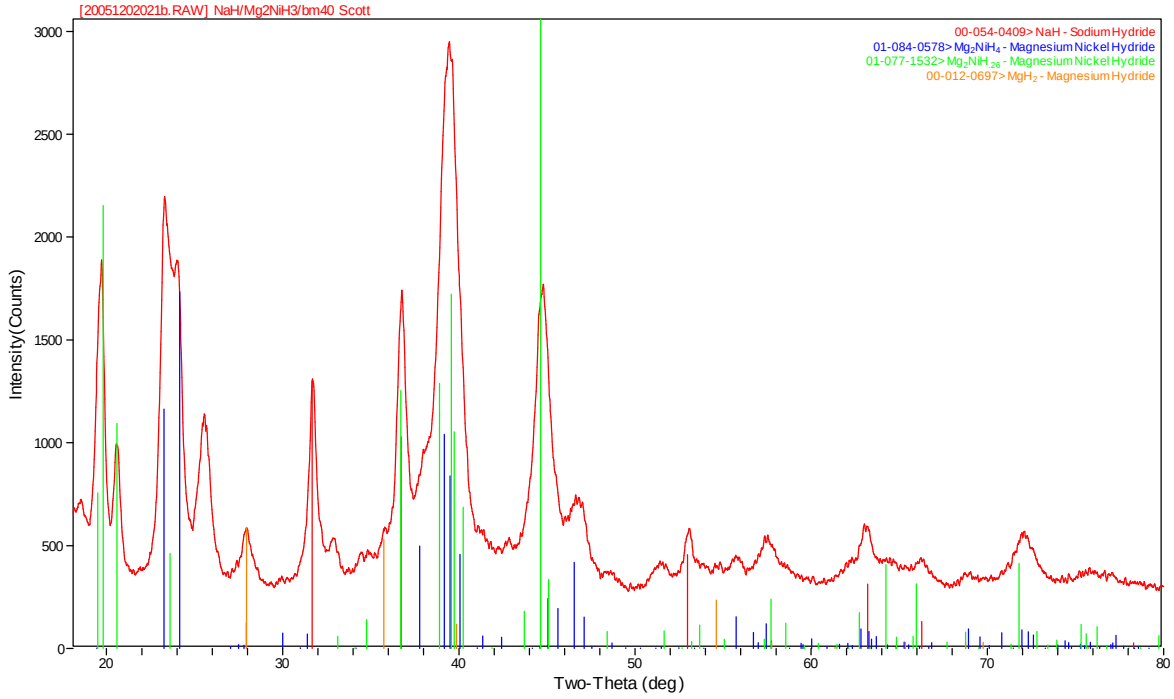

Figure 109: Ball milled NaH / Mg_2NH_4 mixture.

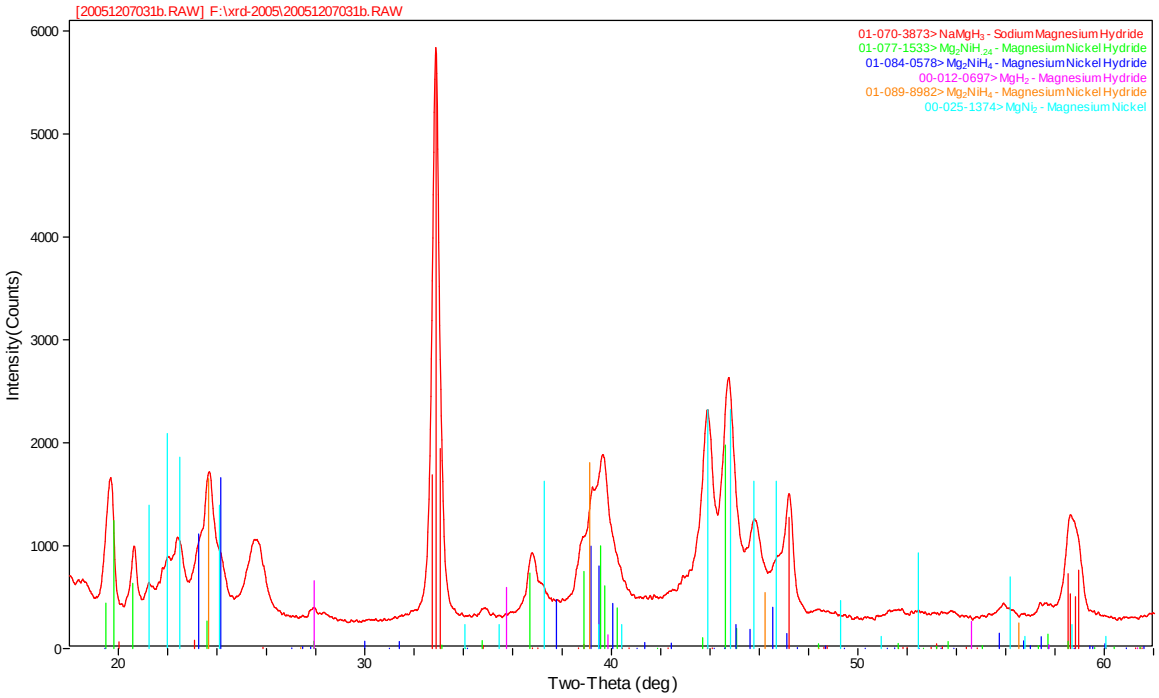

Figure 110: Desorbed NaH / Mg_2NH_4 mixture.

6.7 LiAlH4 + (KH or MgH_2 or CaH_2)

A combination of 0.712 grams of KH, 0.344 grams of $LiAlH_4$, and 0.052 grams of $TiCl_3$ was milled for 40 minutes (Figure 111). The XRD pattern for melt processing of this mixture is shown in Figure 112, indicating little change in composition from the as-mixed state.

In the first trial involving MgH_2, 0.684 grams of MgH_2, 0.967 grams of $LiAlH_4$, and 0.155 grams of $TiCl_3$ were milled for 40 minutes resulting in the XRD pattern of Figure 113. The mixture was melt processed, producing the partially altered XRD pattern of Figure 114 indicating decomposition of the lithium aluminum hexahydride.

A second trial involving a reduced proportion of MgH_2 contained 0.472 grams of MgH_2, 2.034 grams of $LiAlH_4$, and 0.330 grams of $TiCl_3$ which were similarly ball milled for 40 minutes (Figure 115). The mixture was melt processed (Figure 116), producing results similar to trial 1, and a thermal desorption run conducted to 275°C with no desorption related pressure rise occurring. This material was cooled under hydrogen pressure, initially at ~750 psi, to room temperature with no sign of uptake.

For the experiments involving CaH_2, 1.069 grams of CaH_2 (Sigma-Aldrich 99.9%), 0.961 grams of $LiAlH_4$, and 0.152 grams of $TiCl_3$ were ball milled for 40 minutes (Figure 117). The mixture was then melt processed with the resulting XRD pattern of Figure 118, indicating decomposition of the lithium aluminum hexahydride similar to the MgH_2 mixtures.

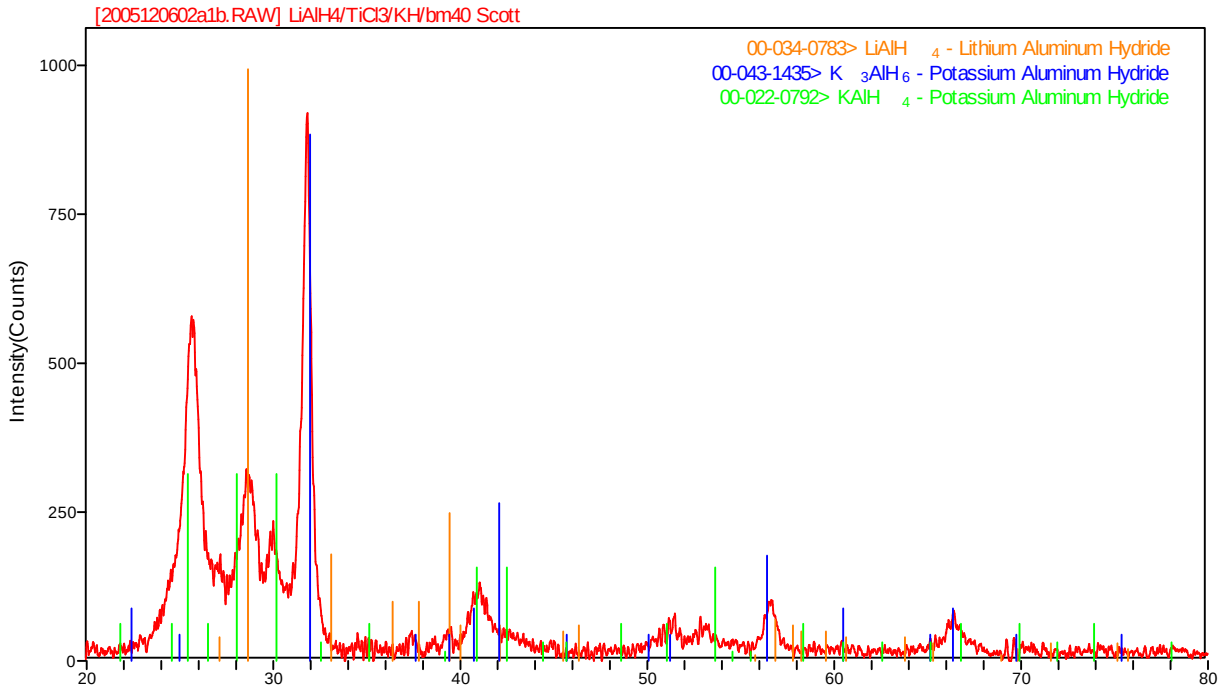

Figure 111: Ball milled $LiAlH_4$ / $TiCl_3$ / KH mixture.

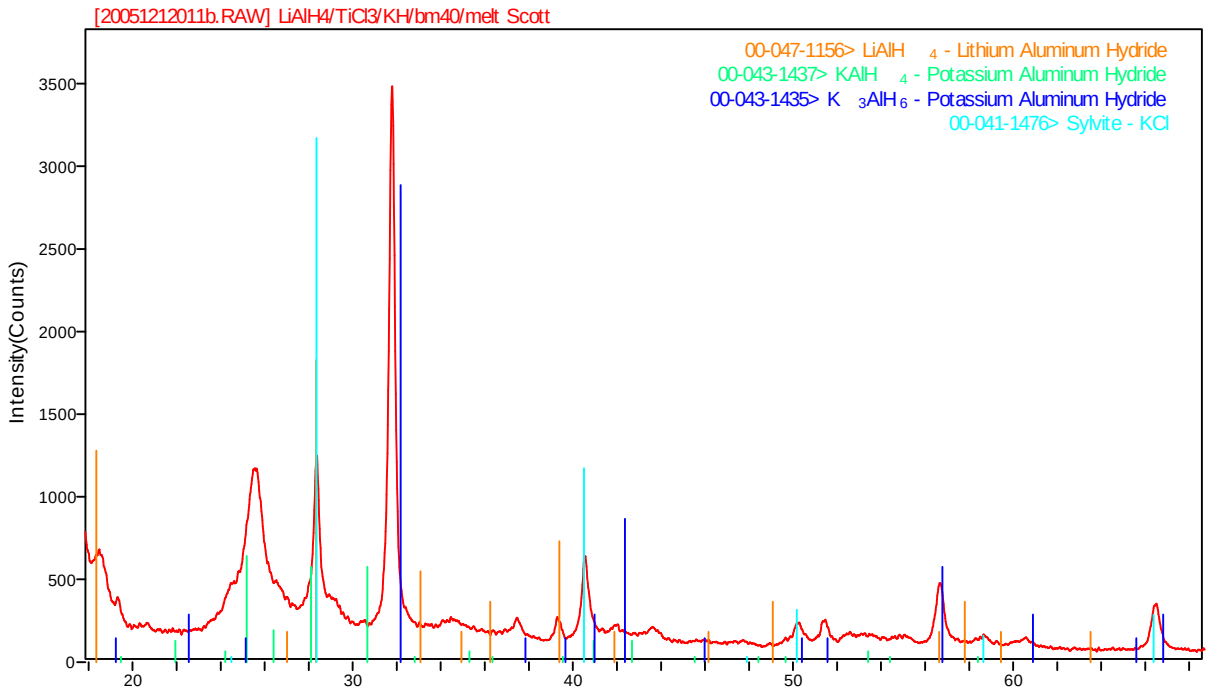

Figure 112: Melt processed $LiAlH_4$ / $TiCl_3$ / KH mixture.

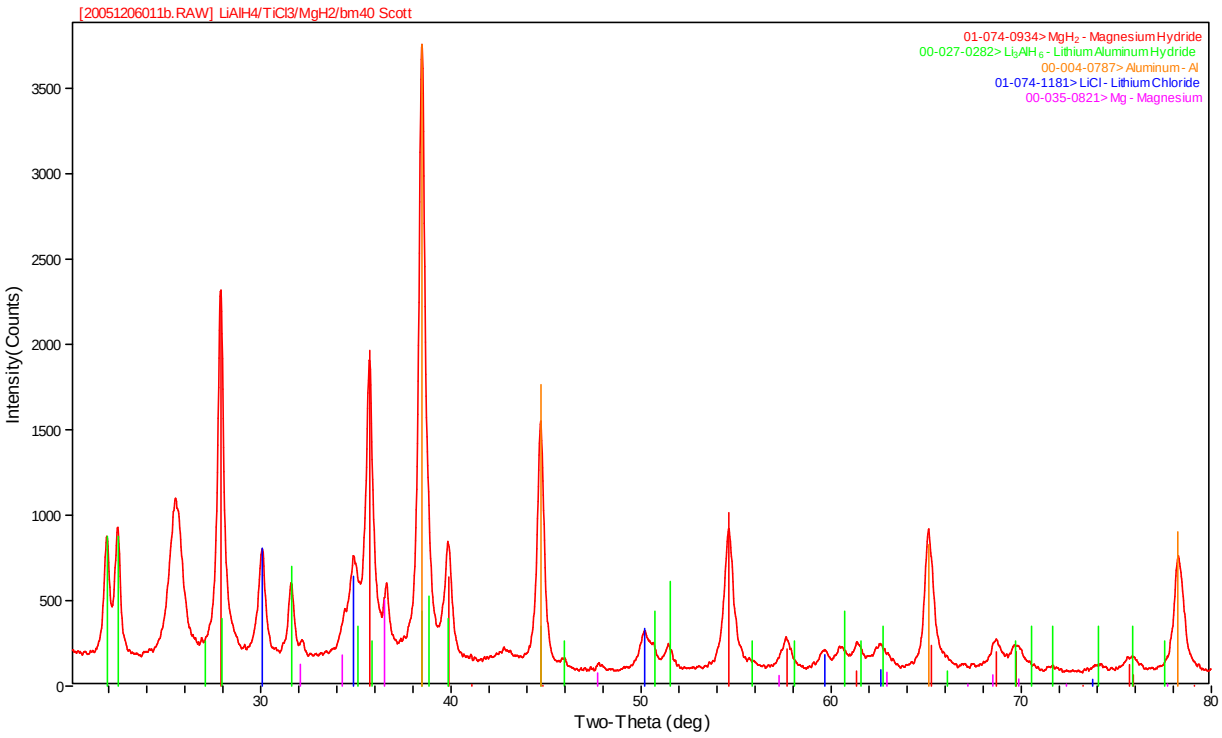

Figure 113: Ball milled $LiAlH_4$ / $TiCl_3$ / MgH_2 mixture – trial 1.

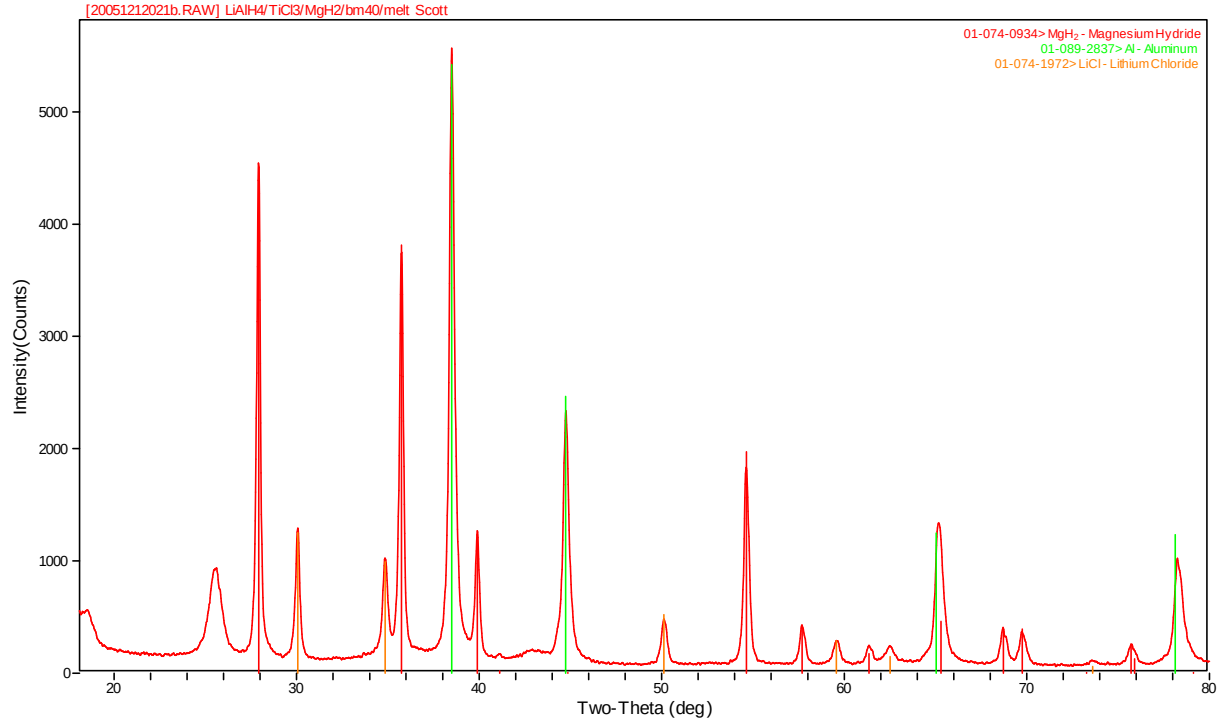

Figure 114: Melt processed $LiAlH_4$ / $TiCl_3$ / MgH_2 mixture – trial 1.

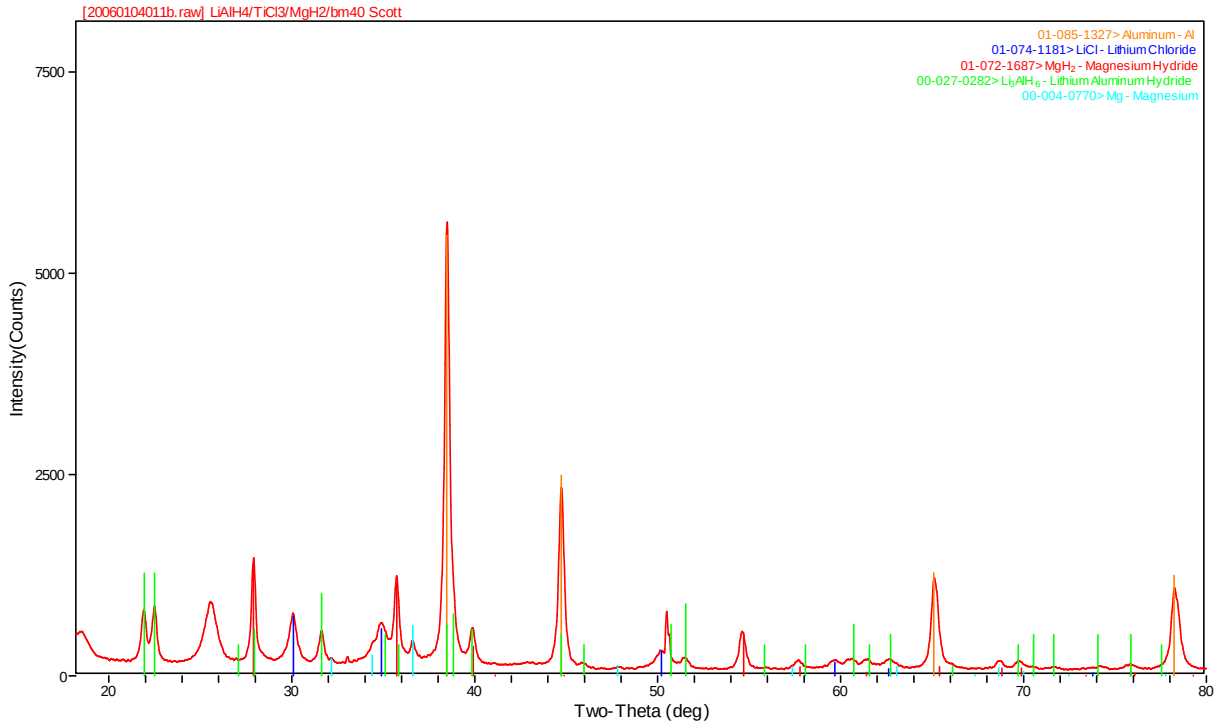

Figure 115: Ball milled $LiAlH_4$ / $TiCl_3$ / MgH_2 mixture – trial 2.

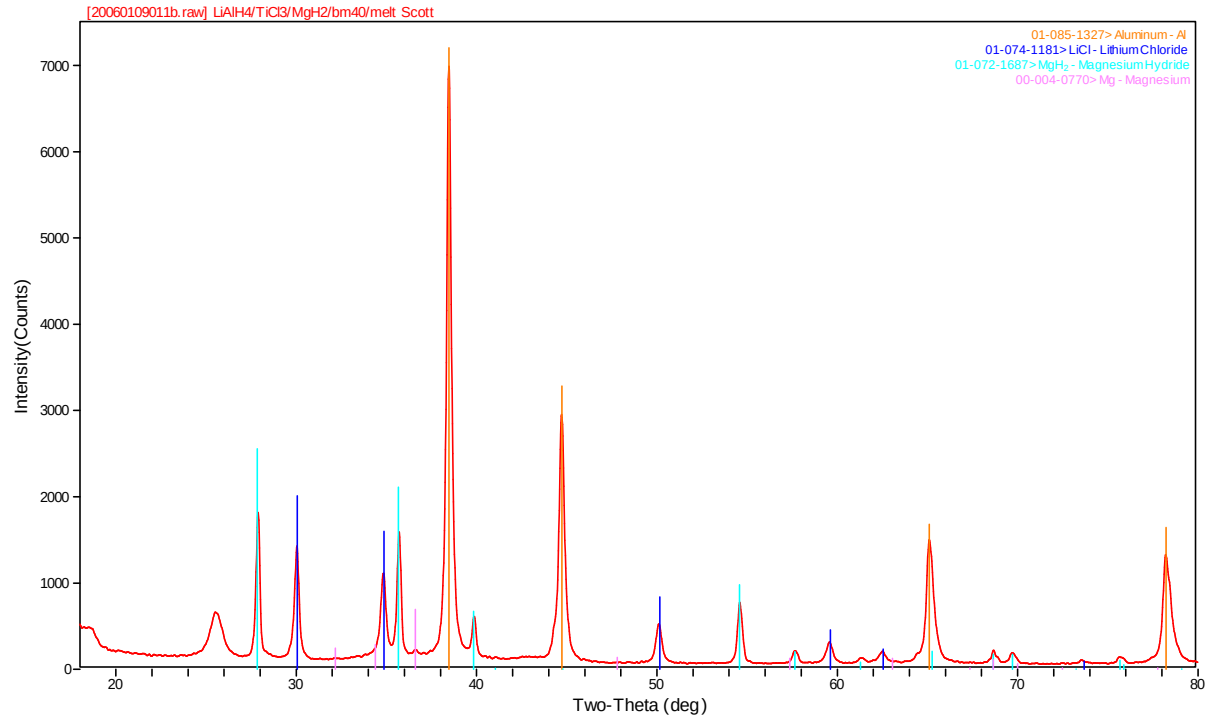

Figure 116: Melt processed $LiAlH_4$ / $TiCl_3$ / MgH_2 mixture – trial 2.

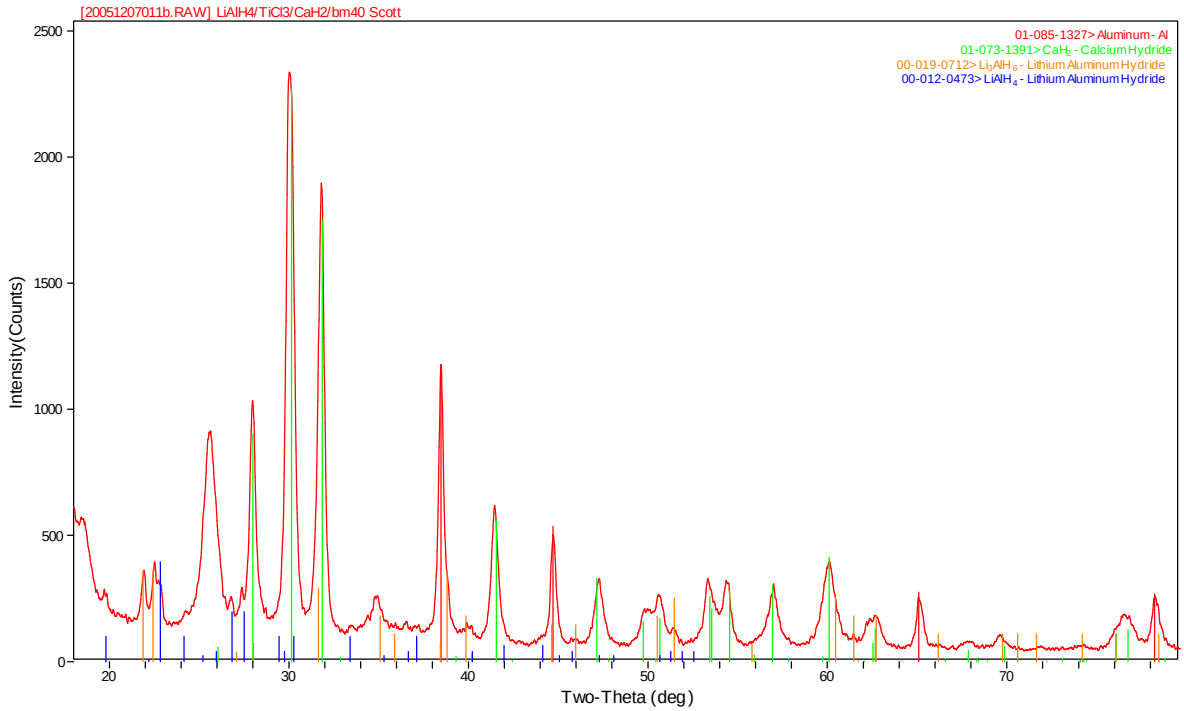

Figure 117: Ball milled $LiAlH_4$ / $TiCl_3$ / CaH_2 mixture.

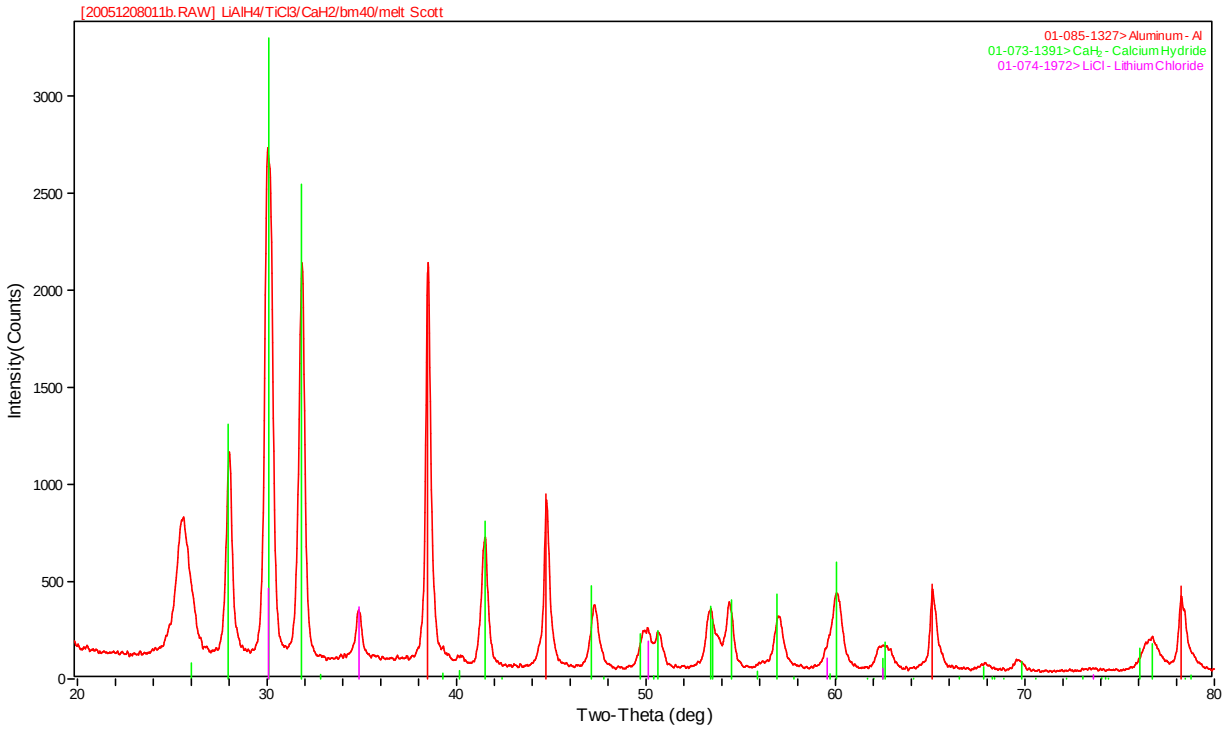

Figure 118: Melt processed $LiAlH_4$ / $TiCl_3$ / CaH_2 mixture.

6.8 Mixtures Involving Mn, Cr or V

Various binary (e.g. $NaAlH_4$:Cr 1:1 mol ratio), ternary (e.g. $NaAlH_4$:$LiAlH_4$:Cr 1:1:1 mol ratio) and quaternary (e.g. $NaAlH_4$:$LiAlH_4$:MgH_2:Cr 1:1:1:1 mol ratio) mixtures involving Mn, Cr or V were examined. For detailed composition descriptions, see Table 19. The mixtures were created by ball milling powders in a SPEX ball mill. These mixtures were then heated under ~4500 psi H_2 pressure in the MSP step. Below are sections for each transition metal element added to the mixture, followed by a general summary.

6.8.1 Mixtures of Mn:

The binary mixtures of Mn ball milled with either $NaAlH_4$ or $LiAlH_4$ yielded starting materials, and in the case of Li alanate, Al metal, presumably from the decomposition of $LiAlH_4$. When heated for MSP, the binary Na mixture produces Na_3AlH_6 in addition to the starting materials. The mixture with Li produces Mn and Al, while any Li species are amorphous as they do not show up in the XRD pattern. The ternary mixture of both alanates with Mn yields starting materials and Al with ball milling. Heating this mixture for MSP at 170°C or 190°C yields $LiNa_2AlH_6$, Mn, Al and possibly NaH. The quaternary mixture of both alanates, MgH_2 and Mn is interesting in that it yields $MnH_{0.07}$ with just ball milling, in addition to the non-Mn starting materials and Al. The H is assumed to originate with $LiAlH_4$ that decomposes with ball milling. When this mixture is heated for MSP, the $MnH_{0.07}$ decomposes leaving Mn, in addition to MgH_2, Al, $LiNa_2AlH_6$, $NaMgH_3$, and possibly NaH.

6.8.2 Mixtures of Cr:

The binary mixtures of Cr ball milled with $NaAlH_4$ or $LiAlH_4$ yield starting materials, and in the case of the Li alanate Al, suggesting that some of the $LiAlH_4$ has decomposed with ball milling. When heated for MSP, the sodium mixture yields starting materials and Na_3AlH_6. The binary mixture with Li forms starting materials, Al, and Li_3AlH_6 with the MSP reaction at 170°C. The ternary mixture of both alanates with Cr gives starting materials and Al with ball milling. The MSP products for this mixture are $LiNa_2AlH_6$, $NaAlH_4$, Al, Cr and possibly NaH. The quaternary mixture, which has MgH_2 in addition to the ternary mixture, forms starting materials and Al with ball milling. When heated, the mixture forms $NaMgH_3$, $LiNa_2AlH_6$, MgH_2, Cr, Al and possibly NaH.

For the quaternary mixture, which has $NaAlH_4$, $LiAlH_4$, and MgH_2, the ratio of starting materials away from the simple 1:1:1:1 mixture was explored. The Cr and the MgH_2 were varied to see if this would change the reaction. When the Cr content was doubled, regardless of the MgH_2 content, ball milling formed starting materials and Al. This mixture of products was also seen with the original Cr ratio of 1. When the 1:1:1:1 mixture is ball milled "cold" by cooling the vial every 10 minutes for a total of 60 minutes of milling, the decomposition of $LiAlH_4$ was prevented and only the starting materials (no Al) were seen in the XRD pattern as shown in Figure 119 below. This mixture was then melt processed at a low temperature of 60°C (usually done at 170°C or higher). The low temperature MSP method yields SM, Al, and Li_3AlH_6. The Na and Mg compounds do not react as they do with higher temperatures, confirming that the $LiAlH_4$ is the least stable hydride in the mixture. When the ratio of Cr is increased to 4, ball milling alone causes the $LiAlH_4$ to decompose completely, forming Al and Li_3AlH_6 in addition to the other 3 starting materials.

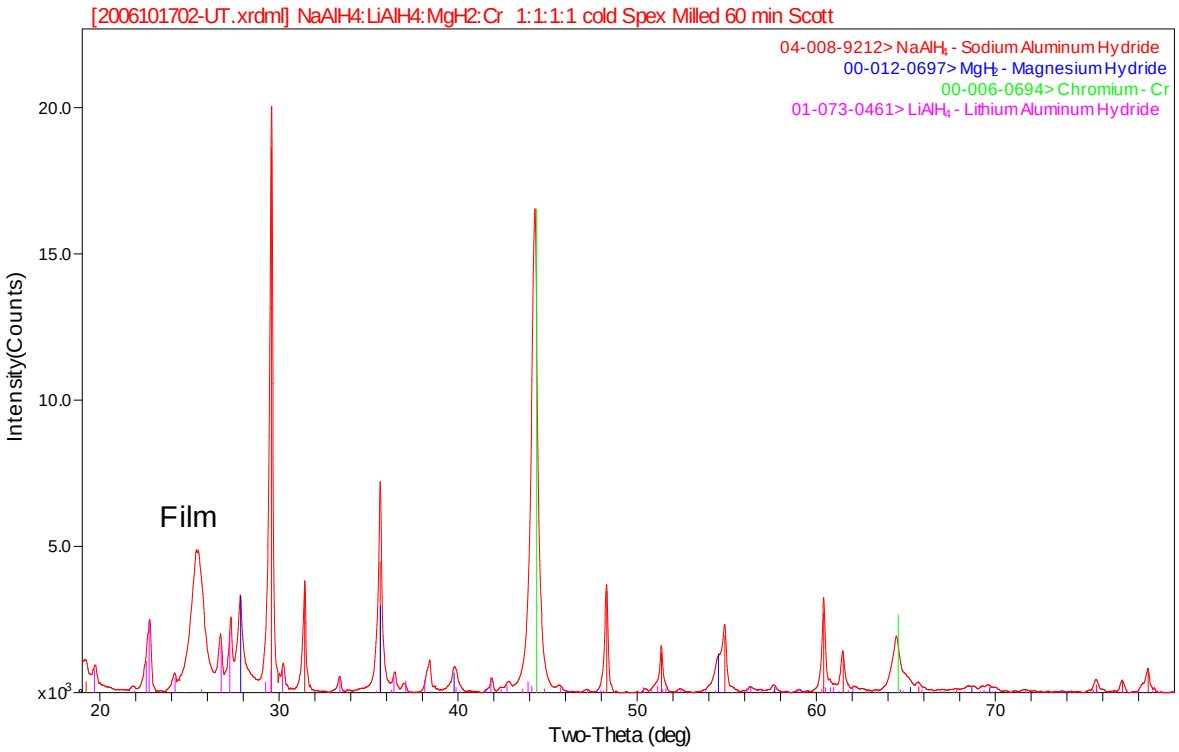

Figure 119: Ball milled $NaAlH_4$:$LiAlH_4$:MgH_2:Cr 1:1:1:4 with cooling.

6.8.3 Mixtures of VH_x:

Vanadium hydride is not commercially available. The hydride was synthesized at SRNL using V metal powder and a high pressure H_2 manifold. The powder was heated to 300°C with active vacuum, and 30 minute cycles of ~4000 psi H_2 were alternated with active vacuum for a total of 3-5 cycles. The material was cooled to room temperature under H_2 pressure. The newly synthesized material dehydrided slightly at room temperature, as seen by a pressure increase with time, so it was evacuated for ~30 minutes to remove residual gas. The material was evaluated by XRD, shown below in Figure 120.

The binary mixture of $NaAlH_4$ with $VH_{0.81}$ outgassed after ball milling, so XRD could not be performed. The quaternary mixture of $NaAlH_4$:$LiAlH_4$:MgH_2:$VH_{0.81}$ 1:1:1:1 forms starting materials and Al after ball milling. The MSP reaction of this mixture at 170°C results in the formation of starting materials $LiAlH_4$, MgH_2 and $VH_{0.81}$ in addition to Al, $LiNa_2AlH_6$ and $NaMgH_3$ as shown in Figure 121.

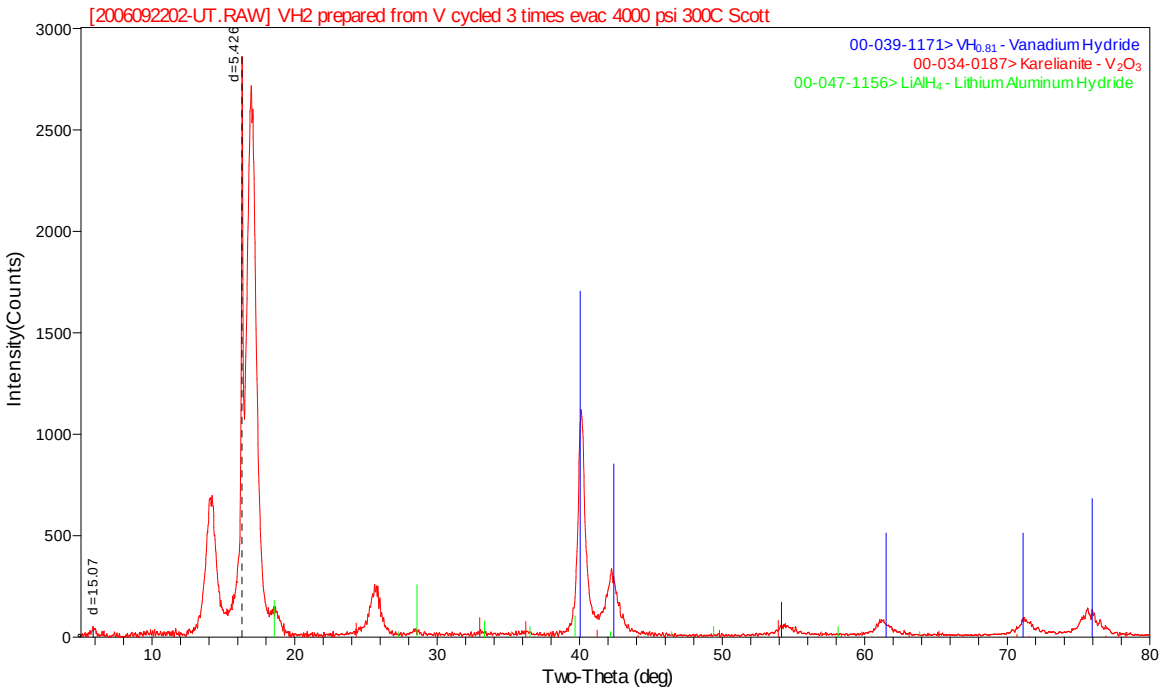

Figure 120: XRD pattern of $VH_{0.81}$ synthesized at SRNL.

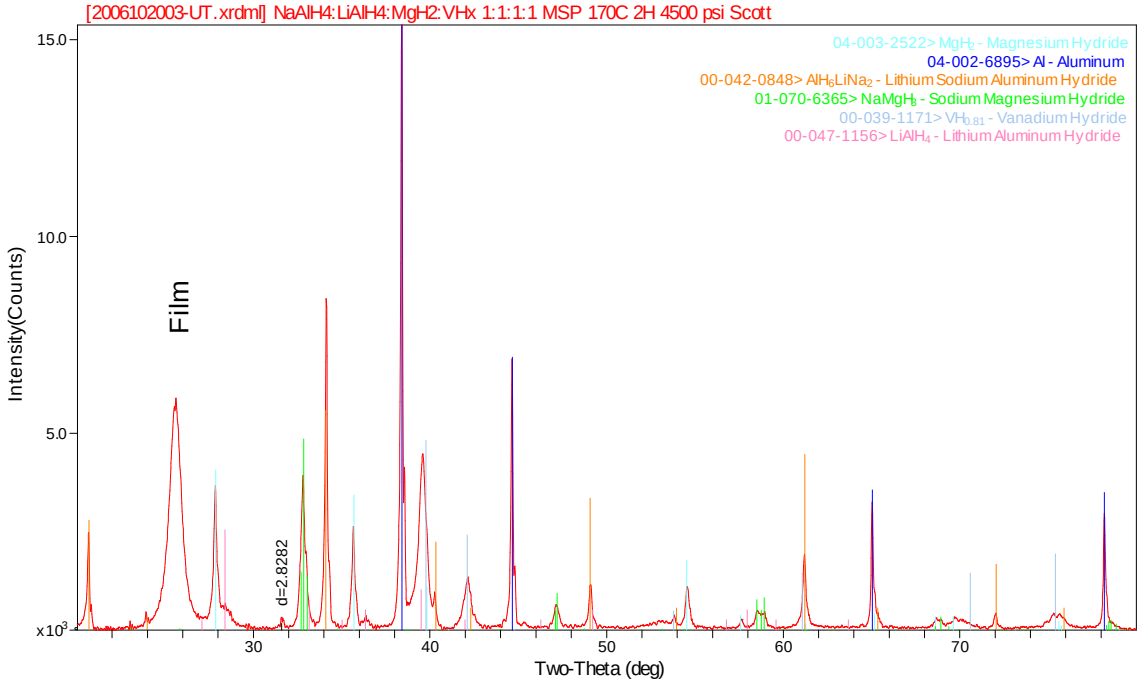

Figure 121: Melt processed (170°C) $NaAlH_4$:$LiAlH_4$:MgH_2:$VH_{0.81}$ 1:1:1:1.

Summary

Table 22 below summarizes the results of these experiments, where starting materials are designated SM. The addition of elements or other hydrides destabilizes $LiAlH_4$, while mixtures with binary hydrides produce the hexahydride, Li_3AlH_6. $NaAlH_4$ in combination with Mg materials produces $NaMgH_3$. As observed in Section 6.4 and consistent with the modeling in Section 3.3.2.2, when the Mg compound used is Mg_2NiH_4, $NaMgH_3$ forms with just ball milling, while mixtures with MgH_2 do not form the mixed metal hydride until heated in the MSP step. Mixtures containing $LiAlH_4$ and $NaAlH_4$ form $LiNa_2AlH_6$ with MSP.

The summary provides a general sense of the reactions seen, and there are occasional exceptions. One is the quaternary mixture mentioned above, $NaAlH_4$:$LiAlH_4$:MgH_2:Mn, which formed a Mn hydride with BM, with the H most likely supplied by $LiAlH_4$ decomposition. Further reaction under MSP conditions reforms elemental Mn as well as other products. The XRD patterns for these two reactions are shown below in Figure 122 and Figure 123.

Table 22: High level conclusions for Na and Li alanate mixtures (BM = Ball Milled; MSP = Molten State Processed; SM = Starting Materials).

Mixture	BM	MSP
$NaAlH_4$ + elements	No reaction	Na_3AlH_6
$LiAlH_4$ + elements	Al and SM	Al, SM and Li_3AlH_6
$NaAlH_4$ + $LiAlH_4$ mixtures	Usually Al and SM.	$LiNa_2AlH_6$, $NaMgH_3$ with Mg mixtures if MSP is at least 170°C. SM, Al and Li_3AlH_6 if MSP is 60°C.
$NaAlH_4$ + Mg_2NiH_4	$NaMgH_3$	
$NaAlH_4$ + MgH_2	No NaMg compounds	$NaMgH_3$
$LiAlH_4$ + binary hydrides	Li_3AlH_6 or ion exchange (with KH - $KAlH_4$)	

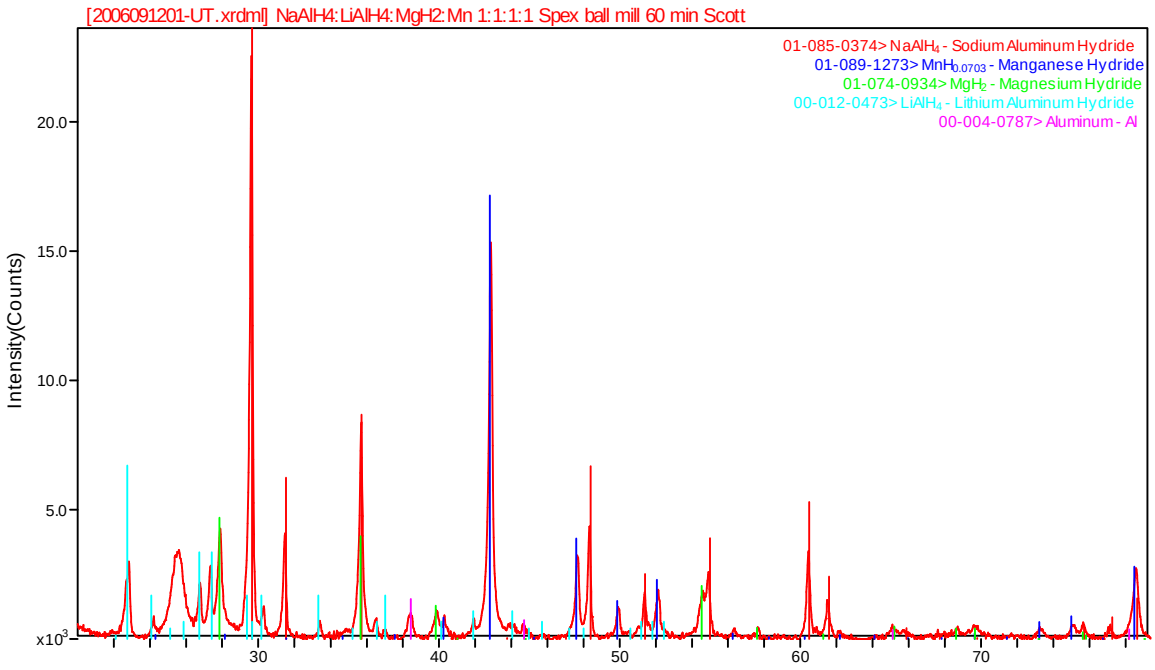

Figure 122: XRD pattern of ball milled 1:1:1:1 mol ratio $NaAlH_4$:$LiAlH_4$:MgH_2:Mn.

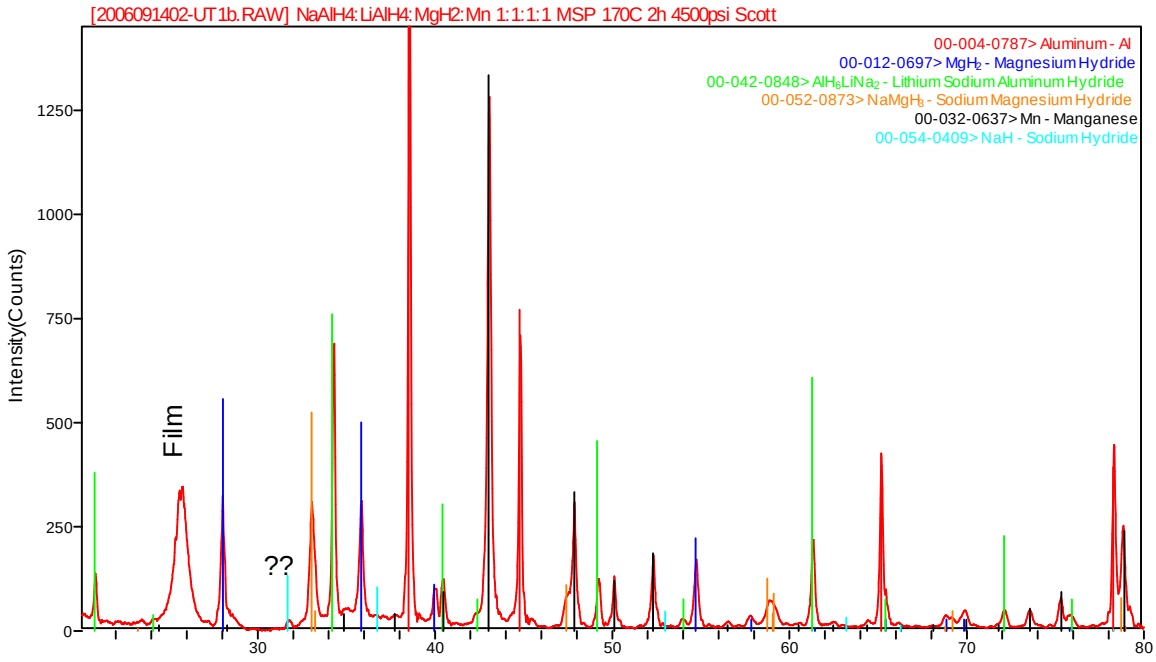

Figure 123: XRD pattern of 170°C MSP 1:1:1:1 mol ratio $NaAlH_4$:$LiAlH_4$:MgH_2:Mn.

6.9 Mixed Metal Borohydrides - MSP

The production of $Mg(BH4)_2$ materials, including mixed metal borohydrides containing Mg was explored through Fritsch milling of MgB_2 alone and MgB_2 mixed with $LiBH_4$ under ~100 psi of H_2 pressure, the maximum pressure rating of the milling vials. The resulting products were evaluated by XRD. The processed mixtures resulted in the formation of starting products and NiCrFe, presumably from a reaction with the stainless steel vials as shown below in Figure 124. The vials were limited to 100 psi of gas pressure, which resulted in a less than stoichiometric H_2 mole ratio for the quantities milled. We attempted to refill the vials with H_2 during the course of ball milling, but found that the valve stem on the vials clogged with powder and therefore were unable to add more hydrogen.

The XRD peaks of the ball milled MgB_2 are significantly broader than those of the material as purchased as shown in Figure 125 and Figure 126 below. The peak width analysis shows that the change is due not only to the crystallite size reduction but also the strain induced by ball milling (see Table 23).

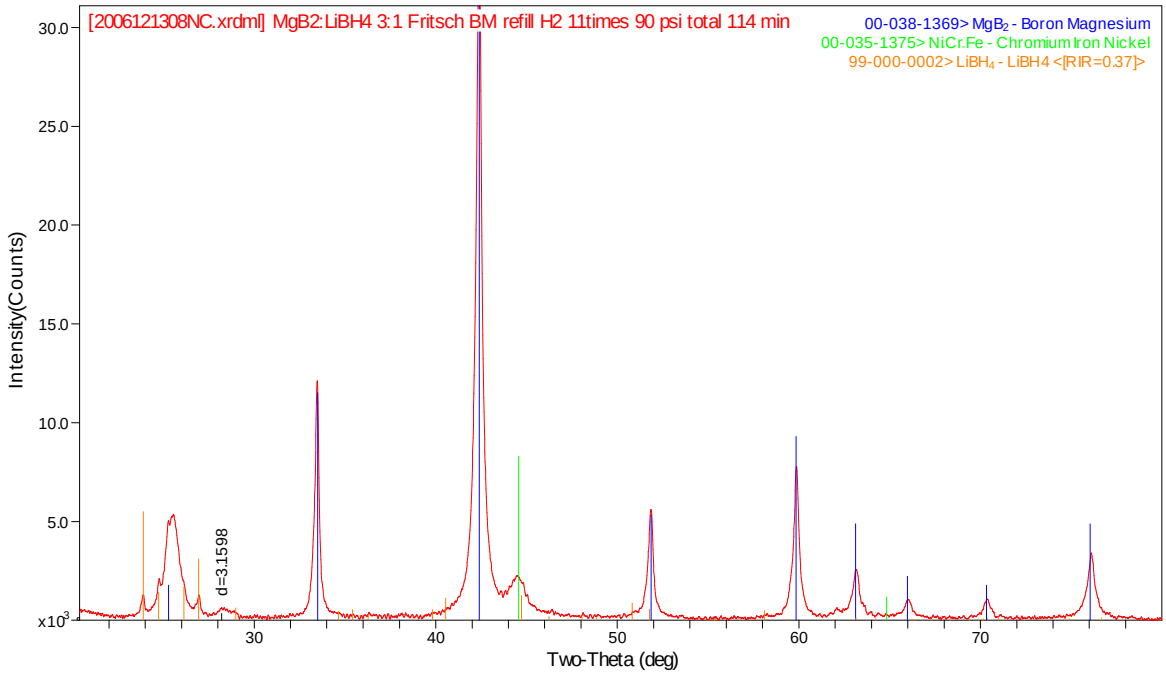

Figure 124: Mixture of MgB_2 and $LiBH_4$ ball milled with H_2.

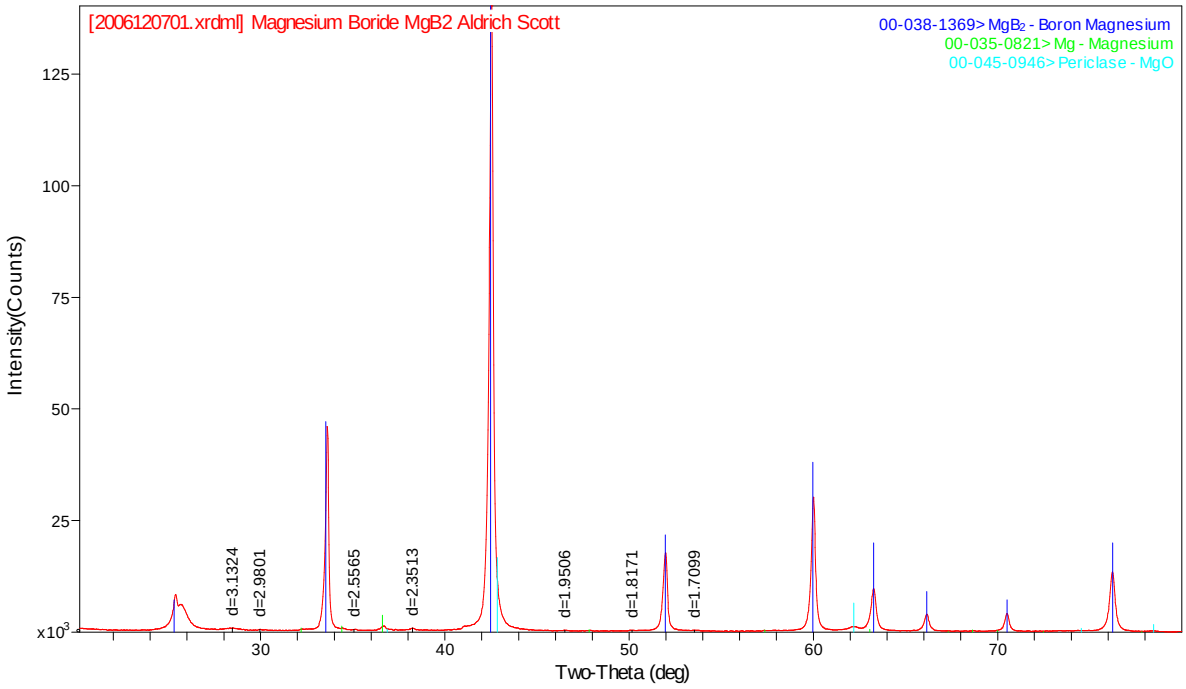

Figure 125: MgB_2 as purchased.

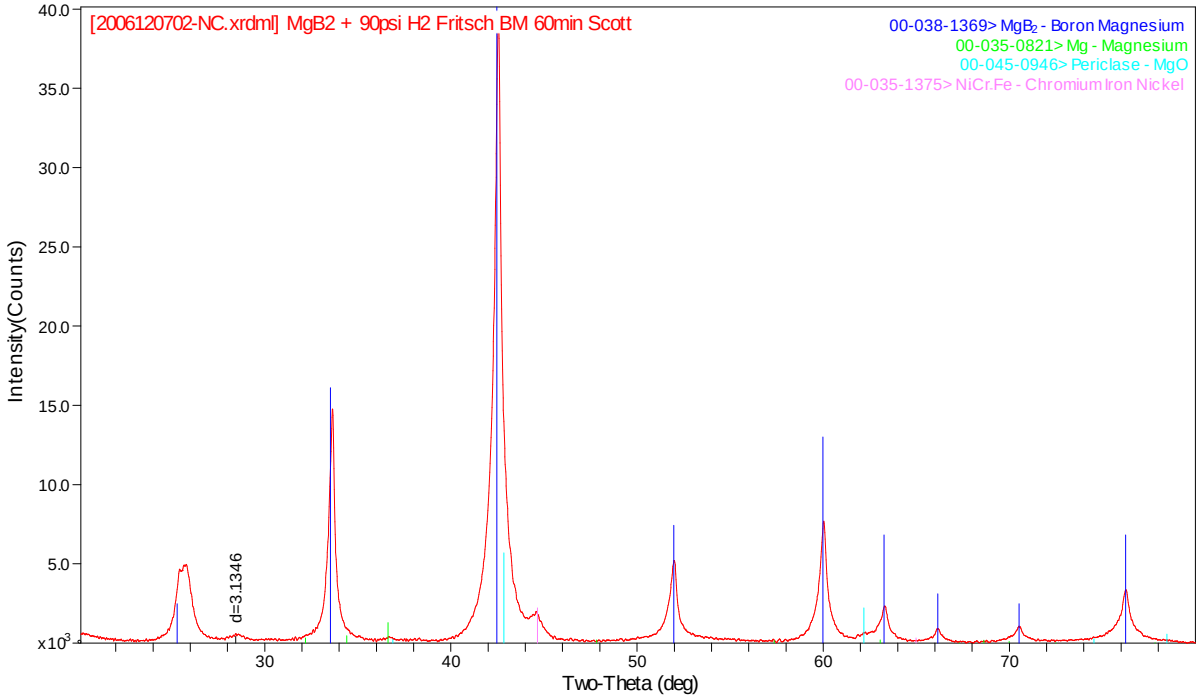

Figure 126: a) MgB_2 ball milled for 60 minutes.

Table 23: MgB_2 strain with ball milling

Sample ID	Crystalline Size (Å)	Strain (%)
Ball milled MgB_2	597(60)	0.331(0.016)
As purchased MgB_2	1051(53)	0.113(0.004)

6.10 Mixed Metal Borohydrides - Solvent Mixing

Two mixtures, $MgCl_2$ combined with $LiBH_4$ and MgB_2 combined with $LiBH_4$ were milled with THF. The first sample products were evaluated by XRD. The second mixture formed a very hard coating on the inside of the ball mill vial. The metathesis reaction between $MgCl_2$ and $LiBH_4$ takes place in the presence of THF to form $Mg(BH_4)_2(THF)_n$ as well as LiCl. The presence of the tri-THF compound was verified by XRD. The XRD pattern is shown below in Figure 127, with the comparison peaks marked. There are unaccounted for peaks associated with minor products which have yet to be identified. To further evaluate this material, UTRC ran TGA-MS analysis, shown in Figure 128. The TGA shows that the material continually loses weight from 30 to 300°C. The mass spectrometry data show that the H_2 evolution begins at 68°C, which corresponds to the boiling point of THF (66°C). This confirms that the THF adducts stabilize the material, as H_2 is liberated by their release. An increase in the H_2 release occurs at 216°C.

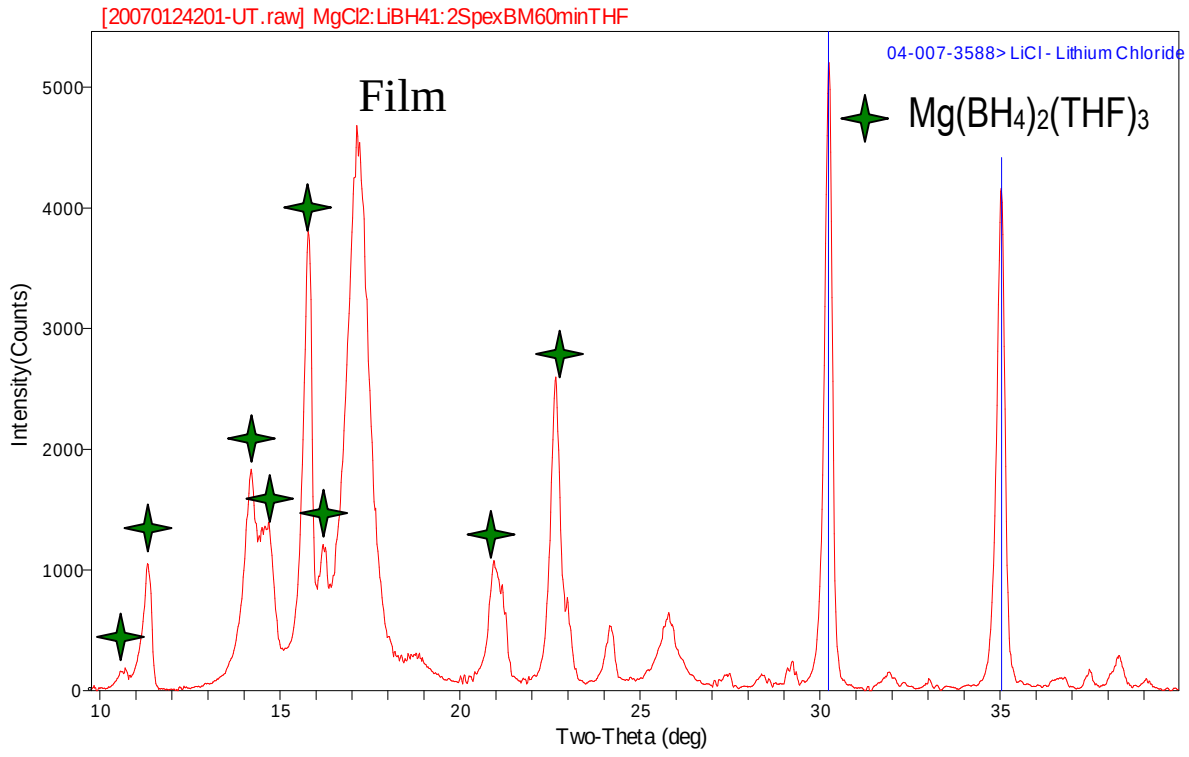

Figure 127: Mixture of $MgCl_2$ and $LiBH_4$ ball milled with THF.

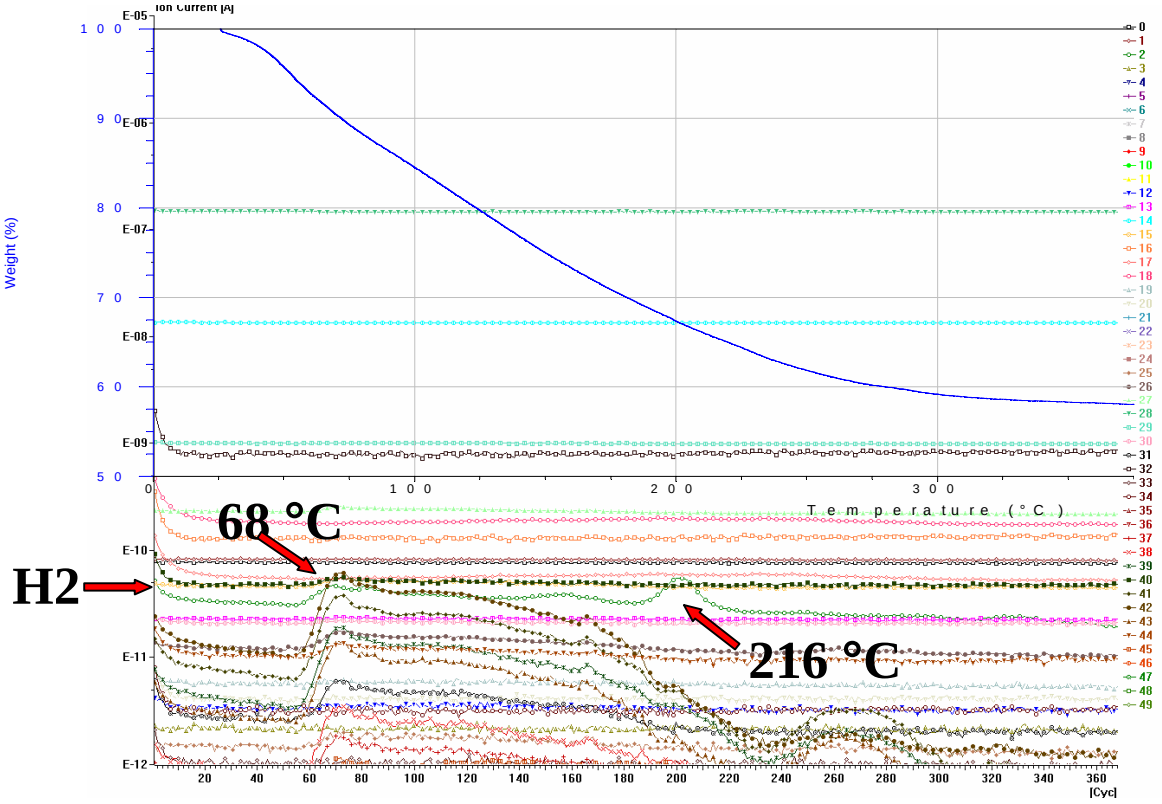

Figure 128: TGA-MS of $Mg(BH4)_2(THF)_3$ containing product.

7 Conclusions

7.1 Summary

Execution of the program evolved dynamically based upon our results and in response to reviewer recommendations. In the first stage, the team surveyed quaternary systems associated with the alkali alanates, implementing atomic modeling methodologies and parallel syntheses. In the second stage, the original approach was expanded to simultaneously pursue high capacity quaternary complex hydrides leveraged with high capacity coupled reactions, applying a triad of first principles modeling, thermodynamics, and experimental methodologies. These methods were iteratively implemented to enable new high capacity systems to be identified, refined, and evaluated. In the third stage, once new quaternary or ligand-stabilized high capacity systems had been identified, additional characterization methods were employed and modeling was utilized to investigate reaction mechanisms.

The primary activities and key results of the project include the following:

General Synthesis and Characterization

- A broad range of 9 quaternary systems was explored, including 6 alanate systems and 3 borohydride systems.
- A wide range of characterization techniques was employed to elucidate reaction mechanisms, and evaluate performance characteristics including XRD, DSC, TGA-MS, ICP, PCI / Sievert's, neutron diffraction and DRIFTS.
- Table 1 summarizes the performance of the best alanate and borohydride materials.

First Principles Modeling

- The implementation of coupled predictive methodologies provided a new capability to survey, simulate, and evaluate new candidate hydrogen storage compounds prior to their identification or preparation in the laboratory.
- These coupled methodologies joined together ground state minimizations using density functional theory, thermodynamic property predictions using direct method lattice dynamics, and phase stability predictions using chemical thermodynamics.
- The tool was extended to optimize the elemental stoichiometry within a compositional space at selected temperature/pressure conditions to obtain the highest theoretical hydrogen storage capacity.
- Significant elements required for implementation of these methodologies included:
    - Approaches for proposing input candidate structures,
    - Criteria for down-selection and refinement of candidate phases,
    - Methods for assessment and incorporation of newly predicted thermodynamic data alongside experimental data,
    - Procedures to predict the relative phase stability of the candidates compared to existing known phases over a wide range of temperatures and pressures.
- The predictive framework was used to survey more than 300 proposed phases:
    - Over 170 candidate phases in the quaternary spaces encompassing known alanate phases: Na-Ti-Al-H, Li-Ti-Al-H, and Na-Li-Al-H,

Conclusions

  - Over 50 phases within the Na-Mg-Al-H and Li-Mg-Al-H quaternary systems. In each system, numerous favorable ground-state minimized candidate structures were identified for the compound stoichiometries Am_2MgAlH_7 and $AmMgAlH_6$, where Am represents the alkaline metals Na or Li,
  - Over 60 complex alanate, boronate, and amine phases as well as lower order phases within the Li-Mg-Na-Al-B-N-H septenary system and over 40 co-reactant phases within related quaternary compositional systems.
- Combined atomistic and thermodynamic modeling has been shown to yield accurate predictions of plateau pressures suitable for guidance on in-situ reversibility.
- Reaction design with co-reactants was implemented, improving complex stability by reducing dehydrogenation exotherms up to a factor of four, lowering H_2 discharge onset temperatures below 100°C and preventing NH_3 side-product formation.
- The $Mg(BH_4)_2*2NH_3$ ligand-stabilized borohydride complex synthesized by SBP was found to change behavior with slightly different synthesis conditions and/or aging. One of the two mechanisms was an amine-borane (NH_3-BH_3) like dissociation reaction, possibly forming MgH_2 and BN which releases 16 wt% H_2. From FPM, the stability of the $Mg(BH_4)_2*2NH_3$ compound was found to increase with inclusion of the NH_3 groups in the inner-Mg coordination sphere, which in turn correlated with lowering the dimensionality of the $Mg(BH_4)_2$ network.

Solid State Processing

- Solid State Processing has been used to characterize the $Na_iLi_jMg_kM_xAl_yH_x$ (M = Ti, Ni, Co, Fe, Cr) systems at 200 bar and temperatures ranging from 80 to 120°C. While no ≥7.5 wt % materials were synthesized, numerous reversible hydrogen storage reactions have been identified *via* combinations of hydrides and alanates, yielding theoretical capacities of 2.6-5.6 wt %.
- The H_2 desorption measurements for the various Ak-Tm-B-H compounds indicated up to 12 wt % of H_2 was generated at 400°C, when the removable LiCl side-reaction product weight was excluded in the capacity calculation. However, the most active material can only be partially recharged up to 2 wt % H_2 at 220-300˚C and 195 bar H_2 pressure. The reversibility of this system is limited due to stable product formation.
- X-Ray Diffraction analysis indicated that most of the Ak-Tm-B-H compounds studied were amorphous in structure.
- Qualitative evidence of reversibility for amorphous borohydrides was obtained using Diffuse Reflectance Infrared Fourier Transform Spectra (DRIFTS) analyses, which is sensitive to various B-H vibrational frequencies.

Solution Based Processing

- Doped $NaAlH_4$ having Ti at 2, 4, 10, and 33% levels were prepared through SBP. Hydrogen storage performance of these compounds was inferior to the corresponding ball-milled materials, presumably due to the larger particle size.
- A novel alanate that was synthesized using SBP was $LiMg(AlH_4)_3$. This material demonstrated a 7.0 wt % capacity with a desorption temperature of 150°C.
- $Mg(BH_4)_2$ was synthesized in a number of ligand stabilized forms. Varying H_2 desorption mechanisms of these complexes were identified through integrated experimental analyses, performance testing and first principles atomic-thermodynamic modeling.

Conclusions

- In order to reduce the generation of ammonia, a co-reactant was mechanically mixed with $Mg(BH_4)_2$*$2NH_3$. Only a trace amount of ammonia was detected at temperatures up to 450˚C.
- Another $Mg(BH_4)_2$ complex was prepared with a less volatile aprotic ligand, in which there is no possibility of the hydrogen release via a BH_3NH_3-like mechanism. The hydrogen release kinetics of this $Mg(BH_4)_2$ system represents unambiguous evidence that the ligand has a significant destabilizing influence which does not require a boron nitride intermediate.
- The compound $NaTi(BH_4)_4$•DME has the potential for up to 7.3 wt% capacity, including the solvent ligand weight (the capacity would be ~12 wt% without the ligands). The synthesis has a very high yield using inexpensive starting materials. The complex discharges H_2 coupled with ligand release at temperatures as low as 60°C, and partially recharges as low as 20°C in the presence of the released ligand.

Molten State Processing

- A stoichiometric mix of $NaAlH_4$ and LiH subjected to the MSP temperature and pressure conditions produced the compound Na_2LiAlH_6 with partial conversion.
- Mixtures of $NaAlH_4$ and TiH_2 that were melt processed produced NaH rather than catalyzed $NaAlH_4$, indicating TiH_2 is a very efficient decomposition catalyst.
- The addition of the elements Mn, Cr and V or other hydrides destabilize $LiAlH_4$, while mixtures with binary hydrides produce the hexahydride, Li_3AlH_6 as summarized in Table 22. $NaAlH_4$ in combination with Mg materials produces $NaMgH_3$.
- As observed in Section 6.4 and consistent with the modeling in Section 3.3.2.2, when the Mg compound used is Mg_2NiH_4, $NaMgH_3$ forms with just ball milling, while mixtures with MgH_2 do not form the mixed metal hydride until heated in the MSP step.
- Mixtures containing $LiAlH_4$ and $NaAlH_4$ form $LiNa_2AlH_6$ with MSP.

7.2 Recommendations

One of the outcomes of this project was the productive integration of FPM, syntheses and characterization to screen, investigate and evaluate new materials. We have found based on experience that the discovery of new materials from modeling alone is very difficult and that syntheses often precede FPM in materials discovery. FPM yields the greatest value when iteratively coupled with experiments for determination of new material structures, investigation of experimentally observed characteristics and examination of modified chemistries. Therefore, it is important in the execution of such a project to have close collaboration between the modeler(s) and experimentalist(s), with the usual advantages if they are in the same organization or in close proximity.

We also found that there were clear benefits in having multiple organizations with their specific expertise pursue similar, complementary endeavors. The three synthesis methods were distinct and yet were applied on common materials systems, which illuminated the advantages and disadvantages of each. In some cases SSP was superior (catalyzed $NaAlH_4$); in other cases SBP was more successful (stabilized $Mg(BH_4)_2$). If the project had focused on interrogating in detail one material system, then down-selection to a single synthesis route might have been appropriate, but given the broad surveying of the current project, retaining the multiple synthesis methods throughout was the better approach.

Conclusions

Multiple organizations conducting different characterization techniques is an easier activity to separate, coordinate and execute. A potential drawback is the required shipment of materials. This is not a significant issue for small quantities of stable compounds, but it can be problematic if the materials are unstable, as was the case for a number of SBP borohydride materials. Thus, care should be taken to study aging effects at a single location in a well controlled manner and shipping may demand special requirements for temperature uniformity when sharing potentially unstable materials for multi-organizational characterization.

Similar to the transition in material focus which has occurred in the hydrogen storage community, based on the results in the current project, the apparent potential of alanate based compounds has diminished since the inspiring discovery of $NaAlH_4$ reversibility. Our efforts produced numerous compounds / reactions with capacities greater than conventional metal hydrides but less than that of $NaAlH_4$, and one material with a nominal capacity of 7.0 wt % was irreversible. Therefore, we concur that the potential of alanates is insufficient to motivate a strong emphasis in future novel materials research.

Borohydrides have and continue to receive a great deal of attention for both chemical and reversible metal hydride systems. Like other efforts, we have found that a key challenge for this material class is reaction design/control to avoid the formation of stable products which inhibit reversibility. To a lesser extent, the formation of volatile B_xH_y products is an issue, but there are storage system engineering concepts which could address this. The boron oriented reactions observed and simulated in this effort are complex and have exhibited markedly different behavior with minor modifications in synthesis conditions or simulated structure. While no completely viable storage materials were synthesized in this effort, we feel the potential remains to develop high capacity borohydrides with tailored reactions which have adequate reversibility / regenerability.

8 Publications and Presentations

Publications

1. C. Qiu, S. M. Opalka, O. M. Løvvik, and G. B. Olson, "Thermodynamic modeling of Ti-hydride and Ti dissolution in sodium alanates," submitted CALPHAD.
2. S. Sartori, S. M. Opalka, O.M. Løvvik, M. N. Guzik, X. Tang, B. C. Hauback, "Experimental studies of α-AlD_3 and α´-AlD_3 versus first principles modelling of alane isomorphs," accepted J. Mater. Chem.

3. S. Opalka, O.M. Løvvik, H.W. Brinks, P.W. Saxe, B.C. Hauback: "Integrated Experimental – Theoretical investigations of the Na-Li-Al-H system". Inorg. Chem. (2007) 46, 1401-1409.
4. H. Grove, H.W. Brinks, R. Heyn, F.-J. Wu, S.M. Opalka, X. Tang, B.L. Laube, B.C. Hauback: "The structure of $LiMg(AlD_4)_3$". J. Alloys and Compounds (in press).

4. X. Tang, S. M. Opalka, B. L. Laube, F. – J. Wu, J. R. Strickler, D. L. Anton, "Hydrogen Storage Properties of Na-Li-Mg-Al-H Complex Hydrides," J. Alloys Compd. (2007) 446–447, 228-231.
5. C. Qiu, S. M. Opalka, G. B. Olson, and D. L. Anton, "Thermodynamic modeling of the sodium alanates and the Na-Al-H System," Int. J. Mat. Res. 97 (2006) 1484-1494.
6. O. M. Lovvik and S. M. Opalka, "The stability of Ti in $NaAlH_4$," Applied Physics Letters 88, 161917-1-3(2006). Also published in the May 1, 2006 issue of Virtual Journal of Nanoscale Science & Technology. http://www.vjnano.org

7. C. Qiu, S. M. Opalka, G. B. Olson, and D. L. Anton, "The Na-H System: from First Principles Calculations to Thermodynamic Modeling," Int. J. Mat. Res. 97 845 (2006).
8. O. M. Lovvik, O. Swang, and S. M. Opalka, "Modelling alkali alanates for hydrogen storage by density-functional band-structure calculations" J. Mater. Res., 20(12) 3199-3213 (2005).
9. O. M. Lovvik and S. M. Opalka, "First-principles calculations of Ti-enhanced $NaAlH_4$," Phys. Rev. B 71 054103-1-10 (2005).
10. C. Qiu, G. B. Olson, S. M. Opalka and D. L. Anton, "A Thermodynamic Evaluation of the Al-H System," J. of Phase Equilibria and Diffusion 25(6) 520-527 (2004).
11. O. M. Løvvik, S. M. Opalka, H. W. Brinks and B. C. Hauback, "Crystal structure and thermodynamic stability of the lithium alanates $LiAlH_4$ and Li_3AlH_6," Phys. Rev. B 69 134117-134125 (2004).
12. S. M. Opalka and D. L. Anton, "First Principles Study of Sodium-Aluminum-Hydrogen Phases," J. of Alloys and Compounds 356-357 486-489 (2003).

Publications and Presentations

Presentations

1. S. Sartori, H. Grove, M.H. Sørby, S.M. Opalka, B.C. Hauback: "Synthesis, Structure and Properties of Alanates based on Li-Mg and K for Hydrogen Storage". Gordon Research Conference Hydrogen-Metal Systems, USA, July 2007.

2. S. M. Opalka, P. W. Saxe, and O. M. Løvvik, "Atomic simulations of alane phase transformations and dehydrogenation mechanisms," presentation at the American Physical Society Annual Meeting, Denver, Colorado, USA, March 5-9, 2007.

3. H. Grove, H.W. Brinks, R.H. Heyn, A. Klaveness, R.F.-J. Wu, S.M. Opalka, X.T. Tang, B.L. Laube, B.C. Hauback: "Synthesis and properties of lithium magnesium alanate". 19th Nordic Structural Chemistry Meeting, Norway, January 2007.

4. O. M. Lovvik, and S. M. Opalka, "Theory of complex hydrides," invited presentation to be made at the International Symposium on Metal-Hydrogen Systems, Lahaina, HI, October 1-6, 2006.

5. O. M. Løvvik and S. M. Opalka, "Density-functional calculations of new alanates," invited presentation to be made at the International Symposium on Materials Issues in Hydrogen Production and Storage, Santa Barbara, CA, August 20-25, 2006.

6. S. M. Opalka, C. Qiu, and O. M. Løvvik, "First Principles Contributions to the Thermodynamic Assessment of Solid Sate Metal Hydride and Complex Hydride Phases," invited presentation at the DOE Theory Focus Session on Hydrogen Storage Materials, Crystal City, MD, May 18, 2006.

7. S. M. Opalka, T. H. Vanderspurt, S. C. Emerson, D. A. Mosher, Y. She, X. Tang, and D. L. Anton, "Theoretical Contributions Towards the Development of Storage Media and Related Materials for Hydrogen Processing", invited presentation at the 2006 TMS Annual Meeting to be held at San Antonio, Texas, March, 2006.

8. S. M. Opalka, D. A. Mosher, X. Tang, D. L. Anton R. Zidan, K. Shanahan, J. Strickler, F.-J. Wu, O. M. Lovvik, H. Brinks, and B. Hauback, "Complex hydride compounds with enhanced hydrogen storage capacity,"Experts' SemiAnnual Workshop of the IEA Hydrogen Implementing Agreement Task 17 – Solid and Liquid State Hydrogen Storage Materials at Tateshina, Japan, October 23-27, 2005.

9. C.Qiu, G. B. Olson, S. M. Opalka, and D. L. Anton, "Thermodynamic Modeling of Sodium Alanates and the Effect of Ti," presentation at the 2005 Fall MRS Meeting, Boston, MA, November 29-Dec. 3, 2005.

10. O. M. Lovvik, O. Swang, S. M. Opalka, and P. N. Molin, "Alanates for Hydrogen Storage – Density Functional Calculations of Structural, Electronic, and Thermodynamical Properties," invited presentation at the 2005 Fall MRS Meeting, Boston, MA, November 29-Dec. 3, 2005.

Publications and Presentations

11. S. M. Opalka, O. M. Lovvik, H. W. Brinks, B. C. Hauback, Paul W. Saxe, and D. L. Anton, "Combined Experimental-Theoretical Investigations of the Na-Li-Al-H System," Materials Science & Technology 2005 Pittsburgh, PA, on September 25-28, 2005.

12. C. Qiu, S. M. Opalka, D. L. Anton, G. B. Olson, "Thermodynamic Modeling of Sodium Alanates," Materials Science & Technology 2005 Pittsburgh, PA, on September 25-28, 2005.

13. O. M. Løvvik and S. M. Opalka, "First-principles calculations of Ti-enhanced NaAlH4." Presentation at the International Symposium of Metal Hydrogen Systems (MH2004), Krakow, Poland, September 10, 2004.

9 References

1. E. Wiberg, and R. Uson, Z. Naturforsch.,B, 6 (1951) 392.
2. B. Bogdanovic and M. Schwickardi, J. Alloys Compd., 253 (1997) 1.
3. C. M. Jensen and K. J. Gross, Appl. Phys. A 72 (2001) 213.
4. K. J. Gross, G. Thomas, and C. M. Jensen, J. Alloy Compd. 330-332 (2002) 683.
5. C. Qiu, S. M. Opalka, G. B. Olson, and D. L. Anton, Int. J. Mat. Res.(formerly Z. Metallkd.) 97, (2006) 1484.
6. O. M. Løvvik and S. M. Opalka, Appl. Phys. Lett. 88 (2006) 161917.
7. E. H. Majzoub and K. J. Gross, J. Alloys Compd. 356-357 (2003) 363.
8. K. Hashi, K. Ishikawa, K. Suzuki, and K. Aoki, Mat. Trans., 43(11) (2002) 2734.
9. G. Kresse and J. Hafner, Phys. Rev. B, 47(1) (1993) 558.
10. G. Kresse and J. Fürthmuller, Comput. Mater. Sci., 6 (1996) 15.
11. G. Kresse and J. Fürthmuller, Phys. Rev. B, 54(16) (1996) 11169.
12. W. Kohn and L. J. Sham, Phys. Rev., 140 (1965) 1133.
13. G. Kresse and D. Joubert, Phys. Rev. B, 59(3) (1999) 1758.
14. J.P. Perdew, J.A. Chevary, S.H. Vosko, K.A. Jackson, M.R. Pederson, D.J. Singh, and C. Fiolhais, Phys. Rev. B, 46(11-15) (1992) 6671.
15. S. M. Opalka and D. L. Anton, J. Alloys Compd., 356-357 (2003) 486.
16. C. Qiu, S. M. Opalka, G. B. Olson, and D. L. Anton, Int. J. Mat. Res., 97 (2006) 845.
17. O. M. Løvvik and S. M. Opalka, Phys. Rev. B, 71 (2005) 054103.
18. MedeA-Phonon Version 1.0 using Phonon Software 3.11, Copyright Prof. K. Parlinski.
19. K. Parlinski, Z. Q. Li, Y. Kawazoe, Phys. Rev. Lett. 78, 4063 (1997).
20. Materials Design MedeA Phonon application note.
21. Thermo-Calc Software A.B., Stockholm, Sweden.
22. HSC Chemistry 5, Outokumpu Research Oy, Pori, Finland.
23. C. Qiu, G. B. Olson, S. M. Opalka and D. L. Anton, J. Phase Equil. Dif., 25(6) (2004) 520.
24. O. M. Løvvik, S. M. Opalka, H. W. Brinks and B. C. Hauback, Phys. Rev. B, 69 (2004) 134117.
25. S. M. Opalka and E. Rönnebro, Sandia-UTRC Collaboration Plan, 8/19/2005.
26. Endeavor Version 1.3, Klaus Brandenburg and Holger Putz, © 2000-2005, Crystal Impact GbR.
27. H. Putz, J. C. Schön, and M. Jansen, J. Appl. Cryst., 32 (1999) 864.

References

28. TC Matlab Toolbox Version 3.01, © 1995-2004, Foundation of computational Thermodynamics, Stockholm, Sweden.

29. H. Kohlmann, "Metal Hydrides," Encylcopedia of Physical Sciences and Technology, (R. A. Meyers, Ed.) 3rd Ed., Academic Press: 9 (2002) 441.

30. K. Yvon, "Hydrides: Solid State Transition Metal Complexes," Encyclopedia of Inorganic Chemistry (Ed. R. B. King) , John Wiley and Sons: 3 (1994b) 1401.

31. K. Yvon, Z. Kristallogr., 218 (2003) 108.

32. W. Bronger, J. Alloys and Compd., 229 (1995) 1.

33. W. Bronger and G. Auffermann, Chem. Mater., 10 (1998) 2723.

34. E. C. Ashby, Chem. Ind. (London), (1962) 208.

35. B. Siegel and G. G. Libowitz, "The Covalent Hydrides and Hydrides of the Groups V to VIII Transition Metals," in Metal Hydrides, (Eds. W. M. Mueller, J. P. Blackledge, and G. G. Libowitz) AcademicPress: (1968) 545.

36. T. N. Dymova, Y. M. Dergachev, V. A. Sokolov, and N. A. Grechanaya, Doklady Akademii Nauk SSSR, 224 (1975) 556.

37. G. J. Thomas, S. E. Gunthrie, and K. Gross, Proc. 1999 DOE Hydrogen Program Annual Peer Review, (1999).

38. K. J. Gross, G. J. Thomas, and C. M. Jensen, J. Alloys Compd., 330-332 (2002) 683.

39. B. Bogdanovic, R. A. Brand, A. Marjanovic, M. Schwickardi, and J. Tolle, J. Alloys Compd., 302 (2000) 36.

40. O. M. Løvvik, O. Swang, and S. M. Opalka, J. Mater. Res., 20(12) (2005) 3199.

41. S. M. Opalka, O. M. Løvvik, H. W. Brinks, P.W. Saxe, and B. C. Hauback, Inorg. Chem., 46(4) (2007) 1401.

42. A. Fossdal, H. W. Brinks, J. E. Fonnelop, B. C. Hauback, J. Alloys Compd., 397 (2005) 135.

43. J. Graetz, Y. Lee, J. J. Reilly, S. Park, T. Vogt, Phys. Rev. B 71 (2005) 1844115.

44. C. Qiu, S. M. Opalka, O. M. Løvvik, and G. B. Olson, submitted CALPHAD.

45. H. W. Brinks, B. C. Hauback, C. M. Jensen, R. Zidan, J. Alloys Compd., 392 (2005) 27.

46. J. Hout, S. Boily, V. Guther, R. Schultz, J. Alloys Compd., 383 (1999) 304.

47. M. Mamatha, B. Bogdanovic, M. Felderhoff, A. Pommerin, W. Schmidt, F. Schuth, and C. Weidenthaler, J. Alloys Compd., 416 (2006) 303.

48. COST507 Light Alloys Database, COST507 Project: Round II, European Commission.

49. Binary Alloy Phase Diagrams CDROM, ASM International, Materials Park, OH.

50. H. Grove, H. W. Brinks, R. H. Heyn, F.-J. Wu, S. M. Opalka, X. Tang, B. L. Laube, B. C. Hauback, J. Alloys Compd., in press, doi:10.1016/j.jallcom.2007.01.150.

References

51. X. Tang, S. M. Opalka, B. L. Laube, F.-J. Wu, J. R. Strickler and D. L. Anton, J. Alloys Compd., 446–447 (2007) 228.
52. H. Grove, H. W. Brinks, O. M. Løvvik, R. H. Heyn and B. C. Hauback, J. Alloys Compd., in press, doi:10.1016/j.jallcom.2007.06.029.
53. P. Chen, Z. Xiong, J. Luo, J. Lin, and K. L. Tan, Nature, 420 (2002) 302.
54. J. F. Herbst and L. G. Hector, Phys. Rev. B, 72 (2005) 125120.
55. B. M. Bulychev and A. G. Burlakova, Khimiya, 19(4) (1978), 498.
56. Z. Lodziana and T. Vegge, Phys. Rev. Lett., 93 (2004) 145501.
57. P. Vajeeston, P. Ravindran, A. Kjekshus, and H. Fjellvåg, Appl. Ohys. Let., 89 (2006) 071906.
58. X. Tang, B. L. Laube, D. L. Anton, S.-J. Hwang, and R. C. Bowman, presentation at American Physical Society Meeting, Denver, Co, March 5-9, 2007.
59. B. Bogdanovic, M. Schwickardi, J. Alloys Comp. 253-254 (1997)
60. P. Claudy, B. Bonnetot, J. P. Bastide, J. M. Letoffe, Mater. Res. Bull. 17 (1982) 1499.
61. E. Ronnebro, D. Noreus, K. Kadir, A. Reiser, B. Bogdanovic, J Alloys Comp. 299 (2000), 101.
62. M. Mamatha, B. Bogdanovic, M. Felderhoff, A. Pommerin, W. Schmidt, F. Schueth, C. Weidenthaler, J Alloys Comp. 407 (2006) 78.
63. Y. Nakamori, H.-W. Li, K. Kikuchi, M. Aoki, K. Miwa, S. Towata and S. Orimo, J Alloys Comp. 446-447 (2007) 296.
    B. Bogdanovic, M. Schwickardi, J. Alloys Comp. 253-254 (1997) 1.
64. J. R. Strickler, *U.S. patent* 5,264,590, 1993.
65. B. Bogdanovic and M. Schwickardi, *J. Alloys Compds.* 1997, 253, 1.
66. Graetz et al., *Applied Physics. Let.* 2004, 85, 3, 500.
67. B. M.Bulychev, K. N. Semenenko, K. B. Bitcoev, *Koord. Khim*, 4 (1978), 374-380.
68. Bogdanovic et al., *J. Alloys compd.* (2006), 407 (1-2), 78-86.
69. Adriaan Sachtler, 2005 Hydrogen Program Annual Review, Washington D.C., Project ST-5.
70. V. N. Konoplev, *Zh. Neorg. Khim.* 25 (1980) 1737-1740.
71. K. Franz and H. Noth, *Z. Anorg. Allg. Chem.* **397**, 247 (1973).
72. B. D. James and B. E. Smith, *Synth. React. Inorg. Met.-Org. Chem.* **4**, 461 (1974).
73. Borisov *et al., Zhurnal Neorgnicheskoi Khimii* (1986), 31(1), 86-92.
74. U.S. patent 0046930, 2006.
75. Levason et al., *J. Chem. Soc. Dalton Trans*, 2000, 3001-3006.
76. Schormann et al., *Acta Cryst*, 2003, E59, 674-675.

References

77. Streltsova et al., *Koord. Khim*, 1988, 14, 421-429.

10 Appendix

10.1 Semi-Quantitative XRD Analysis of Alanate Phases

Results from semi-quantitative X-Ray Diffraction analysis for the majority of the alanate materials synthesized *via* Solid State Processing are given in the current appendix. The bar graphs display the composition evolution from starting materials, as-milled and thermal/hydrogen pressure processing.

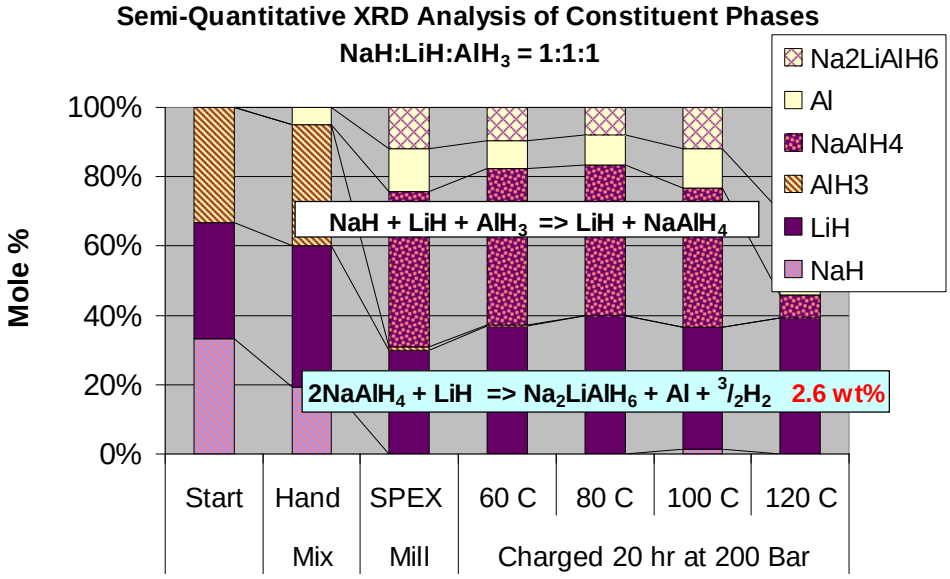

Figure 129: $NaH:LiH:AlH_3$ = 1:1:1.

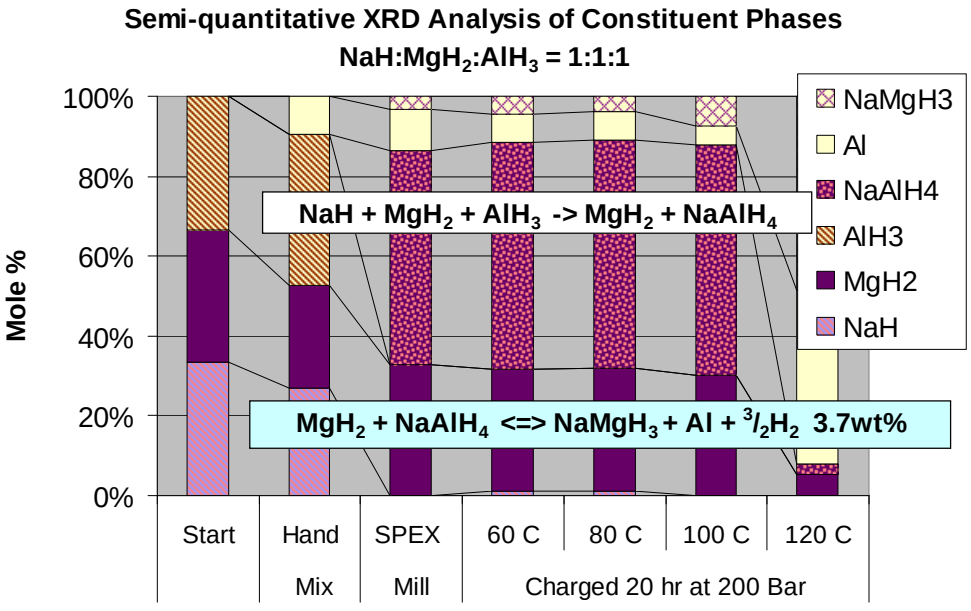

Figure 130: $NaH:MgH_2:AlH_3$ = 1:1:1.

Appendix

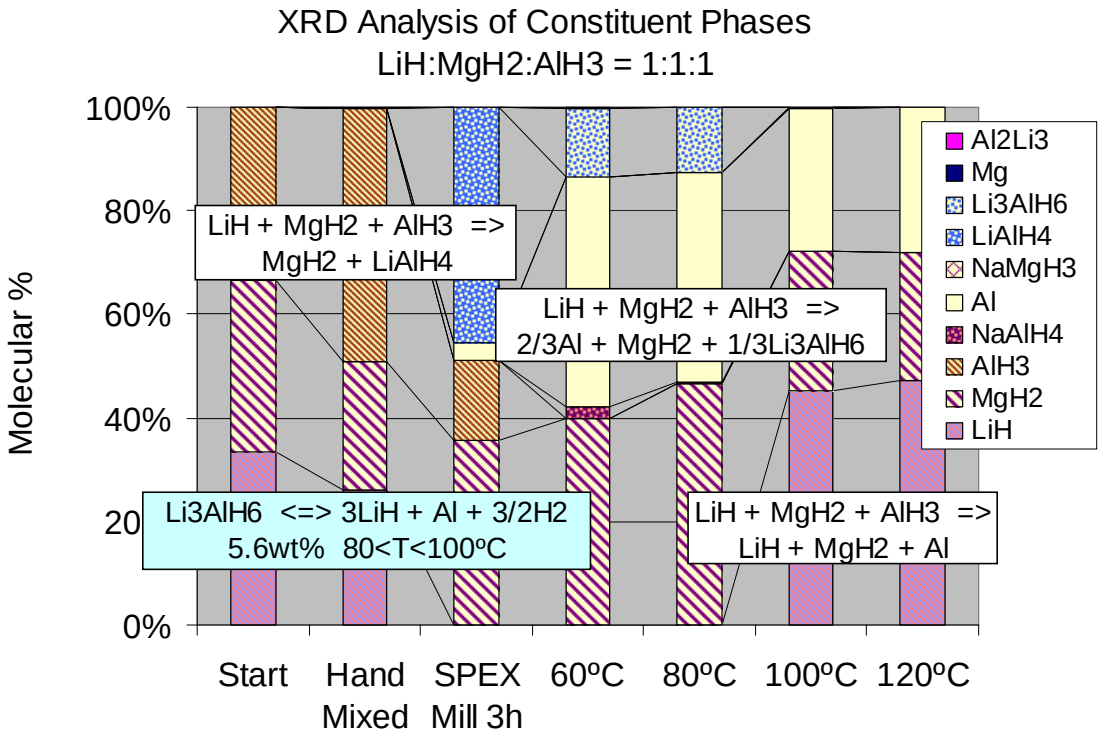

Figure 131: $LiH:MgH_2:AlH_3$=1:1:1.

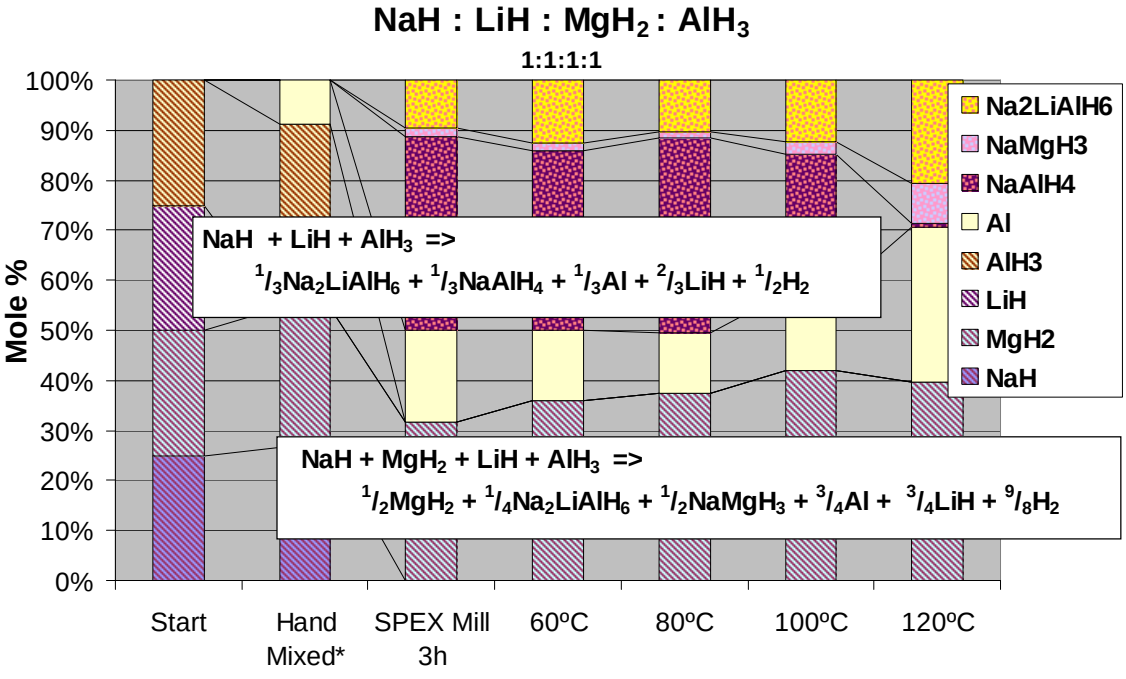

Figure 132: $NaH:LiH:MgH_2:AlH_3$=1:1:1:1.

Appendix

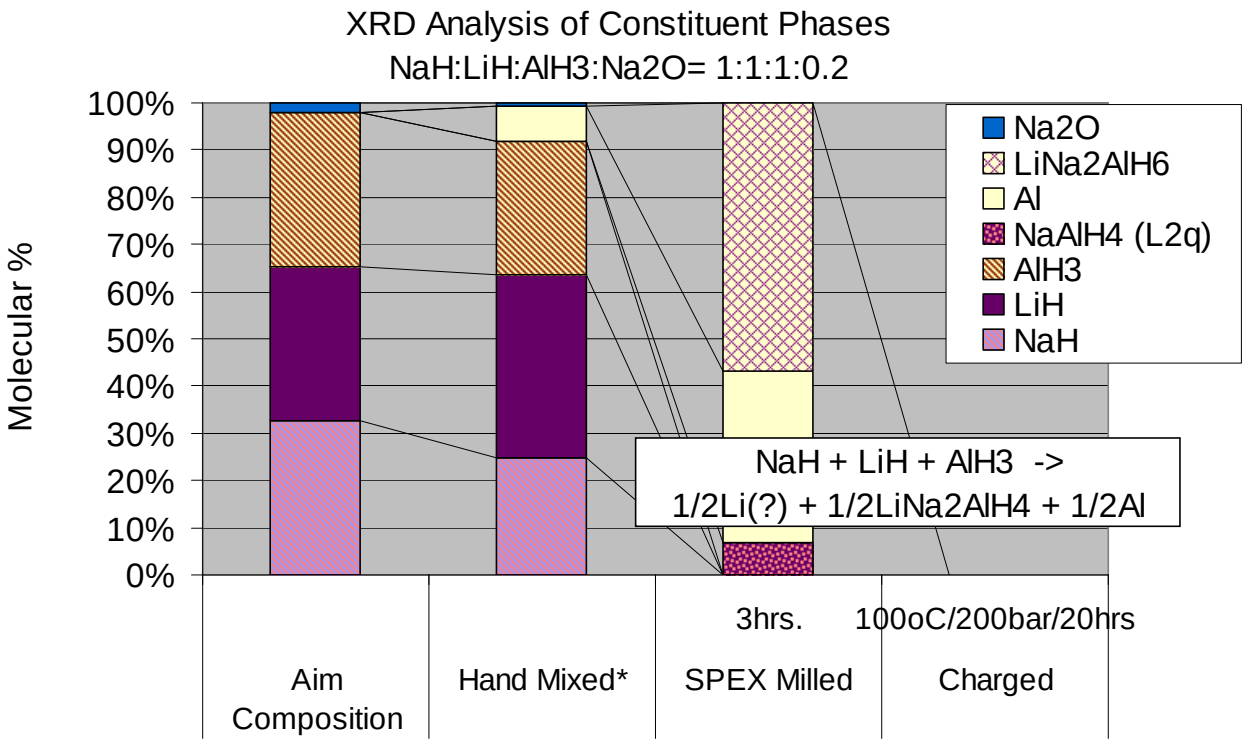

Figure 133: NaH:LiH:AlH_3:Na_2O = 1:1:1:0.2.

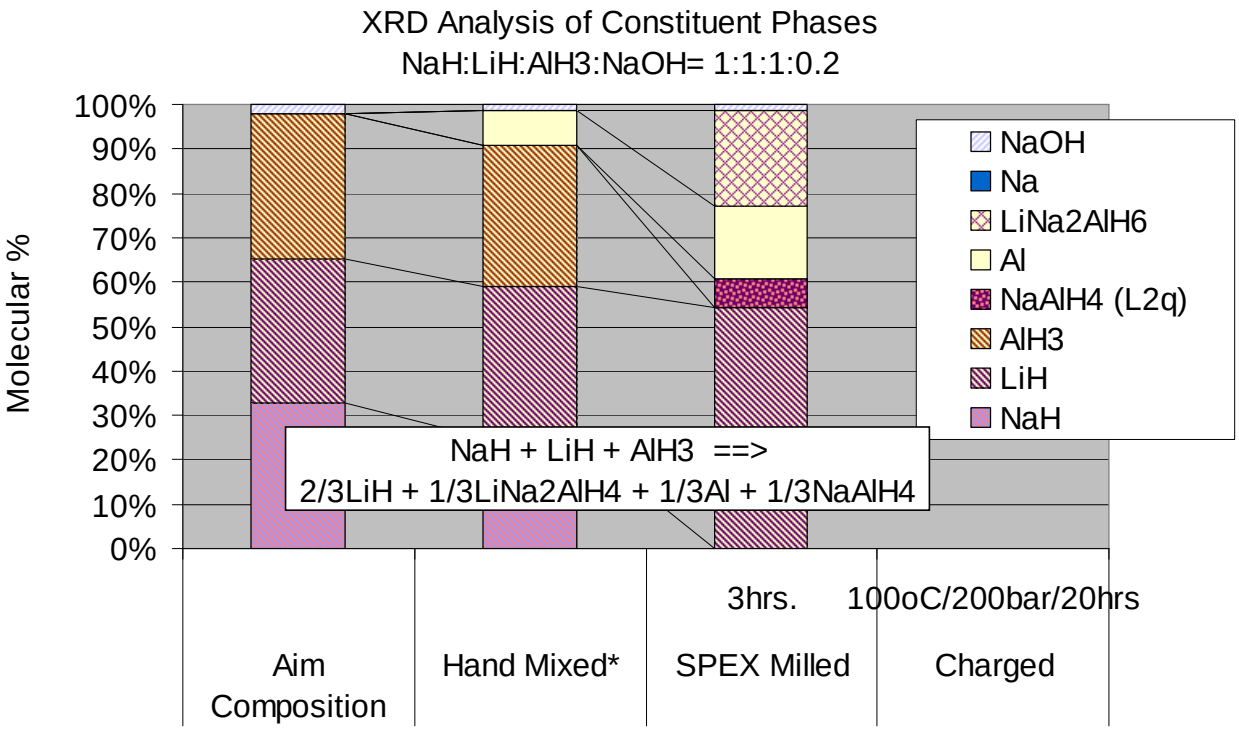

Figure 134: NaH:LiH:AlH_3:NaOH = 1:1:1:0.02.

Appendix

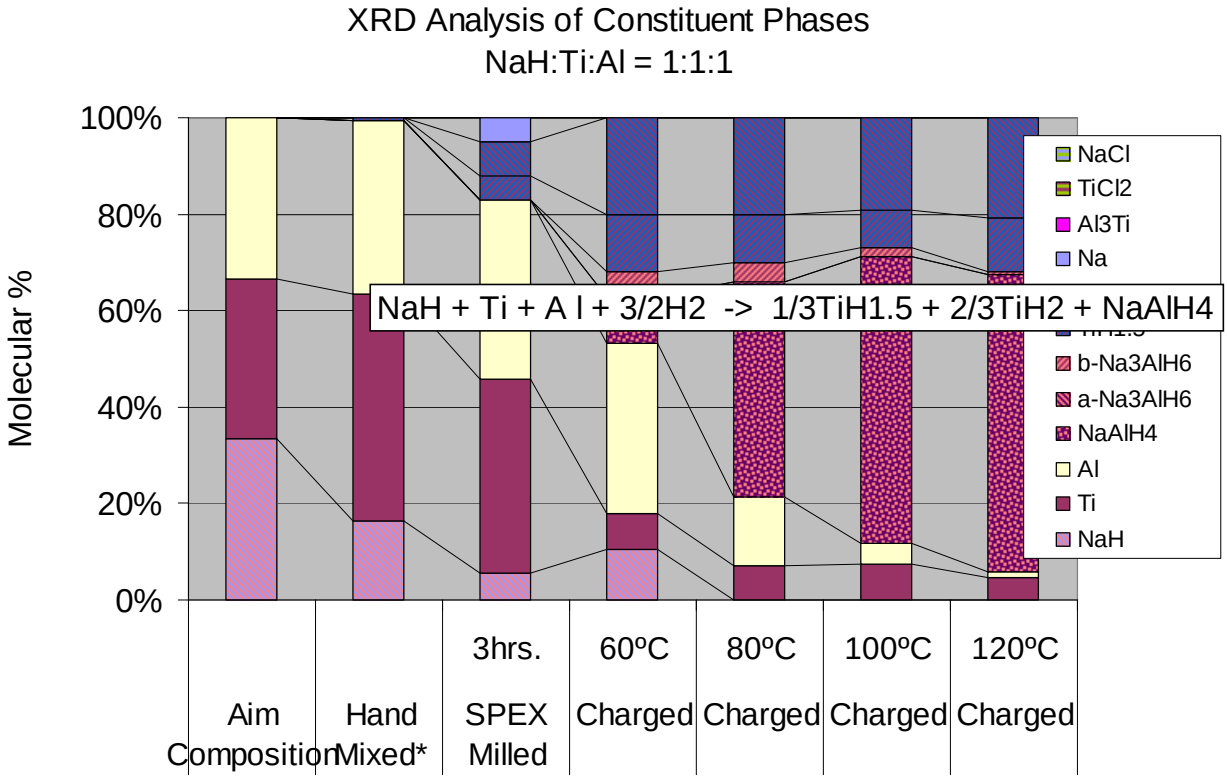

Figure 135: NaH:Ti:Al=1:1:1.

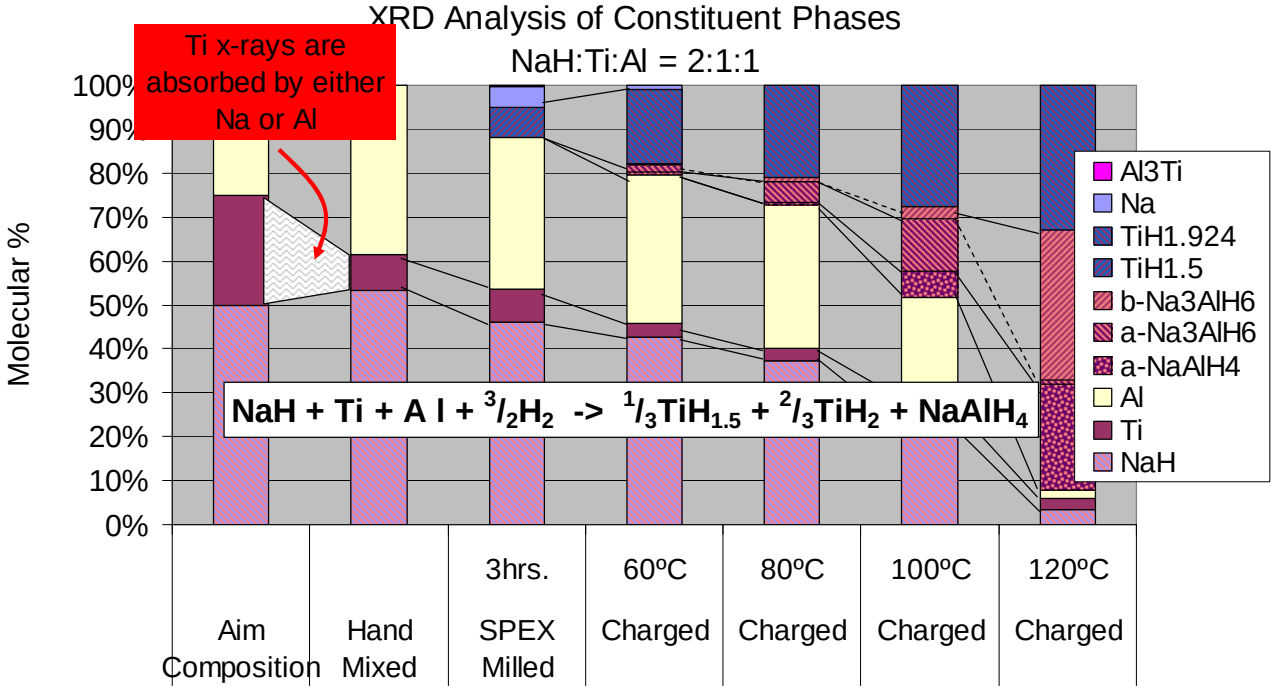

Figure 136: NaH:Ti:Al=2:1:1.

Appendix

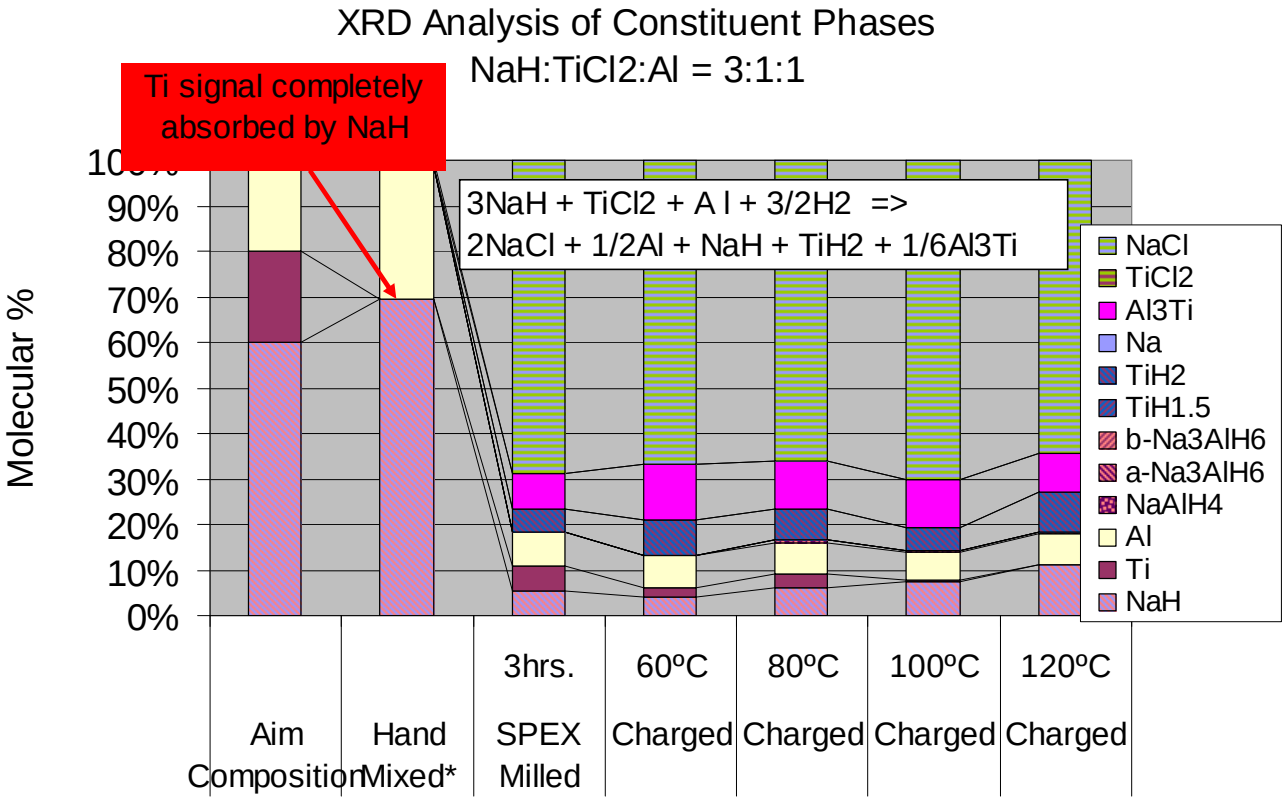

Figure 137: NaH:TiCl2:Al=3:1:1.

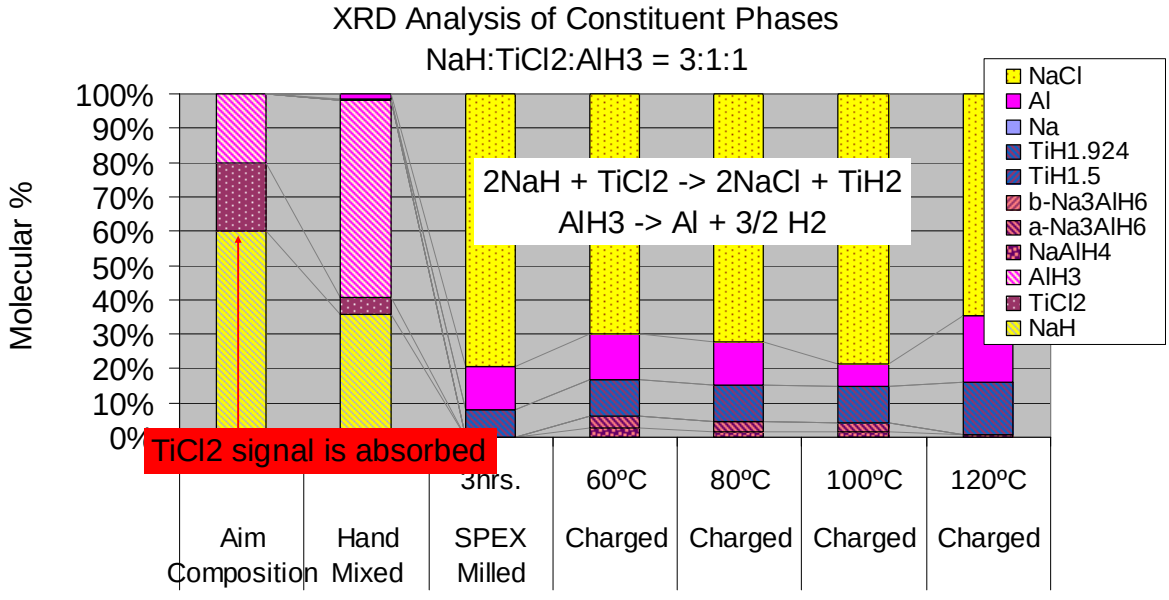

Figure 138: NaH:$TiCl_2$:Al = 3:1:1.

Appendix

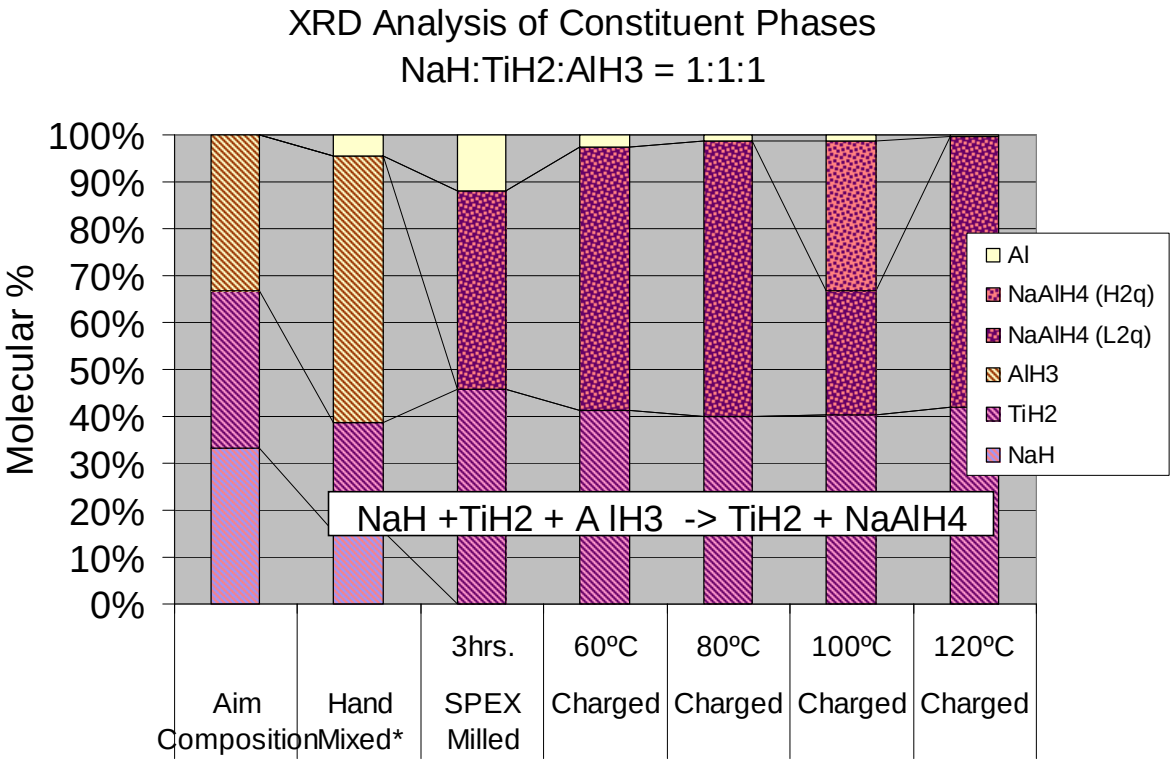

Figure 139: $NaH:TiH_2:AlH_3$=1:1:1.

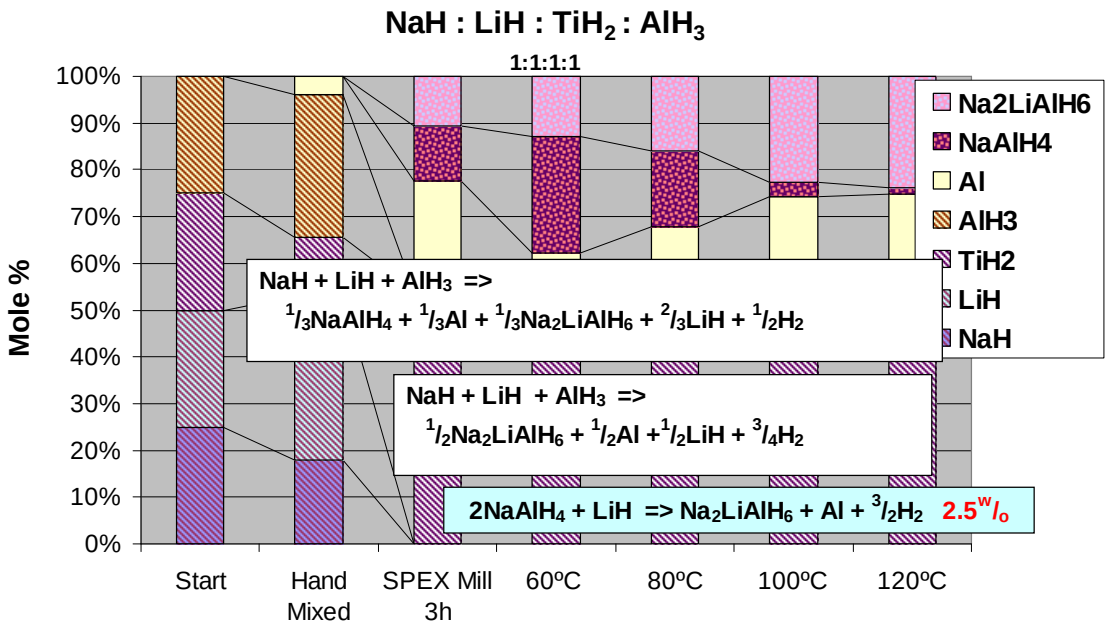

Figure 140: $NaH:LiH:TiH_2:AlH_3$=1:1:1:1.

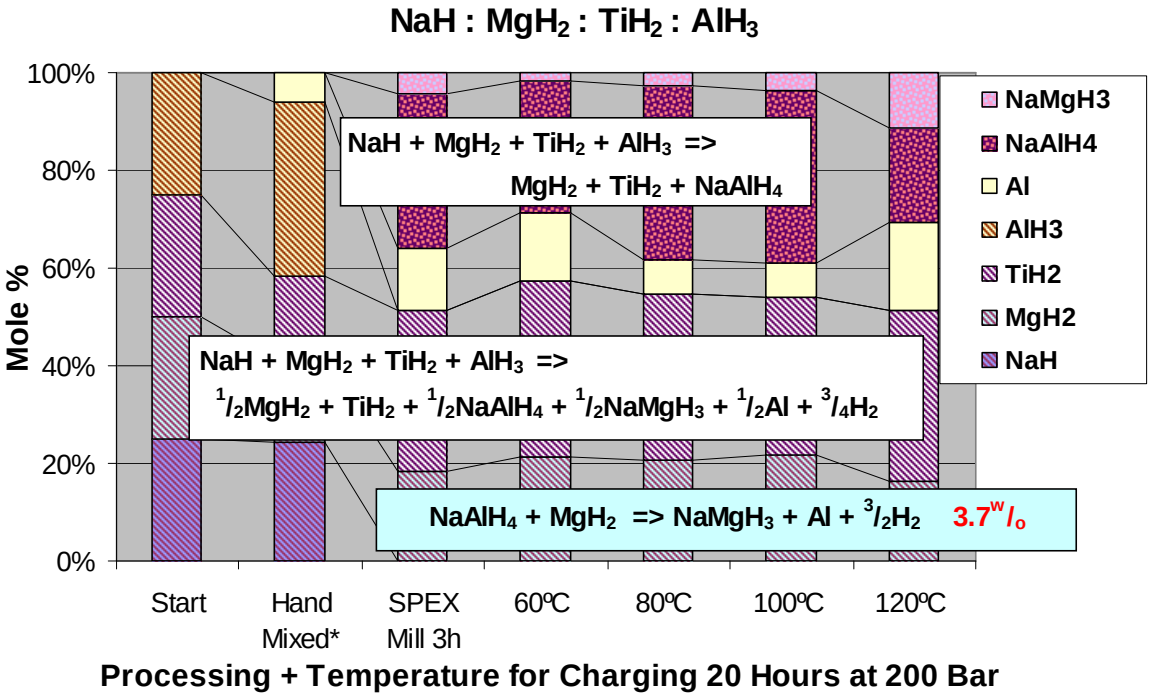

Figure 141: $NaH:MgH_2:TiH_2:AlH_3=1:1:1:1$.

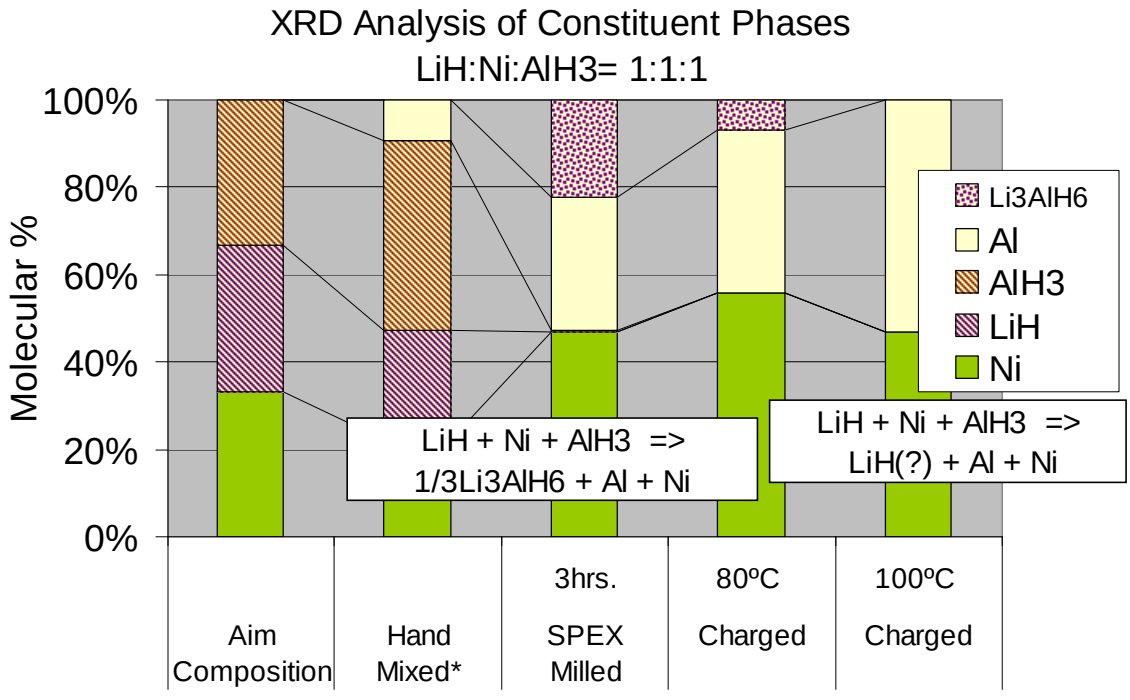

Figure 142: $LiH:Ni:AlH_3=1:1:1$.

Appendix

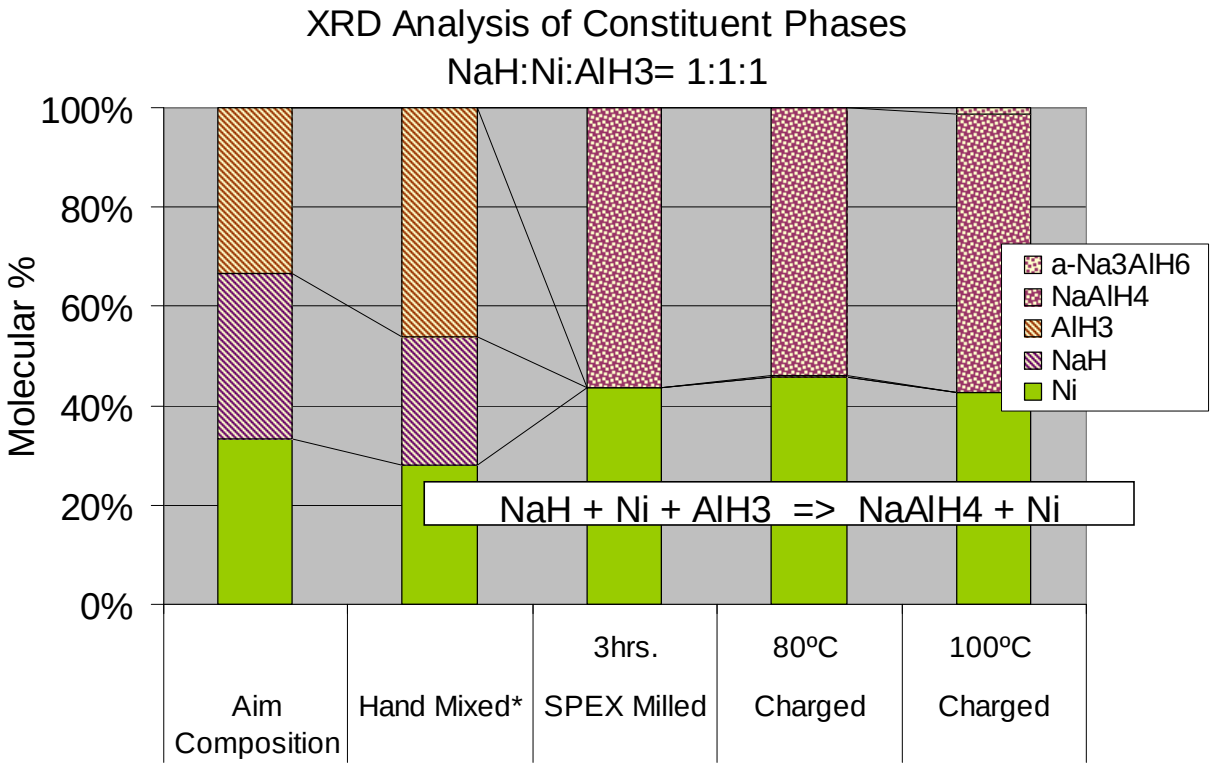

Figure 143: $NaH:Ni:AlH_3$ = 1:1:1.

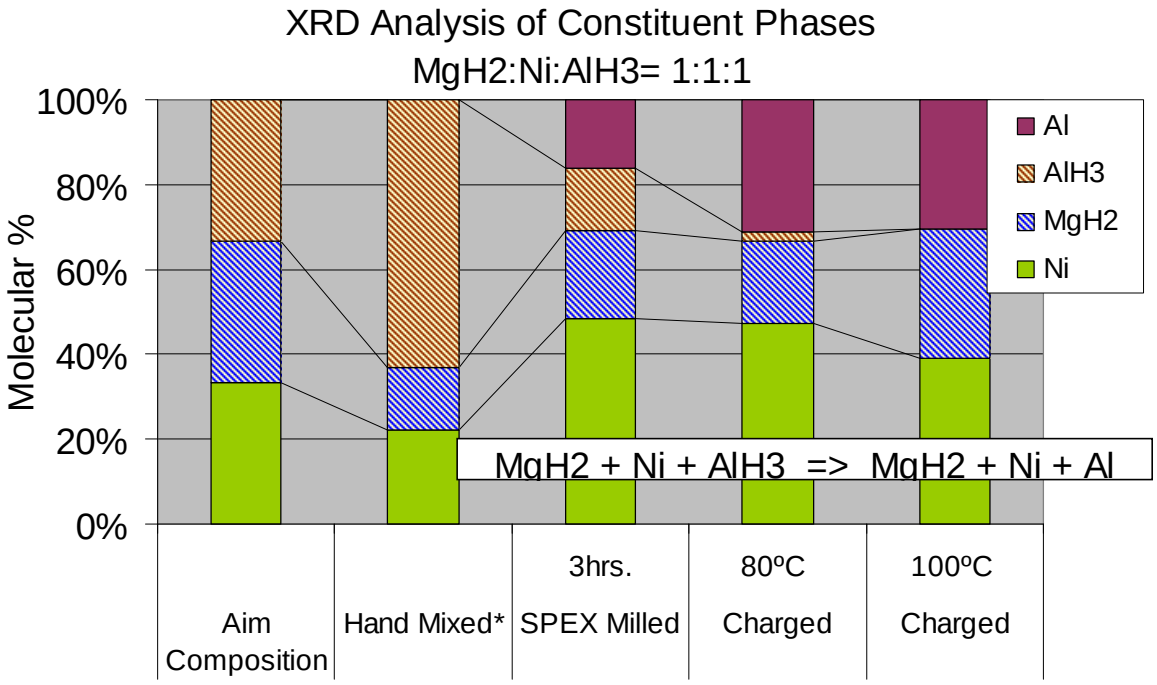

Figure 144: $MgH_2:Ni:AlH_3$ = 1:1:1.

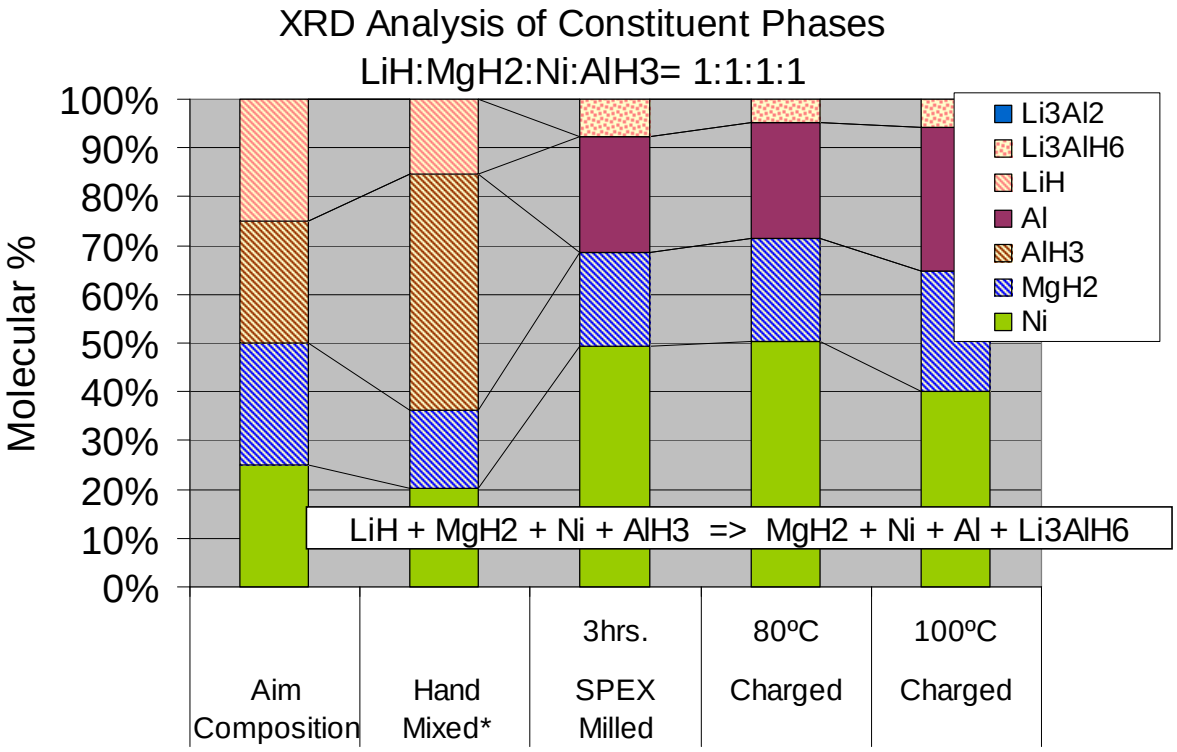

Figure 145: $LiHMgH_2$:Ni:AlH_3 = 1:1:1:1.

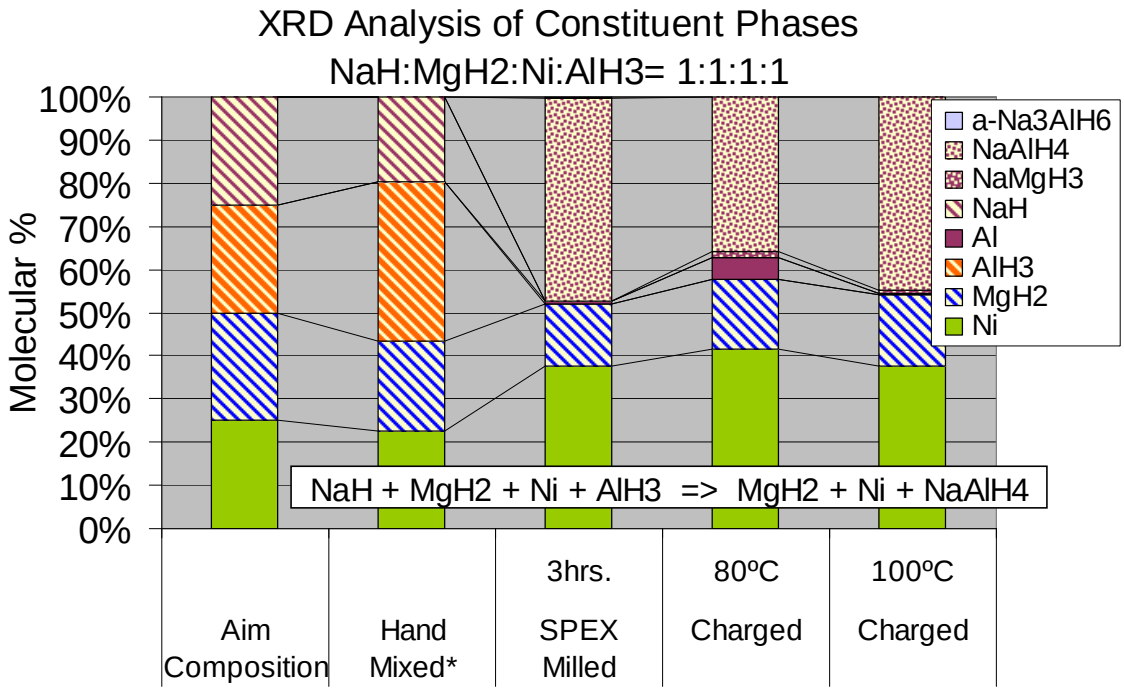

Figure 146: NaH:MgH_2:Ni:AlH_3 = 1:1:1:1.

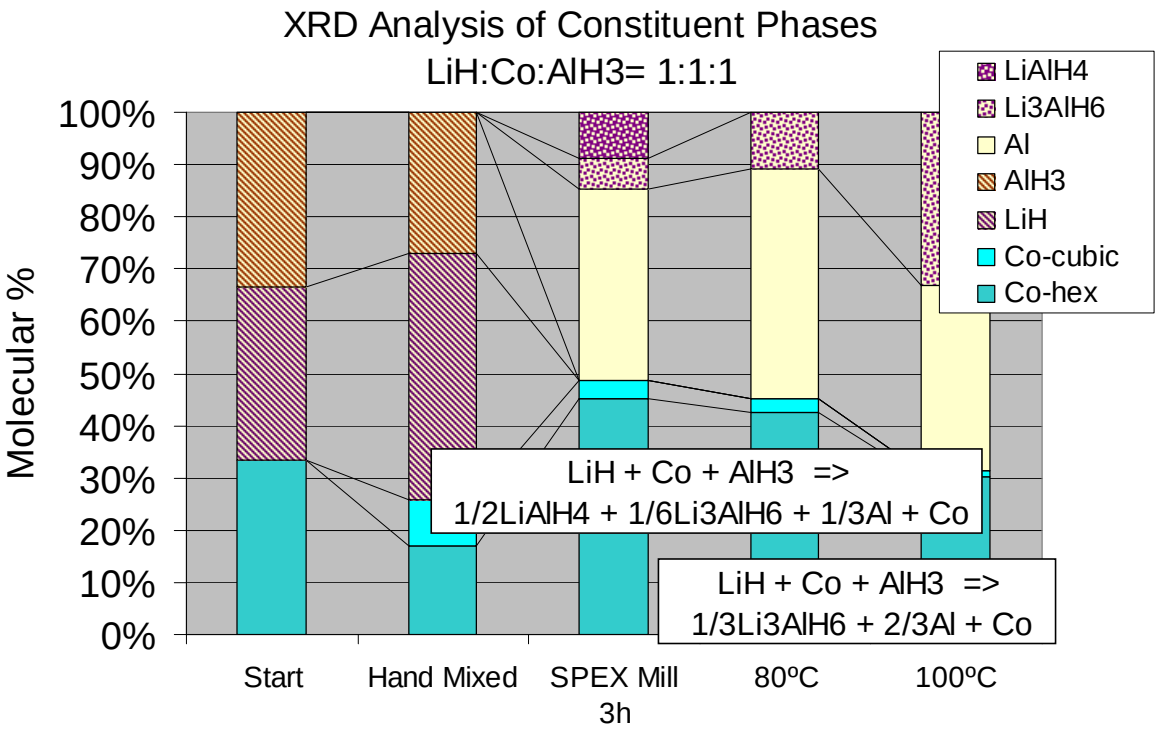

Figure 147: LiH:Co:AlH_3 = 1:1:1.

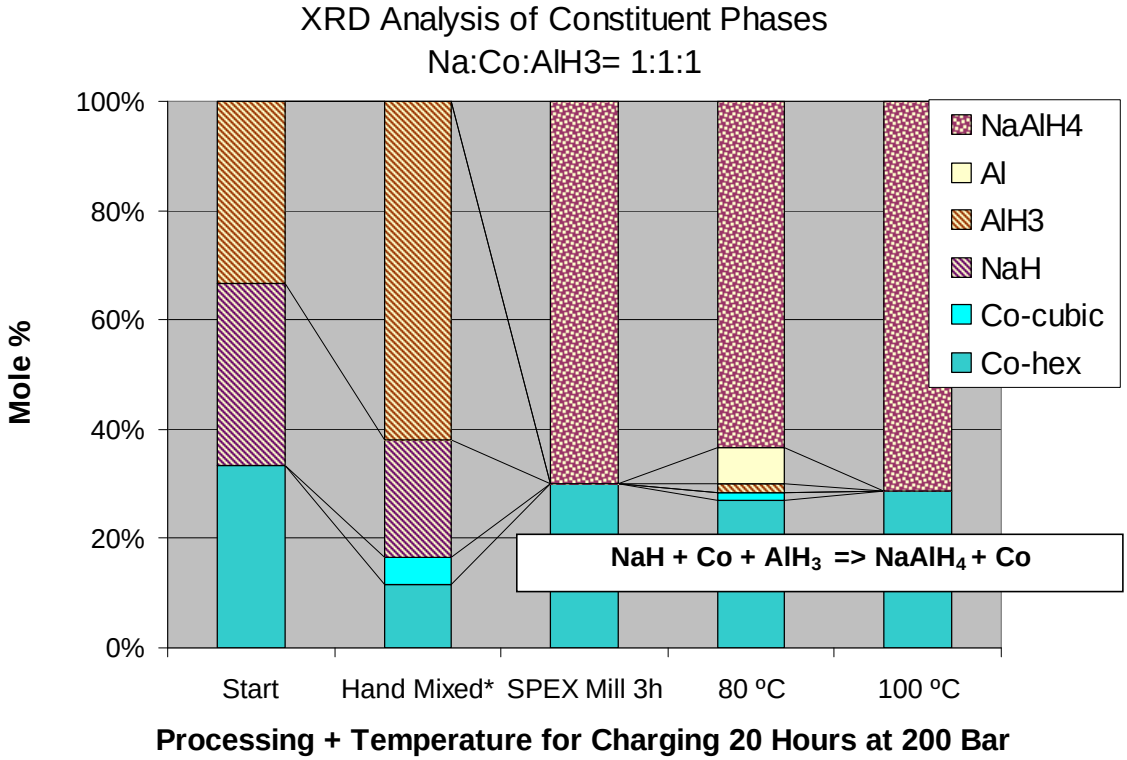

Figure 148: Na:Co:AlH_3 = 1:1:1.

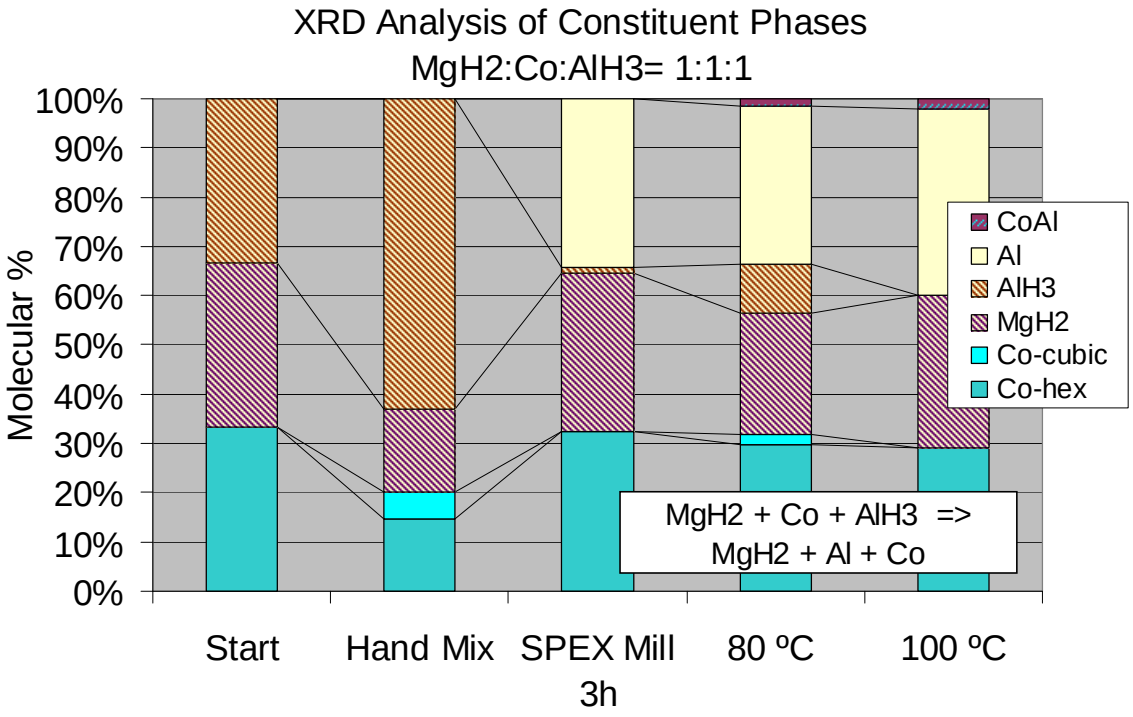

Figure 149: MgH_2:Co:AlH_3 = 1:1:1.

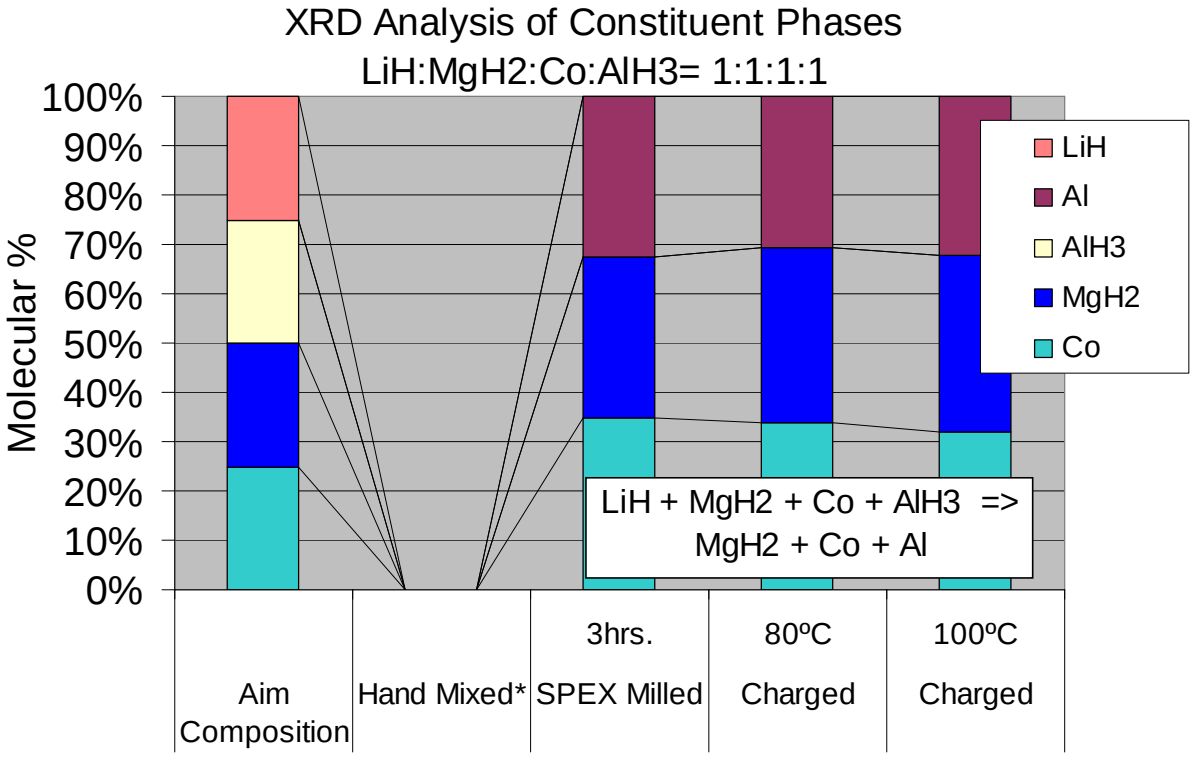

Figure 150: LiH:MgH_2:Co:AlH_3 = 1:1:1:1.

Appendix

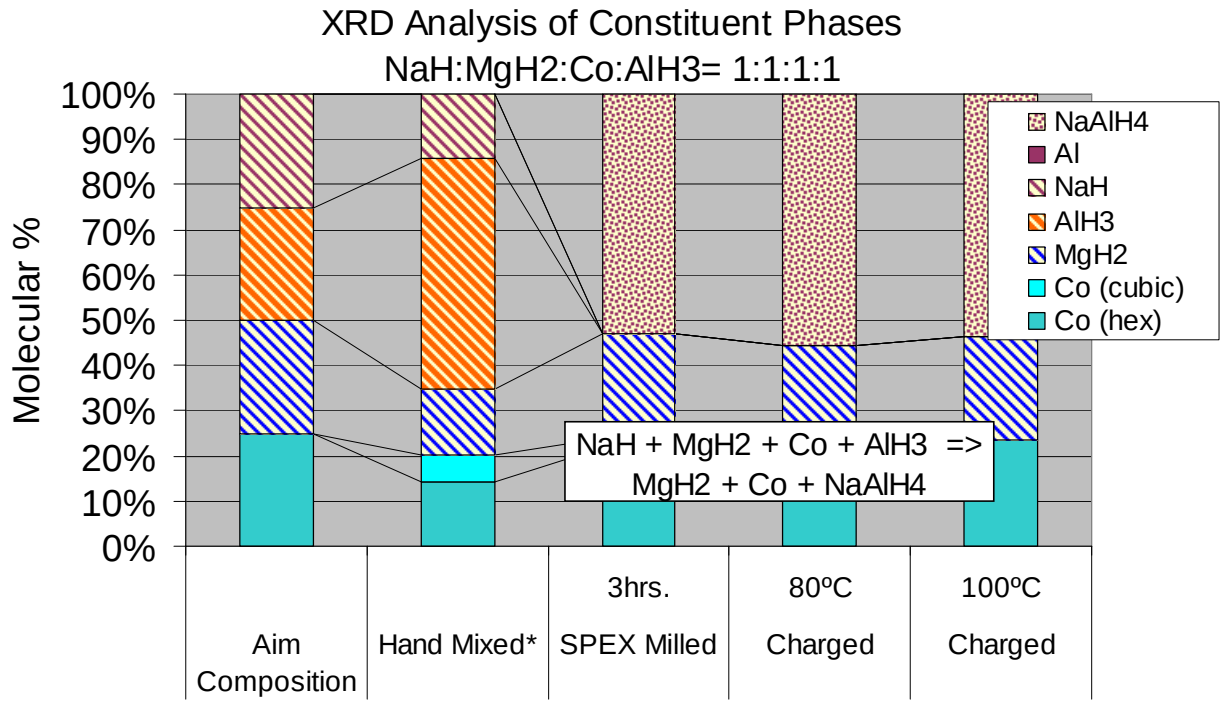

Figure 151: $NaH:MgH_2:Co:AlH_3$ = 1:1:1.

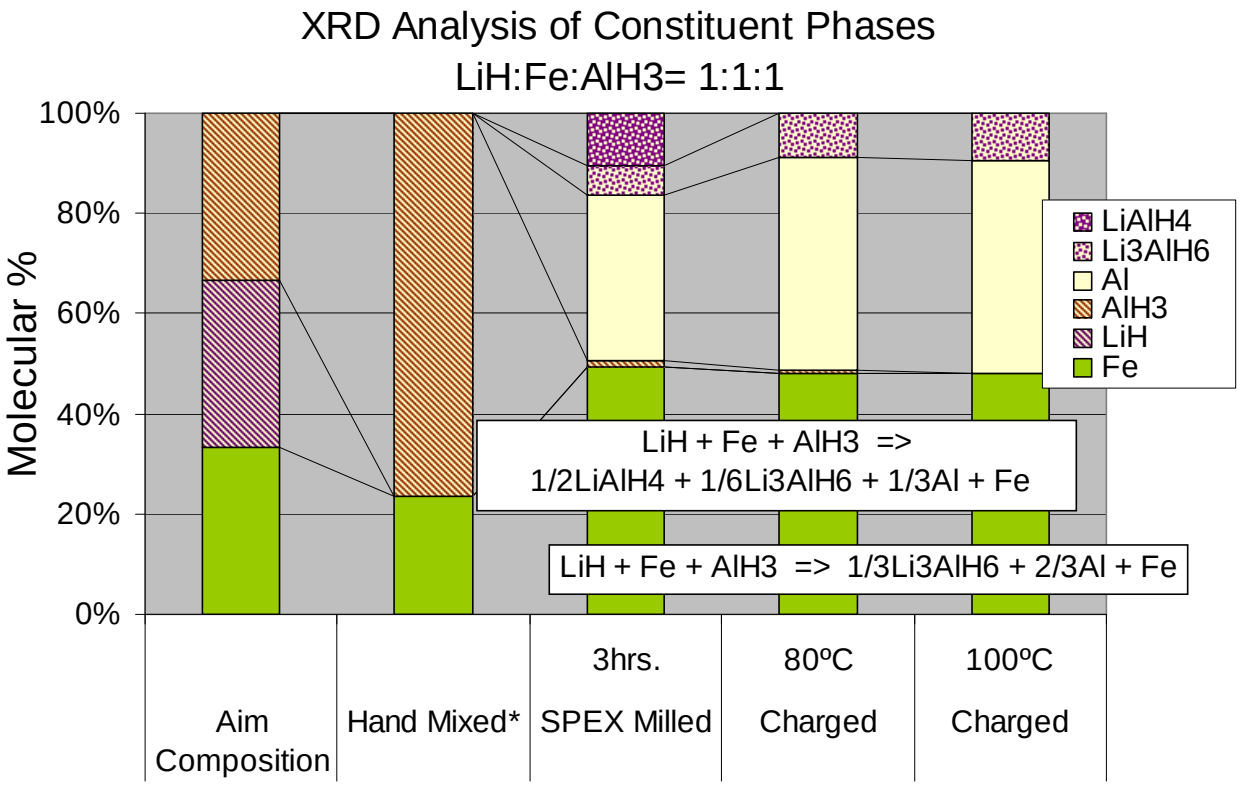

Figure 152: $LiH:Fe:AlH_3$ = 1:1:1.

Appendix

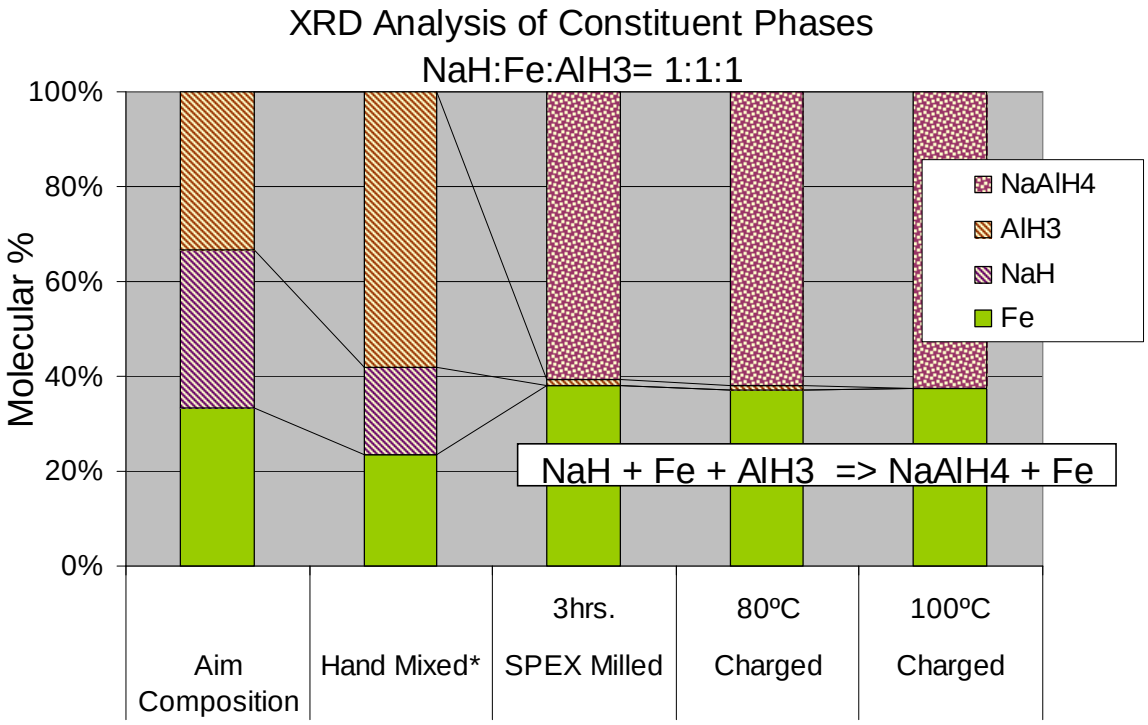

Figure 153: $NaH:Fe:AlH_3$ = 1:1:1.

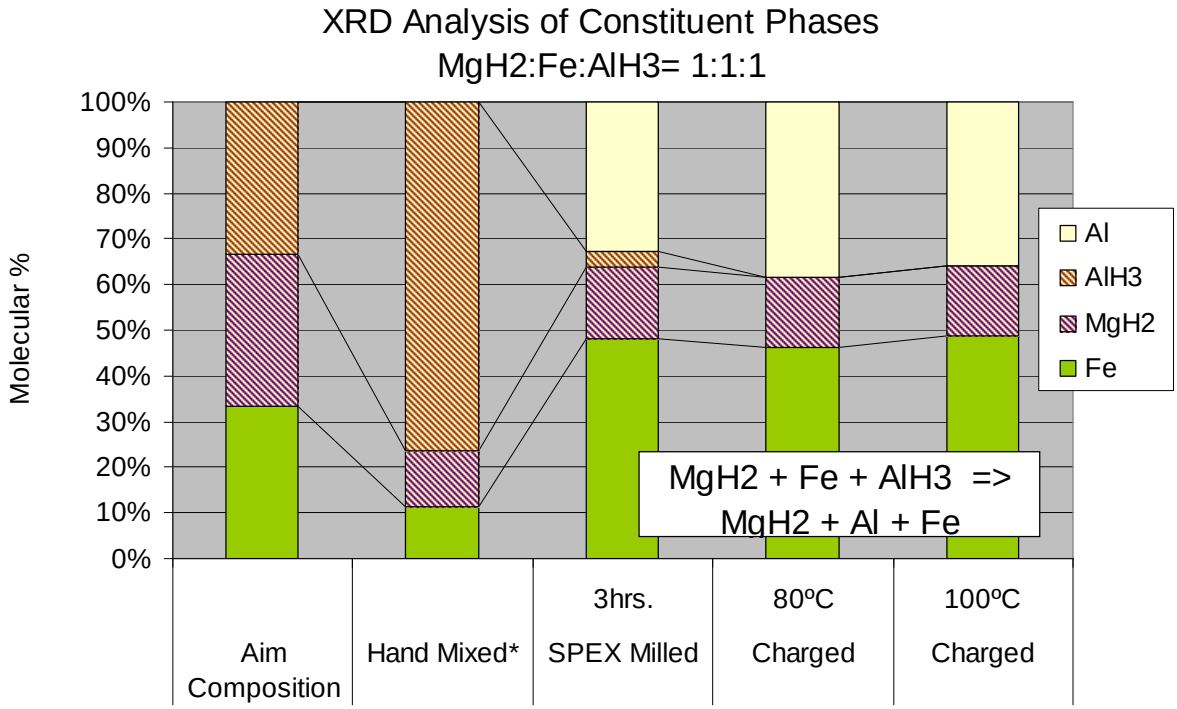

Figure 154: $MgH_2:Fe:AlH_3$ = 1:1:1.

Appendix

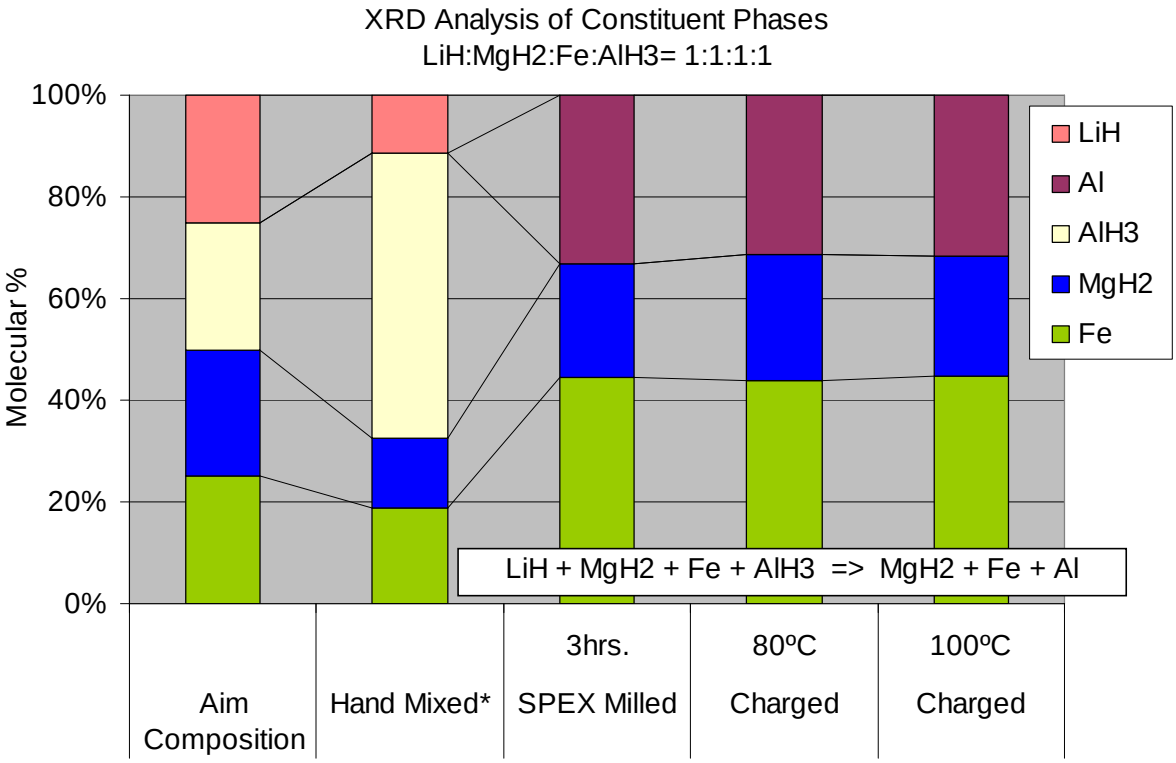

Figure 155: $LiH:MgH_2:Fe:AlH_3$ = 1:1:1:1.

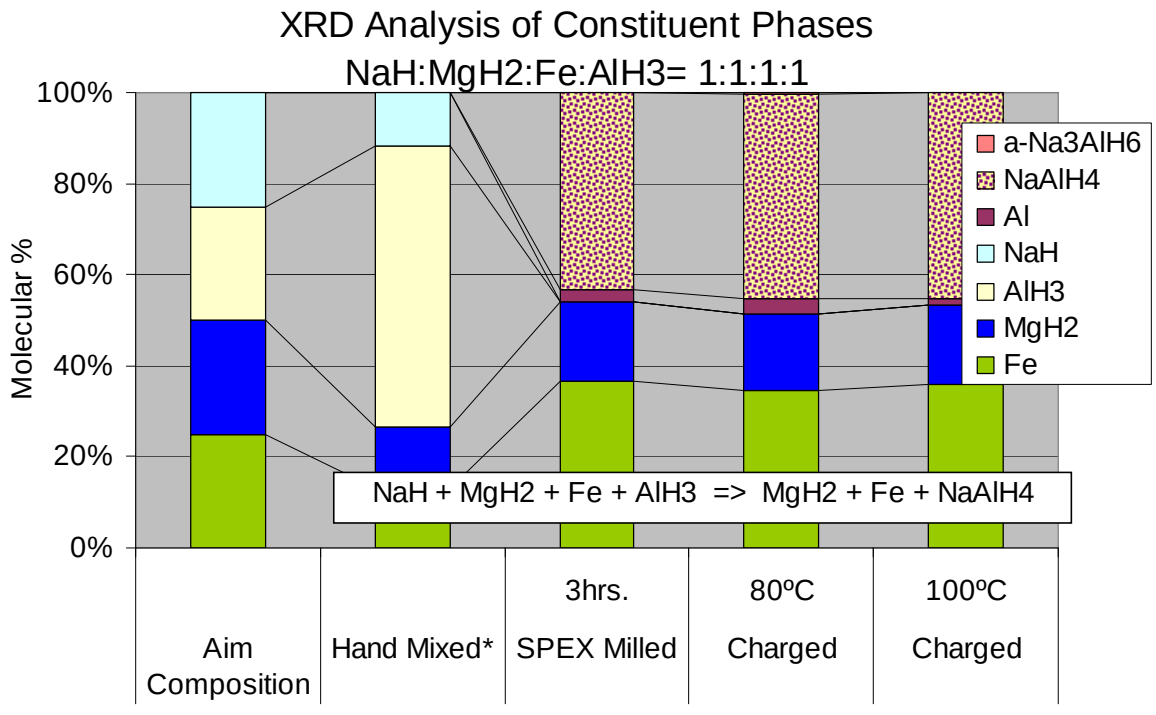

Figure 156: $NaH:MgH_2:Fe:AlH_3$ = 1:1:1:1.

Appendix

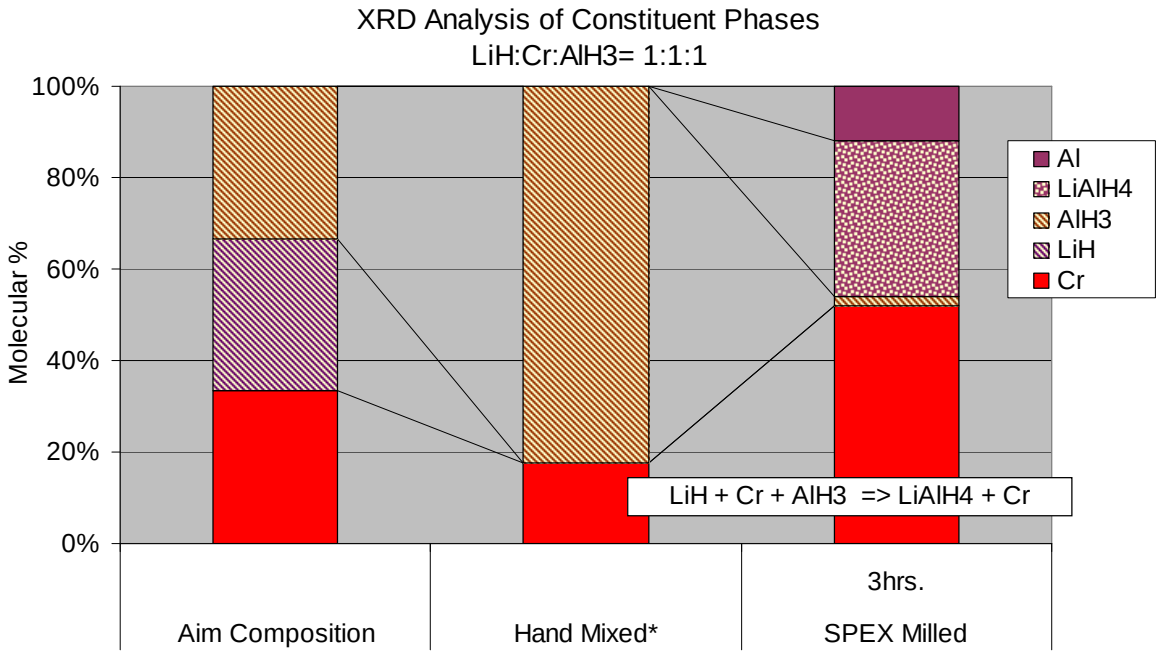

Figure 157: $LiH:Cr:AlH_3$ = 1:1:1:1.

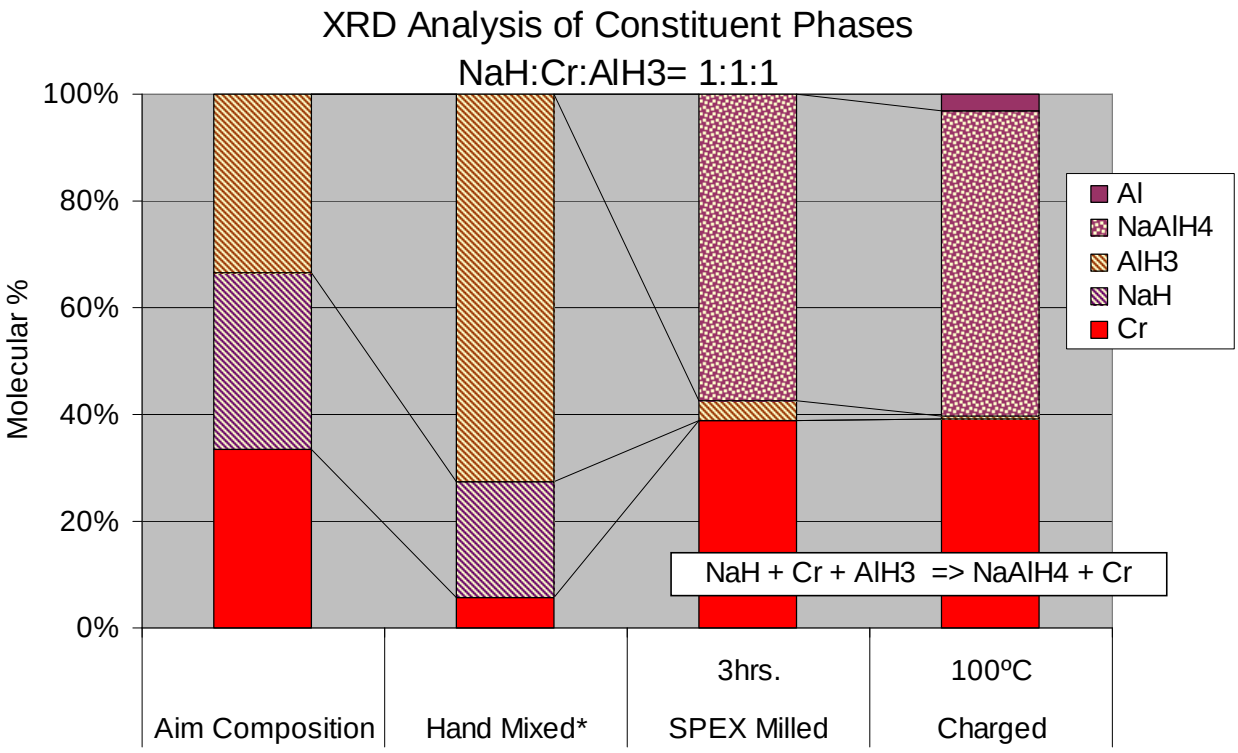

Figure 158: $NaH:Cr:AlH_3$ = 1:1:1.

Appendix

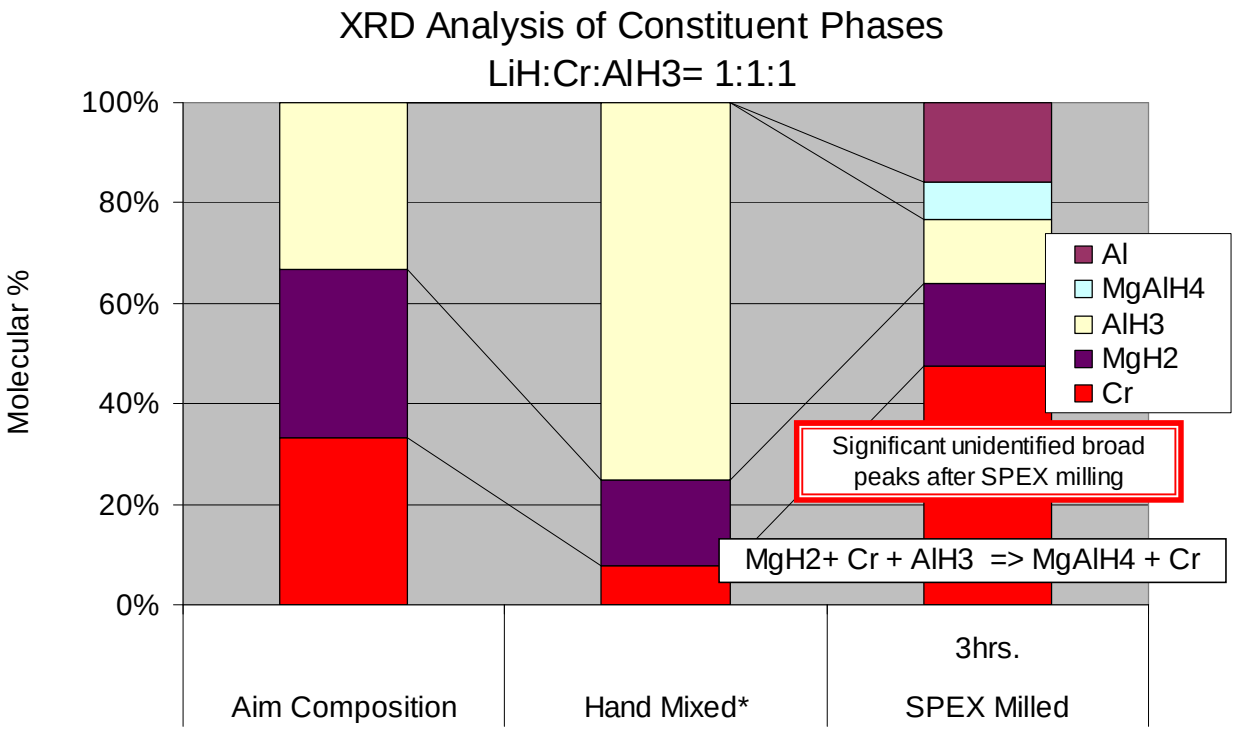

Figure 159: MgH_2:Cr:AlH_3 = 1:1:1.